UNIVERSITÀ DEGLI STUDI DI PALERMO

Dottorato di Ricerca in Scienze Fisiche
Dipartimento di Fisica e Chimica-Emilio Segré
Settore Scientifico Disciplinare – FIS/05 – Astronomia e Astrofisica

A high-resolution study of powerful winds in highly accreting supermassive black holes

IL DOTTORE
YERONG XU

IL COORDINATORE
Prof. MARCO CANNAS

IL TUTOR
Dr. GIANCARLO CUSUMANO

CO TUTOR
Dr. CIRO PINTO

CICLO XXXVI
ANNO CONSEGUIMENTO TITOLO 2024

Declaration

I hereby declare that except where specific reference is made to the work of others, the contents of this dissertation are original and have not been submitted in whole or in part for consideration for any other degree or qualification in this, or any other university. This dissertation is my own work and contains nothing which is the outcome of work done in collaboration with others, except as specified in the text and Acknowledgements. This dissertation contains fewer than 75,000 words including appendices, bibliography, footnotes, tables, and equations, and has fewer than 150 figures.

The chapters of this thesis based on published or submitted work are as follows:

- **Chapter 3**

  Y. Xu, C. Pinto, S. Bianchi, P. Kosec, M. L. Parker, D. J. Walton, A. C. Fabian, M. Guainazzi, D. Barret, G. Cusumano, 'Wind-luminosity evolution in NLS1 AGN 1H 0707-495', *Monthly Notices of the Royal Astronomical Society*, Vol. 508, Issue 4, p. 6049-6067, December 2021

- **Chapter 4**

  Y. Xu, C. Pinto, D. Rogantini, S. Bianchi, M. Guainazzi, E. Kara, C. Jin, G. Cusumano, 'Constraints on the ultrafast outflows in the narrow-line Seyfert 1 galaxy Mrk 1044 from high-resolution time-and flux-resolved spectroscopy', *Monthly Notices of the Royal Astronomical Society*, Vol. 523, Issue 2, p. 2158-2171, August 2023

- **Chapter 5**

  Y. Xu, C. Pinto, E. Kara, M. Masterson, J. A. García, A. C. Fabian, M. L. Parker, D. Barret, W. N. Alston, G. Cusumano, 'Ejection–accretion connection in NLS1 AGN 1H 1934-063', *Monthly Notices of the Royal Astronomical Society*, Vol. 513, Issue 2, p. 1910-1924, June 2022

- **Chapter 6**

  Y. Xu, C. Pinto, J. Ebrero, E. Kara, S. Bianchi, D. Rogantini, M. Guainazzi, D. Barret, W. N. Alston, G. Cusumano, 'A systematic study of the ultra-fast outflow responses to luminosity variations in active galactic nuclei', submitted to *Astronomy & Astrophysics*, December 2023

Yerong Xu
January 2024

Acknowledgements

First and foremost, I would like to thank my supervisors, Giancarlo Cusumano and Ciro Pinto. I am thankful to Giancarlo for providing me with the opportunity to embark on this PhD journey. My deepest gratitude goes to Ciro for his unwavering patience, meticulous guidance, and continuous encouragement. I consider myself extraordinarily fortunate to have had Ciro, such a wise and charismatic astrophysicist, as my supervisor. Throughout the last three years, he has provided me with invaluable advice, ensuring that my papers, proposals, reports, and applications were the best they could have been. Without his immeasurable support, this thesis would not have materialized.

Secondly, I would like to acknowledge my collaborators who have played pivotal roles in my growth as a researcher. Peter Kosec, Daniele Rogantini, Stefano Bianchi, Matteo Guainazzi, Didier Barret, and all of my co-authors have been particularly indispensable to the research presented in this thesis. My scientific results would not be possible without the IT support of Giacomo Fazio and Antonino D'Aì. I would also like to acknowledge Michael Parker for sharing the SPEX-to-XSPEC codes which I have made great use of in this thesis.

Thirdly, I would like to convey my appreciation to Jacobo Ebrero and Erin Kara for their warm hospitality during my visits to ESAC and MIT. These experiences have further solidified my determination to pursue an academic career. I am also deeply grateful to Javier García and Cosimo Bambi, who introduced me to the field of astronomy and taught me how to 'do science'.

Next, I would like to express my gratitude to everyone at INAF-IASF Palermo and UNIPA thanks to whom my time in Palermo was incredible: Alessandra Robba, Alessio Anitra, Vincenzo Sapienza, Francesco Barra, Wladimiro Leone, Carlotta Miceli, Alberto Ulgiati, Rosario Iaria, and Tiziana Di Salvo. Special thanks to my colleagues Alessio Marino, Antonio Tutone, and Elena Ambrosi, who gave me a warm welcome when I first arrived in Palermo without any knowledge of Italian.

Pursuing a PhD is incredibly stressful, and this was exacerbated by the fact that more than half of my PhD journey took place during the COVID-19 pandemic. I am immensely grateful to my ex-girlfriend Yuying Tang, for her steadfast support during this challenging period. Despite our eventual peaceful breakup due to diverse career plans, our long-distance

relationship of over two years and her dedicated efforts in our daily video calls provided me with immeasurable strength and prevented me from falling into depression. Furthermore, I would also like to express my gratitude to Pengxiao Yao, Zhenlin Zhu, Jingtian Xu, Feng Chen, and my other friends for their emotional support and companionship throughout my PhD journey. Special gratitude goes to my friends Yizhou Hu, Yanchun Yang, Zhixin Jiang, Zhuyun Tao, and Yiming Qian for their consistent presence, marked by daily check-ins in our group and occasional life-related exchanges. Your support and friendship have made a significant and positive difference.

Lastly, my deepest appreciation goes to my family. I can never find sufficient words to fully express my gratitude to my parents, Bin Wu and Xuejun Xu, who have given me endless support throughout my life. None of my achievements would have been possible without you.

Yerong Xu

Palermo, 2024

Abstract

An active galactic nucleus (AGN) is powered by the accretion of matter infalling onto a supermassive black hole (SMBH), found at the core of most galaxies. The accretion process releases an enormous amount of radiation, while concurrently propelling matter away through winds, especially for those accreting close to or above the Eddington limit. Black holes at Eddington accretion rates are growing fast but are also expected to launch powerful winds of hot plasmas due to the extreme radiation pressure from the underlying accretion disk. These outflows, when intersecting our line of sight to the radiation source, leave imprints in X-ray spectra of the accretion disk in the form of Doppler-shifted lines. AGN winds play a critical role in regulating SMBH growth and the host galaxy's evolution by carrying away a significant portion of infalling matter. Notably, certain AGN outflows, known as ultra-fast outflows (UFOs), can achieve speeds exceeding 3% and even reach 40% of the speed of light. Due to their extreme velocities, UFOs are regarded as a promising candidate to affect the galaxy evolution by depositing significant kinetic energy into the surrounding gas, thereby heating the interstellar medium and quenching the star formation rate of the host galaxy. However, the uncertainties in the geometries, launching mechanisms, and outflow rates of such outflows imply substantial uncertainty in determining their effects on SMBH evolution and the impacts on host galaxies.

By using both the currently most advanced photoionization modeling method and the data from the currently best instrument for soft X-ray high-resolution spectroscopy, *XMM-Newton* Reflection Grating Spectrometer (RGS), I studied the nature of UFOs in soft X-ray bands of a super-Eddington narrow-line Seyfert 1 (NLS1) galaxy and a high-Eddington NLS1 AGN and extend the analysis to a large sample of high-Eddington AGN. UFOs in the soft X-ray bands are largely overlooked before my works and commonly exhibit a cool temperature. My results reveal that UFOs in these systems are driven by the radiation pressure and are sufficiently energetic to affect the evolution of their host galaxies, while the radiative acceleration may decrease as the accretion rate increases, probably due to the change in the geometry of accretion flows. Additionally, I also achieved the first discovery of evidence for the connection between the accretion inflows and UFOs in the soft X-ray band of an NLS1 galaxy.

Table of contents

List of figures

List of tables

Chapter 1

Introduction

1.1 Active Galactic Nuclei (AGN)

Abundant observational evidence strongly supports the presence of supermassive black holes (SMBHs) with masses in the range of $M_{BH} \sim 10^6$–$10^{10} M_\odot$ situated at the core of nearly all galaxies [81, 122], where $M_\odot$ is the mass of the sun. These supermassive objects may be formed from the direct collapse of matter in the early Universe [21], or from stellar-mass black holes undergoing super-fast accretion, or by the mergers of smaller black holes [232]. At any moment, the majority of galaxies host a dormant SMBH, i.e. it is not actively accreting materials [169]. When the SMBHs undergo significant accretion, they emit radiation across the entire electromagnetic spectrum, ranging from radio to gamma-rays. Consequently, such galaxies are named active galaxies, and their central regions are recognized as active galactic nuclei (AGN).

1.1.1 Unified Model

The taxonomy of AGN is rather complex including a large variety of sub-classes. AGN are broadly categorized into three main types according to their brightness: quasars [312], where the AGN component overwhelmingly dominates the radiative output of the entire host galaxy; Seyfert galaxies [315], where the nuclear regions significantly contribute to the energy output of host galaxies without outshining it; and Low Luminosity AGN (LLAGN), where the nucleus emits only a small fraction of the galaxy's radiative output.

A further categorization of AGN is based on the optical and ultra-violet (UV) spectral features. AGN are classified into Type 1 and Type 2, depending on whether broad lines (with a full width at half maximum FWHM ≥ 1000 km/s) are present or absent in their spectra, respectively. Additionally, the classification of AGN can depend on their degree of radio

loudness. Approximately 10%-20% of all AGN exhibit significantly brighter (> 10 times) radio emission compared to their optical brightness and are identified as radio-loud (RL) AGN while the others are referred to as radio-quiet (RQ) AGN [161].

A unification model was thus invoked to explain different AGN phenomena, based on the idea that different AGN are fundamentally similar, but viewed at different orientations [9, 348]. Fig.1.1 illustrates a schematic picture of AGN in this unified model, with various AGN types denoted in *green* depending on the viewing angles, and the fundamental components highlighted in *white*. In this model, an AGN includes a SMBH at its core, a sub-parsec (sub-pc) accretion disk surrounding the SMBH, a broad line region (BLR) made up of high-density ($n_{\rm e} \gtrsim 10^8\,{\rm cm}^{-3}$) and dust-free gas clouds in Keplerian motion at a distance of 0.01–1 pc from the SMBH [237], an axisymmetric dusty torus situated 0.1–10 pc from the SMBH [177, 236], an outflowing radio jet directed generally along the disk's axis, and the narrow line region (NLR) composed of low-density, low-velocity and ionized gas extending to 100–1000 pc [236, 237]. The key element in this unified model is the optically thick torus, which absorbs the optical, UV, and X-ray emissions from the nucleus and the BLR. However, the narrow line region remains visible due to its extension. In this framework, the Type 1/2 bimodality arises as an orientation effect: Type 1 AGN are those whose viewing angle allows the central engine together with the BLR to be directly seen. In contrast, Type 2 AGN are those whose nuclear region is obscured by the opaque torus.

While the orientation-based unified model successfully explains the spectral diversity observed in most AGN, some recent observations have posed challenges to its validity. One of the challenges arises from the discoveries of unobscured Type 2 AGN [246, 243]. These sources exhibit only narrow emission lines in the optical band and little or no obscuration in the X-ray band, contradicting the predictions of the unified model. Another notable challenge comes from the infrared observations of AGN. Recent mid-infrared interferometry observations of Type 1 galaxies reveal that the majority of infrared emission originates from the dust in the polar region instead of in the disk plane, suggesting a potential deviation from the presumed shape of torus [125]. On the other hand, the unified model does not account for changes in accretion rates. A peculiar subclass of AGN, known as Changing-look AGN (CLAGN), presents transitions between Type 1 and 2 classifications with relatively short timescales, typically $\sim$ 1–10 years or even shorter [103, 238, 342]. These timescales are significantly less than the expected viscous timescales for AGN $\sim$ 400 years [297]. The origin of these rapid transitions is generally attributed to variations in the accretion flow, including disk instabilities [193, 13, 238] and major disk perturbations, such as stellar tidal disruption events (TDEs, [349]). These phenomena provide an additional challenge to the unified model, which assumes a static and uniform AGN population.

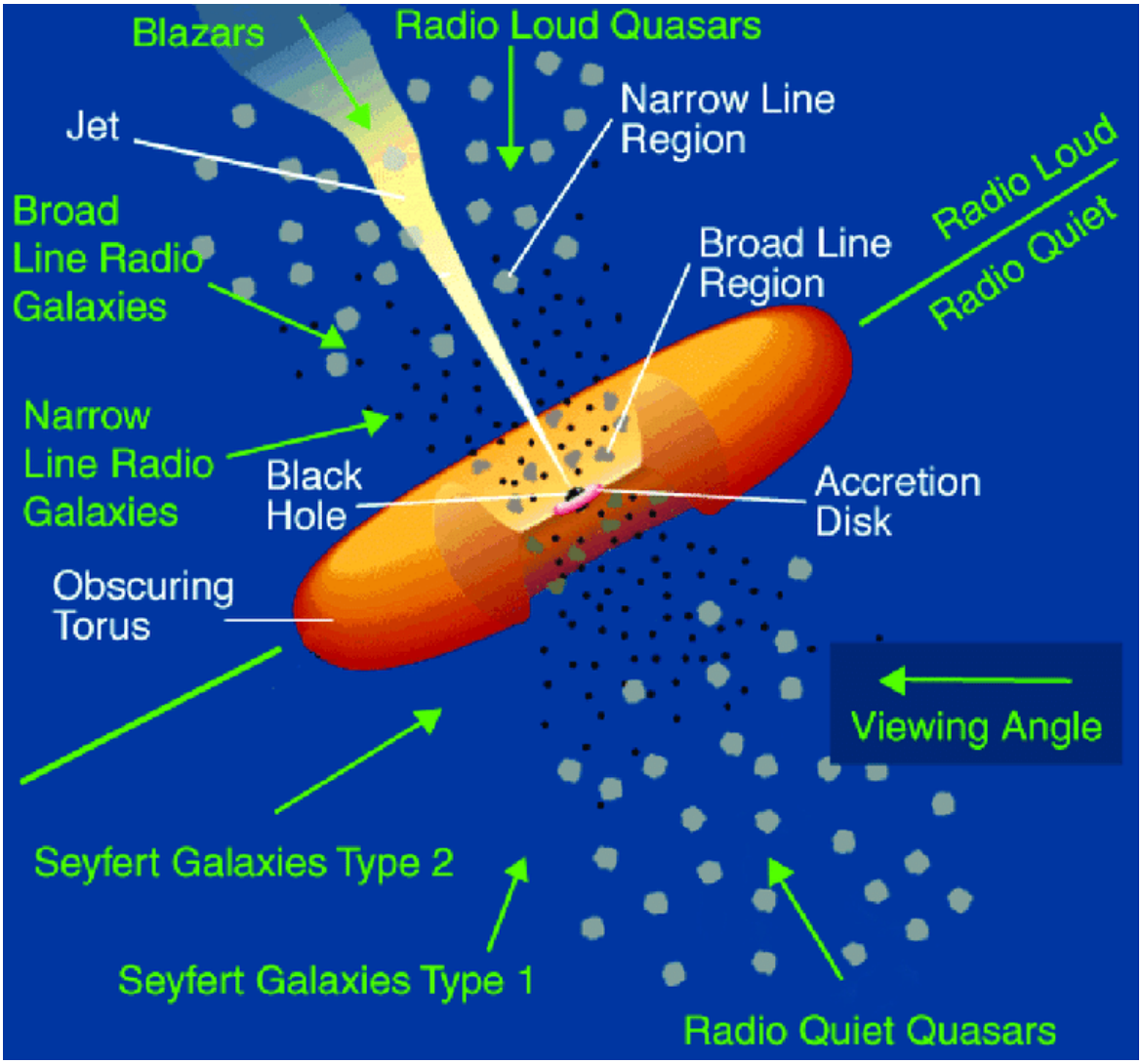

Fig. 1.1 The AGN unified model (credit: NASA, based on [348]). Different AGN regions are labeled in *white* while different types of AGN are labeled in *green*. The manifestation of an AGN heavily depends on our line of sight (LOS) towards the system, although it is also linked to its accretion state, which is beyond the scope of the unified model. When the LOS traverses the obscuring dusty torus, the broad line region is not observable, leaving only narrow optical/UV lines in the spectrum and the AGN is classified as Type 2. Otherwise, the AGN is categorized as Type 1. Additionally, AGN can also be split into two subclasses depending on the presence of a radio jet: radio-loud and radio-quiet.

1.1.1.1 Narrow-line Seyfert 1 galaxies

This thesis focuses on a subset of Seyfert 1 galaxies known as narrow-line Seyfert 1 galaxies (NLS1). The primary criterion for categorizing them as NLS1 involves the width of the broad component in their optical Balmer emission lines, coupled with the relatively weak [OIII]λ5007 emission (the full width at half maximum of Hβ, $\mathrm{FWHM}_{\mathrm{H}\beta} \leq 2000\,\mathrm{km/s}$ and the intensity ratio between the [OIII] and Hβ emission, [OIII]/H$\beta < 3$, [242, 108]). NLS1 galaxies exhibit notable features such as FeII emission [29, 353], with the ratio FeII/Hβ being twice as strong as that in other Seyferts. NLS1s also display rapid temporal X-ray variability [351, 189, 221]. Furthermore, these objects are typically characterized by lower black hole masses compared to other Seyferts, ranging between $10^{6-7}\,M_{\odot}$ [28, 111, 217, 245], and high accretion rates, often approaching or surpassing their Eddington limits, $L_{\mathrm{Edd}} = 4\pi G M_{\mathrm{BH}} m_{\mathrm{p}} c/\sigma_T$, to be defined by Eq.1.7 in Sec.1.2.1 [42, 360].

1.1.2 Spectral Energy Distribution of Active Galactic Nuclei

In Fig.1.2, a schematic illustration depicts the spectral energy distribution (SED) of an AGN, spanning from radio frequencies to hard X-rays. The figure illustrates the various physical components believed to constitute the overall observed SEDs of AGN. Nevertheless, it is important to emphasize that the proportional contribution of these components can vary dramatically among different types of AGN.

1.1.2.1 Accretion Disk

The standard radiatively-efficient AGN model involves an SMBH surrounded by an optically thick accretion disk [316, 375]. The disk can be geometrically thin or thick depending on the accretion state [2]. The resulting continuum spectrum is expected to be thermal, characterized by a black-body temperature of $\sim 10^5$ K that peaks in the UV band ($\approx$ 10–400 nm). Unfortunately, this UV coverage is a region of the electromagnetic spectrum that is challenging to observe from the Earth due to the interstellar medium (ISM) absorption.

1.1.2.2 Hot corona

Within the inner region of the accretion disk, it is observed that there exists an optically thin and high-temperature ($\approx 10^8$ K) electron plasma, known as a hot corona [326, 113, 114], where the UV and optical photons, produced at the accretion disk, undergo Compton up-scattering. As a result, the spectrum in the X-ray band above a few keV can be roughly

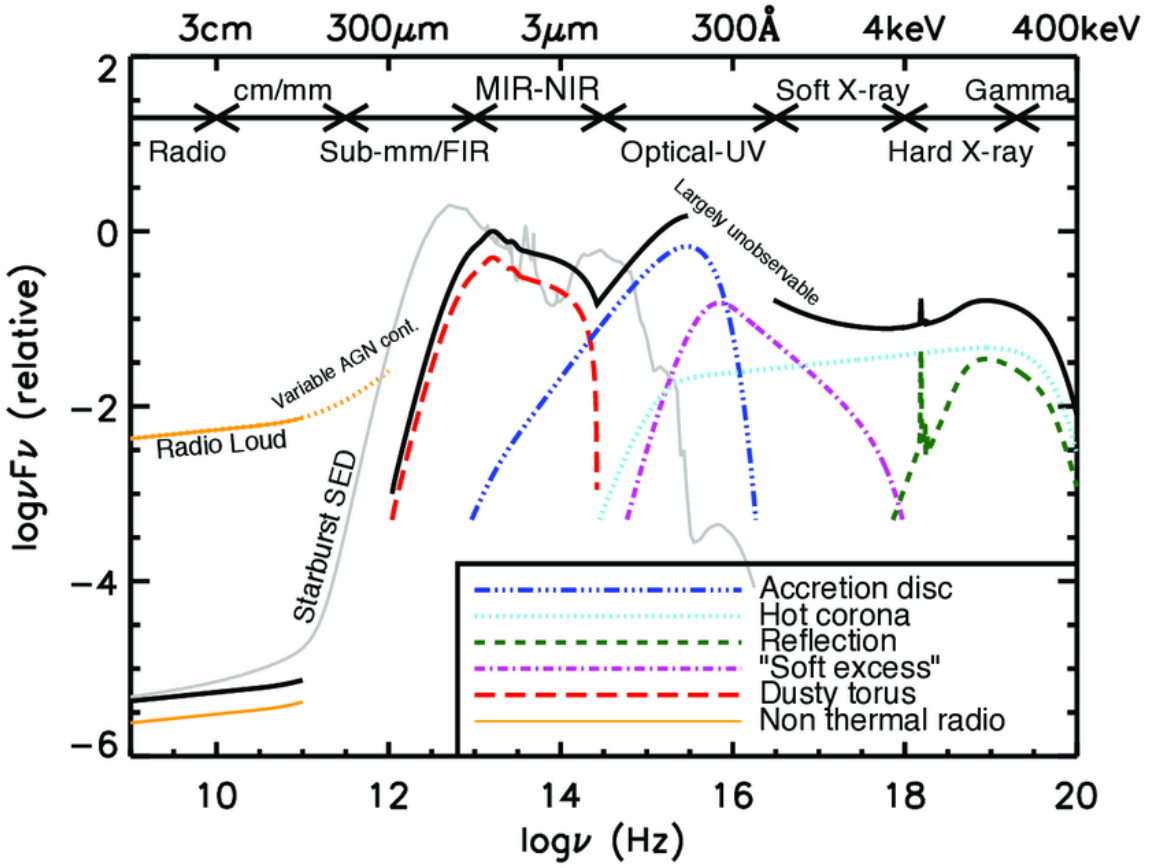

Fig. 1.2 Schematic representation of the AGN spectral energy distribution including all the main physical components (credit to [117, 121]). The total observed spectrum is shown in *black*. The individual components are: 1) the synchrotron radio emission from a jet distinguishes radio-loud from radio-quiet AGN (*orange*); 2) the thermal infrared emission from the dusty torus (*red*); 3) the accretion disk emitting as a color temperature corrected blackbody peaking in UV band (*blue*); 4) the soft X-ray excess which may arise from the Comptonization of disk photons in the 'warm' region of the inner disc or from the relativistically blurred reflection ([62, 98, 257, 229, 256, 371], *purple*); 5) primary X-ray power-law continuum arising from the Comptonization of disk photons in the hot X-ray corona (*cyan*); 6) reprocessed X-ray photons from the primary continuum in the accretion disk, featuring the iron K line at 6.4–7.0 keV and the Compton hump at 20–30 keV (*green*).

modeled as a power-law, with an exponential high-energy rollover depending on the temperature of the plasma, typically in the range of 20–200 keV [298].

1.1.2.3 X-ray Reflection

A fraction of coronal emission serves to illuminate back the accretion disk or the torus, creating an additional 'reflection' component, i.e. reprocessed X-ray photons, that consists of the Compton hump and fluorescent emission lines [100, 304, 305]. The Compton hump typically peaks at 20–30 keV, where the low-energy side is shaped by the photoelectric absorption of the iron and the high-energy side stems from the Compton down-scattering of high-energy coronal photons reprocessed in the accretion disk or distant matter [273]. The most prominent atomic features are Fe K lines at 6.4–7.0 keV (depending on the ionization state of the reflecting material). These lines are often broadened and distorted by Doppler relativistic effects due to the strong gravitational field around the black hole, particularly when the reflection occurs in the proximity of the SMBH [74, 188]. Such distortion provides valuable insights into the properties of the inner accretion disk and SMBH, such as the black hole spin and the innermost radius of the disk. Alternatively, the iron K line can appear narrow if the reflected emission originates from mainly the outer disk or torus [218].

1.1.2.4 Soft Excess

The soft excess, a broad and featureless spectral component, is commonly observed below $\sim$2 keV in the soft X-ray band of the majority of Type 1 AGN [344]. It can be effectively described by a thermal black body component with a temperature of $\sim$0.1 keV [320]. However, a consensus regarding the origin of the soft excess remains elusive. Comptonization of disk photons in a warm ($\sim 10^6$ K), optically thick plasma (warm corona) is a viable mechanism to extend the disk emission to soft X-ray energies. The warm corona may be situated in the inner regions of the accretion disk [62] or in an extended corona located above the disk surface [256]. Another explanation involves the reflection of the primary radiation in a high-density ionized disk [305, 46, 98, 99]. In this scenario, the soft X-ray spectrum of the reflected radiation contains a wealth of fluorescence emission lines, and their intensity will be boosted by the inner high-density disk. The strong gravity in the vicinity of the black hole can smooth these lines into a featureless component, thereby creating the observed excess. Consequently, detecting relativistically blurred reflection lines in the soft X-ray band would strengthen the reflection explanation for the soft excess, which will be shown in Chapter 5.

1.1.2.5 Dusty Torus

According to the unified model, enveloping the nuclear region of an AGN is a toroidal dusty region that is both geometrically and optically thick. The dust within this region is heated by absorbing photons from the accretion disk and BLR, consequently re-emitting thermal radiation in the infrared ($\approx$ 1–1000μm, [258, 306]). Numerous observations of nearby AGN indicate that the torus is multi-phase and multi-dynamic rather than a continuous structure [177, 355]. An inner hot structure exists in close proximity to the dust sublimation radius ($T_{\rm dust} \sim$ 1500–2000 K), while the cold outer dust ($T_{\rm dust} \sim 10$ K) is located between 5–10 pc from the SMBH and is thought to function as a reservoir connecting the host galaxy to the accretion structure [124].

1.1.2.6 Relativistic Jets

The synchrotron radio emission emanating from a jet serves as a distinguishing feature between radio-loud from radio-quiet AGN. Unlike the focus of this thesis on winds, which are wide-angle and at most sub-relativistic, jets are usually highly collimated and relativistic. The formation of a jet occurs when the black hole is spinning, and the accretion disk possesses strong magnetization. Powerful jets can emerge from their galactic nuclei in a relativistic, supersonic, and proton-dominated state, extending to strong, hot spot shocks with a range spanning orders of Mpc. In contrast, weak jets degrade into buoyant plumes and bubbles [23].

1.1.3 AGN Feedback and Outflows

AGN might significantly influence the evolution of their host galaxies, which seems incredible given the nine orders of magnitude difference in physical size scales between an SMBH and its host galaxy - equivalent to the contrast between the size of a coin and the Earth. Several observational results indicate a correlation between the SMBH mass and the stellar velocity dispersion of the host galaxy (Fig.1.3, [168]). According to the virial theorem, the velocity dispersion reflects the kinetic energy, which is directly linked to the potential energy of the system. Consequently, the stellar velocity offers an indirect gauge of the depth of the gravitational potential well of the galaxy, providing an indirect measurement of the galaxy mass. Thus, it is now established that the SMBH is correlated with the host galaxy, as evidenced by correlations between the SMBH mass and 1) the stellar velocity dispersion [82, 81]; 2) the bulge luminosity [205, 112]; and 3) the mass of the galaxy bulge [212, 292].

Furthermore, it has been observed that the evolution of the cosmic star-formation rate density and the growth of cosmic black holes follow a similar pattern with respect to redshift

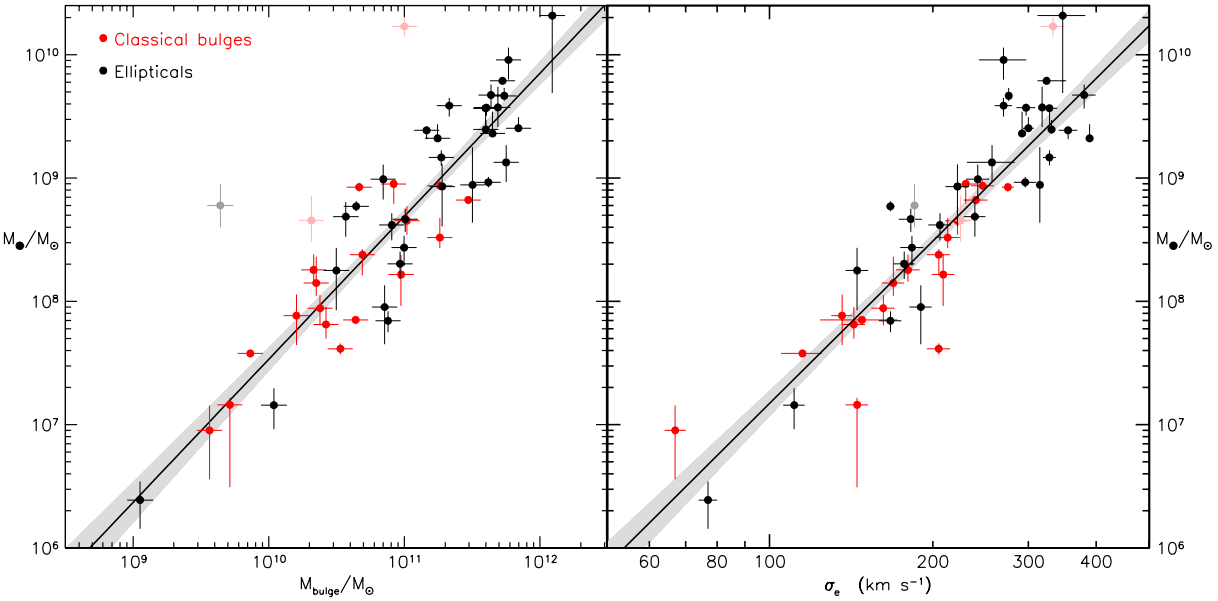

Fig. 1.3 The linear correlations between the mass of the central SMBH $M_\bullet$ and the properties of the host galaxy bulge, i.e., the mass $M_{\rm bulge}$ (*left*) and the effective stellar velocity dispersion $\sigma_{\rm e}$ (*right*). See further details in [168] and references therein.

(Fig.1.4, [4, 168]). The cosmic space density of SMBH growth (i.e. mass accretion rate) peaks at redshift $z \approx 1$–3 [346, 213, 128], aligning with the epoch when the space density of the most intense star-forming galaxies also peaks, concurrent with the maximum in cosmic star formation density [203].

These findings collectively indicate the presence of a self-regulating feedback mechanism, named AGN feedback. This mechanism operates through the interaction between the energy and radiation generated by accretion onto the SMBH and the gas within the host galaxy. The interaction may arise where the intense flux of photons and particles produced by an accreting AGN sweeps and heats the ISM of the galaxy bulge, ultimately terminating star formation. This, in turn, hinders the growth of the SMBH [71].

Outflows from AGN primarily act in two modes. The kinetic or radio mode, involving powerful and highly collimated jets, typically operates when the galaxy is a massive brightest cluster galaxy (BCG) at the cool core of galaxy clusters. This mode plays a crucial role in hindering the efficient cooling of the intracluster medium (ICM, [224, 255, 76, 223]), which is effective on large scales (up to $\gtrsim 100$ kpc). The other mode is the radiative or wind mode, characterized by direct radiation pressure on dust ($\sim$kpc scale) [132, 134, 133] or wide-angle winds [163] prevalent in luminous AGN, where jets are inefficient at depositing energy into the host galaxies [317, 71]. This thesis specifically delves into the investigation

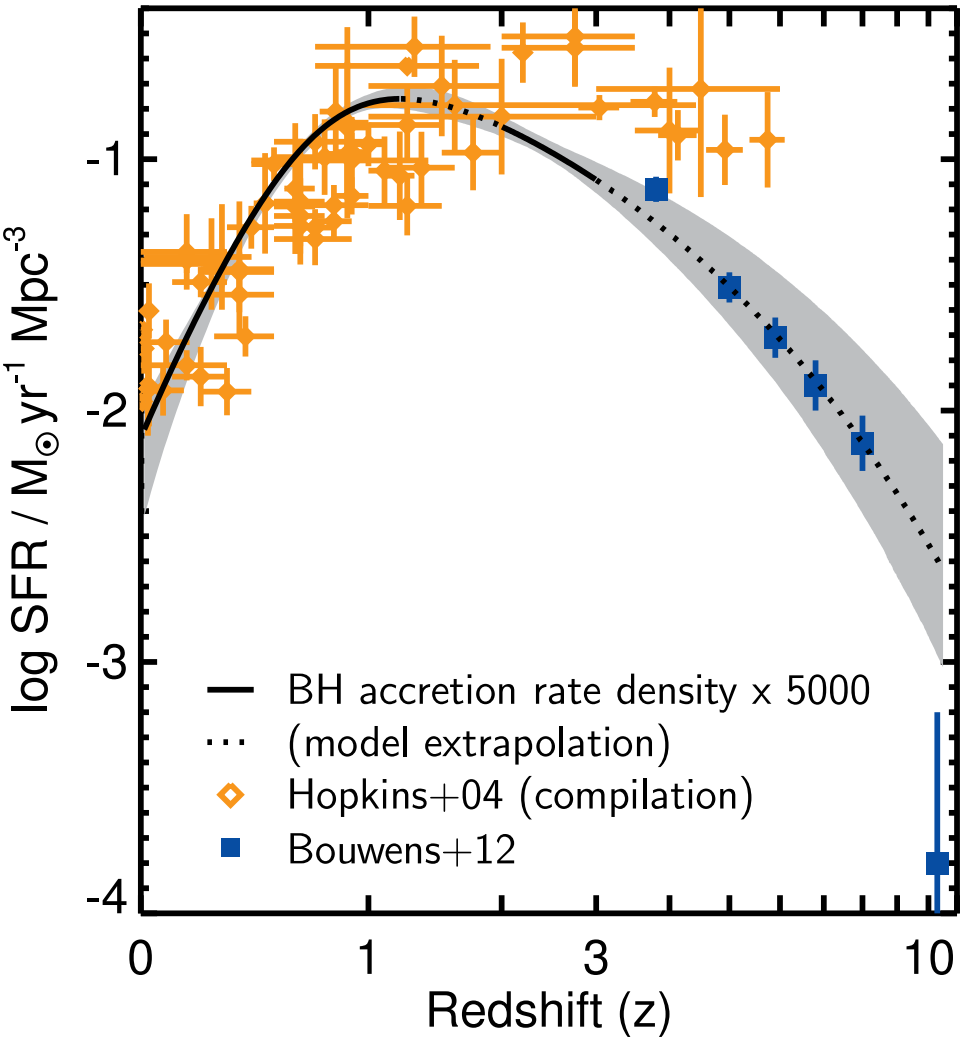

Fig. 1.4 The evolution with redshift of the volume density of black hole accretion rate, scaled up by a factor of 5000 (credit to [4] and [168]). This closely tracks the evolution of the cosmic star formation rate (SFR) compiled by [126, 30]. Both the density peaks of BH growth (i.e. mass accretion) and star formation occurred at similar epochs ($z \approx 1$–3), with both declining towards lower redshift.

of winds in the radiative mode, primarily detected as ionized blue-shifted absorption lines in the X-ray spectra of AGN in the nearby Universe [294, 45, 222, 186]. X-ray-detected winds are anticipated to originate from the nuclear region of AGN, i.e., the accretion disk (<1 pc). To exert a global impact on the host galaxy, these winds must couple with the ISM and propel the gas across galaxy scales ($\approx$ 1 kpc). Therefore, comprehending the energetics and physics of ionized winds becomes crucial for understanding their impacts on the galaxy and determining the driving mechanism behind AGN feedback.

1.1.3.1 Warm Absorber

Warm absorbers (WAs) [294] are ionized outflows usually observed in the soft X-ray spectra of AGN. Initially discovered by Halpern [116], these absorbers were employed to account for variable absorption observed in AGN spectra over timescales of years, originally modeled with prominent O VII and O VIII absorption edges (0.74 and 0.87 keV, respectively, [101]). The importance of warm absorber features was soon recognized since they were detected in at least half of Seyfert galaxies [102, 25], establishing them as a common feature of AGN.

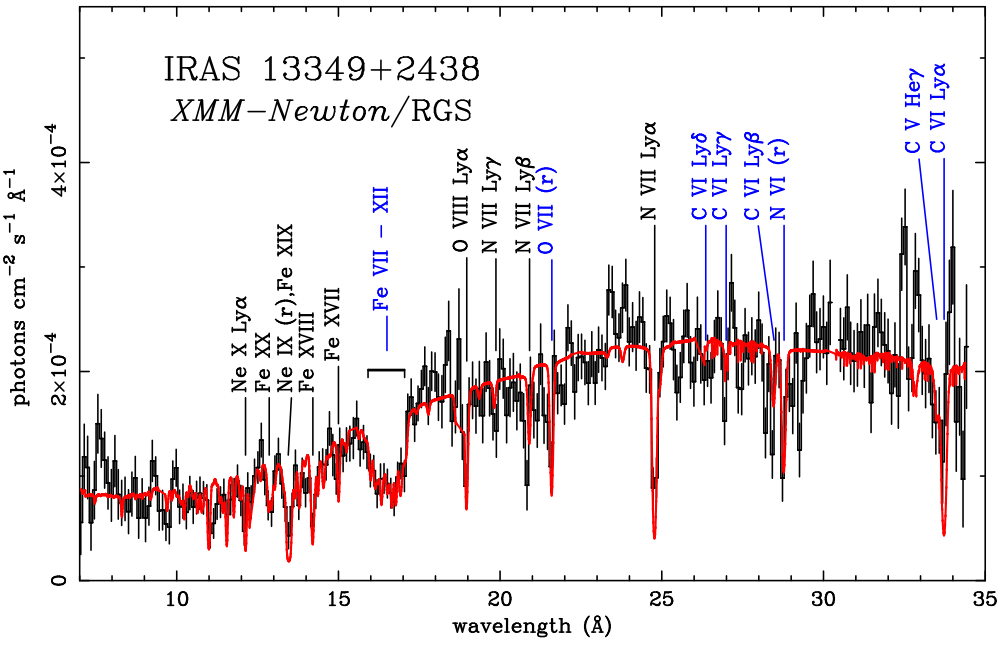

Fig. 1.5 The soft X-ray spectrum of IRAS 13349+2438 (credit to [308]). Within this spectrum, a diverse array of absorption lines is evident, originating from ions spanning the range from He-like Carbon to H-like Neon. Additionally, there are observable lines arising from low-ionization iron (Fe VII-XII) in the form of the M-shell Unresolved Transition Array (UTA). As indicated by the different color labels, at least two distinct ionization states of absorbers are required to adequately describe the data.

The advent of *XMM-Newton* [135] and *Chandra* [361] has significantly advanced our understanding of WAs in AGNs. Detailed studies [147, 158, 58], using high-resolution spectra from reflection grating spectrometers (RGS, [57]) onboard *XMM-Newton* [135], High-Energy Transmission Gratings (HETG, [33]) and Low Energy Transmission Gratings (LETG, [31]) onboard *Chandra* [361], have unveiled numerous blueshifted narrow absorption lines, indicative of a broad range of ionization states (as shown in Fig.1.5 [308]). These observations suggest that WAs are not confined to a single region, but rather span multiple zones with velocities ranging from 0 to 5000 km/s, column densities from 10^{20} to $10^{24}\,\mathrm{cm}^{-2}$, and ionization parameters from $\log\xi = -1$ to 3 [186, 187] (with $\xi = L_{\mathrm{ion}}/nR^2$ defined by Eq.1.9 in Sec.1.2.2.1.1). The precise location of WAs remains elusive, although their relatively lower velocities imply an origin further away from the accretion disk [145, 362], possibly extending from the BLR to distances greater than 10 pc, consistent with the NLR [44]. Furthermore, there have been instances where faster components, at speeds on the order of several thousand km/s, have been observed in the soft X-ray band (0.3–2 keV), possibly linked to a disk wind [345, 322, 123]. Moreover, determining the geometry of outflows remains a challenging task. It is unclear whether the wind is a spherical shell, a continuous stream [324, 323], or clumpy clouds [182], which also depends on the adopted launching mechanism.

1.1.3.2 Ultra-fast Outflows

Ultra-fast outflows (UFOs), distinct from WAs, represent the most extreme category of AGN outflows and are the center of this thesis. Characterized by their significantly blueshifted absorption lines in AGN X-ray spectra, UFOs exhibit extraordinary velocities exceeding 0.033c (over 10000 km/s) and reaching up to 0.4c, where c denotes the speed of light [38, 276, 339, 341, 338, 106, 288]. These outflows are typically associated with resonant absorption features from Fe XXV and Fe XXVI K shell (as illustrated in Fig.1.6, [235]), originating regions with massive column densities ($N_{\mathrm{H}} \sim 10^{22}$–$10^{24}\,\mathrm{cm}^{-2}$) and high ionization states ($\log\xi \sim 4$–6), suggesting their proximity to the SMBH [187]. UFOs are a prevalent phenomenon in AGN, being detected in >34% of Seyfert AGN [337].

In addition to traditional UFOs characterized by Fe K absorption features in the hard X-ray band, there have been noteworthy UFO detections involving oxygen K, Fe M, and Fe L absorption lines in the soft X-ray (<2 keV) high-resolution spectra from the *XMM-Newton*/RGS and *Chandra*/HETG detectors. The advanced resolution capabilities of these instruments can distinguish UFOs from the slow WAs even in the same soft X-ray coverage, such as in PG 1211+143 [276, 269], IRAS 17020+4544 [197], and PDS 456 [286]. The soft X-ray UFOs typically share a comparable velocity range with their hard X-ray counterparts.

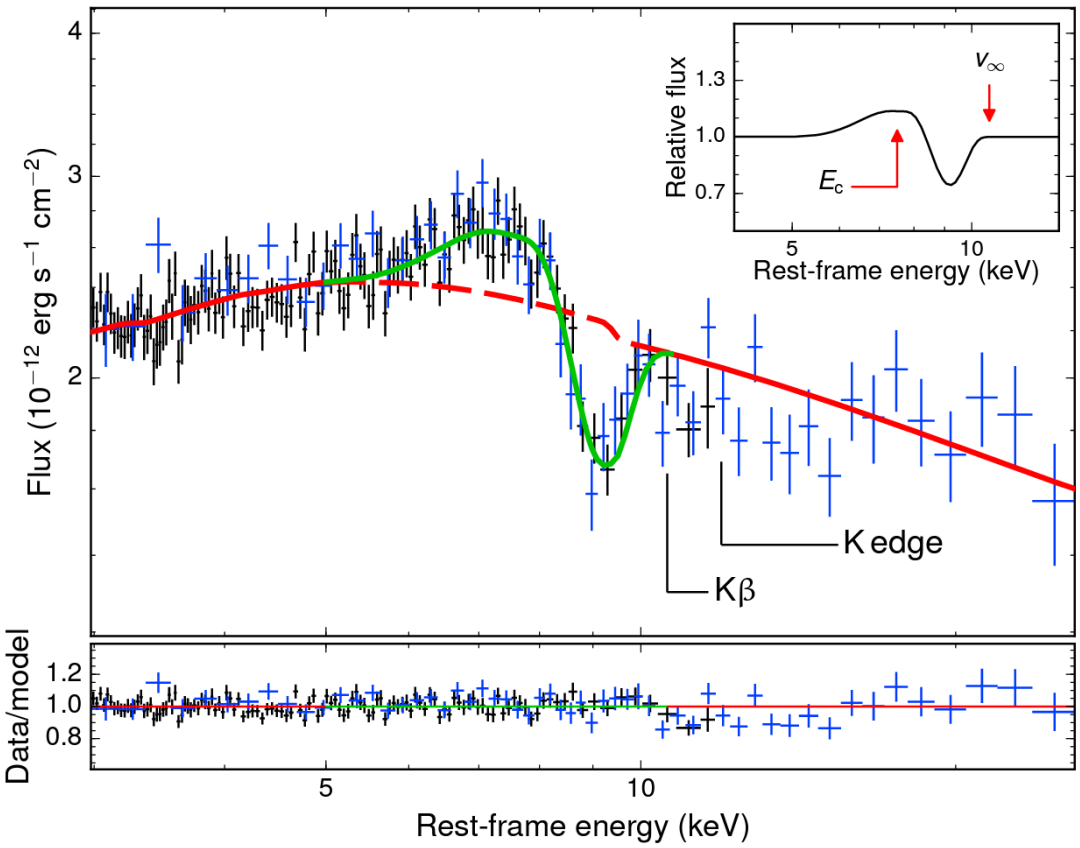

Fig. 1.6 The hard X-ray spectrum of a highly accreting quasar PDS 456 (credit to [235]) showing UFO absorption in the 7–10 keV band. The absorption feature is most likely imprinted by a powerful wind outflowing at a velocity reaching approximately 0.25c, originating from the accretion disk.

However, they exhibit substantially lower column densities ($N_{\rm H} < 10^{22}\,{\rm cm}^{-2}$) and ionization parameters ($\log\xi < 4$).

In some sources, UFOs have been concurrently detected in both the soft and hard X-ray bands [287, 272, 288, 26, 181]. These observations have given rise to the hypothesis that UFOs may possess a multi-phase origin as if a clumpy-ISM becomes entrained by an inner UFO. This phenomenon, known as entrained UFOs (E-UFOs), results in a simultaneous presence of both WAs and UFOs [314]. Fig.1.7 illustrates significant correlations among the properties of WAs, soft and hard X-ray UFOs. This suggests that these winds represent different parts of the same stratified large-scale outflow [337, 271], located at various distances from the nuclear SMBH. The UFO winds are postulated to originate from the accretion disk [339], while the WA winds stem from the torus [25]. E-UFOs follow the correlation within the $N_{\rm H}-\log\xi$ parameter plane, although their velocities deviate from the correlation, indicating an intermediate state between WAs and hard X-ray UFOs.

UFOs show clear signatures of variability in multi-epoch deep observations, suggesting a possible transient nature. Notable instances of such variability have been observed in AGN such as APM 08279+5255 [37], Mrk 509 [50], 1H 0707-495 [54], PG 1211+143 [381], and PG 1448+273 [289], with variability timescales ranging from 10 ks to several years. Studies focusing on IRAS 13224-3809 have unveiled an anti-correlation between the strength of absorption features, both in the soft and hard X-ray bands, and the luminosity [252], pointing towards a connection between the accretion process and the generation of outflows. Furthermore, investigations into the variable quasar PDS 456 and IRAS 13224-3809 have revealed a correlation between UFO velocity and AGN X-ray luminosity, which indicates that the wind is predominantly propelled by the intense radiation pressure [220, 259].

1.2 The physics of accretion onto black holes

Black holes, as the most extreme objects in the Universe, possess gravitational fields so intense that not even light can escape. They are described by Einstein's General Relativity (GR, [68]), except at their centers (known as the singularity), where even GR fails to provide a complete description. Astrophysically, black holes are characterized by three fundamental properties: mass $M_{\rm BH}$, spin angular momentum J, and electric charge Q. In what follows, we will focus on uncharged black holes, as any electric charge in astrophysical scales is typically negligible [34, 15]. Broadly, black holes can be categorized into two types based on their spin: non-rotating Schwarzschild black holes [313], and rotating Kerr black holes [16, 239], with the latter possessing nonzero angular momentum. The radius of a Schwarzschild black

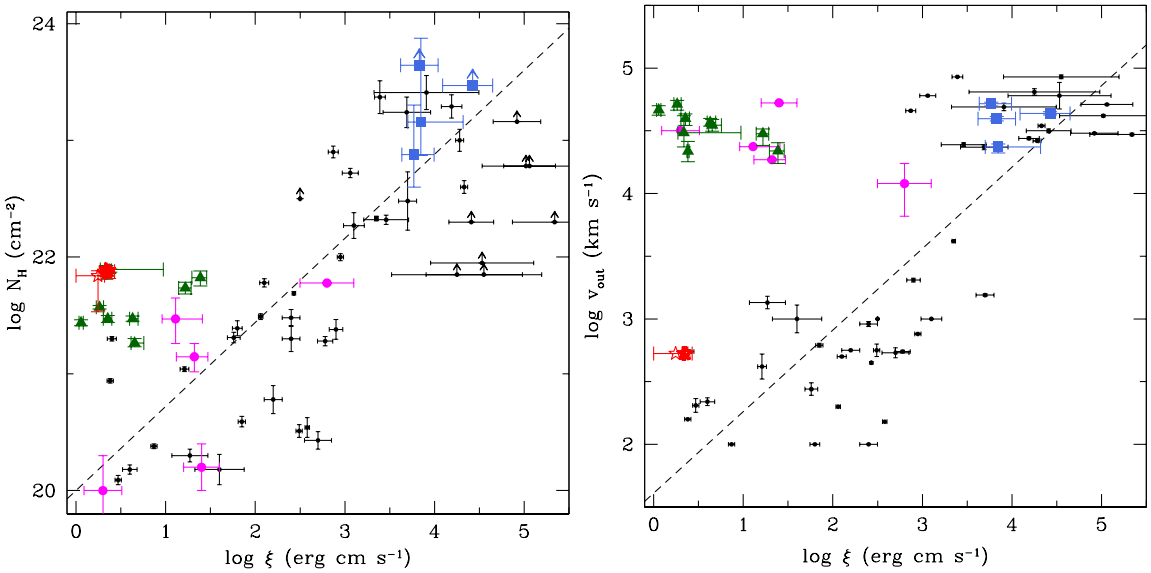

Fig. 1.7 Plots of column density (*left*) and velocity (*right*) against ionization parameter of various absorbers in PG 1114+445 (Figures adapted from [314]). WAs are denoted by *red* stars, soft X-ray UFOs are marked with *green* triangles, and hard X-ray UFOs are indicated by *blue* squares. The *black* points and dashed line represent other absorbers and the linear fit of [337]. Additionally, the *magenta* points correspond to other soft X-ray UFOs reported in the literature [197, 272, 287]. WAs, soft X-ray UFOs, and hard X-ray UFOs have a significant correlation in the $N_{\rm H}-\log\xi$ plane while the velocity of soft X-ray UFOs does not follow the correlation.

hole can be expressed as:

$$R_{\rm S} = 2R_{\rm g} = 2\frac{GM_{\rm BH}}{c^2} \approx 3(\frac{M_{\rm BH}}{M_\odot})\,{\rm km} \tag{1.1}$$

where $R_{\rm g}$ is the gravitational radius and G is the Newton gravitational constant. The dimensionless spin $a_\star$ of a black hole is defined such that

$$a_\star = \frac{cJ}{GM_{\rm BH}^2} \tag{1.2}$$

In the GR, the spin changes the position of the event horizon. The radius of the event horizon of a Kerr black hole in the Boyer-Lindquist coordinates is

$$R_{\rm Horizon} = R_{\rm g}(1+\sqrt{1-a_\star^2}) \tag{1.3}$$

Therefore, in astrophysical contexts, $a_\star$ typically ranges from -1 to 1. Specifically, a positive value of $a_\star$ (i.e. $a_\star > 0$) is employed when considering a black hole with angular momentum aligned with that of the surrounding material (prograde), while a negative value of $a_\star$ (i.e. $a_\star < 0$) when the angular momentum is in the opposite direction, resulting in counter-rotating motion (retrograde).

1.2.1 Theory of Accretion

Accretion is one of the most energetic and efficient phenomena in our Universe, exhibiting a mass-scale invariance that spans from stellar-mass black holes, approximately 1–10$M_\odot$, to supermassive black holes as large as $10^{6-10}M_\odot$. These SMBHs, with their immense gravitational forces, are capable of pulling in material from surrounding regions ($\sim$pc scales). Due to the angular momentum of this infalling material, it does not directly fall into the SMBH but instead forms an orbiting accretion disk in a Keplerian motion.

The widely accepted model for such a disk, especially when it is geometrically thin and optically thick, is the Novikov-Thorne (NT) model [239], an extension of the standard Shakura-Sunyaev (SS) disk model [316], which considers relativistic effects. Within the disk, collisions between gas and dust particles transform kinetic energy into thermal energy through viscous friction, thereby heating the disk. This process leads to a loss of angular momentum for the material, causing it to spiral inwards and increase its velocity. It is noted that the role of mechanical viscosity in generating the luminosity observed in accreting systems is considered inadequate [279], pointing towards magnetic effects, particularly magneto-rotational instability (MRI, [13, 14]), as the likely driver of viscosity.

The local effective blackbody temperature $T_{\rm eff}$ of the accretion disk depends on the distance from the SMBH r as,

$$T_{\rm eff}^4(r) = \frac{3GM_{\rm BH}\dot{M}}{8\pi\sigma r^3}(1-\sqrt{\frac{R_{\rm in}}{r}}) \tag{1.4}$$

where $\dot{M}$ is the mass accretion rate, σ is the Stefan-Boltzmann constant, and $R_{\rm in}$ is the inner radius of the accretion disk. For regions where the distance from the center greatly exceeds the inner disk radius $r \gg R_{\rm in}$, the temperature profile of a stationary Keplerian accretion disk follows approximately as $T_{\rm eff} \propto r^{-3/4}$. Consequently, the temperature increases radially inwards, suggesting that the structure of the disk may be characterized by a series of concentric annular segments, each emitting as a blackbody. The overall contribution of these annuli can be described as the composite emission, yielding a multi-color thermal blackbody radiation. In the Novikov-Thorne frame, both the mass accretion rate $\dot{M}$ and the gravitational radius $R_{\rm g}$ scales linearly with the black hole mass $M_{\rm BH}$, leading to a rough estimate of the effective temperature of the inner part of the accretion disk,

$$T_{\rm eff} \propto M_{\rm BH}^{-1/4} \sim (\frac{10M_\odot}{M_{\rm BH}})^{1/4}\,{\rm keV}. \tag{1.5}$$

Therefore, the inner disk regions of SMBHs have temperatures of $\sim 10^5$ K, where the emission peaks in the UV band (see Fig.1.2).

The inner radius of the disk $R_{\rm in}$ is nominally set by the radius of the innermost stable circular orbit (ISCO) where the particles in the accretion disk lose their orbital stability and ultimately spiral into the black hole. The location of ISCO depends on the angular momentum of the SMBH relative to the angular momentum of the accretion disk [15]. For example, ISCO corresponds to $1\,R_{\rm g}$ for a maximally spinning ($a_\star = 1$) black hole and $6\,R_{\rm g}$ for a Schwartzchild black hole. For a retrograde-spinning ($a_\star = -1$) black hole, the ISCO extends further outward to $9R_{\rm g}$.

The bolometric or total luminosity of the accretion disk is given by,

$$L_{\rm bol} = \eta\dot{M}c^2 \tag{1.6}$$

Here, η represents the mass-energy efficiency conversion, (usually assumed to be $\eta = 0.1$), dependent on the black hole spin. For a non-rotating Schwarzschild black hole, the efficiency η is 5.7% and can be as high as 42% for a maximally rotating Kerr black hole [162, 334]). The efficiency of accretion is significantly greater than that of other energy-generation

processes, such as nuclear fusion or fission, both of which typically yield efficiencies below 1%.

The luminosity generated by accretion processes is fundamentally constrained to a critical value at which the outward radiation pressure equals the inward gravitational force exerted on the infalling matter by the SMBH. Under the assumption of spherical symmetry, this critical value is known as the Eddington luminosity [65]:

$$L_{\rm Edd} = \frac{4\pi G M_{\rm BH} m_{\rm p} c}{\sigma_T} = 1.26 \times 10^{38} \frac{M_{\rm BH}}{M_\odot} \,{\rm erg/s} \tag{1.7}$$

where $m_{\rm p}$ is the mass of the proton ($\approx$hydrogen atom mass) and σ_T is the Thomson scattering cross-section for electrons. The Eddington ratio $\lambda_{\rm Edd}$ is defined as the ratio of the accretor's bolometric luminosity to its Eddington luminosity,

$$\lambda_{\rm Edd} \equiv L_{\rm bol}/L_{\rm Edd} \tag{1.8}$$

which serves as a useful metric for comparing BH accretion rates over a wide range of BH masses. The term 'high-accretion rate AGN' is often used to describe sources with substantial values of $\lambda_{\rm Edd} \gtrsim 0.1$. In principle, no accreting systems should exceed $\lambda_{\rm Edd}$. However, in practice, it is possible to surpass this limit by breaking spherical symmetry or by leveraging strong magnetic fields (which can suppress the electron scattering cross-section).

1.2.2 Accretion Disk Winds

The material within the accretion disk typically loses energy and angular momentum due to MRI, causing it to gradually spiral towards the SMBH. However, there are several mechanisms (discussed in Sec.1.2.2.2) that can counteract this inward movement by accelerating the accreting gas outwards, resulting in the formation of a disk wind, as anticipated in Sec.1.1.3.

1.2.2.1 Physical Properties of disk Winds

This section introduces the key properties including the ionization state, location, and energetics of ionized disk winds and the corresponding measurements.

1.2.2.1.1 Ionization Parameter The ionization state can provide crucial information about the winds, particularly the thermal state, and it can be assessed through the definition

of the ionization parameter ξ [331],

$$\xi = \frac{L_{\rm ion}}{n_{\rm H} R^2} \, {\rm erg\,cm/s} \tag{1.9}$$

where $L_{\rm ion}$ is the ionizing luminosity integrated between 1–1000 Rydberg (i.e. 0.0136–13.6 keV), $n_{\rm H}$ is the hydrogen number density and R is the distance between the ionizing source and the gas. The ionization parameter, ξ, quantifies the degree of ionization within the plasma, indicating the number of ionizing photons per particle. Given the knowledge of the ionizing spectrum, the ionization parameter can reveal the ionic composition of the plasma. For instance, Fig.1.8 illustrates the relative abundance of various ions at different ionization states, where the ionic transitions with greater energies tend to peak at higher ionization states (e.g. Fe XXV and Fe XXVI peak above $\log \xi \sim 4$).

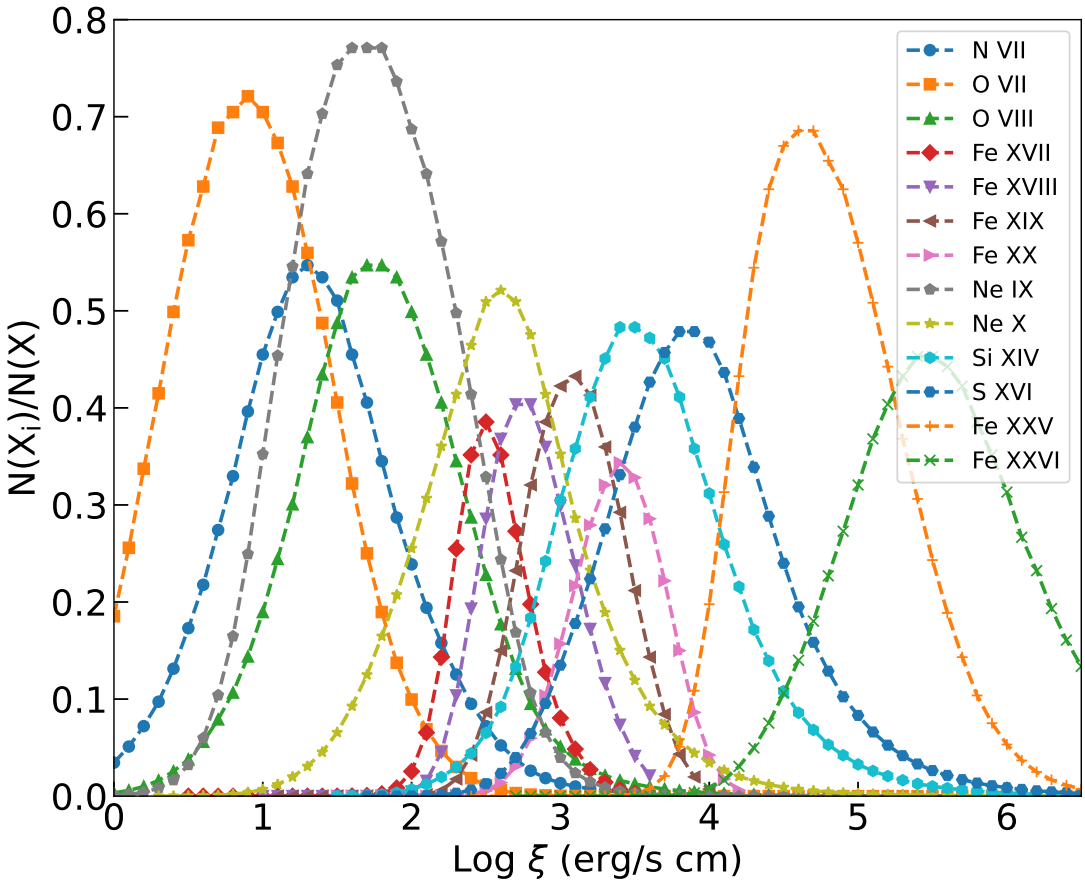

Fig. 1.8 The relative abundance of different ions with respect to elements in a photoionized plasma versus the ionization parameter (credit to [372]). The irradiation spectrum is the time-averaged SED of 1H 0707-495. In general, the ionic lines with larger energies peak at higher ionization states.

1.2.2.1.2 Location For outflows successfully leaving the accretion disk, their launching velocities must exceed the escape velocity,

$$v_{\rm esc} = \sqrt{\frac{2GM_{\rm BH}}{R}}. \tag{1.10}$$

This condition, in turn, establishes a lower limit on the location of outflows,

$$R_{\rm min} \geq \frac{2GM_{\rm BH}}{v_{\rm out}^2}. \tag{1.11}$$

It implies that disk winds, e.g. UFOs with velocities of ~ 0.1c, originate from the inner regions of the disk, $\sim 100R_{\rm g}$, whereas slower WAs emerge from the outer disks or more distant regions, like the torus. On the other hand, the upper limit on the location of outflows can be derived by assuming that the thickness of the outflowing shell (Δr) does not exceed its radial distance from the center ($\Delta r \leq R$). Consequently, the column density can be approximated as $N_{\rm H} \sim n_{\rm H} C_{\rm V} \Delta r \leq n_{\rm H} C_{\rm V} R$, where $C_{\rm V}$ is the volume filling factor. Combined with Eq.1.9, the upper limit on the distance is

$$R_{\rm max} \leq \frac{L_{\rm ion} C_{\rm V}}{\xi N_{\rm H}}. \tag{1.12}$$

Besides the constraints based on several assumptions, the precise measurement of the wind location is theoretically achievable through Eq.1.9. However, although the ionizing luminosity and the ionization parameter can be measured through X-ray spectroscopy, there is a persistent degeneracy between gas density $n_{\rm H}$ and the radial distance R, preventing a direct derivation of the wind distance. In the case of the X-ray line emitting gas, the degeneracy can be broken by density-sensitive He-like triplets. The ratio between the recombination, intercombination, and forbidden emission lines can be used to measure $n_{\rm H}$ and to diagnose the ionizing process of plasma (photoionization dominated or collisional-excitation dominated, [266, 267]). The density-sensitive absorption lines from metastable levels can be another diagnostic of gas density, which is widely used in UV spectroscopy [174, 10]. However, in the X-ray band, this method is not effective, as these metastable absorption lines are rather weak and inaccessible in most AGN [149, 210]. In the absence of density-sensitive lines, timing analysis techniques on outflows may provide another avenue. The plasma density $n_{\rm e}$ is inversely correlated with its recombination timescale [178],

$$t_{\rm rec}^{X^i;X^{i+1}} \propto \frac{1}{\alpha_{\rm X,i+1\rightarrow i} n_{\rm e}} \tag{1.13}$$

where $t_{\rm rec}^{X^i:X^{i+1}}$ is the recombination time for the ion of the element X transitioning from stage $i+1$ to stage i, and $\alpha_{\rm X,i+1\rightarrow i}$ is the recombination coefficient. A higher plasma density leads to a more rapid response to variations in the ionizing continuum. Consequently, the recombination timescale for a specific ion serves as an effective density indicator, enabling the deduction of wind locations. This timescale can be determined by monitoring absorption line variability in response to continuum fluctuations and measuring the delay, or absence thereof, in the response of a particular line [183, 145].

1.2.2.1.3 Kinetic Luminosity A pivotal question in the study of AGN winds is whether these disk winds are energetically important for the host galaxy and drive the AGN feedback. According to theoretical models, an outflow effectively drives the feedback if its kinetic luminosity is comparable, i.e., above 0.5% [60, 127], with the AGN Eddington luminosity $L_{\rm Edd}$. The kinetic luminosity is given by

$$L_{\rm kin} = \frac{1}{2}\dot{M}_w v_w^2 = 2\pi C_{\rm V}\Omega R^2 \rho v_w^3 ({\rm erg/s}) \tag{1.14}$$

where v_w is the wind velocity, $\dot{M}_w = 4\pi C_{\rm V}\Omega R^2 \rho v_w$ is the mass outflow rate of winds, $C_{\rm V}$ is the volume filling factor (or clumpiness), Ω is the solid angle normalized by 4π, R is the distance from the ionizing source, and ρ is the mass density. The mass density is defined as $\rho = n_{\rm H} m_{\rm p} \mu$, where $n_{\rm H}$ is the hydrogen number density, $m_{\rm p}$ is the proton mass and μ is the mean atomic mass per proton. The product of $n_{\rm H}$ and R^2 can be replaced by Eq.1.9 and the mass outflow rate can be rewritten as

$$\dot{M}_w = 4\pi C_{\rm V}\Omega v_w m_{\rm p}\mu \frac{L_{\rm ion}}{\xi} \tag{1.15}$$

Empirical observations have indicated that UFOs with sub-relativistic velocities possess substantial kinetic energy, making them strong candidates for driving AGN feedback, while WAs with low velocities lack enough kinetic energy to affect the host galaxy [337].

1.2.2.2 Launching Mechanisms

The launching mechanisms of the outflows are, to date, not fully understood. There are three main launching mechanism theories for the outflowing winds in the literature: the thermally- [179, 20, 19], radiatively- [282, 280], and magnetically-driven [86, 88, 90] winds.

1.2.2.2.1 Thermally-driven Winds Thermally driven winds are associated with the process in which materials are evaporated off the outer and cooler regions of the accretion

disk due to the hard X-ray radiation from the inner/hotter disk. X-rays can heat low-density gas, through Compton heating, to a high temperature of $T_c \sim 10^7$ K, where T_c represents the Compton temperature. At this temperature, the thermal velocity of the heated particles can become sufficiently high to overcome the gravity of the SMBH (i.e. $v_{\rm th} > v_{\rm esc}$), leading to outflowing winds. This occurs predominantly at larger distances from the SMBH, where the escape velocity $v_{\rm esc}$ is relatively low. This launching mechanism can elucidate the origins of the WAs, which are expected to originate from the outer disk or torus. This kind of wind is also observed in X-ray Binaries (XRBs) at distances greater than the Compton radius, approximately $10^5 R_{\rm g}$ [347].

1.2.2.2.2 Radiatively-driven Winds The Shakura & Sunyaev model has provided a fundamental theoretical framework for radiatively-driven disk winds. At large distances from the SMBH, the material within the accretion disk gradually loses energy and angular momentum due to the MRI and thus spirals inwards. As the material approaches closer to the black hole, the local energy release $GM_{\rm BH}\dot{M}/R_{\rm sph}$ and the force of radiation pressure grows rapidly. The radiation pressure becomes particularly significant at a characteristic distance known as the spherization radius $R_{\rm sph}$, where the local energy release reaches the order of the Eddington luminosity $GM_{\rm BH}\dot{M}/R_{\rm sph} \sim L_{\rm Edd}$. Consequently, the accreting gas is propelled outward in the form of winds. In the case of fully ionized outflows, the radiation pressure exerted onto the outflows is primarily driven by electron scattering, commonly referred to as Thompson (or Compton) scattering [165, 164].

If the material in the accretion disk is not highly ionized, the gas opacity can be significantly higher than the electron scattering cross-section [36]. This increased opacity arises from processes such as bound-free and bound-bound transitions. At low ionization states, the wind can be driven by spectral lines originating from numerous elemental transitions in the UV band [282]. However, this scenario requires that the outflowing materials must be shielded to avoid the over-ionization caused by X-ray radiation from the inner accretion flow. Hydrodynamical simulations (see the left panel of Fig.1.9, [282, 281]) have demonstrated that over-ionized gas from the inner disk will fall back onto the disk as a failed wind, which acts as a shield for the outer disk regions, subsequently permitting the formation of UV line-driven winds in distant regions (< 1 kpc). At larger scales ($\sim$ 1–10 kpc), the radiation pressure can drive galaxy-wide dusty outflows [132, 134, 133], given the dust absorption cross-section σ_d much higher than the Thompson cross-section σ_T ($\sigma_d/\sigma_T \sim 1000$, [77]). Consequently, the effective Eddington limit ($L'_{\rm Edd} \propto 1/\sigma \approx 1000 L_{\rm Edd}$, see Eq.1.7) for dusty gas is much lower than the standard Eddington limit. This lower limit is easily exceeded, leading to the launching of dusty outflows and facilitating the coupling between the radiation

field and the surrounding ISM. As a result, it becomes feasible to launch an outflow at luminosities considerably lower than the Eddington luminosity.

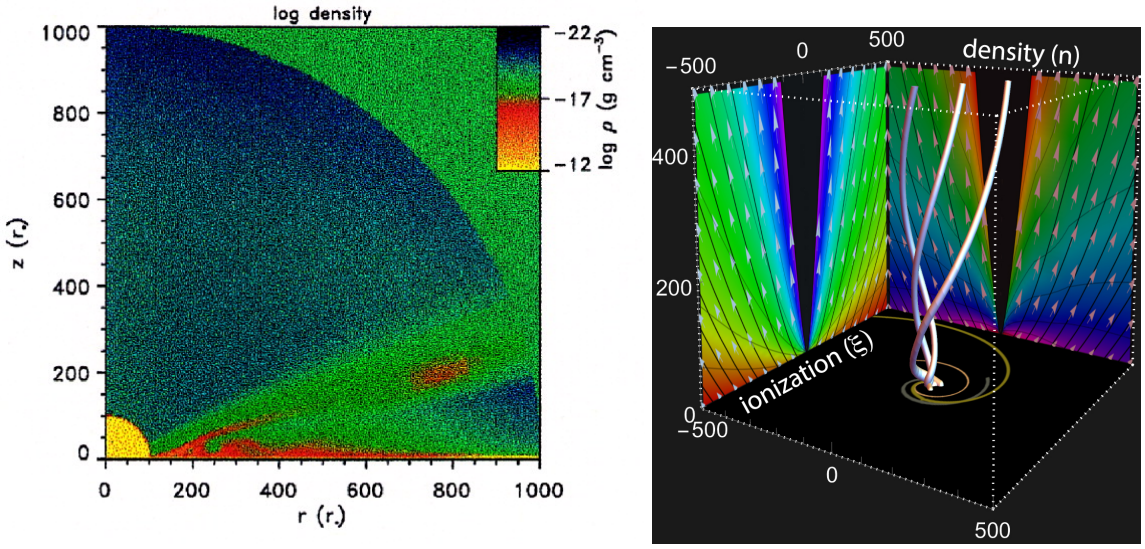

Fig. 1.9 Simulation of line pressure-driven (*left*, [282]) and magnetically-driven (*right*, [89]) outflows from the accretion disk of a SMBH.

1.2.2.2.3 Magnetically-driven Winds Magnetic fields play a crucial role in accretion by transferring angular momentum between the inner and outer regions of the disk through the MRI process [13, 14]. Consequently, it is conceivable that magnetic tension or magnetic pressure could act as a driver for outflows from the disk. Studies have demonstrated that a disk wind can indeed be generated if the poloidal component of the magnetic field has an angle of $> 30^{\circ}$ relative to the normal vector of the disk surface [24]. The magnetocentrifugal force and magnetic pressure accelerate the disk material, resulting in the ejection of highly ionized winds from various regions of the disk. Simultaneously, the magnetic energy is converted into kinetic energy of the plasma wind. Besides, magnetic fields are already known to accelerate collimated jets (radio mode, [24]). A bimodality may exist at low/high accretion rates due to a different configuration of magnetic fields [225]. Notably, magnetically driven winds do not rely on radiation pressure and therefore can be important in low-luminosity AGN. This launching mechanism also offers a plausible explanation for the extreme properties of UFOs, as a promising candidate for driving powerful winds (see the right panel of Fig.1.9, [337, 90]). Moreover, according to magnetohydrodynamic (MHD) simulations, magnetically-driven winds are predicted to have an extended blue wing of absorption lines, while radiatively-driven winds leave absorption lines with an extended red wing in the spectrum [85], which

could serve as a probe for wind launching mechanisms, achieved by X-ray missions with sufficient spectral resolution (see Sec.7.3).

1.3 This Thesis

Outflows have been observed in AGN for decades. However, their underlying physics, launching mechanisms, and their impact on the host galaxies are still unknown. In this thesis, I utilize high-resolution X-ray spectroscopy, complemented by variability analysis, to search and study ionized outflows, with a particular focus on UFOs in the vicinity of highly accreting SMBHs. This thesis aims to understand the launching mechanisms of UFOs around highly accreting SMBHs, to explore the potential links between outflows and inflows within the accretion disk, and to assess whether UFOs can effectively drive the AGN feedback. A brief outline of the content of each chapter in this thesis is provided below.

- **Chapter 2**: This chapter offers an overview of the X-ray observatories utilized in this work (*XMM-Newton* and *NuSTAR*), X-ray spectroscopy of continuum and plasma modeling, and the data analysis methods for searching outflows.
- **Chapter 3 & 4**: These chapters delve into an investigation of the launching mechanism of UFOs in a super-Eddington 1H 0707-495 and a high-Eddington NLS1 AGN Mrk 1044. The research explores the dependence of the absorption and emission components on luminosity, showing that UFOs in both two sources are driven by radiation pressure and instantaneously respond to variations in luminosity. However, the dynamic behaviors of UFOs are quite different in the two sources.
- **Chapter 5**: In this chapter, the connection between accretion and matter ejection is investigated in a high-Eddington NLS1 AGN 1H 1934-063. The high-resolution spectroscopy, for the first time, discovers the evidence for the reprocessing of the inner accretion flow photons off the ejection.
- **Chapter 6**: A systematic study of the launching mechanism of UFOs is conducted in six highly-accreting NLS1 AGN, significantly expanding the total sample of well-studied UFO responses from 4 to 10 sources. This population work unveils complex behaviors of accelerated UFOs and their energetics are assessed to determine their potential impact on the host galaxy.
- **Chapter 7**: This Chapter provides conclusions of works presented in this thesis, along with brief discussions of upcoming X-ray missions and their potential contributions to advancing our understanding of AGN outflows.

Chapter 2

X-ray Observatories and Analysis Methods

2.1 X-ray Observatories

In this thesis, I study the physics of AGN winds through X-ray spectroscopic observations. As X-rays are absorbed by the Earth's atmosphere, these observations necessitate the use of satellite-based observatories. Various observatories are currently operational, each equipped with detectors tailored to their specific scientific objectives. In this section, I provide an overview of the detectors onboard the space telescopes *XMM-Newton* [135] and *NuSTAR* [118] that collected the data utilized in this thesis.

2.1.1 *XMM-Newton*

The X-ray Multi-Mirror Mission-Newton (*XMM-Newton*, [135]) is an X-ray satellite built and launched by the European Space Agency in December 1999 (see Fig.2.1 for the sketch of the mission). The mission aims to investigate cosmic mysteries, from the nature of black holes to the origin of the Universe.

The satellite is equipped with three X-ray telescopes, each composed of 58 concentric mirror shells and featuring a focal length of 7.5 m. These telescopes are paired with three CCD-based European Photon Imaging Camera (EPIC) detectors positioned at their respective focal points. In total, the three EPIC CCD cameras provide an effective area of 2200 cm^2 around 2 keV (see Fig.2.2). The full width at half maximum (FWHM) of the point spread function (PSF, i.e. the mirror spatial resolution) is approximately 4–6 arcseconds at 1.5 keV. Additionally, two of the telescopes, following the Wolter type-I design and designated for EPIC-MOS (see Sec.2.1.1.1) cameras, are additionally equipped with Reflection Grating

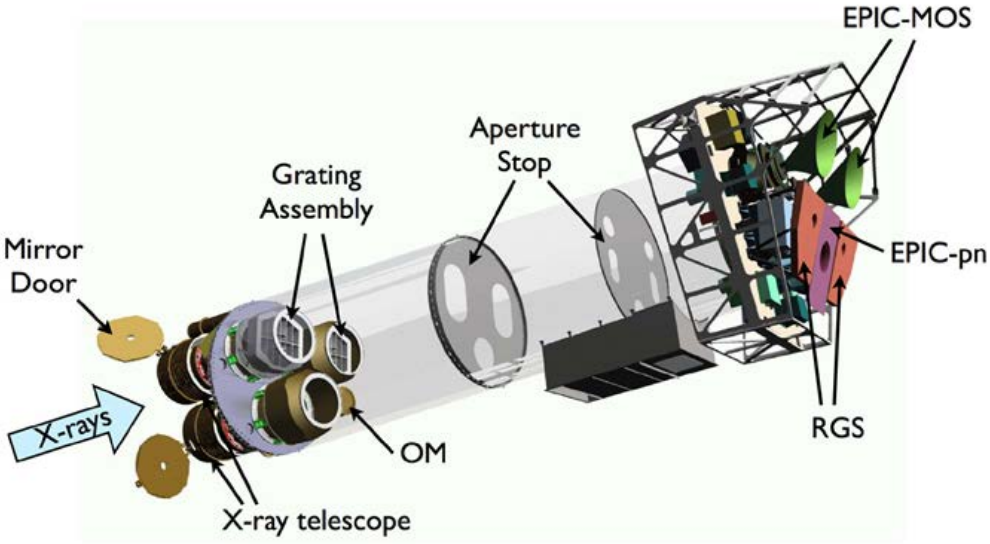

Fig. 2.1 A schematic representation of the *XMM-Newton* payload (credit: ESA and [359]). On the lower left of the figure are the aperture doors alongside the mirror modules with the two Reflection Grating Arrays. The optical monitor (OM) is situated behind the lower mirror module. On the upper right of the figure are the EPIC-MOS cameras (*green*), the EPIC-pn camera (*purple*), and the RGS detectors (*red*). The direction of the incoming X-rays is indicated by the *blue* arrow on the left.

Spectrometers (RGS). While the RGS instruments are primarily geared towards the soft X-ray band (0.3–2.5 keV) and have a ten times smaller effective area than EPIC, they excel in offering remarkably higher (10×) energy resolution. An optical/UV monitor (OM) is co-aligned with the X-ray telescopes on XMM-Newton, which covers 6 energy bands spanning from 180 to 600 nm.

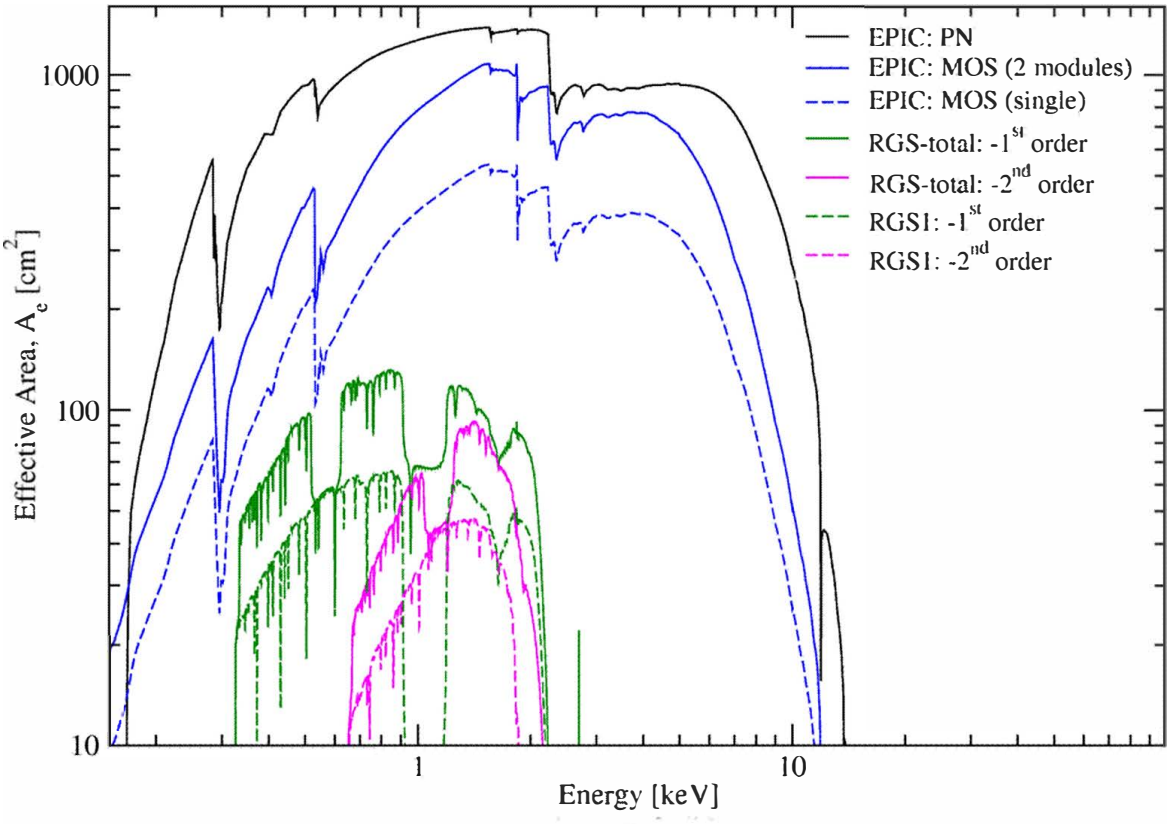

Fig. 2.2 The net effective area of all *XMM-Newton* X-ray telescopes, consisting of EPIC and RGS in the logarithmic scale (credit to ESA).

2.1.1.1 European Photon Imaging Cameras (EPIC)

XMM-Newton carries three broadband X-ray (0.3–10 keV) instruments based on Charge-Coupled Device (CCD) technology. Two of these CCDs, MOS 1 and 2 (metal oxide semiconductor, [343]) are front-illuminated and virtually identical but rotated. The third CCD, known as the pn camera [325], is back-illuminated. Specifically, the EPIC-pn CCD camera [325] offers an on-axis effective area of approximately 1200 cm^2 around 2 keV, while the two EPIC-MOS cameras combine to provide an on-axis effective area of around 1000 cm^2 within the same energy band. Notably, 50% of X-rays from MOS mirrors are reflected towards the RGS instruments. The energy resolution of the three cameras is

comparable, falling within the range of $R = E/\Delta E \sim 20$–50 over the whole energy band. The EPIC cameras offer the possibility to conduct exceptionally sensitive imaging observations over the field of view (FOV) of 30 arcmin, positioning *XMM-Newton* as the second-best X-ray observatory in terms of spatial resolution, just behind *Chandra* [361], but with better effective area and timing capability.

The EPIC cameras offer various operational modes tailored to the specific requirements of observed sources. In instances where sources exhibit high brightness, there is a risk of pile-up, which results from the limited readout frequency of the detectors and can distort the source spectra. In general, for point sources with a count rate exceeding 0.5 count/s in MOS and 2 ct/s in pn, the Large Window mode can be employed to reduce the FOV and decrease the read-out time. In cases of even greater source brightness, options such as Small Window, Timing, and Burst modes are available to further restrict the FOV and reduce read-out times, ensuring accurate measurement of the source spectra.

2.1.1.2 Reflection Grating Spectrometers (RGS)

The RGS instrument [57] incorporates two reflection grating arrays, RGS1 and RGS2, placed in the converging beam at the exit of the X-ray telescope. Each array is equipped with 9 large format CCDs in the reflection direction and records the position and energy of each photon that is reflected by the gratings. The photon position on the CCD is determined by the dispersion relation:

$$m\lambda = d(cos\beta - cos\alpha) \tag{2.1}$$

where λ is the X-ray wavelength, m is the spectral order of the diffraction, d is the groove separation, β is the deflected angle, and α is the incident angle. Both spectrometers cover the same field of view, with the dispersion direction along the spacecraft's Z-axis. In the cross-dispersion direction, the size of the FOV is determined by the width of the CCDs, which is approximately 5 arcmin.

The RGS spectrum of the source, by default, is extracted from a region along the dispersion axis, encompassing all functional CCDs (excluding CCD 7 in RGS 1 and CCD 4 in RGS 2). The background spectrum is extracted from two rectangular regions offset from the source region in the cross-dispersion direction to ensure they lie outside the primary source point spread function. In cases involving crowded fields or extended sources with potentially contaminated background regions, it is possible to use a 'model' background that is appropriately scaled to match the expected background flux.

The RGS instrument achieves a high resolving power within the soft X-ray band (0.3–1.8 keV, 7–38 Å), offering the resolution of $R = 120$–500 in the first spectral order.

The second order provides double the resolution of the first order, but it has a poorer effective area and a limited wavelength band (5 to 20 Å, see Fig.2.2). RGS is the best instrument to use for faint source spectroscopy below $\sim$1 keV (above 12 Å) in the last two decades. The wavelength band spanning from 6 to 38 Å encompasses numerous important transitions of ionized elements, notably those of oxygen, nitrogen, neon, and iron. As a result, RGS stands out as an ideal tool for studies of ionized plasma and accretion disk winds, making it the primary instrument utilized in this thesis.

2.1.1.3 Optical Monitor (OM)

The Optical/UV Monitor Telescope (OM, [215]) onboard *XMM-Newton* is a co-aligned instrument alongside the X-ray telescopes. The OM mirror has a diameter of 30 cm and a focal length of 3.8 m. OM contains a filter wheel comprising eleven different apertures. Among these are six broad-band filters designed for UV and optical wavelengths, covering a wavelength range from 170 to 650 nm: V (5430 Å), B (4500 Å), U (3440 Å), UVW1 (2910 Å), UVM2 (2310 Å), UVW2 (2120 Å). Additionally, OM features a white-light filter that permits transmission across the whole wavelength band. It also includes two grisms (one for UV and the other for optical) and a magnifier for high spatial resolution. OM allows simultaneous observations in both the X-ray and optical/UV domains within a single mission, which is invaluable when constructing optical-to-X-ray spectral energy distributions.

2.1.2 *NuSTAR*

The Nuclear Spectroscopic Telescope Array (*NuSTAR*, [118]) was launched by the National Aeronautics and Space Administration (NASA) in 2012 (see Fig.2.3), focusing on the hard X-ray energy band (3–78 keV). *NuSTAR* is the first X-ray telescope capable of providing focused images in the hard X-ray regime. This consists its two Focal Plane Modules (FPMs), each equipped with a conical approximation mirror based on the Wolter type-I design. These modules comprise 133 nested multilayer-coated concentric mirrors. The combined effective area of the two FPMs at 10 keV totals 800 cm^2. The energy resolution of FPM is around 0.4 keV FWHM at 6 keV and 0.9 keV FWHM at 70 keV. Additionally, *NuSTAR* employs a triggered readout mechanism instead of CCDs, which significantly reduces the likelihood of pile-up effects by minimizing the time over which pile-up can occur, from the frame readout time to the trigger response time. Therefore, one of the advantages of *NuSTAR* is that there are no pile-up effects in most observations. Moreover, albeit a lower resolution and effective area than *XMM-Newton* at < 7 keV, *NuSTAR* has a lower background (despite worse PSF)

thanks to its low-Earth orbit. The instrument is therefore well-suited for studies of X-ray reflection [74, 100] and the properties of coronae [73] in AGN.

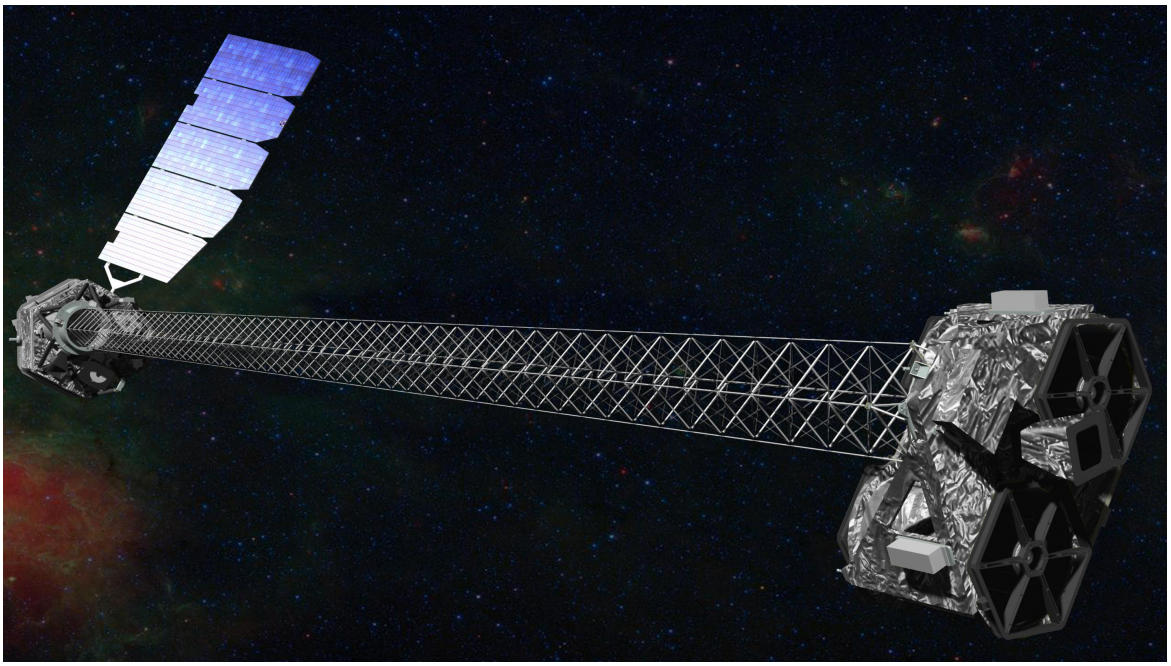

Fig. 2.3 The artist's concept of *NuSTAR* in orbit (credit to NASA/JPL).

2.2 X-ray Spectral Modeling

The instruments collect a large number of photons distributed across various energy channels. By leveraging the knowledge of the energy-dependent effective collecting area of the instrument, the energy of photons can be recovered, ultimately yielding a spectrum. The desired dataset is extracted from a certain source region that includes both the source of interest and background flux. The background flux can originate from other astrophysical sources within the extraction region and instrumental factors. To obtain a net source spectrum, the background flux can be subtracted by selecting an appropriate background region and subtracting the background photon counts (scaled by the ratio of the source and background areas) from the source region photon counts. X-ray spectroscopy is a powerful technique for gleaning the intrinsic properties of the source from spectra through a 'forward-fitting' approach. This approach involves initially defining a hypothetical model source spectrum, followed by a comparison with the actual data. The spectrum is fitted to theoretical models with a spectral fitting package. In this thesis, I employ two such packages: SPEX, which

includes advanced photoionization calculations, [148]), and XSPEC, which is widely utilized in the field [12]).

In addition to converting physical models into detector units, fitting packages employ various statistical tests to assess the goodness-of-fit of a model to a spectrum and to determine plausible parameter ranges. The conventional and still widely used approach is to find the model that minimizes fitting statistics quantifying the difference between the model and the data. χ^2 statistics are frequently employed since a large number of inherently Poisson-distributed photon counts can be approximated as Gaussian. This approximation is valid for bright sources and low-resolution observations with CCDs when the number of photon counts per energy bin is sufficiently large (> 25). However, when photon counts are limited, the distribution necessitates the use of Cash statistics (C-stat, [35]). C-stat exactly accounts for the Poisson nature of photon distributions and is usually applied in cases involving high spectral resolution data, a scenario frequently encountered in this thesis, albeit still requiring spectral bins grouping to satisfy the Nyquist theorem (i.e. oversample the resolution by a factor of 3).

In this section, I describe several frequently utilized models in the analysis of AGN spectra, including the X-ray continuum models (Sec.2.2.1) and photoionization models (Sec.2.2.2).

2.2.1 X-ray Continuum Models of AGN

The phenomenological model, frequently used to parameterize the X-ray continuum (0.3–10 keV) of AGN in the literature, is the combination of a power-law with a high-energy cutoff, a blackbody component characterized by its temperature, a Gaussian emission line possibly distorted by relativistic effects and the consideration of Galactic absorption. Specifically, the power-law component approximates the hot corona emission (Sec.1.1.2.2); the blackbody characterizes the soft X-ray excess (Sec.1.1.2.4); and the Gaussian line explains the most prominent reflection feature: Fe K lines (Sec.1.1.2.3). Then I describe the physical models for these components.

2.2.1.1 Comptonization Model

The physical models for the coronal emission are `nthComp` [378, 382] or `compTT` [335, 336] in XSPEC, and `comt` [335, 336] in SPEX. These models describe the process of inverse Compton scattering of seed photons from the accretion disk in a hot corona. Key parameters in these models include:

- the temperature of seed disk photons $kT_{\rm bb}$ (k is the Boltzmann constant) which undergo Compton scattering
- the temperature of the plasma electrons $kT_{\rm e}$ where the Comptonization process occurs
- the spectral slope of the power-law Γ or the optical depth of the plasma τ. The relation between Γ and τ is given by the equation in [378],

$$\Gamma = \sqrt{\frac{9}{4} + \frac{m_{\rm e}c^2}{\tau kT_{\rm e}(1+\tau/3)}} - \frac{1}{2} \tag{2.2}$$

  where $m_{\rm e}$ is the rest-frame electron mass.

In AGN, the temperature of the accretion disk normally peaks in the extreme UV (EUV) band between 0.01–0.1 keV (see Fig.1.2). The temperature of the corona introduces an exponential rollover in the high-energy part of the power-law spectrum, ranging from 15 to of the order of 100 keV [156, 153]. The spectral slope of the hot corona typically varies between 1.2–3 [153] with an optically thin plasma $\tau < 1$ [295].

2.2.1.2 Relativistic Reflection Model

The currently most advanced model for the X-ray reflection component is the `relxill` [52, 94] package, which includes both the calculation of relativistic effects in the vicinity of SMBHs [55, 53] and the rest-frame disk reflection model [96, 97, 95].

Models for the rest-frame ionized disk reflection spectrum usually assume the disk as a constant-density slab illuminated by incoming photons with a certain spectral shape (e.g. a power-law with a high energy cutoff or a thermal Comptonization model). These models calculate the observed reflected spectra by considering both absorption and emission processes, depending on the ionization paramter ξ, iron abundance $A_{\rm Fe}$, and the inclination angle between our line-of-sight (LOS) and the normal to the accretion disk i. Fig.2.4 illustrates the influence of these disk parameters on observed spectra (see more details in [96]), where the abundance parameter is characterized by that of iron, which is abundant in the Universe.

In the regions close to the SMBH, photons re-emitted by the accretion disk are heavily affected by the relativistic effects due to the extreme velocity and strong gravitational field. Fig.2.5 presents the effects of the Doppler shift, relativistic beaming, and gravitational redshift on an emission line from the accretion disk, resulting in a broad and skewed line profile. These relativistic effects are related to the coronal emissivity profile q (or the height of corona h in the lamp-post geometry), the black hole spin $a_\star$, and the inner and outer disk

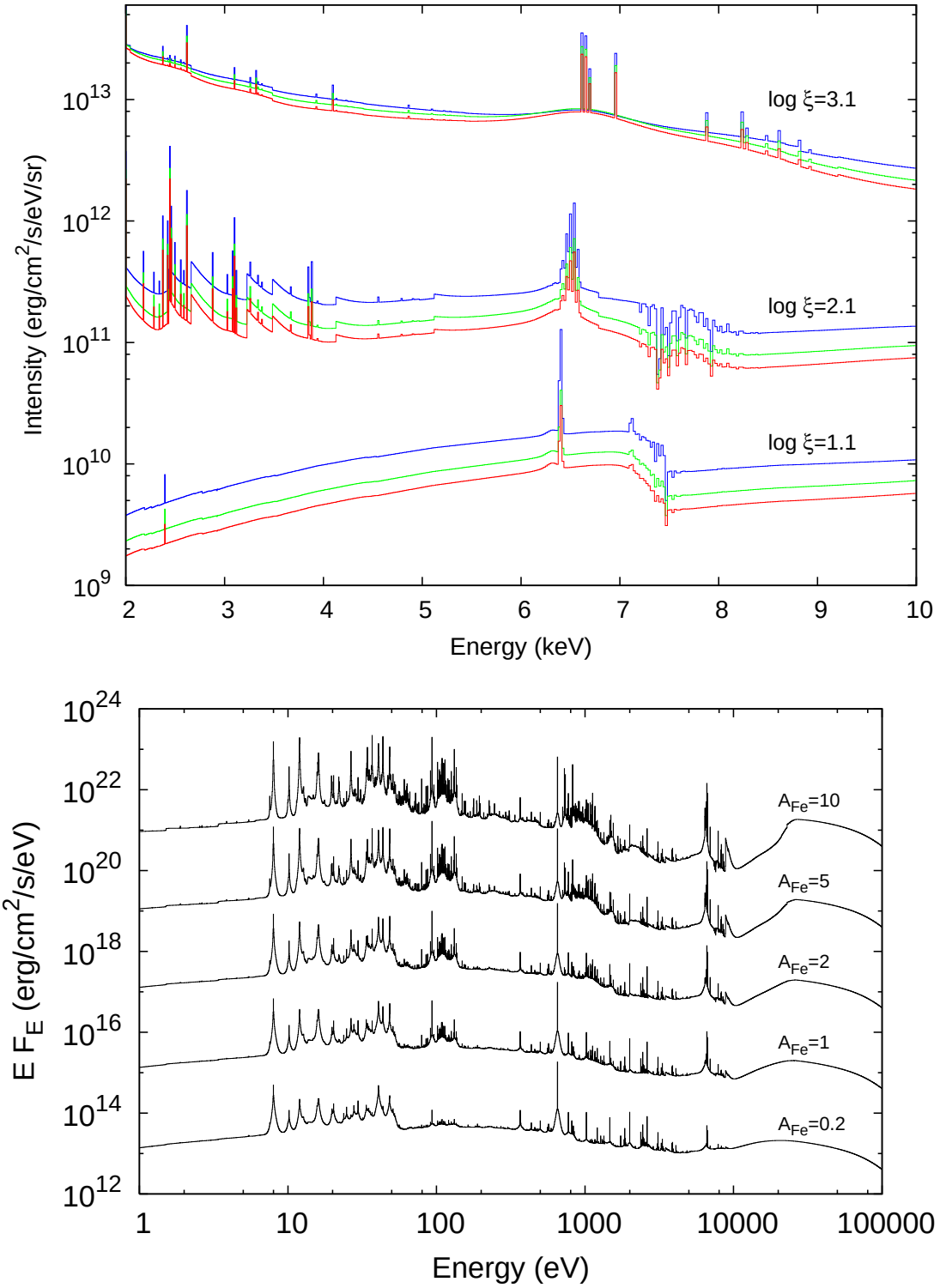

Fig. 2.4 The rest-frame disk reflection spectra (credit to [96]) for different ionization parameters as viewed at three inclination angles (*top*), and various iron abundance (*bottom*). In the *top* panel, the *red* curves correspond to $\mu = \cos i = 0.95$, the *green* curves to $\mu = 0.5$, and the *blue* curves to $\mu = 0.05$, while the ionization parameters are marked in the plot. In the *bottom* panel, for clarity, the curves are shifted by arbitrary factors, and various values of the iron abundance are shown at the top of each curve.

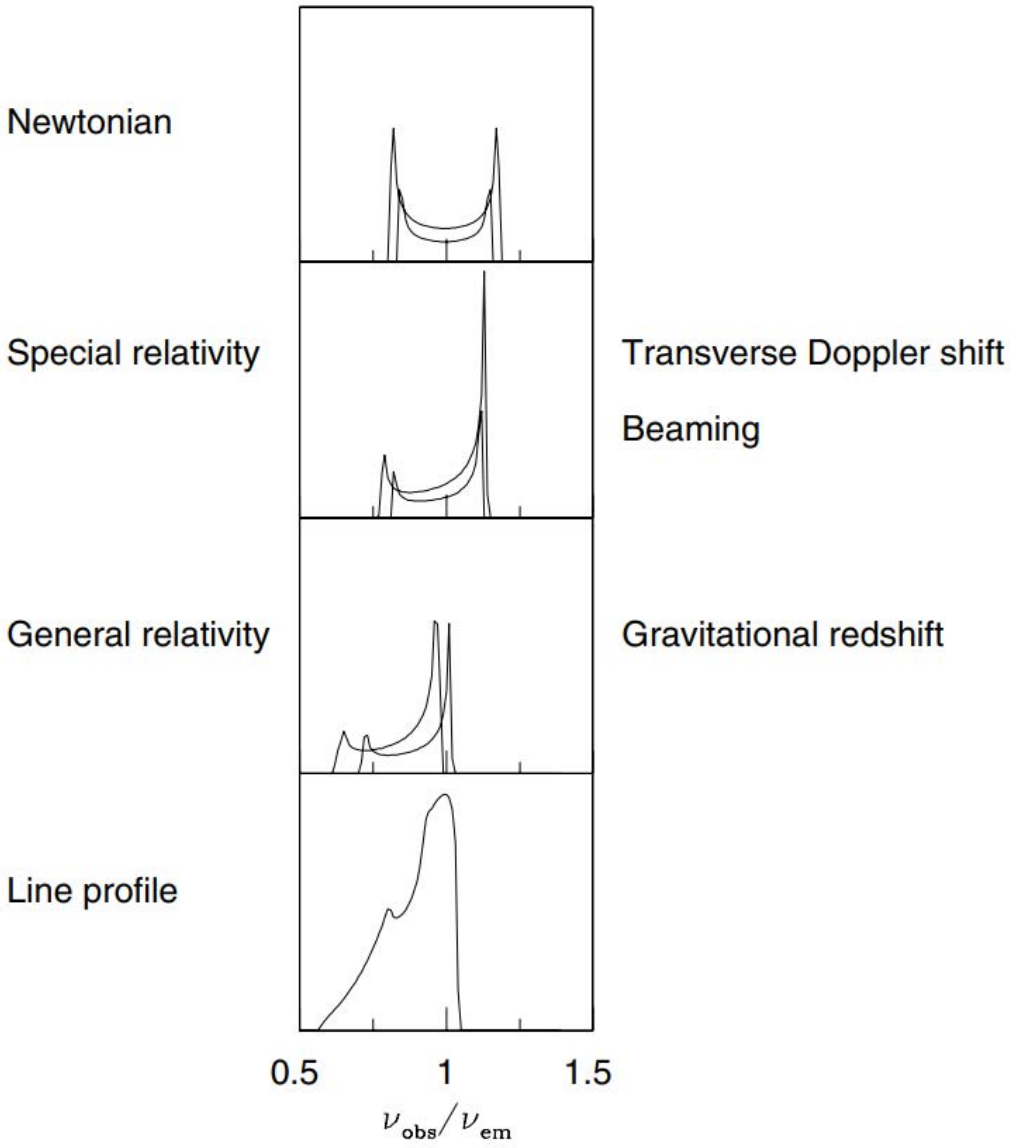

Fig. 2.5 The profile of an intrinsically narrow emission line is modified by the relativistic effects occurring in the accretion disk (credit to [70]). The emission line is intrinsically symmetric and double-peaked due to the Doppler effects (*upper*) in a non-relativistic Newtonian disk. The effects of transverse Doppler shifts (making the profiles redder) and of relativistic beaming (enhancing the blue peak flux) are included in the *second* panel. In the *third* panel, the line profile is redshifted due to the gravitational redshift. All these effects combined give rise to a broad and skewed line profile in the *bottom* panel.

radius $R_{\rm in,out}$. The non-relativistic Newtonian emissivity profile is $q = 3$ for flux $F \propto r^{-q}$ (r is the distance from the source), while the light-bending effect in the strong gravitational field can steepen the index $q > 3$. Alternatively, a simple point-like isotropic lamp-post corona self-consistently defines the emissivity profile, thereby only related to the height of corona h. The relativistically affected line profile is sensitive to the inner radius of the disk $R_{\rm in}$ or the black hole spin $a_\star$, while the outer radius is insensitive to the X-ray spectral fitting and usually fixed at a large radius, e.g. $400\,R_{\rm g}$.

2.2.1.3 Soft Excess Model

The soft excess may originate from the warm Comptonization component of the accretion disk or the relativistically blurred reflection in a high-density disk (see Sec.1.1.2.4). The warm corona can be explained by the same models described in Sec.2.2.1.1. The differences fall in the temperature of electrons, with a cooler temperature range of $kT_{\rm e} \sim 0.1$–$0.2\,$keV, and the spectral slope or the optical depth, with a steeper slope of $\Gamma \sim 2$–3.5 and an optically thick plasma of $\tau \sim 5$–40 [62, 257, 256]. The relativistic reflection scenario can be modeled by a flavor of `relxill`, `relxillD`, where the density of the accretion $n_{\rm e}$ is variable and can be larger than the typically assumed value of $10^{15}\,{\rm cm}^{-3}$ [98]. Fig.2.6 illustrates that numerous fluorescent lines in the soft X-ray band are enhanced in the high-density disk, leading to a smoothed excess component after considering the relativistic effects.

2.2.2 Ionized Plasma Modelling

When X-ray photons from a hot corona traverse an ionized plasma, a fraction of these photons are absorbed at specific energies corresponding to elemental transition, depending on the ionization state or temperature of the plasma. Subsequently, these photons are generally scattered in various directions. This scattering leaves absorption lines imprinted on the continuum spectrum when our LOS aligns with the original direction. On the other hand, if our LOS differs, we observe emission lines resulting from the scattered radiation. In practical scenarios, if we are observing the X-ray radiation from AGN through an ionized outflow, the observed spectrum will be a composite of both absorption and emission features (e.g. Fig.1.6).

The absorption and emission lines produced in the ionized outflow are calculated theoretically by simulating a slab of plasma irradiated by the radiation field with a given SED. In the spectral modeling of this thesis, the plasma is assumed in the photoionization equilibrium, whereby the rate of ionization is equal to the rate of recombination, although in Chapter 4 I make use of the novel out-of-equilibrium photoionization model to account for delayed

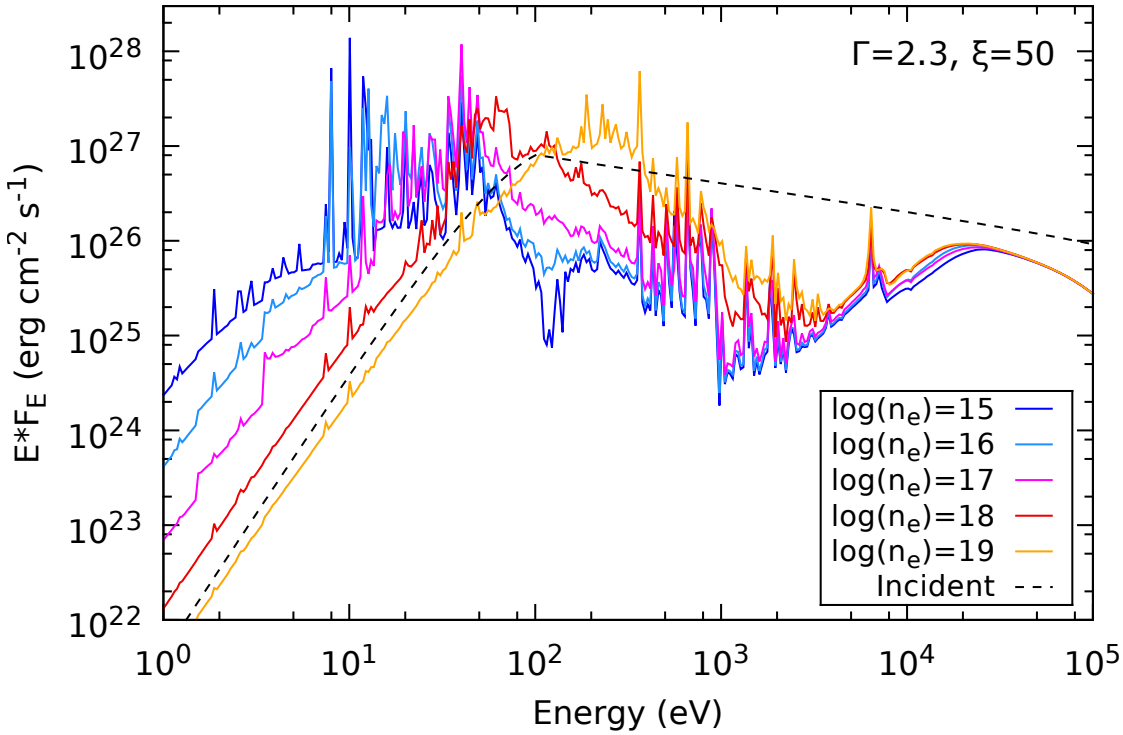

Fig. 2.6 Reflection spectra for different densities of the accretion disk (credit to [98]). The solid curves correspond to the density values indicated in the legend. The dashed curve is the incident power-law spectrum that illuminates the disk. Each curve is normalized by an extra factor for comparison, where the boosted soft X-rays are observed in the high-density spectrum.

responses to luminosity variations. Photoionization models, such as `XSTAR` [151], `CLOUDY` [80], and `PION` [227] in SPEX, calculate all ionic line column densities at the ionization balance based on the properties of plasma and the continuum radiation. The difference between these two codes lies in their usage procedures. `XSTAR` necessitates pre-calculations, whereas `PION` can autonomously run calculations within the SPEX package, making it the most frequently used model in this thesis.

2.2.2.1 Effects of Spectral Energy Distribution

A crucial factor in the photoionization calculation is the broadband SED, which can modify the ionization balance. The influence of different SEDs on the ionization balance of plasma is shown in Fig.2.7, where the *top* panel presents various input SEDs and the *bottom* panel showcases the 'stability curves' [180]. These curves, depicting the ionization parameter as a function of the pressure ratio Ξ, serve as powerful diagnostic tools for illustrating the stable and unstable regions of plasma. The pressure ratio is defined as the ratio between the radiation pressure (F/c) and the thermal pressure ($n_{\rm H}kT$), $\Xi = \frac{F/c}{n_{\rm H}kT} = 19222\frac{\xi}{T}$, where F represents the ionizing flux $F = L_{\rm ion}/4\pi R^2$ and $\xi = L_{\rm ion}/n_{\rm H}R^2$. Along these curves, the plasma is in thermal equilibrium, where the heating rate is equal to the cooling rate. To the left of the curve, cooling dominates over heating while to the right, heating prevails over cooling. On the branches of the curve with a positive gradient, the plasma is thermally stable, because minor perturbations in temperature, either upwards or downwards, are counterbalanced by corresponding increases in cooling or heating. Conversely, on the branches with a negative gradient, the plasma is thermally unstable. As depicted in Fig.2.7, sources with harder spectra exhibit more unstable branches, where plasma should, in principle, not be found for long periods.

2.2.2.2 Key parameters of `PION`

The main parameters of `PION` are the column density $N_{\rm H}$, the ionization parameter ξ, the turbulent velocity σ_v, and the LOS velocity of the outflow $v_{\rm LOS}$. $N_{\rm H}$ is the total number of hydrogen in either ionic or atomic forms, determining the line strength in the spectrum: a higher column density results in more pronounced line features. The ionization parameter ξ (see Eq.1.9) serves as an indicator to quantify the ionization state and temperature of the plasma, with higher ionization states corresponding to enhanced occurrences of absorption and emission lines at higher energies. The turbulent velocity σ_v characterizes the velocity dispersion of the plasma, affecting both widths and the intensities of line features. The LOS

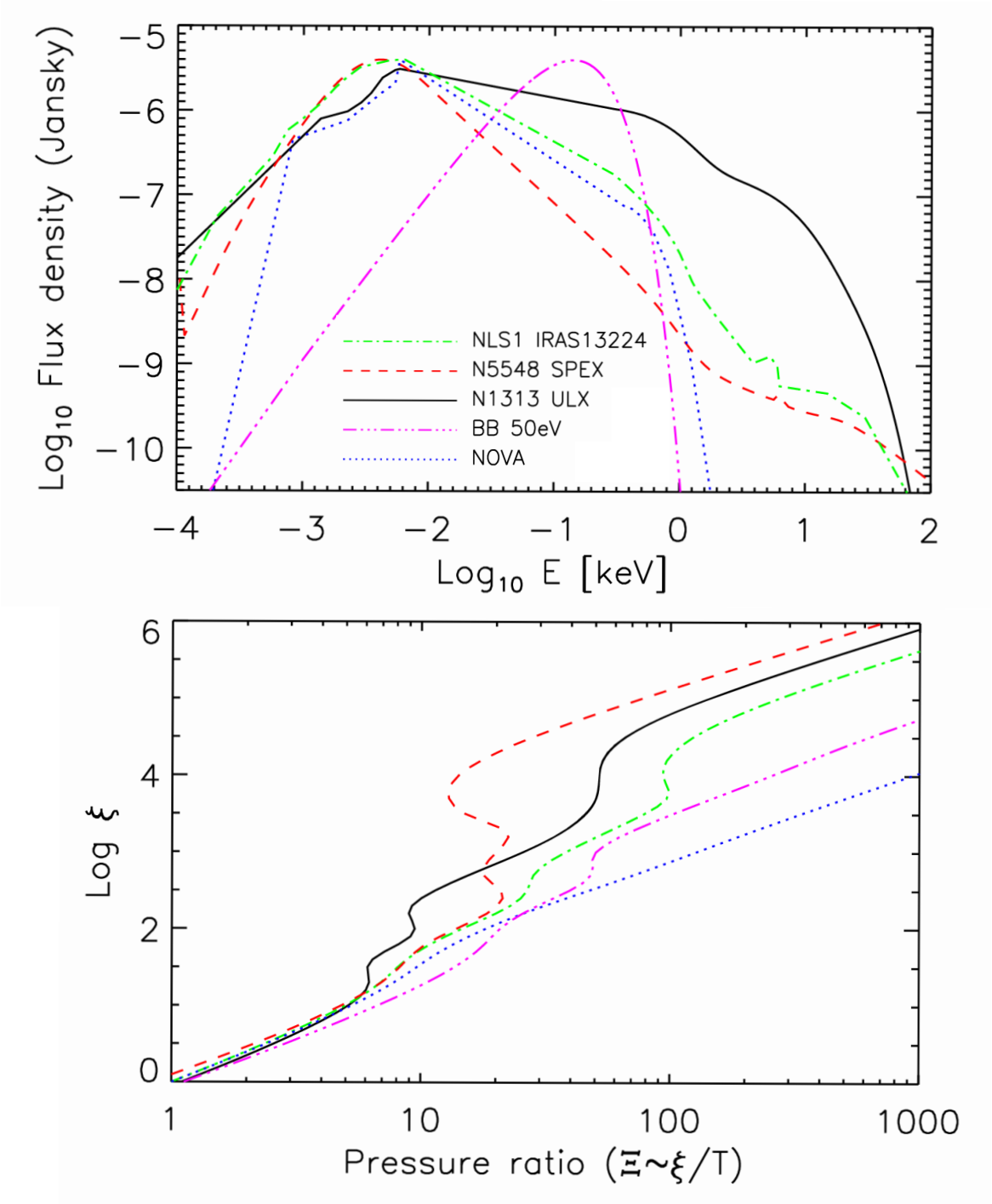

Fig. 2.7 Different SEDs (*top*) and corresponding stability curves (*bottom*) of irradiated plasma (credit to [261]). The SEDs include two AGN IRAS 13224-3809 and NGC 5548 with high and low accretion rates respectively, an ultra-luminous X-ray (ULX) source NGC 1313 X-1, a 50 eV blackbody, and a nova V2491. Additional details regarding the stability curves can be found in Sec.2.2.2.1.

out velocity $v_{\rm LOS}$ is associated with the kinetic energy of plasma, resulting in shifted lines relative to their rest-frame wavelengths.

Elemental abundances, the covering factor for absorbing gas $C_{\rm F}$, and the solid angle for emitting gas Ω are the other three important quantities. Elemental abundances modify the relative strengths of various lines compared with each other. Both the covering factor and solid angle in `PION` range from 0 to 1. The covering factor $C_{\rm F}$ represents the local clumpiness of the gas along the LOS, while the solid angle Ω, normalized by 4π, corresponds to the fraction of the solid angle across the entire sky that is occupied by the emitting plasma as viewed from the corona. Accordingly, `XABS` is a simplified and fast version of `PION` [324], only modeling the absorption features with $\Omega = 0$. In the spectral fitting conducted in this thesis, unless explicitly stated, the covering factor of `XABS` is assumed at $C_{\rm F} = 1$, while `PION` is utilized solely to explain the emission component with $C_{\rm F} = 0$ and $\Omega = 1$.

2.3 Spectral Search Methods

Outflows as well as any other involved plasma such as the ISM leave imprints on the X-ray spectrum in the form of absorption, emission lines, and photoelectric edges. This section introduces two powerful methods, frequently employed in this thesis, to search for ionized outflows through spectral lines (Sec.2.3.1) and physical modeling (Sec.2.3.2) as well as an efficient Monte Carlo (MC) simulation method (Sec.2.3.3).

2.3.1 Individual Line Search

The individual line search is a straightforward method to identify line features on the continua. This approach involves iteratively fitting an additional Gaussian line on top of the best-fit continuum model. In each iteration, the Gaussian line is located at a fixed energy with a predefined line width, while the normalization can vary to be both positive or negative, to reproduce an emission and absorption line, respectively. The line energy spans the energy band of interest with a grid that ideally slightly oversamples the energy resolution of the instrument. The oversampling relies on both the number of the energy grids and the width of the Gaussian lines. In the most common case of jointly fitting the RGS and EPIC spectra (0.4–10 keV) in this thesis, the number of energy grids typically ranges between 300–2000 on a logarithmic scale. Correspondingly the Gaussian line width varies from 5000 to 500 km/s, to keep the balance between instrument resolution and computational costs, and keep the independence of scanned energy bins. The original continuum model is allowed to vary during these iterations.

The statistical improvement to the best-fit continuum model, $\Delta\chi^2$ or ΔC-stat (both are comparable for bright sources, see Sec.2.2 and [144]), is recorded at each step. These values serve as an indicator of the significance of any detected line features. Each fit is a single trial for one additional free parameter (the line normalization) compared with the original continuum model. Consequently, an improvement of ΔC-stat$= 9$ corresponds to a significance level of 3σ [35]. By performing numerous fits for a grid of line energies spanning the energy band of interest, as illustrated in Fig.2.8, we can estimate the detection significance of individual line features in the spectrum.

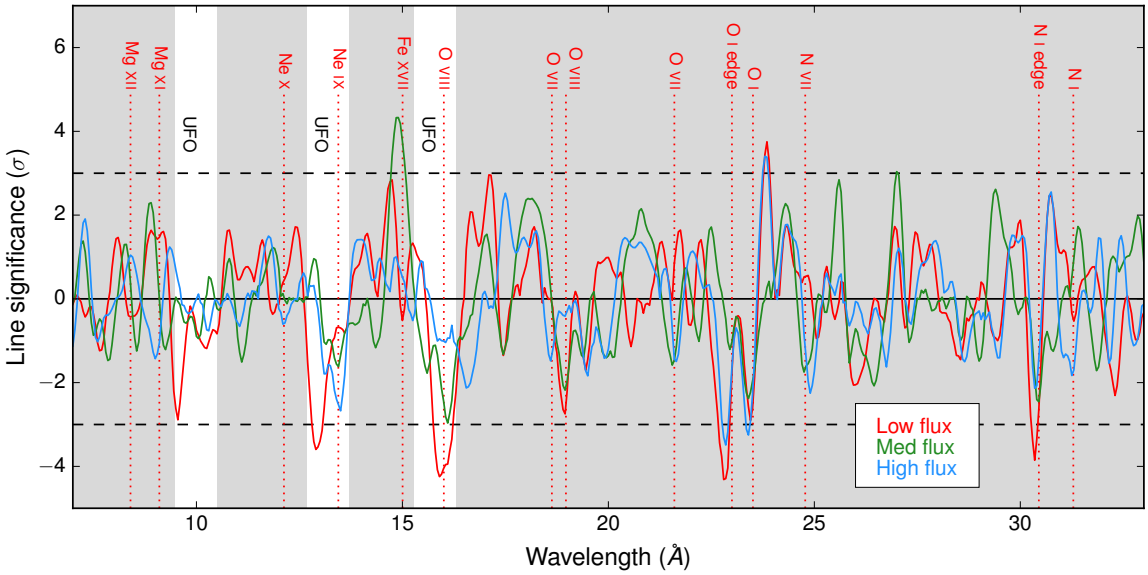

Fig. 2.8 Line significance assessed by a Gaussian, fitting to three flux-resolved RGS spectra over the 7–27Å wavelength range, with increments of 0.05Å and a line width of 1000 km/s (credit to [252]). The labeled transitions represent the rest-frame interstellar absorption lines. The regions of UFO absorption are highlighted by the *white* background. Wavelengths are in the observed frame.

However, it is important to note that this method is merely an approximation, as it does not account for the numerous trials conducted to detect features across the entire energy band, which can be important in limited-statistics spectra. This limitation, known as the "look-elsewhere effect" [352], tends to overestimate the true significance. To determine the actual significance of a line, MC simulations are required. Details regarding an efficient MC simulation approach for Gaussian line searches are provided in Sec.2.3.3.

2.3.2 Physical Model Search

Detecting lines originating from plasma with Doppler-shift significantly larger than the spectral resolution in an X-ray spectrum is challenging. A plasma is usually characterized by multiple physical properties as described in Sec.2.2.2.2, resulting in a large parameter space. Consequently, fitting photoionization models are easy to fall in the local minima of this parameter space. In such cases, the same line features can be comparably explained by various solutions with different ionization states and speeds. In addition, some weak plasma solutions might be overlooked, especially when no single absorption line is notably significant, but multiple moderately significant features are present in the spectra. To address these issues, a physically motivated spectral model search across the parameter space is essential. Such a method to be described is capable of identifying the globally best-fit solution, along with its statistical significance, and revealing the distribution of all potential solutions within the parameter space. This approach is particularly valuable in uncovering multiphase plasma.

The photoionization model is added to the best-fitting broadband continuum model, similarly as done during the Gaussian line search (Sec.2.3.1). The only difference is that an additive spectral model is employed for emission lines, while the multiplicative plasma model is applied for absorption lines. In principle, an ionized outflow can have any Doppler shift, ionization parameter, column density, and turbulent velocity, requiring the search over a multi-dimensional parameter space of photoionization models. In this thesis, a coarse turbulent velocity σ_v grid is chosen to reduce the computational cost. Our search concentrates on the parameter space of ionization parameters $\log \xi$ and outflow LOS velocities $v_{\rm LOS}$. The continuum parameters and the column density of plasma $N_{\rm H}$ are allowed to vary freely in each grid fit, with the other plasma parameters fixed, because the column density will return to zero if the additional plasma component is disfavored by the data. Subsequently, the statistical improvements for each fit are recorded, indicating the significance of the additional component. For instance, Fig.2.9 illustrates the results of an absorption model scan across the spectrum of PG 1448+273 [173]. The results reveal a globally best-fit UFO solution with a LOS velocity of $v_{\rm LOS} \sim -27000\,{\rm km/s}$ and an ionization parameter of $\log \xi \sim 4$. Additionally, a potential secondary moderately ionized ($\log \xi \sim 2$) UFO with a velocity of $v_{\rm LOS} \sim -80000\,{\rm km/s}$ is also identified, demonstrating the effectiveness of the physical model search approach.

As previously discussed in Sec.2.3.1, it is important to note that this method does not account for the look-elsewhere effect, which arises from the increased likelihood of detecting a spurious and strong solution purely from random noises when searching a large parameter space. The real wind detection significance can only be obtained through MC simulations.

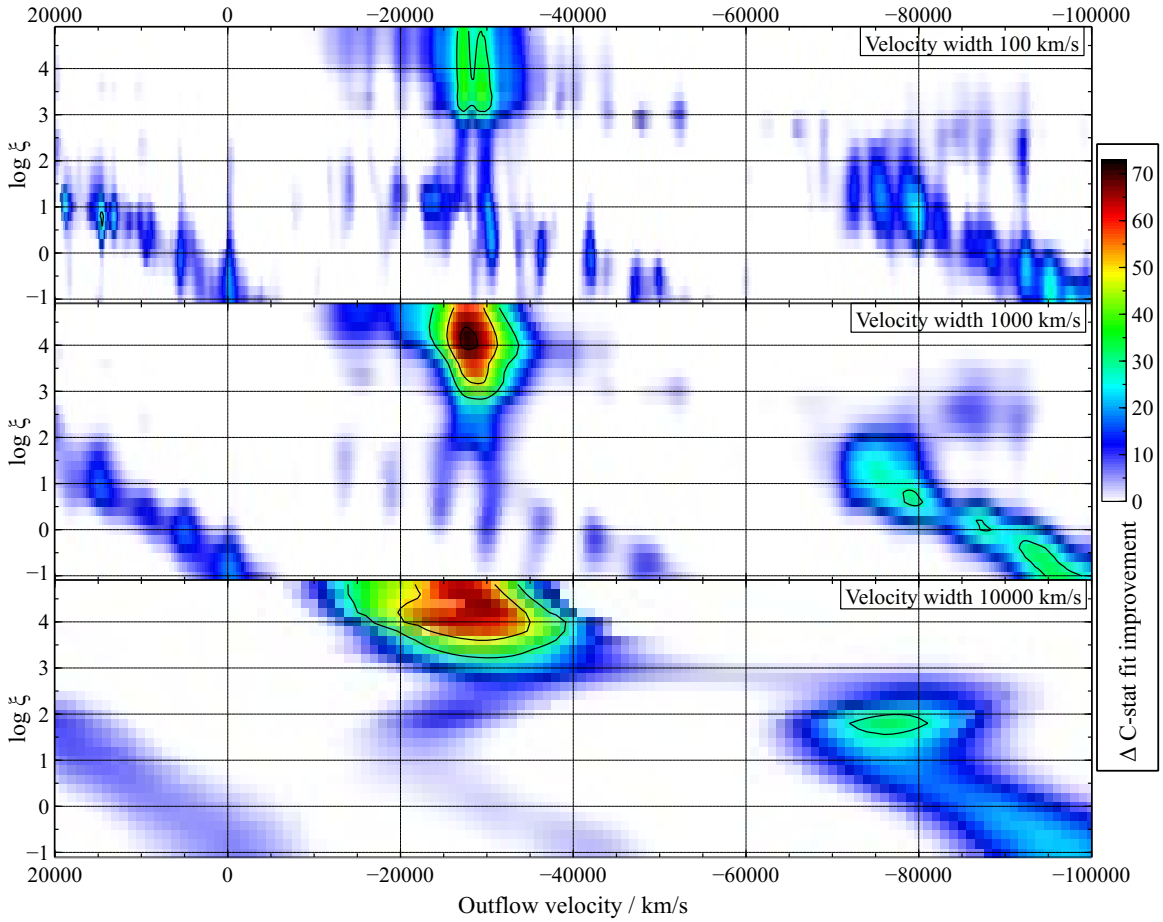

Fig. 2.9 Systematic scan for ionized outflow features in the spectrum of PG1448+273 (credit to [173]). The spectrum is scanned with photonization absorption model `XABS`. The grids encompass systematic velocities between +20000 and -100000 km/s (on the X-axis), ionization parameters $\log \xi$ between -1.0 and +4.8 (on the Y-axis), with turbulent velocities of 100 km/s (*top* panel), 1000 km/s (*middle* panel), and 10000 km/s (*bottom* panel). The color represents the C-stat improvement achieved by adding an absorption component to the baseline continuum model (according to the color bar on the right), and the black contours show C-stat fit improvement of 30, 50, and 70, respectively.

However, such simulations, especially for non-trivial baseline continuum models, can be computationally expensive if carried over the entire parameter space. A more efficient MC simulation method for the line search is described in Sec.2.3.3 and could serve as an inspiration for future efficient physical model searches.

2.3.3 Cross-Correlation Based Monte Carlo Simulation

As mentioned in Sec.2.3.1 and 2.3.2, only through MC simulations to estimate the false positive rate can obtain the actual detection significance of lines or plasma. In each simulation, a fake synthetic spectrum is generated, based on the best-fit continuum model as a template, replicating the characteristics of real data, including the same response matrix and statistical properties. The simulated spectrum ideally only contains Poisson noise without any plasma line features. Subsequently, the same search procedure, as previously described in Sec.2.3, is applied to each simulated spectrum to determine the fraction of spectra with spurious detections that are stronger (i.e. with higher statistical improvement) than the one detected in the real spectra, regardless of the parameter grid associated with the fake detection (i.e. across the entire parameter space). To achieve a 3σ detection (i.e. 99.7 % probability), the search must be conducted on 1000 simulated spectra. This results in a computational cost on the order of approximately 10^3 hours for Gaussian line searches and 10^4 hours for physical model searches.

In this thesis, for the sake of the computational costs, an efficient MC method, recently developed by [172], is employed for the line search, applied in Chapter 5. The innovation of this method is to employ the cross-correlation (CC) approach instead of fitting the Gaussian line spanning a specified energy band. For simplicity, we take an example of a fixed line width and search within the parameter space of the line energy. The CC is calculated in the form of

$$C = \sum_{i=1}^{N} x_i y_i \tag{2.3}$$

where x and y are the arrays of the residual spectrum and the Gaussian line model, respectively, at a predefined line width and energy. The residual spectrum is obtained after modeling the continuum in Y-axis units of Photon/s/keV/cm^2. Then the CC values obtained from real and simulated data are normalized by the root-mean-square (RMS) value of simulated CCs, within each parameter bin, i.e. with a specific fixed line energy. The renormalized CC serves as an indicator of the detection significance, similar to $\Delta\chi^2$ or ΔC-stat. By counting the number of simulated CCs, across all line energy grids, that exceed the real CC, we can calculate the true significance of the line detection at each energy. Notably, this step takes the look-elsewhere effect into account.

The cross-correlation approach provides a substantial boost in the efficiency of MC simulations, making them approximately 10,000 times faster compared to traditional spectral fitting methods. While this approach has been successfully applied to line searches, its potential extension to physical model searches remains an area for future development and exploration (see Sec.7.3.1).

2.4 Variability Analysis

In addition to the presence of line features in X-ray spectra, ionized outflows also manifest their presence through variability in the X-ray emission. Since UFOs are believed to originate from the inner accretion disk, they can exhibit high variability [247, 289]. UFOs are expected to respond rapidly to changes in the continuum emission, with ionization states changing on timescales of hours or less depending on the black hole mass. This rapid response leads to an increased variance in energy bands corresponding to strong UFO features. UFO lines, in practice, appear as positive spikes in variability spectra, as depicted in Fig.2.10 [247]. Therefore, variability analysis is another powerful and model-independent method for detecting ionized outflows [247, 131]. This section describes the details of two variability analysis methods, which are applied in Chapter 5: fractional excess variance spectrum and principal component analysis in Sec.2.4.1 and 2.4.2 respectively.

2.4.1 Fractional Excess Variance Spectrum

The fractional excess variance spectrum, often denoted as $F_{\rm var}$ or RMS spectrum, is a widely used method for quantifying spectral variability [67, 350]. The basic principle involves the following steps: 1) compute the variance of light curves within specific energy bands, 2) subtract the variance contribution expected from measurement errors, 3) normalize the resulting net variance by the mean count rate of light curves, and 4) repeat this process across multiple energy bins to generate an RMS spectrum. This can be accomplished either in the time domain, calculating the variance of light curves in specific energy bands, or in Fourier space by integrating the power spectrum within a given energy band between two frequencies. These two approaches are formally equivalent: the lowest frequency probed for a particular light curve corresponds to the inverse of the light curve duration, while the highest frequency is the Nyquist frequency $1/(2\mathrm{d}t)$, where $\mathrm{d}t$ is the time step of the light curve.

Here we present analytic formulae in the time domain (see details of the Fourier domain approach in [350]). For X-ray light curves or time segments within a given energy band, the

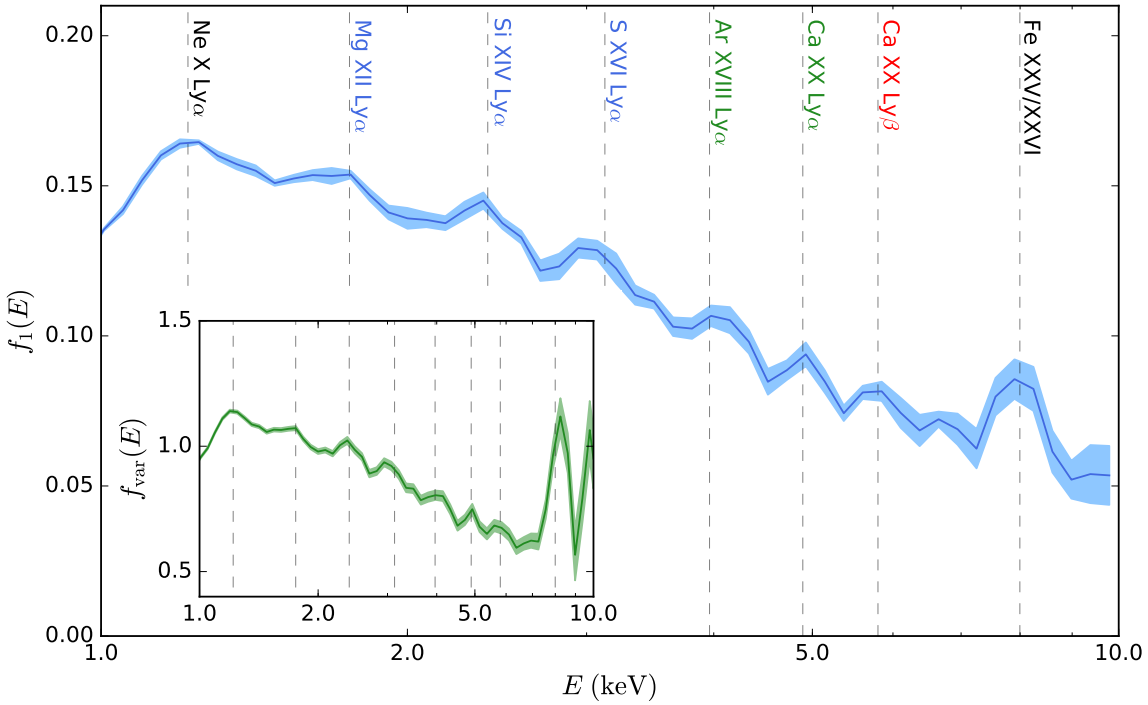

Fig. 2.10 The first principal component (PC1) obtained through principal component analysis (PCA) and the fractional excess variance spectrum (*inset*) for IRAS 13224-3809 from 1 to 10 keV (credit to [247]), with the energies of the strongest UFO lines marked by *dashed* lines. Energies are in the observer's frame.

fractional excess variance $F_{\rm var}$ is calculated as follows:

$$F_{\rm var} = \sqrt{\frac{S^2 - \overline{\sigma_{\rm err}^2}}{\bar{x}^2}} \tag{2.4}$$

Here, $\bar{x}$ represents the mean flux of light curves. S^2 denotes the mean squared variance, given by

$$S^2 = \frac{1}{N}\sum_{i=1}^{N}(x_i - \bar{x})^2 \tag{2.5}$$

where N is the number of light curves. The mean squared error $\overline{\sigma_{\rm err}^2}$ is calculated as

$$\overline{\sigma_{\rm err}^2} = \frac{1}{N}\sum_{i=1}^{N}\sigma_{\rm err,i}^2 \tag{2.6}$$

where $\sigma_{\rm err,i}$ represents the Poisson error of the $x_i^{\rm th}$ light curve or time segment. The uncertainty of $F_{\rm var}$ is defined by

$$\mathrm{err}(F_{\rm var}) = \sqrt{(\sqrt{\frac{1}{2N}}\frac{\overline{\sigma_{\rm err}^2}}{\bar{x}^2 F_{\rm var}})^2 + (\sqrt{\frac{\overline{\sigma_{\rm err}^2}}{N}}\frac{1}{\bar{x}})^2} \tag{2.7}$$

The calculation of $F_{\rm var}$ is then repeated across the desired energy range to produce the RMS spectrum, as exemplified in Fig.2.10, 0.3–10 keV for *XMM-Newton*.

2.4.2 Principal Component Analysis

Principal component analysis (PCA) is a method of decomposing a dataset into a set of orthogonal eigenvectors, or principal components (PCs) to describe the variability of the data [209, 250]. The advantage of this method over the RMS spectrum is that it can isolate contributions from different variable mechanisms rather than just the sum of all variability like the RMS approach. The PCs are calculated by the singular value decomposition (SVD) method, which factorizes an $n \times m$ dimensional data set in the form of

$$M = UAV^{\star} \tag{2.8}$$

where U is an $n \times n$ matrix, V is an $m \times m$ matrix and A is an $n \times m$ diagnoal matrix. The matrices U and V then each describe a set of orthogonal eigenvectors associated with the matrices $MM^{\star}$ and $M^{\star}M$, respectively. The corresponding eigenvalues are given by the diagonal values of A, and are equal to the square of the variability in each component.

In practice [250, 247], the matrix M could be a grid of background-subtracted spectra $F(E,t)$ extracted from a specific time interval, with columns corresponding to energy and rows corresponding to time. Then it is transformed to normalized residual spectra:

$$f(E,t) = \frac{F(E,t) - \bar{F}(E)}{\bar{F}(E)} \tag{2.9}$$

where $\bar{F}(E)$ represents the time-averaged spectrum at E energy bin. PCA then decomposes this grid into a set of spectral components $f_i(E)$ and light curves for components $A_i(t)$ such that

$$f(E,t) = \sum_{i=1}^{n} a_i f_i(E) \times A_i(t) \tag{2.10}$$

with a set of eigenvalues corresponding to each PC a_i as coefficients. Errors are determined through the MC approach of [231] by perturbing the input spectra with Poisson noise and repeating the analysis, then measuring the standard deviation.

By plotting the fractional variability of each component (i.e. the squared root of a_i) on a log scale (see Fig.2.11), the real variable components can be distinguished from the noise, where the variability of noise components follows a geometric decay, as a straight line on the diagram. As a result, PC1 spectra typically exhibit the most significant variability in the source spectra, and they can be compared with the RMS spectrum calculated using the same dataset. The difference between them can diagnose the correlated and uncorrelated variability. For example, Fig.2.10 illustrates that the Fe XXV peak is weaker in the PC1 spectrum than the RMS spectrum, suggesting a weaker correlation between Fe XXV and the continuum compared to other lines.

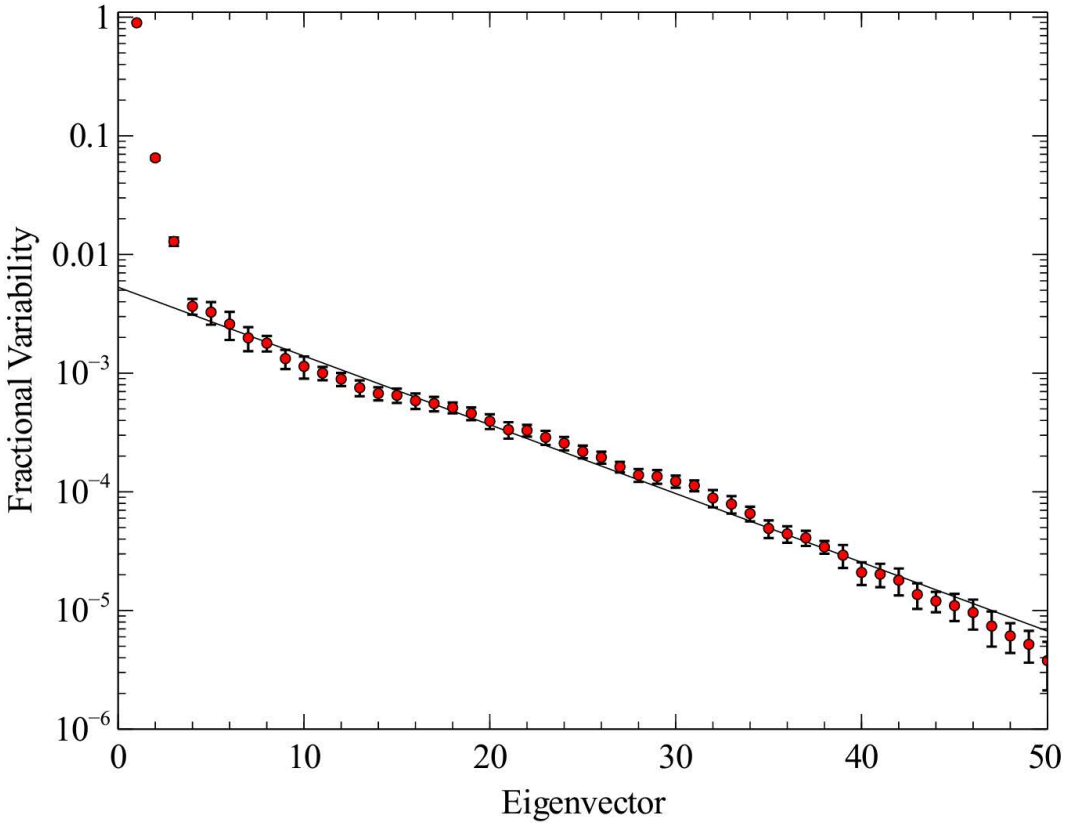

Fig. 2.11 Log-eigenvalue (LEV) diagram for Ark 564 (credit to [250]). This diagram illustrates the fractional variability of each eigenvector obtained from the PCA of Ark 564. The *black* line represents the best-fit geometric progression, expected from the noise. Notably, the first three components are highly significant due to their deviation from the expected noise level.

Chapter 3

Wind-luminosity evolution in narrow-line Seyfert 1 AGN 1H 0707-495

Abstract

In this chapter, we perform a flux-resolved X-ray spectroscopy on a super-Eddington and variable NLS1 AGN, 1H 0707-495, using all archival *XMM-Newton* observations to study the structure of the UFO. We find that the wind spectral lines weaken at higher luminosities, most likely due to an increasing ionization parameter as previously found in a few similar sources. Instead, the velocity is anti-correlated with the luminosity, which is opposite to the trend observed in the NLS1 IRAS 13224-3809. Furthermore, the detection of the emission lines, which are not observed in IRAS 13224-3809, indicates a wind with a larger opening angle in 1H 0707-495, presumably due to a higher accretion rate. The emitting gas is found to remain broadly constant with the luminosity. We describe the variability of the wind with a scenario where the strong radiation extends the launch radius outwards and shields the outer emitting gas, similarly to super-Eddington compact objects, although other possible explanations are discussed. Our work provides several hints for a multi-phase outflow in 1H 0707-495.

3.1 Introduction

Radiation pressure due to a high accretion rate is a popular theory for the origin and acceleration mechanism of UFOs [e.g. 291, 220]. It is therefore of great interest to investigate UFOs in sources accreting near or above their Eddington limit. NLS1 galaxies are an ideal population, characterized by low-mass, high-accretion-rate SMBHs (Sec.1.1.1.1). In the past few years, UFOs have been discovered in many NLS1 galaxies, e.g., IRAS 13224-3809 [hereafter IRAS 13224 252], WKK 4438 [138], 1H 0707-495 [hereafter 1H 0707, 170], PG 1448+273 [173], IRAS 00521-7054 [a Seyfert 2 galaxy, 357], and PG 1211+143 [a narrow emission line quasar, 276], showing a blueshifted Fe absorption line above 7 keV.

A series of deep studies on IRAS 13224, on the basis of a 1.5 Ms *XMM-Newton* observation campaign, found an anti-correlation between the equivalent width of the absorption lines and the hard X-ray flux, suggesting that the disappearance of absorption lines in the brightest state is due to the almost completely ionized gas [252, 247, 259]. The blueshift of

absorption lines is also correlated with the luminosity, suggesting a radiatively-driven UFO. It is therefore of crucial importance to determine whether such UFO-luminosity dependence is also present in other NLS1 AGN and use it to probe the wind nature.

1H 0707 is selected for three reasons: 1) 1H 0707 and IRAS 13224 share many similarities among the broadband spectra [380], timing behavior [155], and UV emission features [192]. 1H 0707 shows strong UFO absorption in the low-flux state, which was suggested to weaken with increasing flux by Kosec et al. [170, hereafter PK18]. 2) 1H 0707 has been observed by *XMM-Newton* for ~ 1.4 Ms, providing enough counts for the flux-resolved analysis. 3) The high spectral resolution of the gratings aboard *XMM-Newton* allows us to use also soft X-ray features rather than only iron absorption lines, which is crucial as the Fe K lines are often affected by the instrumental background.

3.2 Data Reduction and Products

The data analyzed in this chapter comprise archival *XMM-Newton* observations of 1H 0707. These observations span a period from 2000 to 2019, encompassing a total gross exposure time of 1.4 million seconds. We have made full use of the data obtained from the EPIC, RGS, and OM instruments.

3.2.1 Data Reduction

The data are processed with the *XMM-Newton* Science Analysis System (SAS v19.0.0) and calibration files available by February 2021, following the standard SAS threads. Briefly, EPIC-pn and EPIC-MOS data are reduced with EPPROC and EMPROC tools respectively. The background flare contamination is filtered with a standard filtering criterion of 0.5 and 0.35 counts/sec (in the 10–12 keV band) for pn and MOS separately. The source spectra are extracted from a circle region with a radius of 20 arcsec centered on the object (X-ray flux peak), and the background spectra are extracted from a nearby circular region with a radius of 60 arcsec away from the source and the copper hole. We adopt a radius of 20 arcsec for the source extraction to decrease the background contamination following Chartas and Canas [39]. The RGS data are reduced with the RGSPROC task, for which high-background contamination is corrected by a threshold of 0.2 counts/sec. We extract the first-order RGS spectra in a cross-dispersion region of 1 arcmin width, and the background spectra are generated by photons beyond the 98 percent of the source point spread function as default. We only use the good time intervals common to both RGS 1 and 2 and stack their spectra.

Only image mode OM data are available, which are reduced using the standard OMICHAIN pipeline, including all necessary calibration processes.

3.2.2 Light Curve

We extract EPIC-pn (0.3–10 keV) light curves from each observation and create an integrated light curve (see the upper left panel of Fig.3.1). For completeness, we have checked that the shapes of light curves for EPIC-MOS and RGS are identical to those for EPIC-pn. The corresponding hardness ratio (HR, H: 2–10 keV; S: 0.3–2 keV) and the count rate histogram are plotted separately in the lower left and right panel of Fig.3.1. 1H 0707 went into a low hard state after 2011. The change has been reported and explained with the light bending effect [79]. An extreme soft variability was also discovered in the 2019 joint observation with *eROSITA*, interpreted with partial covering absorption [27, 248]. To investigate the variability of the UFO with the luminosity, we divide the entire light curve into 7 flux intervals using the good time interval (GTI) files generated by TABGTIGEN script, and the thresholds are selected so that the number of counts in each interval is comparable (see Tab.3.1). The levels from the lowest to highest flux are referred to as F1, F2 ... F7, and their thresholds are marked in different colors in Fig.3.1.

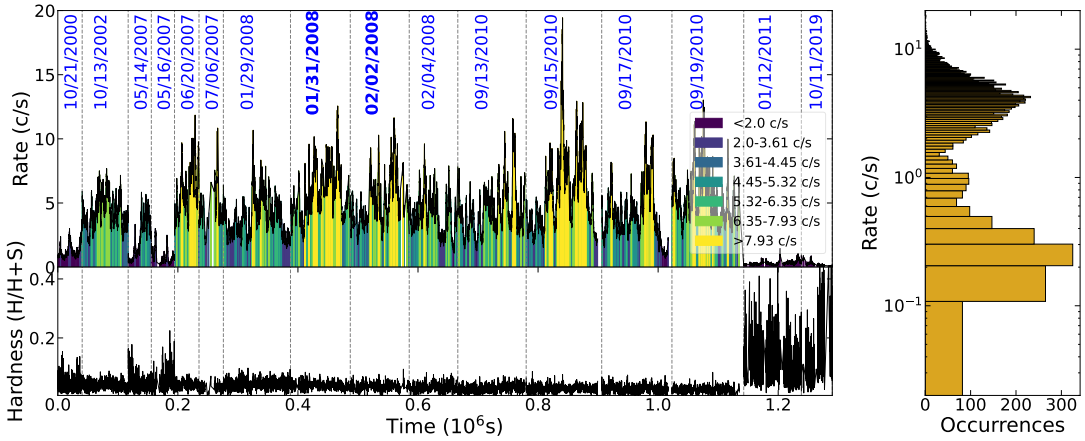

Fig. 3.1 *Upper left:* An overall EPIC-pn light curve (0.3–10 keV) from 2000 to 2019 *XMM-Newton* observations, where the time gaps between observations are ignored and the observation dates are marked. The vertical dashed lines indicate the begin and end time for each observation. The colors represent the different flux intervals, which have comparable counts. *Lower left:* The corresponding X-ray hardness-ratio of EPIC-pn light curves. S and H denote the counts in the soft and hard energy bands defined as 0.3–2 and 2–10 keV, respectively. *Right:* The count rate histogram.

Table 3.1 Details of EPIC-pn flux-resolved level selection in 1H 0707-495

Level	Minimum (counts s^{-1})	Maximum (counts s^{-1})	Frame[a] (ks)	Exposure (ks)
F1	0.0	2.0	1.15	215
F2	2.0	3.61	0.54	254
F3	3.61	4.45	0.28	183
F4	4.45	5.32	0.24	152
F5	5.32	6.35	0.23	128
F6	6.35	7.93	0.29	106
F7	7.93	20.0	0.59	77

[a] Frame means the average duration time for each segment in EPIC-pn light curves for a given flux level.

3.2.3 Time-averaged and Flux-resolved Spectra

We stack the EPIC (0.4–10 keV) and RGS (0.4–1.77 keV) spectra from different observations into time-average broad-band spectra using EPICSPECCOMBINE and RGSCOMBINE scripts. RGS 1 and 2 spectra are combined to increase the signal-to-noise (S/N) ratio per energy bin. We cut off the energy coverage below 0.4 keV because we focus on the wind features, which usually appear well below 30 Å ($\geq$ 0.4 keV), and want to avoid the RGS high background regions (see the bottom panel of Fig.3.2). To obtain flux-resolved spectra, we split each observation according to the defined count rate limits (shown in Fig.3.1 and Tab.3.1) by applying the generated GTI files and extract the spectra following the same steps for time-resolved spectra. We then obtain 21 EPIC (one pn and two MOS for each flux level) and 7 RGS spectra by stacking the spectra within the same flux level.

For clarity, only EPIC-pn and RGS source and background spectra are shown in Fig.3.2. The spectra are plotted in the same colors as the thresholds in Fig.3.1. The $\sim$ 1.5 keV peak in the EPIC background spectra is due to the blend of the strong instrumental Al K and Si K emission lines [e.g. 199]. The background spectrum is comparable to the source spectra above 8 keV for EPIC and on both ends ($>$ 30 Å and $<$ 7 Å) for RGS. The typical UFO feature in EPIC spectra is the broad Fe absorption among 7–8 keV, although there are other absorption lines of Si XIV and S XVI between 1.5 and 3 keV (see PK18). The two dips in the RGS spectra near 13 and 21 Å are not UFO features but RGS instrumental chip gaps. They will not affect our detection of UFOs since these dips are very narrow.

We check the OM light curve for different filters and find that the variability amplitudes of each light curve are less than 20%, which is orders of magnitude smaller than the X-ray variability (see light curves in Fig.3.1), as commonly observed in NLS1s [3]. Therefore,

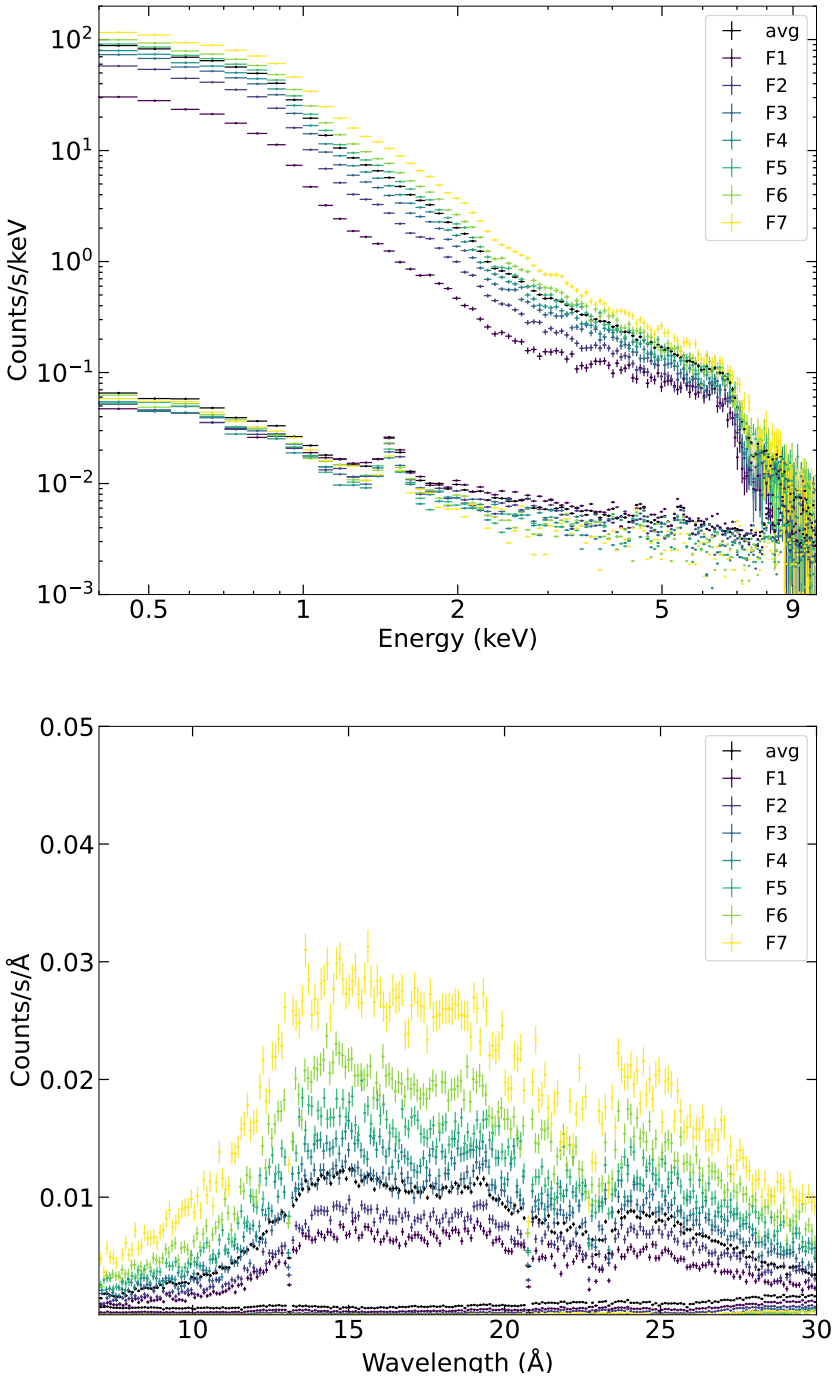

Fig. 3.2 The time-average and flux-resolved source spectra of 1H 0707 using EPIC-pn (*Upper*) and RGS (*Lower*) instruments. The background spectra are also plotted, comparable to the source spectra above 8 keV for EPIC-pn and on both ends of the spectral range of RGS. The spectra have been rebinned for clarity.

we assume that the emission in each OM band is steady and only extract the time-average spectra of different filters. The 'canned' response files are used in our spectral analysis[1].

To obtain high-quality data and avoid over-sampling for spectroscopy, we group EPIC spectra with SPECGROUP, and employ `obin` command for RGS and EPIC spectra in SPEX so that each group is not narrower than 1/3 of the spectral resolution, enabling us to resolve emission and absorption lines in soft energies [144].

3.3 Methods and Results

3.3.1 EPIC+RGS Continuum Modelling

We use the SPEX (v3.06.01) package [148] in this paper to analyze the spectra. All *XMM-Newton* spectra are thus transferred into the format which can be read by SPEX using OGIP2SPEX script. We employ the Cash-statistics [35] and estimate all parameter uncertainties at the 68% confidence level, i.e. $\Delta C - \mathrm{stat} = 1$. The calibration differences between the detectors are taken into account by allowing a relative instrument normalization free to vary (with that of EPIC-pn fixed to unity). The Galactic ISM absorption is described by the `hot` model, using the default proto-solar abundances of Lodders et al. [196]. The temperature is fixed at 0.02 eV to have a quasi-neutral ISM. The Galactic column density is set at $N_{\mathrm{H}}^{\mathrm{Gal}} = 4 \times 10^{20}\,\mathrm{cm}^{-2}$ [150] during the spectral fitting. The redshift of the source is also taken into account by a `reds` model with a fixed redshift $z = 0.04057$.

We begin the broadband X-ray spectroscopy by fitting the high-quality time-average spectra (EPIC+RGS). After checking the consistency of the residuals between EPIC and RGS spectra to the continuum model in soft energies, we adopt EPIC and RGS data between 1.77–10 and 0.4–1.77 keV respectively, because EPIC has a relatively low spectral resolution in the soft band but complements the RGS in the hard band. The physical properties of the spectral components in 1H 0707 continua have been discussed in many papers with great detail [54, 79, 27] and are beyond the purpose of this paper. Therefore, we just describe the continuum with phenomenological models as we mainly focus on the outflow properties. The spectral shape of 1H 0707 has been reported to be characterized by a power-law component, a soft excess, and two strong skewed and broad emission lines [78]. We initially applied a typical continuum model (`hot*reds*(pow+bb)`) to the time-average spectra, where the blackbody reproduces the soft excess, and clearly found two broad emission lines peaking at around 0.9 and 6.5 keV.

[1] https://www.cosmos.esa.int/web/xmm-newton/om-response-files

Therefore, the data can be described by a continuum model plus two broad lines, which are related to the inner-disk reflections: `hot*reds*(pow+bb+laor*(delt+delt))`. This model was also adopted by Fabian et al. [78]. The result reveals a power-law component with a photon index of $\Gamma = 2.75^{+0.01}_{-0.01}$, a soft excess described by a black body with a temperature of $T_{\rm in} = 0.123^{+0.001}_{-0.001}$ keV, and two relativistically-broadened emission lines characterized by energies of ~ 0.9 and ~ 6.5 keV, an innermost radius of $\sim 1.2\,r_{\rm g}$ ($r_{\rm g} = GM_{\rm BH}/c^2$), a fixed outermost radius of $400\,r_{\rm g}$, an emissivity index of $q = 5.3^{+0.1}_{-0.1}$ and an inclination angle of 50.7°. This phenomenological model is then applied to the seven flux-resolved spectra. Since the innermost and outermost radius and the inclination angle are not expected to significantly change within the observation period, we fix them at the best-fit values derived from the time-averaged spectrum. The parameters are summarized in Tab.3.2. The spectral slope gradually increases with the flux level, consistent with the 'softer-when-brighter' trend shown in Fig.3.1. The statistics suggest a general tendency of a better fit appearing at a higher flux level (i.e. the C-statistics are smaller for comparable degrees of freedom). This indicates that the residuals are weaker when the flux is higher, compatible with what was previously seen in IRAS 13224 [252, 259].

3.3.2 Gaussian Line Scan

To confirm the weakening trend for the absorption lines with the luminosity, following the approach described in Sec.2.3.1, we search for narrow spectral features by fitting a Gaussian line spanning the 0.4–10 keV energies. We adopt a logarithmic grid of 1000 energy steps between 0.4 and 10 keV, which maintains the balance between the computational cost and the instrumental resolving power. For the high S/N ratio and easy recognition of the lines, we start the scan for the time-average spectra and test several line widths between 500 km/s, and 10000 km/s.

Results of the line scan over the time-average spectra are expressed as the square root of ΔC–stat times the sign of the Gaussian normalization in Fig.3.3. Based on `ATOMDB`[2], emission lines are identified, and corresponding rest-frame energies are labeled. Since the UFO has been confirmed by PK18, drops next to peaks are assumed to be the blue-shifted absorption lines corresponding to the identified emissions. After several trials of shifting the rest-frame absorption lines, we find that many absorption lines match a typical UFO blueshift of $z \sim -0.15$: N VII, O VIII, Fe XVII, Ne X, Si XIV, S XVI, and Fe XXV/XXVI. The Si XIV emission line is not detected possibly due to the superposition of the absorption line from another ion. Our results are consistent with most of the absorption lines already reported

[2] http://www.atomdb.org/Webguide/webguide.php

Table 3.2 Best-fit parameters of the continuum model for time-averaged and flux-resolved spectra of 1H 0707-495.

Description	Parameter	avg	F1	F2	F3	F4	F5	F6	F7
`hot`	$N_{\rm H}^{\rm Gal}$ (10^{20} cm^{-2})				4*				
	kT (10^{-5} keV)				2*				
`pow`	Γ	$2.75^{+0.01}_{-0.01}$	$2.20^{+0.04}_{-0.04}$	$2.61^{+0.03}_{-0.03}$	$2.71^{+0.03}_{-0.02}$	$2.76^{+0.03}_{-0.02}$	$2.84^{+0.03}_{-0.02}$	$2.91^{+0.02}_{-0.02}$	$2.99^{+0.02}_{-0.02}$
	$N_{\rm PL}$ (10^{51} ph/s/keV)	$3.52^{+0.05}_{-0.04}$	$1.49^{+0.05}_{-0.05}$	$2.49^{+0.07}_{-0.07}$	$3.87^{+0.10}_{-0.10}$	$4.97^{+0.12}_{-0.12}$	$6.34^{+0.15}_{-0.15}$	$8.0^{+0.2}_{-0.2}$	$12.6^{+0.03}_{-0.03}$
`bb`	$T_{\rm in}$ (keV)	$0.123^{+0.001}_{-0.001}$	$0.117^{+0.001}_{-0.001}$	$0.111^{+0.002}_{-0.002}$	$0.109^{+0.002}_{-0.002}$	$0.107^{+0.002}_{-0.002}$	$0.110^{+0.002}_{-0.002}$	$0.117^{+0.003}_{-0.003}$	$0.121^{+0.004}_{-0.004}$
	$N_{\rm BB}$ (10^{20} cm^2)	841^{+22}_{-18}	922^{+51}_{-47}	1322^{+91}_{-86}	1774^{+140}_{-124}	2173^{+220}_{-190}	1906^{+223}_{-171}	1566^{+155}_{-134}	1121^{+175}_{-147}
`de1t1`	LineE1 (keV)	$0.914^{+0.001}_{-0.001}$	$0.922^{+0.004}_{-0.009}$	$0.905^{+0.002}_{-0.002}$	$0.909^{+0.005}_{-0.003}$	$0.922^{+0.003}_{-0.003}$	$0.935^{+0.002}_{-0.002}$	$0.920^{+0.003}_{-0.003}$	$0.976^{+0.003}_{-0.002}$
	$N_{\rm delt1}$ (10^{51} ph/s)	$2.5^{+0.1}_{-0.1}$	$1.7^{+0.1}_{-0.1}$	$2.2^{+0.2}_{-0.2}$	$3.0^{+0.2}_{-0.2}$	$4.0^{+0.3}_{-0.3}$	$4.5^{+0.4}_{-0.3}$	$4.7^{+0.4}_{-0.4}$	$7.3^{+0.7}_{-0.7}$
`delt2`	LineE2 (keV)	$6.47^{+0.02}_{-0.02}$	$6.40^{+0.04}_{-0.04}$	$6.48^{+0.04}_{-0.03}$	$6.49^{+0.05}_{-0.05}$	$6.53^{+0.06}_{-0.06}$	$6.54^{+0.05}_{-0.04}$	$6.47^{+0.05}_{-0.05}$	$6.72^{+0.09}_{-0.07}$
	$N_{\rm delt2}$ (10^{50} ph/s)	$0.67^{+0.02}_{-0.02}$	$1.65^{+0.09}_{-0.09}$	$0.77^{+0.06}_{-0.05}$	$0.80^{+0.05}_{-0.05}$	$0.88^{+0.06}_{-0.06}$	$1.00^{+0.07}_{-0.06}$	$0.95^{+0.07}_{-0.07}$	$1.32^{+0.11}_{-0.10}$
`laor`	q	$5.3^{+0.1}_{-0.1}$	$5.6^{+0.1}_{-0.1}$	$5.3^{+0.1}_{-0.1}$	$5.3^{+0.2}_{-0.1}$	$5.5^{+0.2}_{-0.2}$	$5.5^{+0.1}_{-0.1}$	$5.2^{+0.1}_{-0.1}$	$6.4^{+0.2}_{-0.2}$
	i (deg)	$50.7^{+0.3}_{-0.1}$	50.7*	50.7*	50.7*	50.7*	50.7*	50.7*	50.7*
	C-statistic/d.o.f.	3265/1805	2346/1826	2039/1739	1973/1736	2077/1749	1935/1781	1923/1763	1971/1786

* The parameter is pegged at this value.

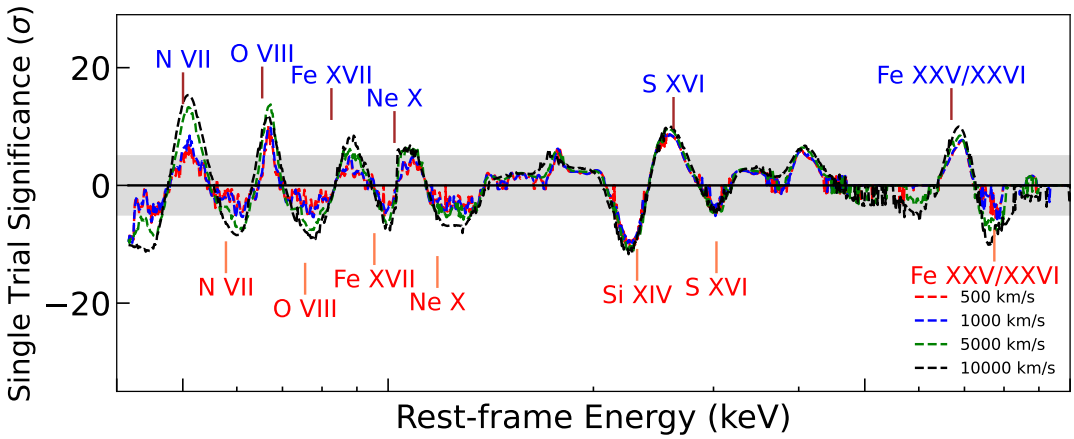

Fig. 3.3 The results of a line search over the *XMM-Newton* broadband time-average spectra (0.4–1.77 keV from RGS and 1.77–10 keV from EPIC) in the AGN rest frame. Four different line widths σ_v (FWHM$= 2.355\sigma_v$) of 500, 1000, 5000, and 10000 km/s are adopted. The single trial significance is calculated as the square root of ΔC–stat times the sign of the Gaussian normalization to distinguish the emission and absorption features. The emission/absorption lines are identified as blue/red. The emission lines are labeled at the rest frame of the transition, while the absorption lines match the blueshift around $z \sim -0.15$. The shaded region corresponds to 5σ of the single trial significance.

in PK18, which focused on the *XMM-Newton* observations before 2010. As we cannot rule out the possibility that the features in the 2–3 keV range are affected by instrumental effects, we prefer to pay more attention to other strong UFO signatures in this paper. Details of the identified lines are listed in Tab.3.3. Ideally, a Monte Carlo simulation should be done to rule out the possibility of the look-elsewhere effect. However, we do not do this because of the extremely high significance of the features (each feature has a ΔC–stat > 25 detection) with the Monte Carlo simulations being redundant to corroborate the detection.

The Gaussian line scan with the same primary settings is then applied to the flux-resolved spectra and the results are shown in Fig.3.4. As previously reported UFOs in other sources [252, 259], there is a general trend that the significance of the flux-resolved spectra residuals weaken at high fluxes. For individual lines, only Fe XVII and Ne X features nearly disappear in the highest flux spectra, while the others, no matter absorption or emission lines, are weak but are still recognizable in the spectrum. This implies that the UFO does not completely disappear in 1H 0707, as PK18 suggested. The variable position of the absorption residuals with respect to the vertical dashed lines indicates that the velocity of the UFO changes with the luminosity, which is investigated with the aid of physical models in Sec.3.3.3.2.

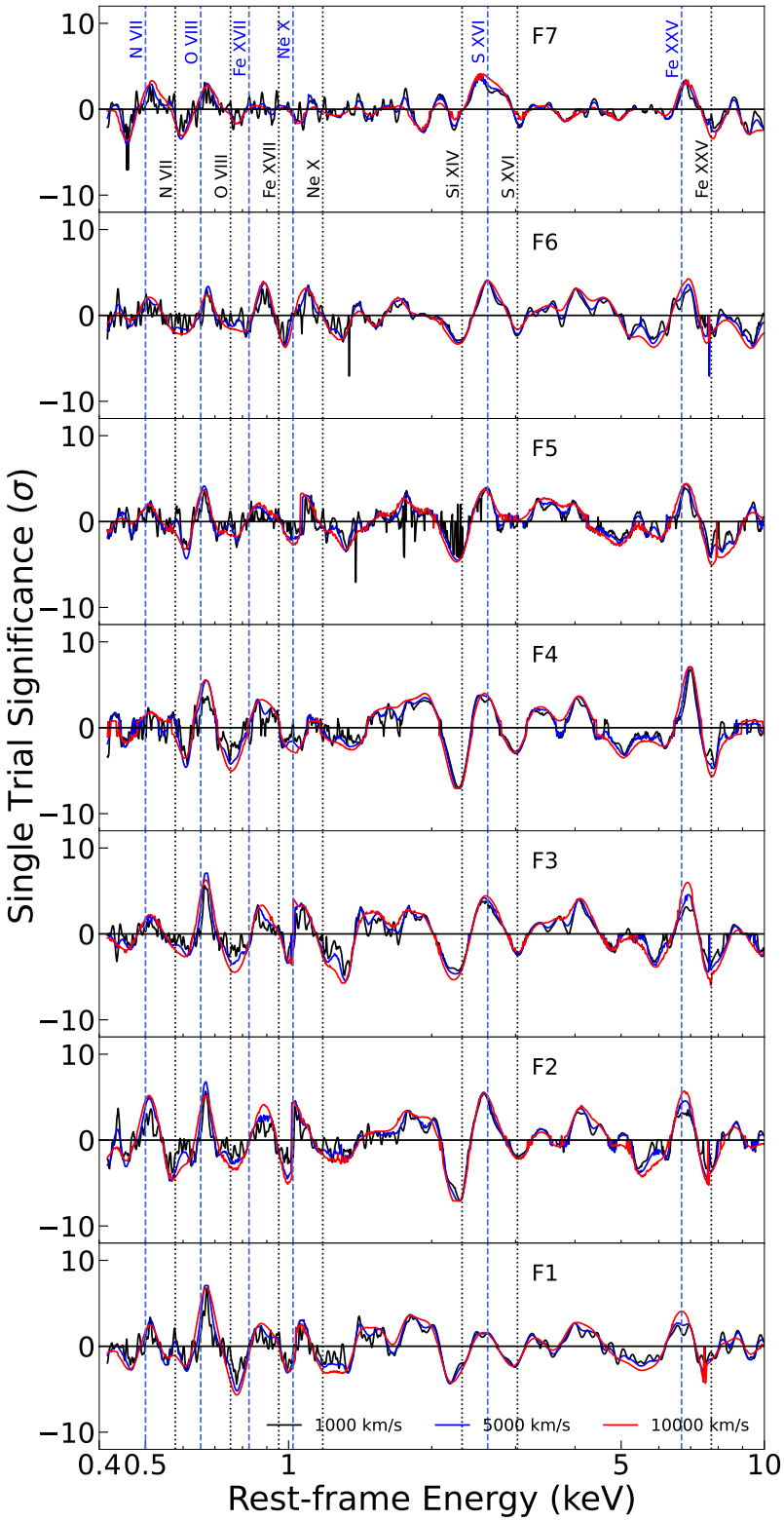

Fig. 3.4 The results of a line search over the flux-resolved RGS-EPIC spectra. Three different line widths (1000, 5000, 10000 km/s) are adopted. The emission and absorption features detected in Fig.3.3 are labeled by vertical blue and black dash lines separately.

Table 3.3 The strongest transition residuals fitted with a Gaussian.

Transition	ΔC-stat	Rest-frame energy (keV)	Best-fitting[a] energy (keV)	Norm (10^{50} ph/s)	FWHM (keV)
Absorption					
N VII	69	0.500	$0.601^{+0.004}_{-0.004}$	$-1.7^{+0.2}_{-0.3}$	$0.047^{+0.006}_{-0.007}$
O VIII	110	0.653	$0.767^{+0.003}_{-0.003}$	$-1.7^{+0.2}_{-0.2}$	$0.093^{+0.008}_{-0.007}$
Fe XVII	65	0.826	$0.996^{+0.003}_{-0.003}$	$-1.0^{+0.2}_{-0.2}$	$0.062^{+0.009}_{-0.008}$
Ne X	122	1.022	$1.216^{+0.009}_{-0.010}$	$-1.7^{+0.4}_{-0.2}$	$0.28^{+0.02}_{-0.02}$
Fe XXV/XXVI	106	6.699/6.973	$7.70^{+0.02}_{-0.02}$	$-0.12^{+0.02}_{-0.01}$	$0.81^{+0.04}_{-0.08}$
Emission					
N VII	251	0.500	$0.508^{+0.001}_{-0.002}$	$3.8^{+0.5}_{-0.3}$	$0.046^{+0.005}_{-0.003}$
O VIII	202	0.653	$0.669^{+0.001}_{-0.001}$	$1.1^{+0.1}_{-0.1}$	$0.021^{+0.003}_{-0.002}$
Fe XVII	79	0.826	$0.884^{+0.003}_{-0.004}$	$1.1^{+0.2}_{-0.2}$	$0.086^{+0.008}_{-0.011}$
Ne X	49	1.022	$1.075^{+0.003}_{-0.007}$	$0.58^{+0.10}_{-0.05}$	$0.066^{+0.008}_{-0.006}$
Fe XXV/XXVI	121	6.699/6.973	$6.86^{+0.02}_{-0.02}$	$0.08^{+0.02}_{-0.01}$	$0.66^{+0.07}_{-0.05}$

[a] The best-fitting energy of the Gaussian is in the AGN rest frame.

3.3.3 Wind Modelling

In this section, we employ the photoionization code `PION`, described in Sec.2.2.2, to model the wind in 1H 0707 and to study the emission and absorption lines produced by the ionized gas. Once a radiation field is provided, this model reproduces the X-ray spectrum of a photoionized plasma.

3.3.3.1 SED and thermal stability

The intrinsic SED of 1H 0707 is computed from UV/optical to hard X-ray energies by taking advantage of the time-average OM fluxes. The UV/optical spectra are described by an additional blackbody component to the best-fit continuum, `hot*reds*(etau*pow+bb+bb+laor*(delt+delta))`, where the additional thermal emission is characterized by a temperature of ~ 14 eV, consistent with [253]. Here, we apply a convolution model `etau` (cut-off at 0.136 keV) to the power-law component, to avoid the unphysical divergence at low energies of the `pow` component. The X-ray continuum parameters remain unaltered after including OM data. The redshift effect and ISM absorption are removed to obtain the intrinsic and rest-frame source spectrum as seen by the winds. Owing to the missing far-ultraviolet (FUV) data due to the interstellar absorption, SEDs covering this domain are interpolated (i.e. assuming a straight line to link the UVW2 and the 0.4 keV X-ray data points) to avoid over-estimating the UV flux, but later on we test how the UV bump affects the ionization

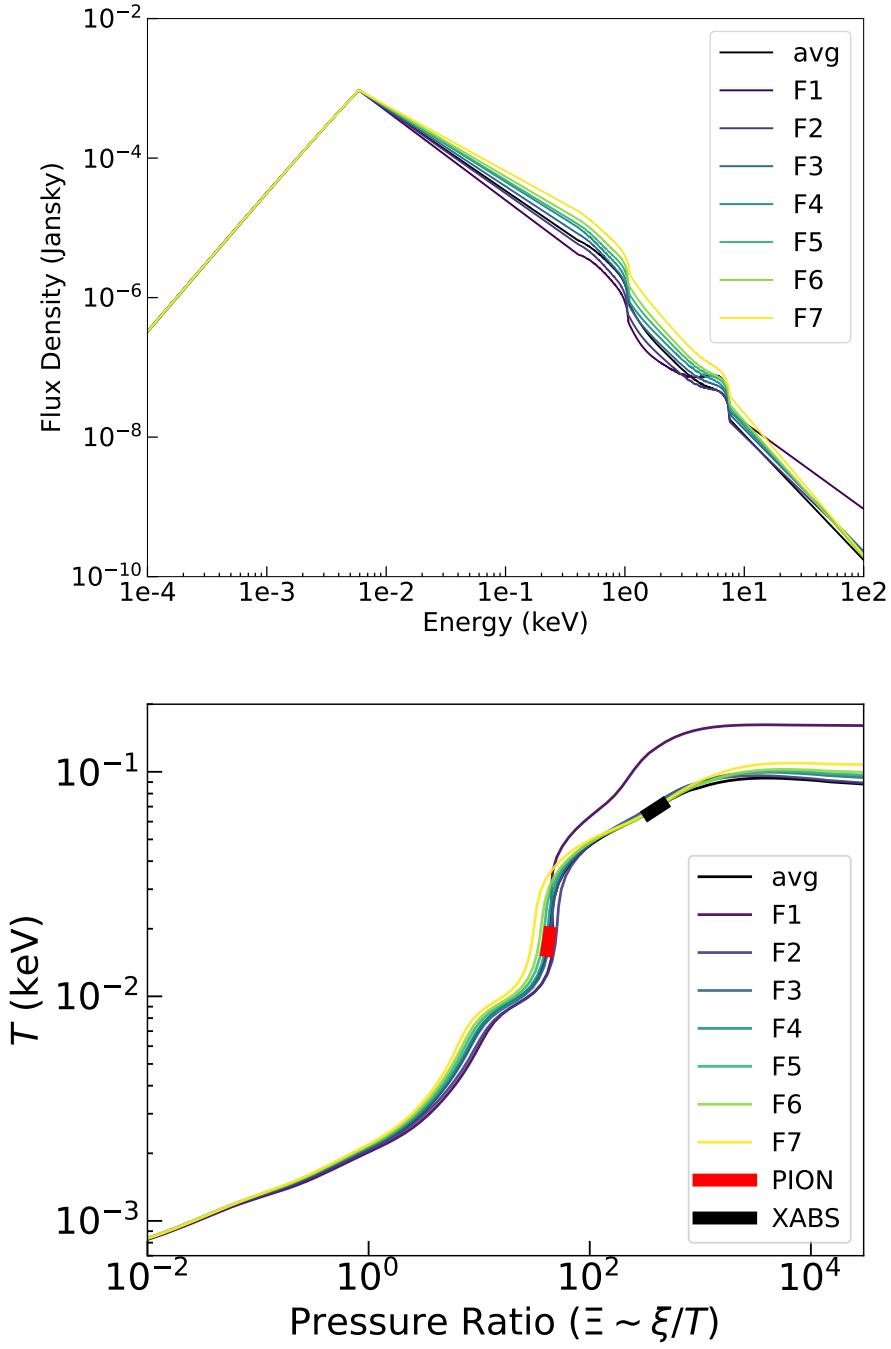

Fig. 3.5 The SEDs (*Upper*) and the corresponding stability curves (*Lower*) of a plasma in the photoionization equilibrium for different 1H 0707 flux levels. The *red* and *black* bold lines in the lower panel represent the best solutions ($\pm 1\sigma$ uncertainty) of the photoionized emitter and absorber respectively for time-average spectrum, where the fits are described in Sec.3.3.3.2. The positive gradient of the curves indicates the winds of 1H 0707 are thermally stable.

balance. The time-average and flux-resolved SEDs of 1H 0707 are shown in the upper panel of Fig.3.5. From the soft to hard energies, the SEDs deviate above 0.01 keV and get close at high energies (≥ 7 keV), which has already been indicated by the steady UV/optical fluxes and smaller X-ray variability above 8 keV (see in Fig.3.2). We caution that the SEDs above 10 keV are predicted by a power-law model without any constraint from *XMM-Newton* data. SEDs, cut at 10 keV, have thus been input in the following analysis to estimate the influence of the high-energy tail and we find that cut does not make any significant difference for our results due to the softness of SEDs.

We then compute the photoionization balance of ionized gas irradiated by the radiation field from 1H 0707 with the `PION` code. We also test the `XABSINPUT` tool in SPEX, which is a pre-calculated model and performs the same calculation. The results obtained from `PION` and `XABSINPUT` are consistent. In the lower panel of Fig.3.5, we illustrate the stability curve (see details in Sec.2.2.2.1). All curves are compatible below $kT \sim 0.03$ keV while F1 displays a slightly different behavior at high-temperature states. The bold lines (`PION` and `XABS`) indicate the best solutions ($\pm 1\sigma$ errors) of the photoionized absorber (*black*) and emitter (*red*) for the time-averaged spectrum, where the fits are described in detail in following Sec.3.3.3.2. In Fig.3.5, the stability curves of the investigated spectra are very similar with a positive gradient, which means that winds of 1H 0707 are likely thermally stable.

3.3.3.2 Full wind model

To determine the physical properties of UFOs in 1H 0707, we employ `XABS` and `PION` models to, respectively, describe the absorption and emission components of the photoionized gas by inputting the calculated SED and ionization balance. We perform the physical model search, described in Sec.2.3.2, to locate the best-fit solutions for absorbing and emitting gas. We adopt a grid of turbulent velocities with the same values as used in Sec.3.3.2 ($\sigma_v = 500$, 1000, 5000 km/s). The grid of ionization parameters $\log \xi$ spans between 0 and 6 with a step of $\Delta \log \xi = 0.1$. $v_{\rm LOS}$ is varied between -105000 and 0 km/s for `XABS`, and between -39000 and 35000 km/s for `PION` (the minus sign implies blueshift), with steps that depend on the turbulent velocity ($\Delta v_{\rm LOS} = 500$, 700, 2500 km/s for $\sigma_v = 500$, 1000, 5000 km/s respectively). Each scan is performed with the corresponding SED and ionization balance. The `PION` model is pre-calculated with the code[3] used in [264] to speed up scans and the volume density is assumed at $n_{\rm H} = 1\,{\rm cm}^{-3}$ as `PION` calculates fast at a low volume density, which has little effect on modeling.

[3] https://github.com/ciropinto1982/Spectral-fitting-with-SPEX/tree/master/SPEX-physical-grid-scan

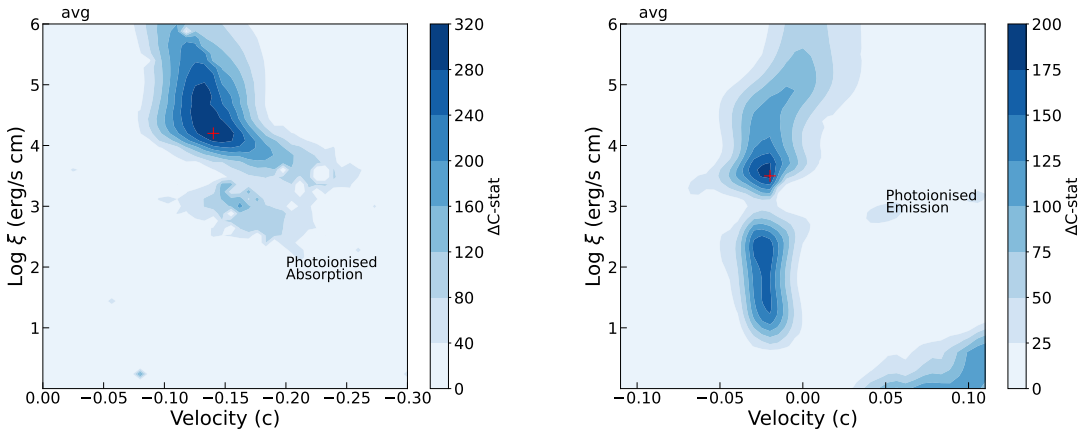

Fig. 3.6 Photoionization absorption (*left*) and emission (*right*) model scan over the time-averaged spectrum of 1H 0707 within two different grids of $\log\xi$ and $v_{\rm LOS}$ with a turbulent velocity of 5000 km/s. The velocities on the X-axis are relativistically corrected. The color shows the statistical improvement ΔC–stat after adding the absorption and emission model to the continuum model. The red cross indicates the best-fit solution.

The results of `XABS` and `PION` scans over the time-averaged spectrum are shown in Fig.3.6. The results with different turbulent velocities are compatible with each other. Therefore, we only present the significance distributions with $\sigma_v = 5000$ km/s, which has the largest statistical improvement. We then correct the velocity in our line-of-sight for the Doppler relativistic effect through the standard equation: $v/c = \sqrt{(1+v_{\rm LOS}/c)/(1-v_{\rm LOS}/c)} - 1$.

For absorbing gas (left panel of Fig.3.6), our search achieves a strong detection of the highly ionized ($\log\xi \sim 4.2$) plasma with a blueshift velocity peaking around $-0.14c$ and a statistical improvement of up to ΔC–stat $= 320$, which aligns with the best-fit solution ($v \sim -0.13c$, $\log\xi = 4.3$) found in PK18. In addition, our results indicate a secondary less significant (ΔC–stat ~ 160) peak of a lower ionization state ($\log\xi \sim 3$), appearing also in flux-resolved results, which itself could be considered significant if it is detected alone. The presence of the secondary peak could suggest a multi-phase absorbing wind in 1H 0707, consistent with the discovery in PK18.

For emitting gas (right panel of Fig.3.6), the peak corresponds to a solution at $\log(\xi/{\rm erg\,cm\,s^{-1}}) \sim 3.6$ with a blueshift velocity of $v \sim -0.02c$. The ionization parameter is over one order of magnitude larger than that (~ 2.4) of PK18, while the velocity is consistent with theirs. Their results were derived by explaining both emission and absorption components, while here we just consider the emission component. Moreover, the plot shows two potential solutions of $\log\xi < 3$ and > 3. The peak of the `PION` scan shows that the emitting gas is increasingly ionized at a higher luminosity ($\log\xi$ ranging from ~ 2 to 4).

However, we have to caution that the wind properties of the model scan might not be ultimate, as they are obtained by scanning an individual photoionization model, either XABS or PION, without simultaneously taking both of them into account. Therefore, we apply a full wind model, including both PION and XABS, on the top of the continuum model and link their line width, σ_v, for saving computational time and avoiding further degeneracy, as it has insignificant effects on the fit. Then we directly fit the spectra starting from the solutions obtained with the emission and absorption model scans. The line width is assumed at 5000 km/s during F7 spectrum fitting due to its loose constraint at the highest flux level.

The parameters of the absorbing/emitting gas at different flux levels are listed in Tab.3.4. The wind properties of the emitting and absorbing gas derived from the time-averaged spectrum are similar to those of PK18. Some differences may come from the data selection and the SED inputted into PION as they used the data before 2010 and the default SED in SPEX (i.e. NGC 5548 SED). We find an increasing ionization parameter of the absorber as the source luminosity rises. The most significant change in the full wind model compared with the individual XABS or PION scan is that the best-fit solution of the emission component falls in the low-ionization region. The fitting result to the time-averaged spectrum, as an example, and the corresponding residuals are shown in Fig.3.7. Most of the lines detected in Sec.3.3.2 are well explained while the N VII feature and Fe XXV/XXVI emission are still not modeled.

As for the flux-resolved results, the absorber displays an increasing ionization state, a slightly higher column absorption, and a slower velocity with the brighter source. The properties of the emitter are instead not that variable at different luminosities, indicating a stable emitting gas, although there is a weakly decreasing trend of the ionization parameter and column density. The line width is relatively stable and supports our assumption of $\sigma_v = 5000\,\mathrm{km/s}$ for F7. In terms of statistics, the full wind model provides of course better fits than the individual photoionization models (see for a comparison the ΔC–stat between Tab.3.4 and Fig.3.6). The extent of the improvement decreases with the increasing fluxes as expected due to the weakening wind features. Furthermore, the statistical improvement of a full wind model ΔC-stat$_{\mathrm{pion+xabs}}$, is not simply the sum of that of applying an individual XABS and PION on the continuum, ΔC-stat$_{\mathrm{xabs}} + \Delta$C-stat$_{\mathrm{pion}}$, but usually smaller than the sum, which indicates that some residuals are explained by the overlapping of the emission and absorption components.

Table 3.4 Best-fit parameters of the photoionization absorption (XABS) and emission (PION) models applied on the continuum model for the time-average and flux-resolved spectra. The line width, σ_v, of them are linked together. Here the velocity, $v_{\rm LOS}$, are the absolute values, which have not been relativistically corrected yet. The uncertainties are estimated at 68% confidence level.

Description	Parameter	avg	F1	F2	F3	F4	F5	F6	F7
xabs	$N_{\rm H}$ (10^{23} cm^{-2})	$0.26^{+0.09}_{-0.02}$	$0.18^{+0.05}_{-0.05}$	$0.80^{+0.05}_{-0.23}$	$0.6^{+0.2}_{-0.1}$	$1.0^{+0.4}_{-0.2}$	$1.2^{+0.4}_{-0.4}$	$1.2^{+0.3}_{-0.3}$	$3.2^{+1.1}_{-2.4}$
	$\log\xi$ (erg cm s^{-1})	$4.20^{+0.08}_{-0.01}$	$3.93^{+0.05}_{-0.06}$	$4.59^{+0.01}_{-0.11}$	$4.32^{+0.08}_{-0.08}$	$4.52^{+0.07}_{-0.08}$	$4.90^{+0.17}_{-0.17}$	$4.87^{+0.18}_{-0.15}$	$5.70^{+0.30}_{-0.27}$
	$\lvert v_{\rm LOS}\rvert$ (km/s)	46594^{+577}_{-1806}	53197^{+1765}_{-1985}	44788^{+1395}_{-1364}	45827^{+1475}_{-1543}	$45602^{+2250.64}_{-1466.45}$	44094^{+1548}_{-1290}	40738^{+1563}_{-2110}	41832^{+3169}_{-2796}
	σ_v (km/s)	4986^{+709}_{-276}	4630^{+973}_{-774}	4630^{+787}_{-981}	4535^{+1088}_{-622}	8373^{+1279}_{-1194}	4800^{+2767}_{-1529}	7077^{+1400}_{-1258}	5000*
pion	$N_{\rm H}$ (10^{21} cm^{-2})	$1.8^{+0.2}_{-0.2}$	$2.3^{+0.6}_{-0.5}$	$2.9^{+0.4}_{-0.4}$	$2.5^{+0.6}_{-0.5}$	$2.5^{+1.0}_{-0.5}$	$1.2^{+0.5}_{-0.2}$	$1.9^{+0.5}_{-0.4}$	$0.6^{+0.5}_{-0.3}$
	$\log\xi$ (erg cm s^{-1})	$2.68^{+0.02}_{-0.04}$	$2.69^{+0.07}_{-0.08}$	$2.75^{+0.06}_{-0.06}$	$2.64^{+0.07}_{-0.08}$	$2.54^{+0.08}_{-0.07}$	$2.44^{+0.13}_{-0.14}$	$2.59^{+0.05}_{-0.05}$	$2.35^{+0.20}_{-0.25}$
	$\lvert v_{\rm LOS}\rvert$ (km/s)	7574^{+572}_{-437}	8457^{+760}_{-973}	6654^{+954}_{-913}	9269^{+726}_{-928}	8007^{+1418}_{-1055}	7117^{+1157}_{-1122}	9736^{+1001}_{-2369}	9088^{+1808}_{-2316}
	C-statistic/d.o.f.	2639/1800	2233/1820	1906/1733	1801/1730	1957/1743	1866/1775	1873/1757	1936/1781

* The parameter is pegged at this value.

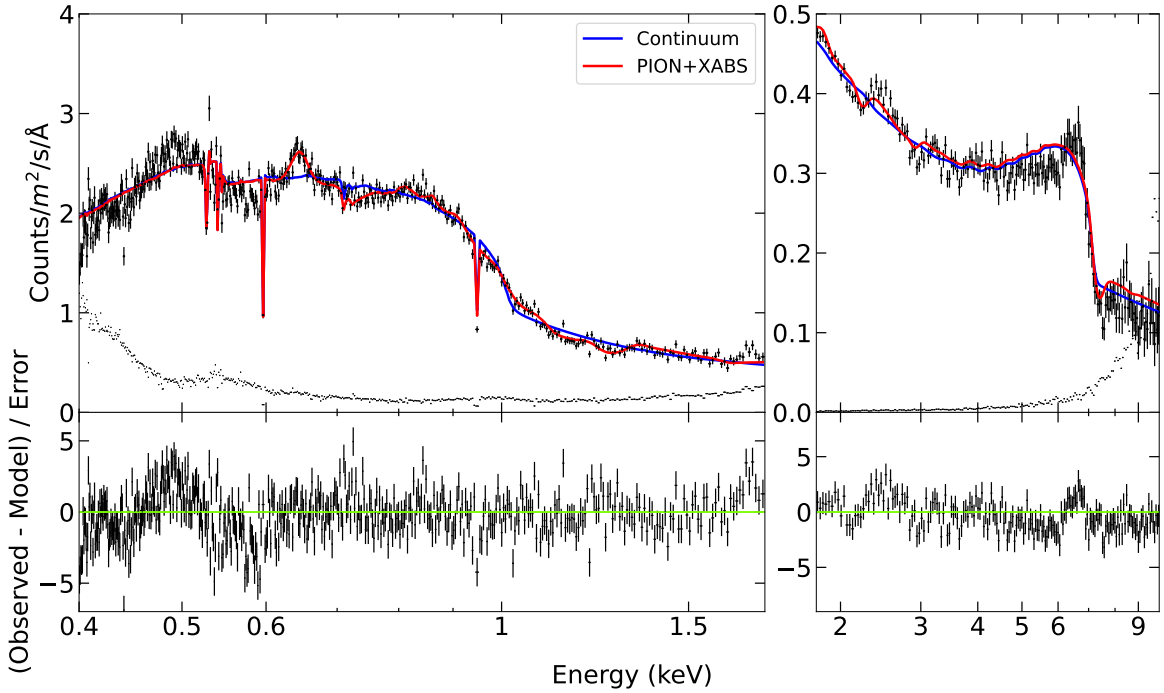

Fig. 3.7 The time-averaged X-ray spectrum (*top*) of 1H0707 using RGS (*left*) and EPIC-pn (*right*) data. The top two panels contain fits with the baseline continuum model (*blue*) and the continuum plus a `PION` and `XABS` model (*red*). The background is shown in dots. The bottom two panels are the corresponding residuals to the broadband continuum fit with the emission and absorption included. The spectrum is well explained except residuals among 0.5–0.6 and 6–7 keV.

3.4 Discussion

3.4.1 Systematic Effects

3.4.1.1 Eddington Accretion Rate

UFOs are expected to be mainly driven by the radiation pressure when the black hole is accreting at a high, super-Eddington, accretion rate [330]. 1H 0707 has been reported to accrete either just below [78] or above the Eddington limit [63]. Accordingly, we estimate the accretion rate by measuring the bolometric luminosity of 1H 0707 from our interpolated time-average SED (0.01 eV–1000 keV), which is $L_{\rm bol} \sim 2 \times 10^{44}$ erg/s. We adopt a BH mass of $2 \times 10^6 M_\odot$ [379, 155, 63] and the corresponding Eddington limit is $L_{\rm Edd} \sim 2.8 \times 10^{44}$ erg/s. This means 1H 0707 is accreting close to the Eddington limit ($\dot{m} \sim 0.7$).

However, we caution that the interpolation between the FUV and the soft X-ray bands only provides a lower limit for the bolometric luminosity, as we do not know the actual SEDs of 1H 0707. To investigate the effect of the interpolation, we calculate the non-interpolated SED predicted by continuum models (i.e. using the additional blackbody spectrum instead of a straight line between the UV and soft X-rays) on the top panel of Fig.3.8. The corresponding bolometric luminosity is estimated at $L_{\rm bol} \sim 5.5 \times 10^{45}$ erg/s, which is a super-Eddington accretion rate for 1H 0707, ($\dot{m} \sim 20$), as suggested by Done and Jin [63]. As a result, the high accretion rate of 1H 0707 has been confirmed whether we adopt the interpolated or non-interpolated SED. We also repeat the ionization balance calculation (see the bottom panel of Fig.3.8) and the full wind modeling. The solutions of the photoionization models are also illustrated in the stability curve. The inclusion of the FUV bump cools the plasma down, while the temperature of the emitter remains unchanged. Although the stability curves are different, the photoionized plasma exposed to a non-interpolated SED is still thermally stable. Furthermore, we have tried to fit the photoionization models on the flux-resolved spectra with non-interpolated SEDs, and still found the trends we discovered in Tab.3.4, apart from a systematic shift in the absolute values. Therefore, we confirm that the interpolation of SED has negligible influence on our conclusion about the UFO variability, but it will likely underestimate the actual accretion rate.

3.4.1.2 Screening Effect

It is worth noting that there might be differences between the SED that we observe and the SED portions that ionize all the different regions of the wind. In the case of super-Eddington accretion, the thick inner disk [316, 1] and the wind itself may self-screen the inner regions of the wind from some UV/optical emission from the outer part of the disk. Therefore, we also

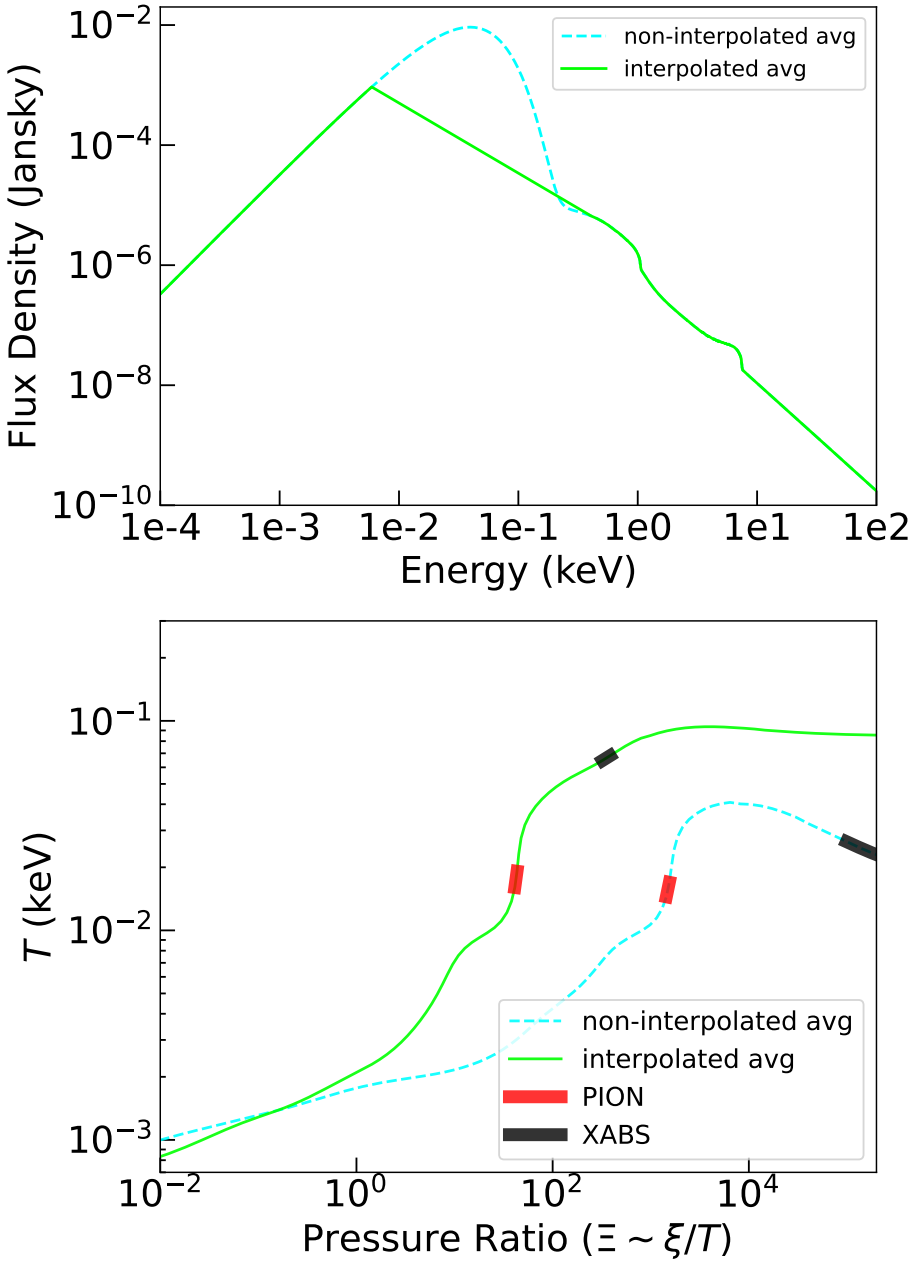

Fig. 3.8 The time-average non-interpolated SED (*top*) predicted by models and the corresponding stability curve (*bottom*) compared with the interpolated SED and its stability curve. The ionization parameters of the photoionized absorber (*black*) and emitter (*red*) for each SED are also shown in the curves.

simulate the self-screening effect for 1H 0707 by manually constructing pseudo-SEDs with just 10% and 1% of the UV/optical emission received by winds as well as the corresponding stability curves. Results show that the variation in the optical-UV flux by a factor of 10–100 in 1H 0707-495 does not lead to a thermally unstable wind due to its soft SEDs. As a result, the effect of UV/optical screening will not affect the our wind modeling.

3.4.1.3 Relativistic Effect

It has been recently reported that the special relativistic effects are of importance for UFO modeling [202, 200], because the radiation received by the ultra-fast outflows would decrease with an increasing outflow velocity. They argued that most UFO velocities from the literature cannot be reproduced in a radiatively-driven scenario within the relativistic treatment, unless the winds are launched at a radius of $> 50\,r_{\rm g}$, with a velocity up to $0.15\,c$, in an Eddington or Super-Eddington luminosity case.

Coincidentally, 1H 0707 potentially satisfies all of these conditions. Its relativistically corrected outflow velocity is $\sim 0.145\,c$ derived from the time-average spectrum, which is not extreme like the $0.3-0.4\,c$ seen in some quasars [288, 357]. Furthermore, if we assume the launching radius to be equal to the escape radius, $r_{\rm esc} = 2GM_{\rm BH}/v_{\rm out}^2$, the lower limit on the location of the wind is $> 95\,r_{\rm g}$. Moreover, the accretion rate of 1H 0707 ($\dot{m} > 0.7$, as estimated in Sec.3.4.1.1) likely surpasses Eddington, meaning that the radiation force must be very high and that magnetic fields might not be necessarily required although still potentially helping to accelerate the wind at the observed speeds.

3.4.1.4 F1" spectrum (low state)

We note that the F1 spectrum also includes the full observations affected by the AGN intrinsic variability event after 2010 and, therefore, we need to investigate how much the variability affects our result. We produce F1" spectra by excluding the latest two observations, and find that the observations before 2010 contribute about 85% of the total counts in the F1 spectra. This implies that F1" is not very different from the F1 spectrum. However, we perform the same analysis for F1" as done for the F1 spectrum, i.e., the spectral fitting, ionization balance calculation, and photoionization modeling. The X-ray spectroscopy demonstrates that F1" has a softer spectrum ($\Delta\Gamma \sim 0.2$) with other parameters similar to the F1. The SED and stability curve of F1" also do not dramatically change and only show a slightly steeper spectrum and a hotter plasma, which would not affect our results. We conclude that the inclusion of the final observations in the low-flux spectrum does not significantly affect the wind modeling.

3.4.2 Evolution of the Wind Components

In Sec.3.3.3.2, we have measured the wind properties at different flux levels and discovered several potential trends of the parameters. We thus plot the column density, ionization parameter, and the relativistically corrected velocity of the absorption and emission components in Fig.3.9 and 3.10, respectively. We take the observed fluxes measured by the continuum model as the X-axis because they are not affected by the modeling of the photoionized gas and supply the lower limits of the source luminosity. The results obtained from the time-average spectrum are also marked for comparison. The grey points present another solution of the emitting gas, which has a high ionization parameter ($\log \xi > 4$) and column density ($N_{\rm H} > 10^{22}\,{\rm cm}^{-2}$), indicated by the `PION` model scan (see Fig.3.10). Their fitting statistics are comparable with that of the low-ionization solution in the F6 spectrum (ΔC–stat < 1) and marginally better fits in the F7 spectrum (ΔC–stat ~ 4), while in the other spectra, the low-ionization solution is preferred to the high-ionization one. This suggests that there might be another emission component, which becomes more important at high-flux levels.

3.4.2.1 Absorbing gas

Fig.3.9 suggests a possible correlation between the ionization parameter of the absorbing gas and the X-ray flux, while the velocity is anti-correlated with the X-ray flux. The Pearson correlation coefficient of the ionization parameter, column density, and velocity versus the flux are 0.93, 0.92, and 0.75 respectively, implying a strong correlation. Here, we perform a linear fit with a slope fixed at unity in a logarithmic (1:1 Log) space among the ionization parameter and the flux, to compare with the definition of the ionization parameter (Eq.1.9). We also fit another linear function with a free slope (Log/Log), which supplies a slightly better fitting result. The Log/Log fit provides

$$\log \xi = (3.00 \pm 0.58) + (1.83 \pm 0.77) \log(\frac{F_{0.4-10}}{10^{-12}}), \tag{3.1}$$

corresponding to $\chi^2/\nu = 13/5$. The positive slope means the absorbing gas is increasingly ionized with the enhanced radiation field, which would lead to a decline of the equivalent widths of the lines at the same column density of the wind. Furthermore, the slope is consistent with unity within less than $2\,\sigma$, indicating that $n_{\rm H}R^2$ is relatively constant with the luminosity. It also suggests that the wind in 1H 0707 can respond to the ionizing luminosity instantaneously, which is not achieved by IRAS 13224 [259], perhaps due to a more severe degeneracy between the two solutions (Fe XXV and Fe XXVI dominated UFO). Regarding

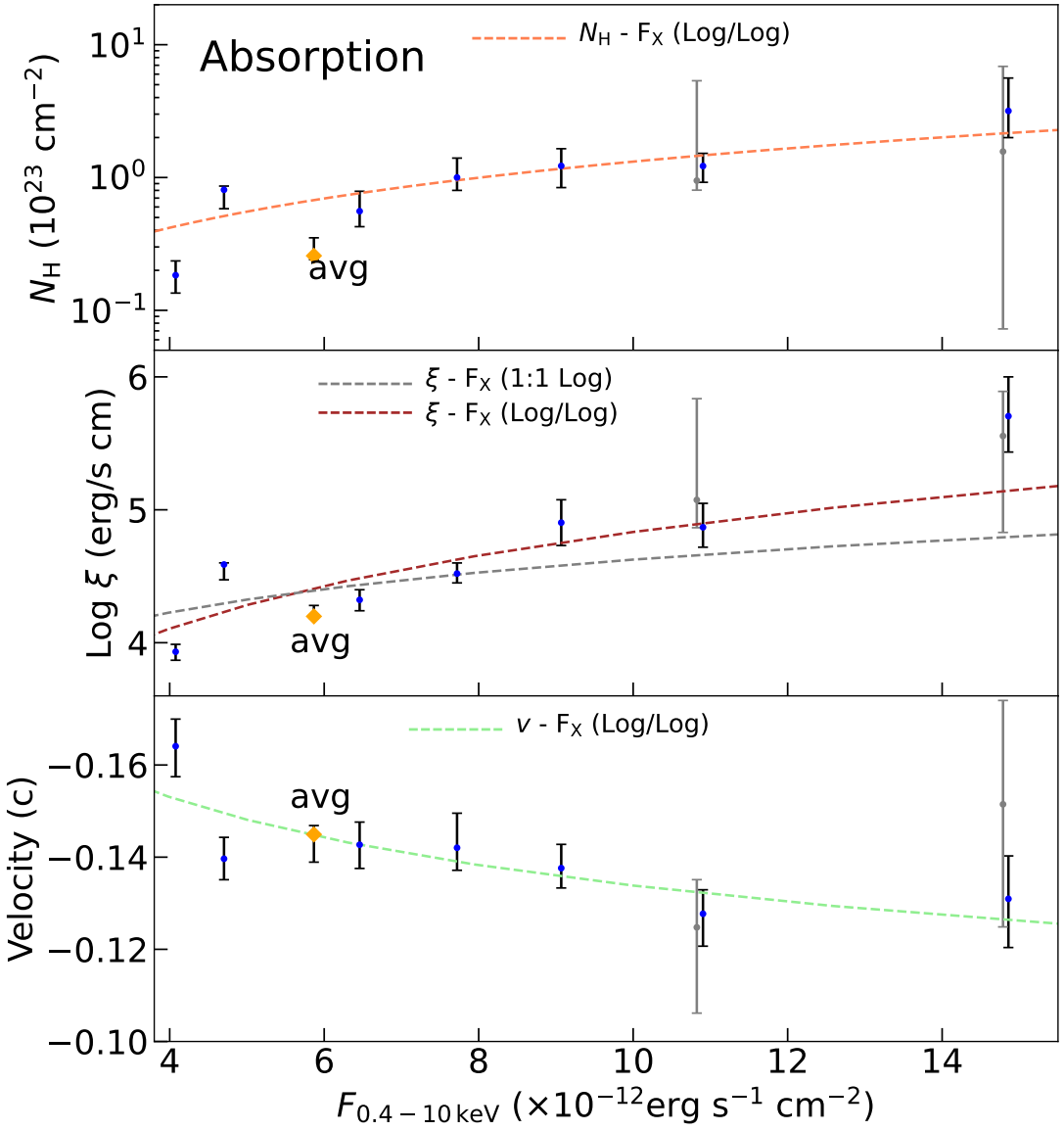

Fig. 3.9 The column density (*top*), ionization parameters (*middle*), and velocities (*bottom*) of the photoionization absorbing plasmas versus the absorbed X-ray fluxes of the flux-resolved spectra. The uncertainties within the 68% confidence level are shown in *black*. The time-average results are also marked and shown with *orange* points. The linear fits with (1:1 Log) and without (Log/Log) a slope fixed at unity are performed in a logarithmic space for the ionization parameters of the absorbing gas, and also for the logarithmic of column density and the absolute value of the velocity of the absorber (Log/Log). Another solution (*grey*), comparable in statistics, is also shown in the plots, and its flux is slightly shifted for clarity.

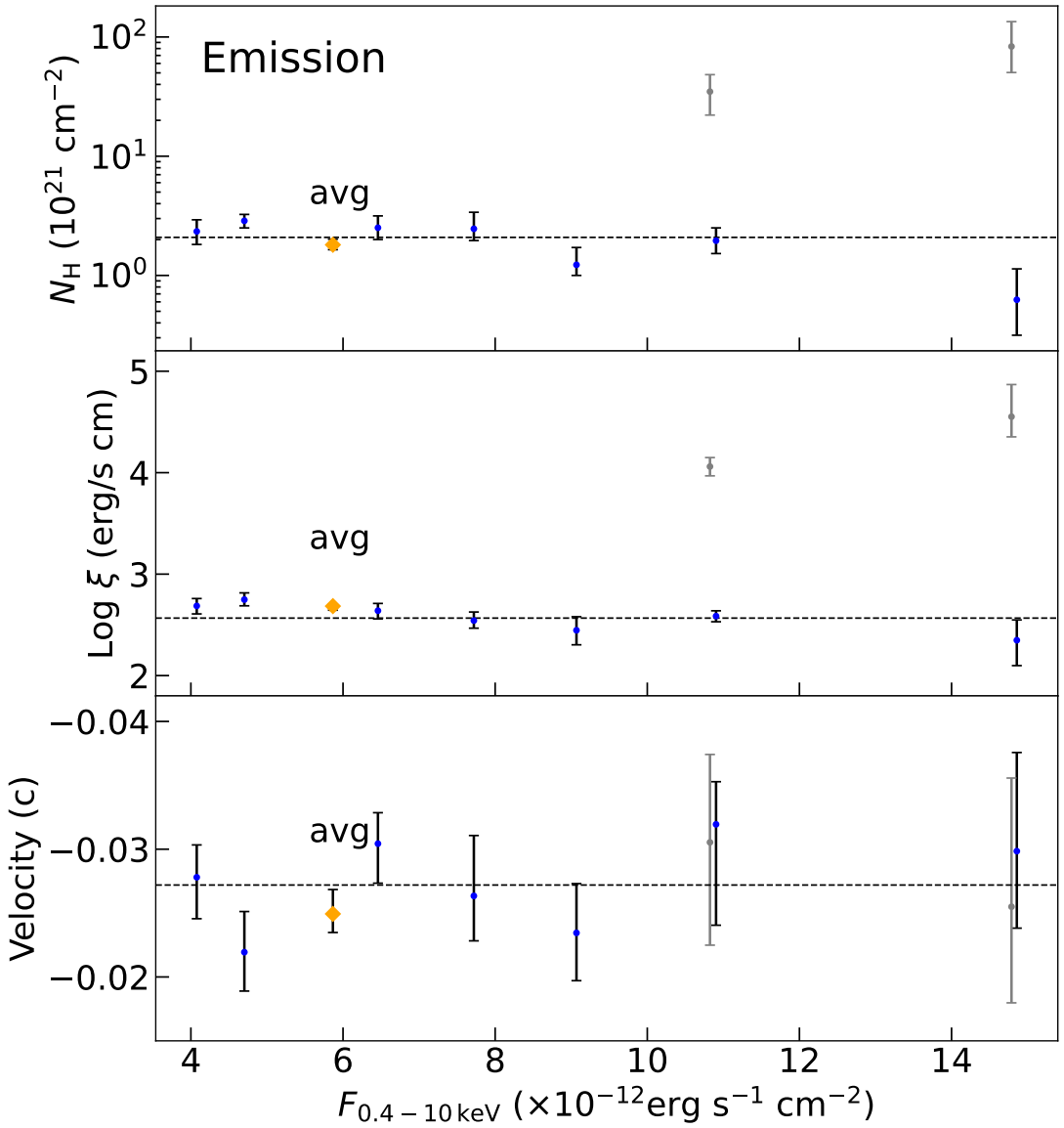

Fig. 3.10 The column density (*top*), ionization parameters (*middle*), and velocities (*bottom*) of the photoionization emitting plasmas versus the absorbed X-ray fluxes of the flux-resolved spectra. The uncertainties within the 68% confidence level are shown in *black*. The time-average results are also marked and shown with *orange* points. The black horizontal dash lines display the average values of parameters calculated from those of flux-resolved points, indicating a more or less stable emitting gas. Another solution (*grey*), comparable in statistics, is also shown in the plots, and its flux is slightly shifted for clarity.

the possibility of a steeper slope (> 1), this might be due to small, local, changes in the density and the position of the absorbing gas.

In addition, we apply the linear fit in a logarithmic space (Log/Log) on the column density and velocity of the absorbing matter, $\chi^2/\nu = 4/5$ and $\chi^2/\nu = 7/5$, respectively. The Log/Log fit gives

$$\log \frac{N_{\rm H}}{10^{23}\,{\rm cm}^{-2}} = (-1.13 \pm 0.42) + (1.25 \pm 0.51) \log(\frac{F_{0.4-10}}{10^{-12}}), \tag{3.2}$$

$$\log \frac{|v|}{{\rm km/s}} = (4.75 \pm 0.05) + (-0.15 \pm 0.05) \log(\frac{F_{0.4-10}}{10^{-12}}), \tag{3.3}$$

where c is the speed of light.

This anticorrelation between the wind velocity and X-ray flux is opposite to the correlation observed in PDS 456 [220] and IRAS 13224 [259], where they interpret that the winds are mainly accelerated by the strong radiation field in high-accretion sources. Alternatively, based on the simulations for a purely MHD driven wind with some parameter assumptions, Fukumura et al. [89] indeed predicted a weak anticorrelation in their Fig. 2a when the flux/accretion rate scaling parameter $s = 3$, which is defined by $L_{\rm ion} \propto \dot{m}^s$. In their model, they construct several relations between the ionizing luminosity and wind parameters, such as the ionization parameter, $\xi \propto L_{\rm ion}^{1-2/s}$ and the density $n_w \propto L_{\rm ion}^{2/s}$. For $s = 3$, the wind density increases slower than the X-ray flux, and therefore, an increase in $L_{\rm ion}$ will bring the wind ionization front to larger radii, yielding slower plasma velocities. However, the $s = 3$ case is not quite physical because this scaling parameter tends to be below unity for a high accretion rate ($\dot{m} > 1$) region due to the photon trapping effects [329].

In fact, given the high accretion rate estimated in Sec.3.4.1.1, it is difficult to neglect the role of the strong radiation field. For this reason, we come up with two possible explanations to account for the decreasing trend of velocity. The first is that the gas is driven by the line radiation pressure [282] and is being over-ionized in the higher flux states with a consequent decrease in the driving force and thus the wind velocity. On the other hand, the second explanation is that a stronger radiation field beyond the Eddington limit, presumably due to a region in the disk with higher local $\dot{m}$, increases the wind driving force, thus expanding the wind launching region into disk radii with lower Keplerian velocities, in turn leading to lower outflow velocities. This explanation was also invoked by Pinto et al. [261] for super-Eddington stellar-mass compact objects (ultraluminous X-ray sources, ULXs), in which at higher fluxes the wind showed lower velocities.

As another option, Fabian et al. [75] suggested that when the disk reflection component is strong relative to the primary continuum, the highly blueshifted absorption lines are likely

a consequence of the reflection component passing through an optically thin, highly ionized absorbing layer at the surface of the inner disk rather than a fast wind. The relativistic velocity is interpreted as the orbital motion of the inner disk. In this case, a higher hot corona would reduce the effect of light bending, resulting in a brighter luminosity, a smaller reflection fraction, and therefore weaker absorption lines. Moreover, the greater coronal height means that the reflection peak would come from the larger radius of the disk, leading to a slower velocity, compatible with the anticorrelation observed in 1H 0707. Nevertheless, the ionization state is not determined because it should decrease due to the more distant location in a constant disk, while the density of the disk may drop outwards due to the reduced radiation pressure, perhaps leading to an opposite trend. The validation of this scenario requires a precise calculation of the density structure of the outer Thomson depth of the disk and will be done elsewhere. Therefore, for the rest of this Chapter, we will keep the UFO explanation for the absorption features.

3.4.2.2 Emitting gas

For the parameters of the emitting gas shown in the right panel of Fig.3.10, we find that they are more or less constant at different fluxes, which is illustrated by the consistency with a constant function fitted to the flux-resolved points, despite the potential decrease in ionization parameter and column density. The stable velocity implies that the emitting gas is located at constant radii from the center. The relatively constant emitting gas is compatible with the argument by PK18 that the emission might come from a relatively large-scale wind. The large-scale emission origin is also suggested by Parker et al. [248] who find the Fe and Ne complex emission lines around 1 keV are less variable than the continuum. The emission lines are probably located on large enough scales that they are relatively unaffected by the variability of the absorbed continuum.

Furthermore, if the wind is launched isotropically, in principle, both the blueshifted and redshifted emission lines are detectable and we should observe a centrally peaked or flat-topped emission line profile. However, only blueshifted emission lines are detected. One explanation is that if the wind is indeed launched at a large opening angle, either there might be a particular MHD configuration breaking the symmetry of the wind, or the redshifted part is partially obscured by the blueshifted absorbing gas for some geometrical configurations. The assumption of a large open angle is plausible for a high-Eddington AGN as the matter pushed outwards is likely to form a shield to outer gas, thus absorbing the redshifted emission. This scenario also gives an explanation for the potentially cooler emitting gas in the high flux states, because the stronger radiation field will push more matter away, leading to a stronger screening of the hot inner gas.

Interestingly, in the high flux states (i.e. F6 and F7), there is another solution for the emitting gas, comparable in statistics, with a distinct ionization state and column density, while the other parameters are consistent within the uncertainties. This distinction is also suggested by what we obtained in PION model scans, where a $\log\xi$ gap appears for the emission component. This occurs because an ionization parameter $\log\xi \sim 3$ would lead to Fe complex emission lines around 0.95 keV that are not observed in the spectrum. The Fe XXV/XXVI emission lines are not taken into account in the time-averaged spectrum (see Fig.3.7) but are accounted for by a $\log\xi \sim 4.5$ emitting gas in F7 spectrum. As a result, the alternative high-ionization solution implies that either another weak emission component is hidden in the spectrum or the emitting gas is not constant with luminosity.

3.4.3 A Stratified Wind

3.4.3.1 Multi-wavelength Information

PK18 discovered a trend for which the higher ionization emission lines are more blueshifted in 1H 0707 by combining the N VII and O VIII lines with the low ionization lines observed in the UV spectrum from Leighly and Moore [192]. Here we complement other identified ionization lines in the X-ray band and reproduce the result in Fig.3.11. The outflow velocity of each ion is obtained by the shift obtained in Tab.3.3. The ionization parameter is the value at which the abundance of each ion peaks in a plasma photonionized by 1H 0707 SED. Our result confirms the previous finding and demonstrates that the velocities of ions up to Ne X are monotonically increasing. A power-law function is thus applied to fit and provides,

$$v_{\rm outflow} = (1502 \pm 437)\xi^{(0.39\pm0.06)}\,{\rm km/s}, \tag{3.4}$$

which is compatible with the result from PK18 within the uncertainties. As they suggested, the $\frac{v^3}{\xi}$ is consistent with being constant and hence the outflow energy is conserved if the ion emission results from the same wind producing the UFO absorption lines.

However, the Fe XXV/XXVI ions deviate from the power-law curve with a relatively slow velocity. According to the full wind model fit, we find that the majority of Fe XXV/XXVI features originate from Fe XXV and thus only show Fe XXV ions in the figure. The deviation suggests that the high ionization lines are mainly related to another component. This finding also supports a secondary emission component suggested in Sec.3.4.2.2. On the other hand, we caution that the Fe K band is modeled with a simple laor component rather than a physical reflection model, which might explain the Fe K emission residuals.

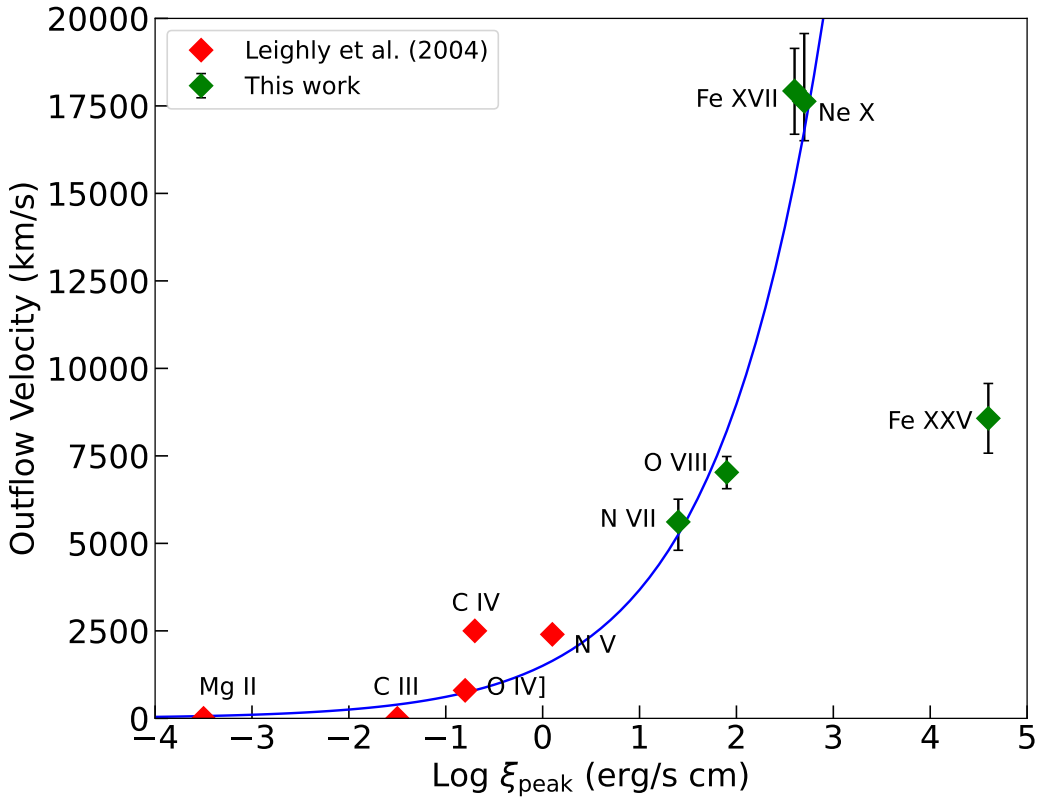

Fig. 3.11 The outflow velocity of different ions in 1H 0707 versus the ionization parameter at the peak abundance of each ion in a photoionized plasma. The velocities for the UV ion are taken from Leighly and Moore [192] and Leighly [190], where the uncertainty is assumed at 500 km/s. The ions up to Ne X are characterized by a power-law function (*blue*), while Fe XXV is not along with the curve.

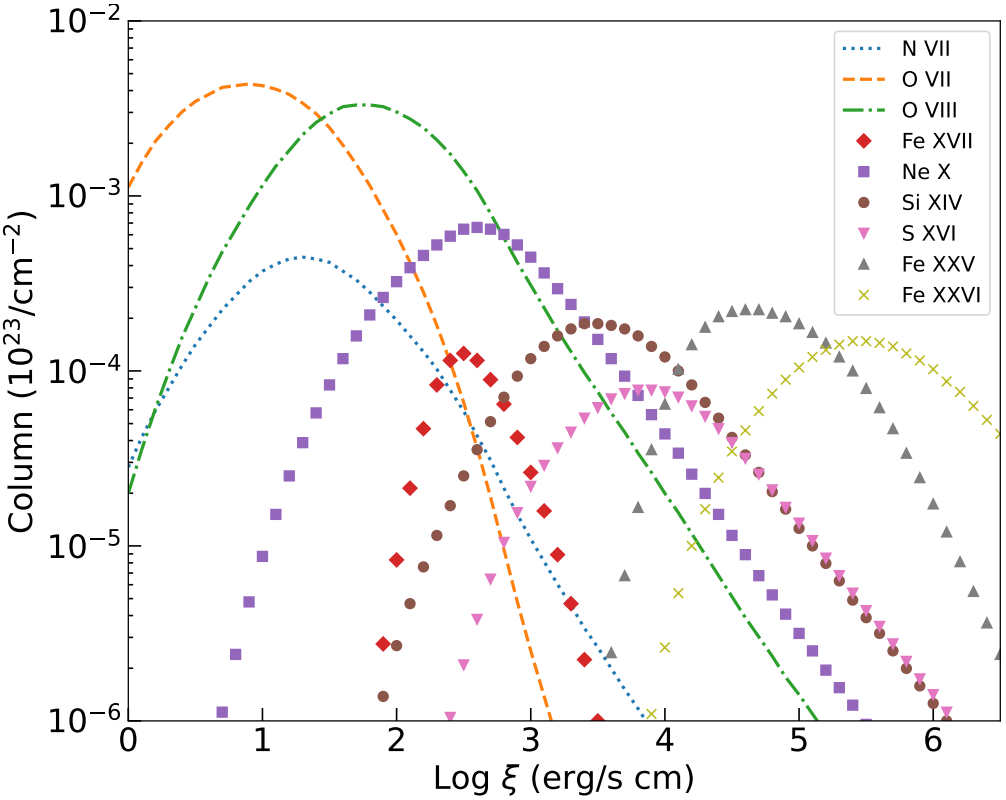

Fig. 3.12 The predicted column densities of different partially ionized ions in a photoionized plasma vs. the ionization parameter assuming $N_{\rm H} = 10^{24}\,{\rm cm}^{-2}$ and the time average SED (see Fig.3.5).

To investigate the abundance distribution of each ion at different ionization states, based on the calculated ionization balance for 1H 0707, we plot the column density of each identified ion line versus the ionization parameter in Fig.3.12. In terms of the emitting gas, it is unlikely to produce both the O VIII and Fe XXV emission using one component with an ionization parameter of $\log\xi \sim 2.7$ without over-predicting lower-ionization iron species. This confirms the need for another emission component to produce the Fe XXV.

3.4.3.2 Zooming on 2008 Epoch

In principle, the secondary emission component might be an artifact of the flux-resolved integration. When we merge the spectra of the same fluxes but different epochs, the time variability could wash out or broaden the emission and absorption features. Dauser et al. [54] indeed discovered evidence for a faster UFO from the 2010 observation than that of the 2008 spectrum. To understand how many phases of outflows are required, we extract a combined spectrum from the 01/31/2008 and 02/02/2008 observations (see the bold dates in Fig.3.1), for the sake of the plenty of counts and closeness in time, and fit it with double photoionization models.

Here we employ double emission or absorption components over the baseline continuum model rather than applying an additional `XABS` or `PION` upon the full wind model, because of the statistical limit. The emitting gas is explained by the precalculated model of $\sigma_v = 5000\,\mathrm{km/s}$ for saving the computational cost. Including one emission component leads to a statistical improvement of ΔC–stat ~ 55 against the baseline continuum and provides an emitting gas characterized by an ionization parameter of $\log\xi = 2.5$ and a LOS velocity of $-0.012^{+0.003}_{-0.004}\,c$. This component is mainly required by the strongest feature, O VIII. The inclusion of an additional highly ionized ($\log\xi = 4.0$) emission component improves the statistics of ΔC–stat$/\Delta$dof $= 43/2$ with a high velocity of $-0.025^{+0.004}_{-0.003}\,c$. This fast component mainly models the Fe XXV line. The improvement of including a secondary emission model is comparable to that of the first emission component, confirming the existence and increasing significance of the high ionization emission component with the source luminosity, since the observations we have chosen are dominated by the highest flux level. This thus might be a hint for a more structured wind.

Regarding the possible secondary absorption, the remaining absorption residuals between 0.5 and 0.6 keV seen in Fig.3.7 provide a hint for a low ionization component. We thus apply double `XABS` models to the baseline continuum of the 2008 spectrum. The primary absorption, similar to the results in Tab.3.4, requires a LOS velocity of $-0.122^{+0.006}_{-0.006}\,c$, an ionization parameter of $\log\xi = 4.86^{+0.12}_{-0.08}$, a line width of $\sigma_v = 7990^{+1295}_{-1263}\,\mathrm{km/s}$ and the column density of $N_\mathrm{H} = 1.5^{+0.5}_{-0.3} \times 10^{23}\mathrm{cm}^{-2}$, with a ΔC–stat $= 62$ improvement. As shown

in Fig.3.7, this component mostly explains the absorption above 0.65 keV. Interestingly, the secondary absorption, which is characterized by a broad line profile ($\sigma_v = 10532^{+1018}_{-1014}$ km/s), a modest velocity ($v_{\rm LOS} = -0.075^{+0.005}_{-0.004}\,c$), a low ionization state ($\log\xi = 1.46^{+0.06}_{-0.09}$) and a low column density ($N_{\rm H} = 4.6^{+0.7}_{-0.8} \times 10^{20}{\rm cm}^{-2}$), has a similar statistical improvement of ΔC–stat = 50 to the primary one. The reason why this component was not detected before, although the XABS scan at some fluxes show local peaks in this area (see Fig.**??**), is due to the limit of the line width. We indeed find a secondary peak through the XABS model scan with $\sigma_v = 10000$ km/s in F7. This component makes a great contribution to the residuals between 0.5 and 0.6 keV, which are mainly N VII and O VII lines.

Resolving time and flux by only looking at the 2008 spectra removes some degeneracies, making us find a slower absorber, which could fit in between the emitter and the fast absorber and describe the complex structure of winds. From this slow absorption component, we might see the outer layers of the wind. Basically, this component with the intermediate velocity could be the absorption part of the P-cygni profile where the emission comes from the primary emitter.

After modeling the 0.5–0.6 keV absorption residuals, a natural question is where the N VII emission comes from. We find that there is no way to fit the N VII by adding a PION component without over-predicting the O VII or Ne IX and Fe complex emission between 0.9–1.0 keV. Therefore, either the N VII originates from another mechanism such as the shock, or the abundances are not solar with over-abundant nitrogen, presumably due to enrichment by Asymptotic giant branch (AGB) stars [369]. The collisional ionization might facilitate a high amount of O VIII and N VII without O VII if the temperature is high (e.g. 1 keV). Hence, as a test, we replace the PION with a cie model in SPEX assuming the solar abundance and free line width, but it cannot explain N VII and O VIII with a high temperature of 1.4 keV, because a lot of Fe L complex ions are also expected. On the other hand, we allow the nitrogen abundance of PION to vary and find it requires an extremely high value of ~ 17 solar abundance, suggesting that the AGB stars (main generators of ISM nitrogen) might be more abundant in the galactic central regions.

3.4.4 Implications for Feedback and Wind properties

It has been well established that UFOs at small scales might carry enough power to affect the evolution of their host galaxies at larger scales such as quenching or triggering star formation [60, 127, 337, 206]. According to simulations, the deposition of a few percent of the source Eddington luminosity into the ISM is sufficient to prompt a considerable effect on the host galaxy. The kinetic power of the UFO in 1H 0707 is estimated by Eq.1.14, described in Sec.1.2.2.1.3.

To estimate the solid angle, we utilize the omeg parameter of PION code in the full wind spectral analysis, which includes direct information on the fraction of solid angle covered by the reprocessing gas shell (omeg$= \Omega/4\pi$). We adopt the time-average spectrum and allow omeg to vary. If we assume the emission and absorption come from the same gas, i.e. a P-cygni profile, we could force omeg to explain the difference between PION and XABS flux by coupling the ionization parameter and column density between the two components, where omeg provides a lower limit of > 0.98. Such a high solid angle indicates a fully covered gas shell, which is likely due to the strong radiation field. If we remove that assumption and decouple the parameters, the obtained solid angle is > 0.725, still suggesting a large opening angle. We would utilize the conservative value of omeg> 0.725 during the estimation.

We estimate the volume filling factor through Eq. 23 in Kobayashi et al. [167] by assuming that most of the mass of the outflow is contained in the clump. Although they focus on stellar mass systems, the volume filling factor is independent of the black hole mass and hence the equation also applies to AGN. By assuming that the mass outflow rate is comparable to the accretion rate and the relativistically corrected LOS velocity of absorbing gas is the wind velocity, we obtain $C \sim 8 \times 10^{-3}$, which is similar to a typical value of the outflow from the supercritical accretion flow.

The ionizing luminosity (1–1000 Rydberg) is estimated from the interpolated SED at $L_{\rm ion} \sim 1.42 \times 10^{44}$ erg/s, which is a lower limit for $L_{\rm ion}$. Therefore, the lower limit on the mass outflow rate is $\dot{M}_w > 0.046 M_\odot/yr$ and the kinetic energy of the UFO wind is then $L_{\rm kin} > 2.74 \times 10^{43}\,{\rm erg/s} \approx 9.8\% L_{\rm Edd}$. This lower limit meets the theoretical condition and demonstrates that 1H 0707 has enough influence on the surrounding medium.

Furthermore, we attempt to constrain the region from which UFOs originate with different methods. As mentioned in Sec.3.4.1.3, the wind is at least launched at $95\,r_{\rm g}$. Alternatively, if the absorption wind responds on time to continuum variations, the light needs to travel a distance between 230–1150 s (see frame time in Tab.3.1), which corresponds to $R_{\rm t} = c\Delta t \sim 23$–$117\,r_{\rm g}$. This should be an approximate distance between the wind and the X-ray emitting source, which is consistent with the former estimate. For the upper limit, if we assume the ionized gas can recombine within each segment at a given flux level, the lower limit of the density could be estimated by using rec_time code in SPEX, which is $n_{\rm H} \geq 2.1 \times 10^6\,{\rm cm^{-3}}$ by adopting $t_{\rm rec} \leq 230\,{\rm s}$ (frame time for F5) and the heating/cooling rate of O VIII line, $n_{\rm H} t = 4.78 \times 10^8\,{\rm cm^{-3}s^{-1}}$. This could be used to estimate the maximal launch radius through $R = \sqrt{L_{\rm ion}/\xi n_{\rm H}} \leq 3 \times 10^{16}\,{\rm cm} \approx 10^5\,r_{\rm g}$. On the other hand, through Eq.1.12 the maximal launch radius is $R \leq C L_{\rm ion}/\xi N_{\rm H} = 5.7 \times 10^{14}\,{\rm cm} \approx 1947\,r_{\rm g}$, when we take the average column density calculated from the flux-resolved results ($N_{\rm H} \sim 1.27 \times 10^{23}\,{\rm cm^{-2}}$). The same procedures are applied to the emission component, obtaining a location

estimation of 3×10^3–$8 \times 10^5\, r_g$. As a result, the launch radius of the UFO is estimated between $95 - 1947\, r_g$ and the density of the wind is thus constrained within the range $n_H = L_{ion}/\xi R^2 = 5 \times 10^{10}$–$1 \times 10^{13}\,\mathrm{cm}^{-3}$. The emission component arises from the outer region of 3×10^3–$8 \times 10^5\, r_g$ and the corresponding density is $n_H \sim 9.5 \times 10^8$–$5.9 \times 10^{13}\,\mathrm{cm}^{-3}$.

3.4.5 Comparison with other AGN

Thanks to the high-resolution grating instruments, the UFO has been discovered among many other AGN that accrete near the Eddington limit. The velocity of the UFO in 1H 0707 ($\sim 0.145\,c$) does not stand out if compared to other AGN, such as PG 1211+143 (0.2 c, [276]), Mrk 1044 (0.08 c, [181]), IRAS 13224-3809 (0.24 c, [252]), PG 1448+273 (0.09 c and 0.26 c, [173, 289]), and IRAS 00521-7054 (0.4 c, [357]). The other parameters also fall in the typical UFO region, where the ionization parameter spans from $\log(\xi/\mathrm{erg\,cm\,s^{-1}}) \sim 3$–$6$, and column density $\log(N_H/\mathrm{cm}^{-2}) \sim 22$–$24$ [339, 187].

IRAS 13224 is a source that shares many similarities with 1H 0707. In particular, the ionization parameter and column density of the UFO observed in IRAS 13224 are similar to our results, despite a faster velocity. However, the trend of the UFO velocity with AGN flux is opposite between these 'twin' sources as discussed in Sec.3.4.2.1. Another main difference is that the strong emission lines are only detected in 1H 0707 [259]. A plausible origin is that the emitting gas has a large opening angle in 1H 0707 ($\Omega/4\pi > 0.725$). If such a large solid angle results from the magnetic field, it would require a peculiar MHD configuration, since MHD-driven winds tend to be along with the polar direction [87]. Alternatively, the high accretion rate is likely to launch more matter at a wide-ranging angle. According to Alston et al. [7], the accretion rate of IRAS 13224 is around $\dot{m} \sim 1$–3, while in our estimation, 1H 0707 probably has a much higher accretion rate ($\dot{m} = 0.7$–20). This explanation is also supported by the discovery of photoionized emission lines in many ULXs, accreting at super-Eddington rates [262, 171, 259, 264].

The number of AGN with multiphase outflows has increased in the last decade. For example, the detection of two fast UFOs at $0.25\,c$ and $0.46\,c$ was reported in the spectrum of PDS 456 [288]. Similarly, up to 4 UFO phases are reported in IRAS 17020+4544 [309] and Mrk 1044 [181]. Our secondary UFO in absorption is similar to the UFO2 in Mrk 1044, of which ionization parameter is $\log\xi \sim 1.6$, velocity $v_{out} \sim 0.086\,c$ and column density $\log(N_H/\mathrm{cm}^{-2}) \sim 21.2$, although our turbulent velocity is larger than their fixed value of 10 km/s. However, as Kosec et al. [170] stated, the difference between these objects and 1H 0707 is that, to our knowledge, 1H 0707 is the currently unique source, which shows significantly blueshifted, probably multiphase X-ray absorption and emission at the same time, likely driven by a higher accretion rate.

3.5 Conclusions

In this Chapter, we perform a flux-resolved X-ray spectroscopy on all available archival *XMM-Newton* data of the highly accreting NLS1 1H 0707 to investigate the variability of UFO at different flux levels. We have found that the ionization parameter of the UFO is correlated and the velocity is anticorrelated with the luminosity. In the brightest state, the wind features are weak, implying the gas is highly ionized, similar to the phenomenon seen in NLS1 IRAS 13224. The emitting gas is nearly constant with a potential cooling tendency with luminosity, indicating that it originates from a large-scale wind. We propose that all of these results might be consistent with a scenario where the stronger radiation field pushes the wind launching region outwards, leading to a slower and broader wind. The inner wind portions would shield the outer gas, resulting in a cooler plasma. We also discuss alternative solutions. Our study confirms the existence of a stratified wind discovered by Kosec et al. [170] and provides hints for multiple phases in both absorption and emission components.

Chapter 4

Constraints on ultra-fast outflows in a narrow-line Seyfert 1 galaxy Mrk 1044

Abstract

In this Chapter, we perform a time- and flux-resolved X-ray spectroscopy on four *XMM-Newton* observations of a highly accreting NLS1 galaxy, Mrk 1044, to study the dependence of the outflow properties on the source luminosity. We find that the UFO in Mrk 1044 responds to the source variability quickly and its velocity increases with the X-ray flux, suggesting a high-density (10^9–$4.5\times10^{12}\,\mathrm{cm}^{-3}$) and radiatively driven outflow, launched from the region within a distance of 98–$6600\,R_\mathrm{g}$ from the black hole. The kinetic energy of the UFO is conservatively estimated ($L_\mathrm{UFO}\sim4.4\%L_\mathrm{Edd}$), reaching the theoretical criterion to affect the evolution of the host galaxy. We also find emission lines, from a large-scale region, have a blueshift of 2700–4500 km/s in the spectra of Mrk 1044, which is rarely observed in AGN. By comparing with other sources, we propose a correlation between the blueshift of emission lines and the source accretion rate, which can be verified by a future sample study.

4.1 Introduction

Under the investigation of the past two decades, UFOs show variable signatures, i.e., variable velocities and transient features, based on multi-epoch deep observations [54, 220, 131]. However, the exact nature of UFO variability and their launching mechanisms are not well understood. They could be driven either by the radiation pressure [282, 319, 115] or by magneto-rotational forces [160, 87, 90] or a combination of both. Variability might be key to determining UFO launching mechanisms. It has been found that the velocity of the UFO in PDS 456 and IRAS 13229-3809 increases with the source luminosity [220, 259], supporting that UFOs in high-accretion systems are mainly accelerated by the strong radiation field. However, in Chapter 3, we find an anti-correlation between the UFO velocity and X-ray luminosity in 1H 0707-495, challenging our understanding of the UFO driving mechanism. Therefore, it is worth investigating the dependence of UFOs on the source luminosity and accretion rate in other sources to better understand the nature of UFOs.

Mrk 1044 is a nearby ($z=0.016$) and luminous ($L_{1\mu\mathrm{m}-2\mathrm{keV}}=1.4\times10^{44}\,\mathrm{erg/s}$, [110]) NLS1 AGN, hosting a central SMBH with a reverberation-mapped mass of $M_\mathrm{BH}=2.8\times$

Table 4.1 General overview of the analyzed observations on Mrk 1044

Obs. ID	Date	Instrument	Net exp. (ks)	Net count rate (cts/s)
0824080301	2018-08-03	EPIC-pn	95	32
		RGS	134	1.07
0824080401	2018-08-05	EPIC-pn	97	24
		RGS	133	0.79
0824080501	2018-08-07	EPIC-pn	93	25
		RGS	131	0.84
0841820201	2019-08-03	EPIC-pn	90	20
		RGS	126	0.63

$10^6\,M_\odot$ [64] or a mass, determined through the FWHM(Hβ) and L_{5100}, of $M_{\rm BH} = 2.1 \times 10^6\,M_\odot$ [110]. Mrk 1044 shows a soft X-ray excess in the spectrum [59]. It was interpreted by relativistic reflection from a high-density accretion disk in Mallick et al. [208], although in general a warm corona model also provides a statistically acceptable description of the soft excess below 2 keV [257, 99, 256]. In the *XMM-Newton*/RGS spectrum, based on a series of narrow absorption lines, Krongold et al. [181] found four distinctive UFOs, explained by a shocked outflow scenario. From the multi-wavelength observations, Mrk 1044 was reported to have multi-phase outflows in optical and UV bands as well, including two unresolved and one resolved ionized gas outflows traced by [O III] in the optical band as well as two Ly-α absorbing components in the ultra-violet (UV) energy range [83, 368].

In this Chapter, we will present the high-resolution spectroscopic analysis on four *XMM-Newton*/RGS observations of Mrk 1044 (PI: C. Jin). In section 4.2, we present the four *XMM-Newton* observations and our data reduction process. Details on our analysis and results are shown in section 4.3, where we expand the work by Krongold et al. [181], find an additional blueshifted photoionized emission component, and further study the relation between the properties of winds and the source luminosity. We discuss the results and provide our conclusions in section 4.4 and section 4.5, respectively.

4.2 Data Reduction and Products

Mrk 1044 has been observed with a large *XMM-Newton* program (PI: C. Jin) for three orbits in 2018 and one orbit in 2019. The details of the analyzed observations in this work are listed in Tab.4.1. This work focuses on the RGS and we use the EPIC and OM data mainly to determine the shape of the SED, for which the MOS results are redundant as pn has a significantly higher effective area in the hard band.

4.2.1 Data Reduction

The data sets are processed with the *XMM-Newton* Science Analysis System (SAS v20.0.0) and calibration files available by September 2022, following the standard SAS threads. We reduced EPIC-pn data using EPPROC package and produced calibrated photon event files. The filter of the background flare contamination is set at 0.5 counts/sec in 10-12 keV for EPIC-pn data. We extracted the source spectra from a circular region of radius 30 arcsec, and the background spectra from a nearby source-free circular region with the same radius. No significant pile-up effect is found with the task EPATPLOT. The EPIC-pn spectra are grouped to over-sample the instrumental resolution at least by a factor of 3 and each energy bin has a minimum of 25 counts to maximize the S/N. We employed the RGSPROC package to process the RGS data with a filter of 0.3 counts/sec to exclude the background flares. The first-order RGS spectra are extracted from a cross-dispersion region of 1 arcmin width. The background spectra are selected from photons beyond 98% of the source point-spread function. The RGS1 and RGS2 spectra are combined. During the observation, Mrk 1044 was also monitored by OM in the UVW1 (2910Å) filter. We reduced OM data with OMICHAIN tool including all necessary calibration processes. The UVW1 flux is less variable than the X-ray flux, i.e., almost stable in 2018 and dropped by 13% in 2019.

4.2.2 Light Curve

By using the task EPICLCCORR, we present the background-substracted and deadtime-corrected light curves extracted from the EPIC-pn (0.3–10 keV) data in Fig.4.1. It reveals that Mrk 1044 is bright and variable during the observations. The corresponding hardness ratio (HR=H/H+S, H: 2–10 keV; S: 0.3–2 keV), plotted in the bottom panel, shows a softer-when-brighter behavior. To investigate the variability of the UFO with the luminosity, we divide three consecutive observations in 2018 into three flux levels, marked by different colors. The reason why we exclude the 2019 observation is to ensure the causality between the variations of the UFO and the luminosity, i.e., we are studying the response of the same absorber to the source. The thresholds are set to make the number of counts of each level comparable. The good time interval (GTI) files for each level are generated with TABGTIGEN task. The flux-resolved EPIC-pn and RGS spectra at the same flux level are extracted and stacked following the steps described in Sec.4.2.1. The observations in 2018 are also stacked into one single spectrum, named 2018. In this work, we will perform the flux-/time-resolved spectroscopy for a total of 8 spectra, where the time-resolved spectra are referred to as T1...T4 chronologically (e.g. T1 refers to Obs. 0824080301) and the flux-resolved spectra are referred to as F1, F2, F3 from the lowest to the highest state.

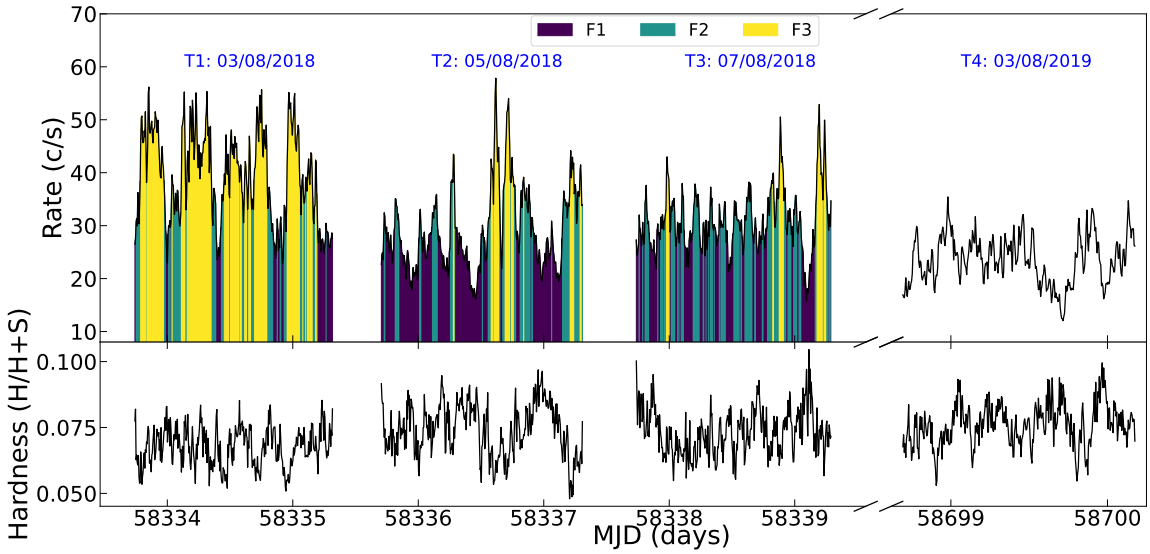

Fig. 4.1 The EPIC-pn (0.3–10 keV) light curve (*upper*) and corresponding hardness ratio (*lower*) of the observations of Mrk 1044, where the observation dates (T1-T4) are marked. The colors represent the different flux intervals (F1-F3) with comparable counts.

4.3 Results

4.3.1 Continuum Modelling

We start the broadband X-ray spectroscopy from the stacked 2018 EPIC-pn and RGS spectra, due to their high statistics, in the XSPEC (v12.12.1) package [12]. The instrumental differences are accounted for by adopting a variable cross-calibration factor. In this Chapter, we use the χ^2 statistics and estimate the uncertainties of all parameters at the default 90% confidence level (i.e. $\Delta\chi^2 = 2.71$), but 1σ ($\Delta\chi^2 = 1$) uncertainty is shown in Fig.4.8 and 4.9. We consider the RGS spectra between 0.4–1.77 keV and the EPIC-pn spectra between 1.77–10 keV in our analysis, not only because of their consistency in the soft X-ray band, but also due to the influence of the lower resolution but higher count rate of EPIC-pn on the detection of atomic features. The luminosity calculations are based on the assumptions of $H_0 = 70\,\mathrm{km/s/Mpc}$, $\Omega_\Lambda = 0.73$ and $\Omega_M = 0.27$.

The broadband X-ray model for Mrk 1044 was proposed by Mallick et al. [208] for the archival *XMM-Newton* data in 2013. We adopt a similar model combination: `tbabs*zashift*(nthComp+relxilllpCp)`, to explain those spectral components. The model takes into account the galactic hydrogen absorption (`tbabs`) with the solar abundance calculated by Lodders et al. [196], the redshift of Mrk 1044 (`zashift`), the soft excess in form of a warm Comptonization component (`nthComp`), and the hot coronal continuum like a

power-law plus a lamppost-geometry relativistic reflection (`relxilllpCp`, RELXILL v1.4.3, [94]). The Galactic column density, $N_{\rm H}^{\rm Gal}$, is allowed to vary due to the discrepancy between $N_{\rm H}^{\rm Gal} = 2.9 \times 10^{20}{\rm cm}^{-2}$ [120] and $N_{\rm H}^{\rm Gal} = 3.6 \times 10^{20}{\rm cm}^{-2}$ (NHtot tool, [366]). The choice of the solar abundance calculated by Lodders et al. [196] instead of Wilms et al. [367] is to keep consistent with the subsequently used photoionization models in Sec.4.3.3, although it does not affect our conclusions (only a $\Delta\chi^2 \sim 10$ difference around O K-edge, ~ 0.53 keV, region). Instead of using the high-density relativistic reflection model adopted in Mallick et al. [208], here we choose the warm Comptonization model plus a standard relativistic reflection component, of which the disk density is fixed at $\log(n_{\rm e}/{\rm cm}^{-3}) = 15$, in our analysis. It is because we find the fitting of the relativistic reflection model is much poorer ($\Delta\chi^2 \sim 670$) than the warm Comptonization scenario when we include the RGS data, probably due to a thick inner disk distorted by strong radiation pressure, breaking the thin-disk assumption of the reflection model. The seed photon of the warm Comptonization is fixed at a disk temperature of 10 eV, which is the value obtained by including the OM data (see Sec.4.3.3).

The fitted parameters of the stacked 2018 spectrum are listed in the third column of Tab.4.2. The data/model ratio in the RGS band is shown in the upper panel of Fig.4.2, featuring a broad absorption feature above 1 keV. The results reveal a primary continuum with a slope of $\Gamma = 2.26^{+0.01}_{-0.01}$ and a plasma temperature above > 196 keV, a warm Comptonization characterized by a temperature of $0.23^{+0.01}_{-0.01}$ keV and a soft photon index $\Gamma_{\rm WC} = 2.52^{+0.06}_{-0.06}$, and a relativistic reflection component with a reflection ratio of $f_{\rm Refl} = 0.19^{+0.03}_{-0.02}$. The corresponding optical depth of the warm corona is $\tau_{\rm e}^{\rm WC} \sim 30$ [377]. The spin of the black hole cannot be constrained and is thus fixed at $a_\star = 0.998$. The inner radius of the disk is within $R_{\rm in} < 23\,R_{\rm ISCO}$, where $R_{\rm ISCO}$ is the innermost stable circular orbit (ISCO). The inclination angle, ionization parameter, and iron abundance of the accretion disk are derived to be $i = 34^{+1}_{-2}$ (deg), $\log(\xi/{\rm erg\,cm\,s}^{-1}) = 3.4^{+0.2}_{-0.1}$, and $A_{\rm Fe} = 3.6^{+0.5}_{-0.6}$ (in units of solar abundance), respectively. The hot corona, if assumed in a lamppost geometry, is measured at the height of $h = 47^{+26}_{-25}\,R_{\rm Horizon}$ above the accretion disk, where $R_{\rm Horizon}$ is the vertical event horizon of the Kerr black hole. The marginal differences between our results and Mallick et al. [208] based on the archival 2013 observation ($i = 46.4^{+1.9}_{-5.0}$ deg, $\log(\xi/{\rm erg\,cm\,s}^{-1}) = 2.96^{+0.04}_{-0.11}$, $A_{\rm Fe} = 2.2^{+0.5}_{-0.6}$ in their fit) may come from the different explanations for the soft excess and the intrinsic variability of the source.

We apply the best-fit model to time-/flux-resolved spectra as well, with several invariable properties (i.e. $N_{\rm H}^{\rm Gal}$, i and $A_{\rm Fe}$) on short-term timescales linked to those of the 2018 results. The results are listed in Tab.4.2. There is no significant change in the broadband continuum during the 2018 observations, T1, T2, T3, within their uncertainties, confirming the prerequi-

Table 4.2 Best-fit parameters of the model `tbabs*zashift*XABS_XS*(nthComp+relxilllpCp+PION_XS)` to the stacked 2018, time- (T) and flux-resolved (F) spectra.

Description	Parameter	2018	T1	T2	T3	T4	F1	F2	F3
`tbabs`	$N_{\rm H}^{\rm Gal}$ (10^{20} cm^{-2})				$4.09^{+0.03}_{-0.05}$				
`zashift`	$z_{\rm Mrk1044}$				$0.016^{\star}$				
`nthComp`	$\Gamma_{\rm WC}$	$2.52^{+0.06}_{-0.06}$	$2.49^{+0.04}_{-0.05}$	$2.51^{+0.05}_{-0.04}$	$2.51^{+0.07}_{-0.06}$	$2.42^{+0.13}_{-0.26}$	$2.57^{+0.05}_{-0.05}$	$2.50^{+0.05}_{-0.06}$	$2.56^{+0.05}_{-0.02}$
	$kT_{\rm e}$ (keV)	$0.23^{+0.01}_{-0.01}$	$0.23^{+0.01}_{-0.01}$	$0.23^{+0.01}_{-0.01}$	$0.22^{+0.01}_{-0.01}$	$0.20^{+0.02}_{-0.02}$	$0.24^{+0.01}_{-0.01}$	$0.22^{+0.01}_{-0.01}$	$0.25^{+0.01}_{-0.01}$
	$N_{\rm WC}$ (10^{-3})	$6.0^{+0.4}_{-0.5}$	$7.5^{+0.7}_{-0.6}$	$5.5^{+0.3}_{-0.4}$	$5.3^{+0.4}_{-0.5}$	$3.7^{+0.4}_{-0.5}$	$4.6^{+0.4}_{-0.2}$	$5.9^{+0.3}_{-0.5}$	$9.3^{+0.5}_{-0.6}$
`relxilllpCp`	h ($R_{\rm Horizon}$)	47^{+26}_{-25}	>46	>40	33^{+21}_{-28}	-17^{+18}_{-12}	>37	26^{+28}_{-20}	>24
	$a_{\star}$ (cJ/GM^2)				$0.998^{\star}$				
	i (deg)				34^{+1}_{-2}				
	$R_{\rm in}$ ($R_{\rm ISCO}$)	<23	<82	<97	<30	15^{+11}_{-11}	<49	<29	<42
	Γ	$2.26^{+0.01}_{-0.01}$	$2.29^{+0.01}_{-0.03}$	$2.23^{+0.01}_{-0.02}$	$2.23^{+0.02}_{-0.02}$	$2.22^{+0.03}_{-0.03}$	$2.18^{+0.01}_{-0.02}$	$2.27^{+0.02}_{-0.02}$	$2.31^{+0.02}_{-0.02}$
	$\log(\xi/{\rm erg\,cm\,s^{-1}})$	$3.4^{+0.2}_{-0.1}$	$3.6^{+0.2}_{-0.3}$	$3.4^{+0.1}_{-0.2}$	$3.3^{+0.1}_{-0.1}$	$3.2^{+0.2}_{-0.2}$	$3.3^{+0.1}_{-0.1}$	$3.3^{+0.2}_{-0.1}$	$2.1^{+0.4}_{-0.2}$
	$A_{\rm Fe}$				$3.6^{+0.5}_{-0.6}$				
	$kT_{\rm e}$ (keV)	>196	>51	>30	>23	>18	>38	>25	>21
	$f_{\rm Refl}$	$0.19^{+0.03}_{-0.02}$	$0.23^{+0.05}_{-0.05}$	$0.20^{+0.04}_{-0.05}$	$0.29^{+0.06}_{-0.06}$	$0.35^{+0.14}_{-0.09}$	$0.25^{+0.03}_{-0.05}$	$0.28^{+0.05}_{-0.05}$	$0.32^{+0.10}_{-0.09}$
	$N_{\rm refl}$ (10^{-5})	$9.4^{+0.8}_{-0.2}$	$9.9^{+1.0}_{-1.1}$	$7.8^{+0.9}_{-0.3}$	$8.8^{+14.0}_{-0.8}$	8^{+11}_{-1}	$6.9^{+5.0}_{-0.3}$	10^{+8}_{-9}	13^{+17}_{-1}
broadband	χ^2/d.o.f.	1319/733	987/731	922/731	956/731	750/730	950/734	933/734	939/733
`XABS_XS`	$N_{\rm H}$ (10^{21} cm^{-2})	$2.3^{+0.5}_{-0.4}$	$2.2^{+3.3}_{-0.4}$	$2.0^{+1.2}_{-0.4}$	$1.9^{+1.1}_{-0.2}$	$0.04^{+0.02}_{-0.02}$	$1.8^{+1.0}_{-0.3}$	$2.1^{+1.7}_{-0.6}$	$5.4^{+4.0}_{-3.2}$
	$\log(\xi/{\rm erg\,cm\,s^{-1}})$	$3.72^{+0.08}_{-0.10}$	$3.73^{+0.23}_{-0.09}$	$3.74^{+0.18}_{-0.14}$	$3.74^{+0.30}_{-0.09}$	$2.01^{+0.31}_{-0.25}$	$3.74^{+0.17}_{-0.11}$	$3.75^{+0.12}_{-0.20}$	$4.0^{+0.1}_{-0.2}$
	$\sigma_{\rm v}$ (km/s)	11800^{+4600}_{-4000}	8600^{+5400}_{-4400}	9500^{+5900}_{-6800}	8500^{+4400}_{-3900}	1000^{+1000}_{-800}	$9000^{\star}$	$9000^{\star}$	$9000^{\star}$
	$z_{\rm LOS}$	$-0.153^{+0.008}_{-0.016}$	$-0.181^{+0.010}_{-0.007}$	$-0.145^{+0.015}_{-0.021}$	$-0.143^{+0.010}_{-0.012}$	$-0.082^{+0.002}_{-0.002}$	$-0.146^{+0.013}_{-0.018}$	$-0.179^{+0.010}_{-0.018}$	$-0.188^{+0.013}_{-0.007}$
broadband+abs	χ^2/d.o.f.	1183/729	925/727	884/727	928/727	724/726	915/731	887/731	895/730
`PION_XS`	$N_{\rm H}$ (10^{20} cm^{-2})	$2.1^{+0.6}_{-0.5}$	$1.2^{+1.3}_{-0.7}$	8^{+7}_{-6}	$2.4^{+0.4}_{-1.4}$	$2.7^{+0.7}_{-1.1}$	$0.3^{+0.1}_{-0.1}$	$2.6^{+0.9}_{-1.8}$	$2.4^{+0.7}_{-1.4}$
	$\log(\xi/{\rm erg\,cm\,s^{-1}})$	$2.5^{+0.1}_{-0.1}$	$2.4^{+0.3}_{-0.3}$	$3.0^{+0.1}_{-0.4}$	$2.3^{+0.1}_{-0.2}$	$2.6^{+0.1}_{-0.2}$	$1.6^{+0.6}_{-0.2}$	$2.6^{+0.1}_{-0.3}$	$2.4^{+0.2}_{-0.1}$
	$\sigma_{\rm v}$ (km/s)	1500^{+800}_{-700}	$1500^{\star}$	1000^{+800}_{-750}	2200^{+3400}_{-1300}	$1500^{\star}$	800^{+750}_{-500}	<3300	1300^{+1200}_{-800}
	$z_{\rm LOS}$ (10^{-2})	$-1.1^{+0.2}_{-0.1}$	$-1.5^{+0.7}_{-0.5}$	$-1.2^{+0.2}_{-0.2}$	$-1.1^{+0.3}_{-0.4}$	$-1.1^{+0.3}_{-0.4}$	$-0.9^{+0.1}_{-0.2}$	$-1.3^{+0.4}_{-0.5}$	$-1.5^{+0.3}_{-0.3}$
broadband+abs+em	χ^2/d.o.f.	1135/725	913/724	853/723	886/723	698/723	877/728	867/728	864/727
Flux (0.4-10 keV)	F (10^{-11} erg/cm^2/s)	$6.34^{+0.03}_{-0.04}$	$7.38^{+0.07}_{-0.06}$	$5.60^{+0.09}_{-0.08}$	$5.90^{+0.12}_{-0.07}$	$4.56^{+0.06}_{-0.07}$	$4.92^{+0.09}_{-0.08}$	$6.45^{+0.10}_{-0.10}$	$8.59^{+0.09}_{-0.11}$

* The parameter is fixed.

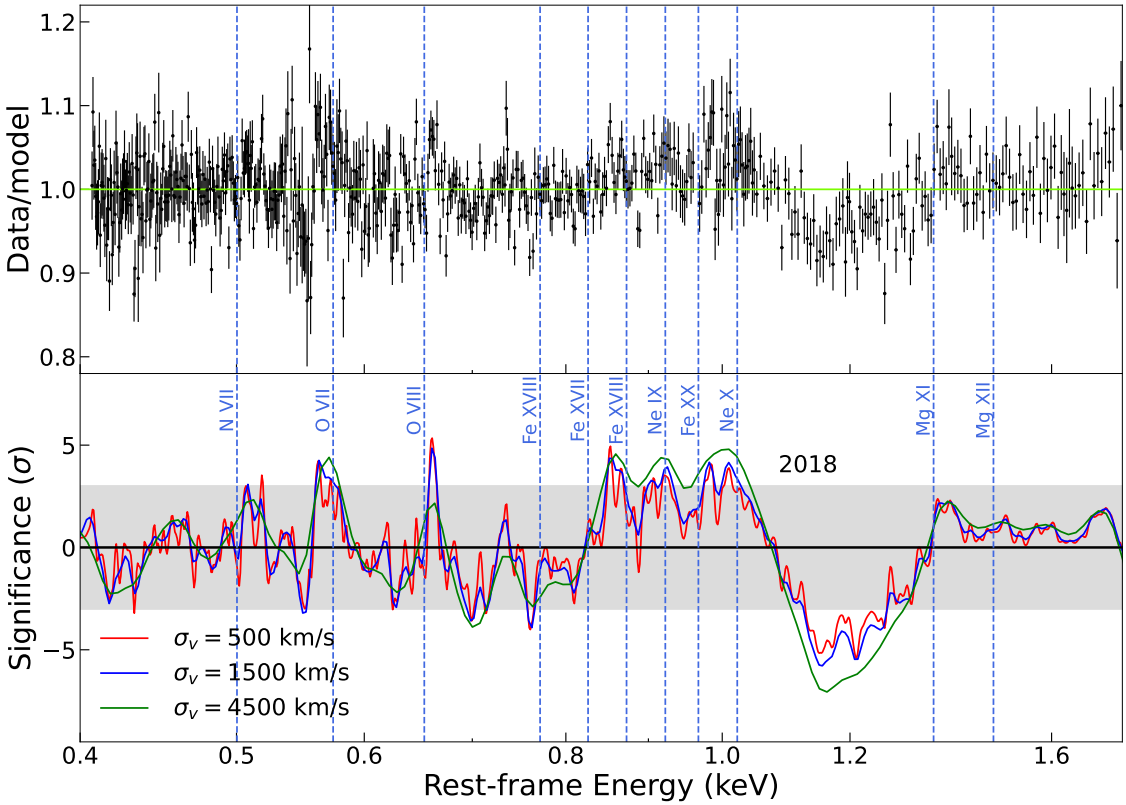

Fig. 4.2 The data/model ratio (*upper*) and single trial significance (*lower*) obtained from the Gaussian line scan with different line widths (500, 1500, 4500 km/s) over the rest-frame stacked 2018 spectrum in RGS band. The vertical dashed lines represent the rest-frame positions of the known ion transitions as a reference. The grey region marks the significance of 3σ.

site of the flux-resolved spectroscopy. The spectral slopes derived in flux-resolved spectra verify the softer-when-brighter behavior observed in Fig.4.1.

4.3.2 Gaussian Line Scan

To better visualize and identify the atomic features upon the continuum, we launch a blind Gaussian line scan over the spectra (see details in Sec.2.3.1). We adopt three line widths σ_v of 500, 1500, 4500 km/s and the corresponding numbers of energy steps are 2000, 700, 300, respectively, in order to match the RGS spectral resolution power ($R_{\rm RGS} \sim 150$–800).

The scan results over the 2018 spectrum in the RGS band are shown in the bottom panel of Fig.4.2. The rest-frame energies of the known strong ionic transition lines in the soft X-ray band are marked by the vertical blue *dashed* lines. We identify the O VII and O VIII emission lines close to their rest-frame positions as well as several emission features in the Ne IX/X and Fe XVII-XX region. No absorption features are found at/close to their rest frames. The strongest absorption feature is located around 1.2 keV with a broad line width, likely from blueshifted Fe and Ne ionic absorption lines.

Table 4.3 Best-fit parameters of an additional `Gaussian` model over the continuum model for the absorption feature around 1.2 keV and the O VIII emission line.

Parameter	F1	F2	F3
$E^{\rm abs}_{\rm rest}$ (keV)	$1.160^{+0.015}_{-0.016}$	$1.193^{+0.024}_{-0.021}$	$1.239^{+0.022}_{-0.024}$
$EW_{\rm abs}$ (eV)	50^{+19}_{-13}	74^{+24}_{-19}	73^{+30}_{-22}
$\Delta\chi^2_{\rm abs}$	40	45	39
$E^{\rm em}_{\rm rest}$ (keV)	$0.660^{+0.001}_{-0.001}$	$0.663^{+0.004}_{-0.004}$	$0.663^{+0.002}_{-0.001}$
$EW_{\rm em}$ (eV)	$1.4^{+1.0}_{-0.7}$	< 6.4	$2.2^{+1.5}_{-1.3}$
$\Delta\chi^2_{\rm em}$	27	7	10

The same approach is then applied to the time-/flux-resolved spectra with the same primary settings, of which results are shown in Fig.4.3 and Fig.4.4, separately. There are no significant differences among the results of time-resolved spectra, except for the T4 spectrum. Due to its low flux, the T4 result has a weaker detection significance of lines and the strongest absorption feature becomes around 0.7 keV, suggesting a different ionization state of the absorber in T4 observation. In the other three spectra, the emission (O VII, O VIII and 0.8–1 keV emission) and absorption (~ 1.2 keV line) features observed in the 2018 spectrum are all obvious. The absorption feature in T1 spectrum, the brightest observation, seems to be more blueshifted than others. In addition, the line width of the 1.2 keV trough is not as broad as that of the 2018 spectrum, due to the stack effect of the variable feature. Comparing the flux-resolved results, we notice a decreasing significance of the O VII and O VIII lines

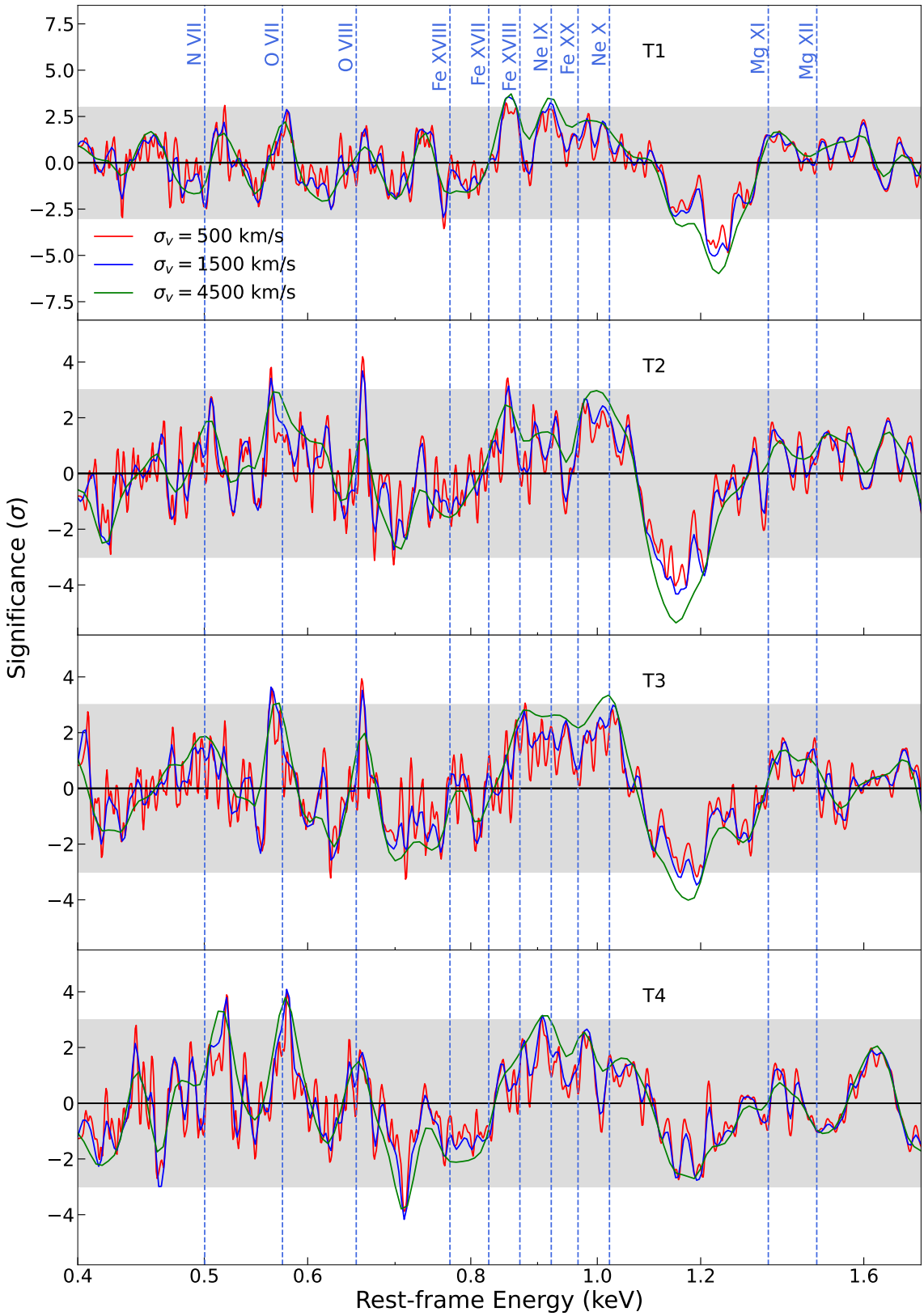

Fig. 4.3 Similar to the bottom panel of Fig.4.2 but the scan is performed on the time-resolved spectra.

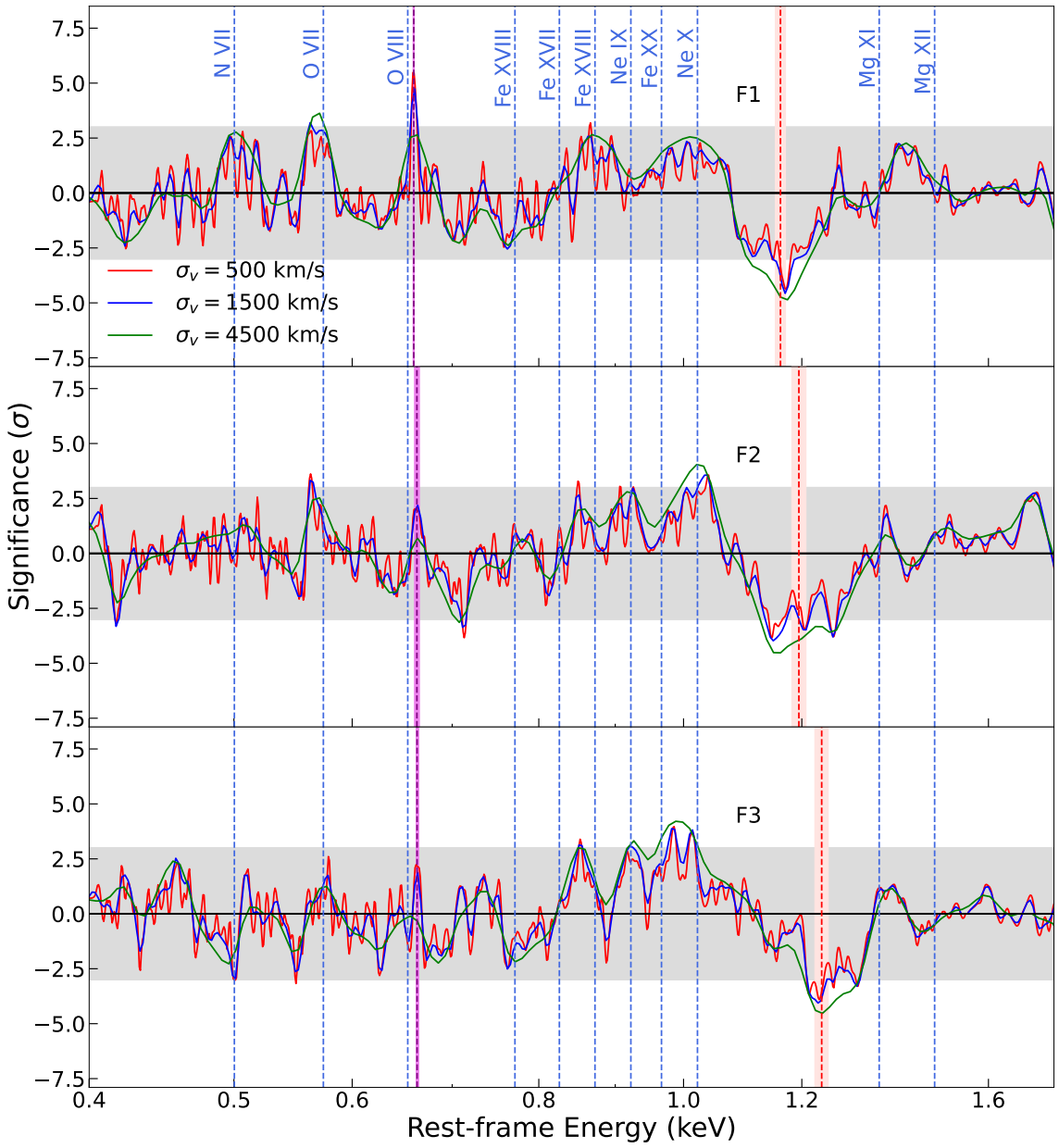

Fig. 4.4 Similar to the bottom panel of Fig.4.2 but the scan is performed on the flux-resolved spectra. The vertical dashed red/purple lines and the red/purple shadowed areas indicate the position of the centroid of the absorption/emission feature and the corresponding uncertainty. (see Tab.4.3).

and an increasing blueshift of the absorption feature with the source luminosity, implying the existence of possible wind-luminosity relations. We thus fit the absorption feature with a `Gaussian` model and the parameters are listed in Tab.4.3. The energy centroid of the absorption feature increases with the flux and is highlighted in *red* in Fig.4.4. The best-fit parameters for the O VIII emission line are also listed in Tab.4.3 and depicted in *purple* in Fig.4.4, indicating a slightly increasing blueshift.

4.3.3 Search For Outflows

To further study these emission/absorption lines, we employ the physical photoionization model, `PION`. The intrinsic spectral energy distribution (SED) of Mrk 1044 inputted into `PION` is derived from the UV to hard X-ray energies. Due to the stability of the OM flux, we stack the OM spectra and model it with an additional `diskbb` component, characterized by a temperature of 10^{+21}_{-6} eV. Such a temperature is relatively low for the accretion disk around an SMBH with a mass of $\sim 3\times10^6 M_\odot$ [316], might be explained by the truncated disk (suggested by the inner radii $R_{\rm in}$ in `relxilllpCp`, see Tab.4.2). The interstellar extinction [$E_{\rm B-V}=0.031$, 214] is also considered. The SED of Mrk 1044 in 2018 is shown in Fig.4.5 compared with other Seyfert galaxies, where it shares a similar soft SED with 1H 1934-063. The observed data are shown on top of the SED, where the deviations from the best-fit SED come from the removal of the Galactic absorption, redshift, and dust-reddening components. By measuring the bolometric luminosity (10^{-3}–10^3 keV) predicted by the model, $L_{\rm Bol}\sim 1.4\times10^{44}$ erg/s, we thus estimate the Eddington ratio of Mrk 1044 at $\lambda_{\rm Edd}=L_{\rm Bol}/L_{\rm Edd}\sim0.4$, adopting a SMBH mass of $2.8\times10^6 M_\odot$ [64]. Although our estimated Eddington ratio is slightly different from the literature [$\lambda_{\rm Edd}=0.59$, 110], due to the different masses adopted [$M_{\rm BH}=2.1\times10^6 M_\odot$, 110], it still implies a high-accretion system.

To take advantage of both the advanced reflection model (RELXILL), implemented in XSPEC, and the `PION` model in SPEX, we adopt the code used in Parker et al. [251] to construct the tabulated model, which is an XSPEC version of `PION` and `XABS` (see details in Sec.2.2.2.2), called `PION_XS` and `XABS_XS`. The LOS outflow velocity $v_{\rm LOS}$ is replaced by the LOS redshift $z_{\rm LOS}$.

4.3.3.1 Absorption

We launch a systematic scan over a multi-dimension grid of the parameters ($\log\xi, z_{\rm LOS}, \sigma_v$) of `xabs_xs`, as introduced in Sec.2.3.2. The range of $\log\xi$ is 0–5 with a step of $\Delta\log\xi=0.1$. The grid of the turbulent velocity σ_v is the same as that of the Gaussian line scan ($\sigma_v=500, 1500, 4500$ km/s). The LOS velocity, $z_{\rm LOS}$, ranges from -0.35 to 0, with an increment

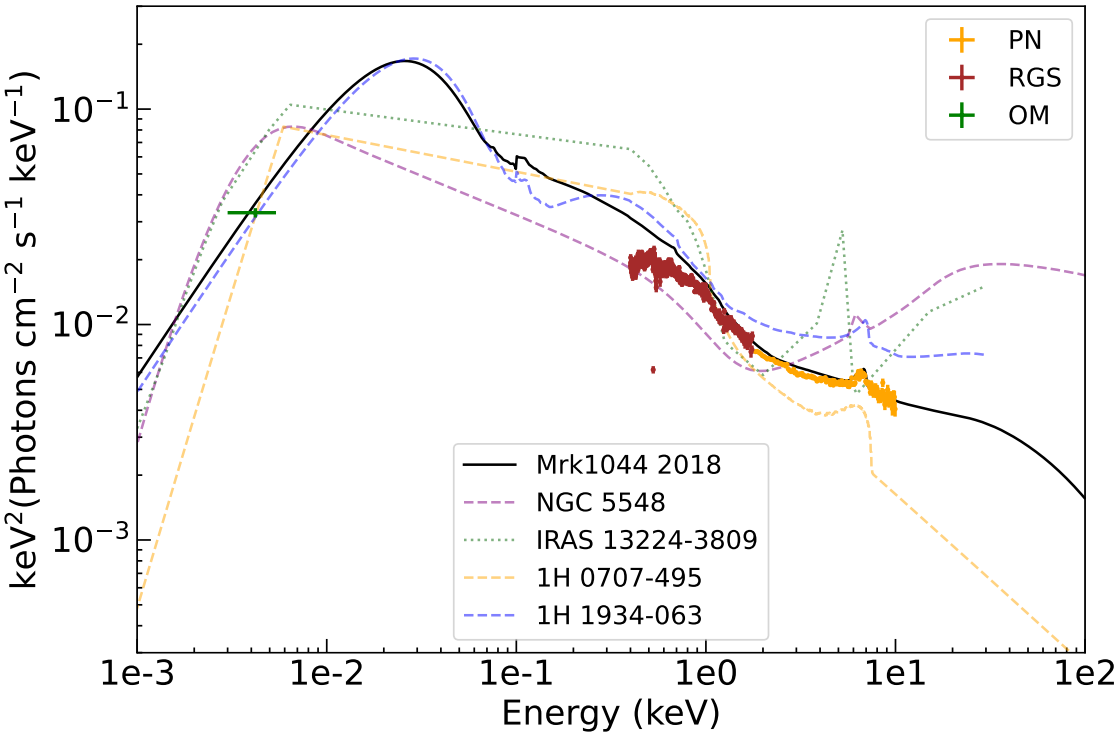

Fig. 4.5 The averaged spectral energy distribution of Mrk 1044 in 2018 compared with other Seyfert galaxies (NGC 5548, [228]; IRAS 13224-3809, [137]; 1H 0707-495, [372]; 1H 1934-063, [373]). The EPIC-pn, RGS, and OM data are shown as well, where the deviations from the best-fit SED come from the removal of the Galactic absorption, redshift, and dust-reddening components.

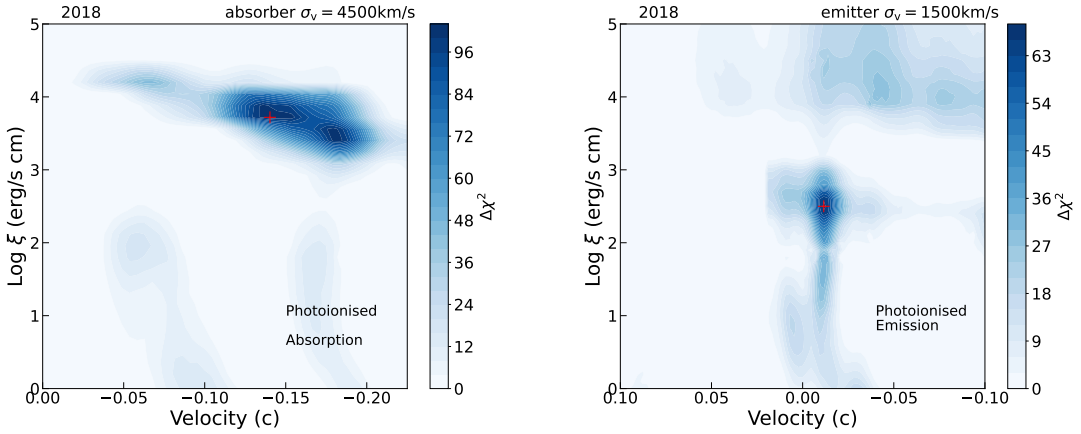

Fig. 4.6 Photoionization absorption (*left*) /emission (*right*) model search over the stacked 2018 spectrum of Mrk 1044 upon the broadband model. The color illustrates the statistical improvement after adding an absorption/emission component. The best-fit solution is marked by a red cross.

depending on the choice of σ_v ($c\Delta z_{\rm LOS} = 500, 700, 1500$ km/s for $\sigma_v = 500, 1500, 4500$ km/s respectively). The scan is performed upon the best-fit model obtained in Sec.4.3.1.

The scan result of the 2018 spectrum is shown in the left panel of Fig.4.6, where the best solution is marked with a red cross. Because of the consistent solutions with different turbulent velocities, we only present the result with $\sigma_v = 4500$ km/s in this paper, which has the largest detection significance. The velocity on the X-axis is the relativistically corrected velocity. It reveals a strong detection ($\Delta\chi^2 = 103$) of a highly ionized ($\log\xi = 3.72$) and ultra-fast ($z_{\rm LOS} = -0.15$) absorber. If we allow the line width to vary, the solution of the direct fit ($\sigma_v \sim 12000$ km/s, $N_{\rm H} = 2.3 \times 10^{21}$ cm^{-2}) is listed in Tab.4.2, consistent with our scan result. The contribution of this absorber to the modeling is mainly around 1.2 keV from blueshifted Fe XXII-XXIV and Ne X (see Fig.4.3), without any absorption features detected in the EPIC band probably due to its relatively low column density and the soft SED.

The same scan is also performed for the time-/flux-resolved spectra and their best-fit solutions are summarized in Tab.4.2. The UFO detection significance in each spectrum is at least 4σ, i.e. $\Delta\chi^2 = 24.5$ for 4 d.o.f. We also calculate the X-ray flux between 0.4 and 10 keV with the `cflux` model in Tab.4.2.

Among the time-resolved spectra, apart from T4, the ionization state and column density of the UFO are consistent within their uncertainties. The UFO velocity indicatively has an increasing trend with the source flux. As for T4, instead of the 1.2 keV feature, the best-fit solution of T4 explains the blueshifted O VIII line around 0.7 keV (see the bottom panel of Fig.4.3 and the secondary solution in the left panel of Fig.4.6). It means that a completely

different absorber dominates the T4 spectrum, which was observed one year apart from the others. Although according to the T4 scan result, a similar high-ionization and fast region exists with a lower significance than that of the best fit, that solution is weakly detected ($\Delta\chi^2$/d.o.f. $= 13/4$) after including a primary absorber and an emitter (see Sec.4.3.3.2). Therefore, we do not consider this secondary component of T4 in the following as the constraints on its parameters are too loose for meaningful discussions.

The flux-resolved spectroscopy is likely to smear/broaden the variable line features, which may lead to degenerate solutions. To reduce the influence of this effect, we fix the line width of XABS_XS at 9000 km/s, the average value of the time-resolved results, although the trend discovered below remains the same with a free line width. Among the flux-resolved spectra, we find that a faster, more ionized, and Compton-thicker plasma tends to appear in a brighter state.

4.3.3.2 Emission

The same systematic scan is applied to the PION_XS model over the continuum model to study the photoionization emission component. The only difference is the searched velocity grid, ranging from 0.1 to -0.1, as we do not find strongly shifted emission lines in the bottom panel of Fig.4.2. The scan result of the 2018 spectrum is shown in the right panel of Fig.4.6 with a fixed line width of 1500 km/s. It reveals the highly significant detection ($\Delta\chi^2 = 69$) of a blueshifted ($z_{\rm LOS} = -0.011$) photoionized emitter with a modest ionization state ($\log\xi = 2.5$). The statistical improvement shown in Tab.4.2 is smaller ($\Delta\chi^2 = 48$) than that of the scan because some residuals fitted by PION_XS in the scan over the continuum model have been explained by the model including a XABS_XS. The primary emitter is not as highly ionized as the absorption component (perhaps related to UFO in T4). The potential secondary solution ($\log\xi > 3.5$) in the scan plot is discussed in Sec.4.4.

We do not perform the emission model scan over the time-/flux-resolved spectra as the velocity of the emission component is generally not as variable as the absorption [e.g. 159, 287, 172]. The best-fit parameters of PION_XS are shown in Tab.4.2. Each solution, except T1, has at least 3.5σ (i.e. $\Delta\chi^2 = 20$) detection significance. The unconstrained line width in T1 and T4 is fixed at 1500 km/s. In general, the line width of the emission component is narrower than that of the absorption. The column density, ionization state, and velocity of the emitter are stable within their uncertainties among the time-resolved spectra, while those parameters are tentatively correlated with the source luminosity in the flux-resolved results. The velocities are all blueshifted at least more than 2700 km/s. Apart from F1, the PION_XS model mainly explains the O VIII and Fe/Ne lines around 1 keV, while it models the O VII and O VIII lines in F1 spectra (see Fig.4.4).

4.4 Discussion

By analyzing the RGS data of a large *XMM-Newton* campaign on Mrk 1044 in 2018 and 2019, we find a highly-ionized UFO and a blueshifted photoionized emitter in the spectra. The UFO detection confirms the existence of the UFO1 reported in Krongold et al. [181] from the 2013 *XMM-Newton* observation, sharing a similar ionization state and velocity, although the UFO in their paper was associated with a fixed narrow profile ($\sigma_v = 10\,\mathrm{km/s}$). The reported multi-phase outflow is also marginally supported by the UFO detected in T4, which has similar parameters to their UFO2 component, while we do not find other cold UFOs like their UFO3/4 phases in Mrk 1044. The emitter shows a much lower ionization state and column density than UFO, implying the average photoionization emission component originates from a different gas from absorption, while the UFO in T4 perhaps might be related to the emitter due to their similar column density, ionization state, and turbulent velocity.

In the scan of the photoionization emission model (see the right panel of Fig.4.6), we may discover a potential secondary emitter, which is trying to complement the blue wing of the Fe K emission. The best fit ($\Delta\chi^2 = 37$) of the secondary emitter requires an ultra-fast ($z_{\rm LOS} = -0.12^{+0.02}_{-0.02}$) and highly ionized ($\log\xi = 3.7^{+0.1}_{-0.2}$) plasma with a column density of $N_{\rm H} = 3.6^{+1.8}_{-1.5} \times 10^{21}\,\mathrm{cm}^{-2}$ and an unconstrained turbulent velocity fixed at $\sigma_v = 9000\,\mathrm{km/s}$. This emitter shares common properties with the absorber, indicating the same origin of the absorption. We plot the stacked 2018 EPIC spectra and the best-fit model including two emitters in the top panel of Fig.4.7, compared with the continuum plus one emitter. The corresponding data-to-model ratios are shown in the second and third panels. However, we are concerned about the requirement of this secondary emitter as the not well-explained Fe K profile might result from the imbalance between the statistics of the RGS and EPIC data, where the grating data have more bins (a factor of 4) than CCD data and the model is mainly adjusted to fitting soft X-ray residuals. To test this possibility, we fit the continuum model to only EPIC data (1.77–10 keV) and show it in Fig.4.7 as well as the corresponding ratio. Compared with the results in Tab.4.2, the continuum model only requires a harder spectral slope ($\Gamma = 2.16^{+0.03}_{-0.02}$) and explains the blue wing of Fe emission well, while the other parameters remain unchanged. In terms of fitting the EPIC data, this continuum model is much better ($\Delta\chi^2 = 86$) than the continuum plus two emitters fitted to the RGS+EPIC data. It suggests that the additional emission component is spurious, although we cannot exclude the possibility of an intervening outflow contributing to a part of the Fe K profile. Therefore, we tend not to discuss the evolution of the secondary emitter in the following.

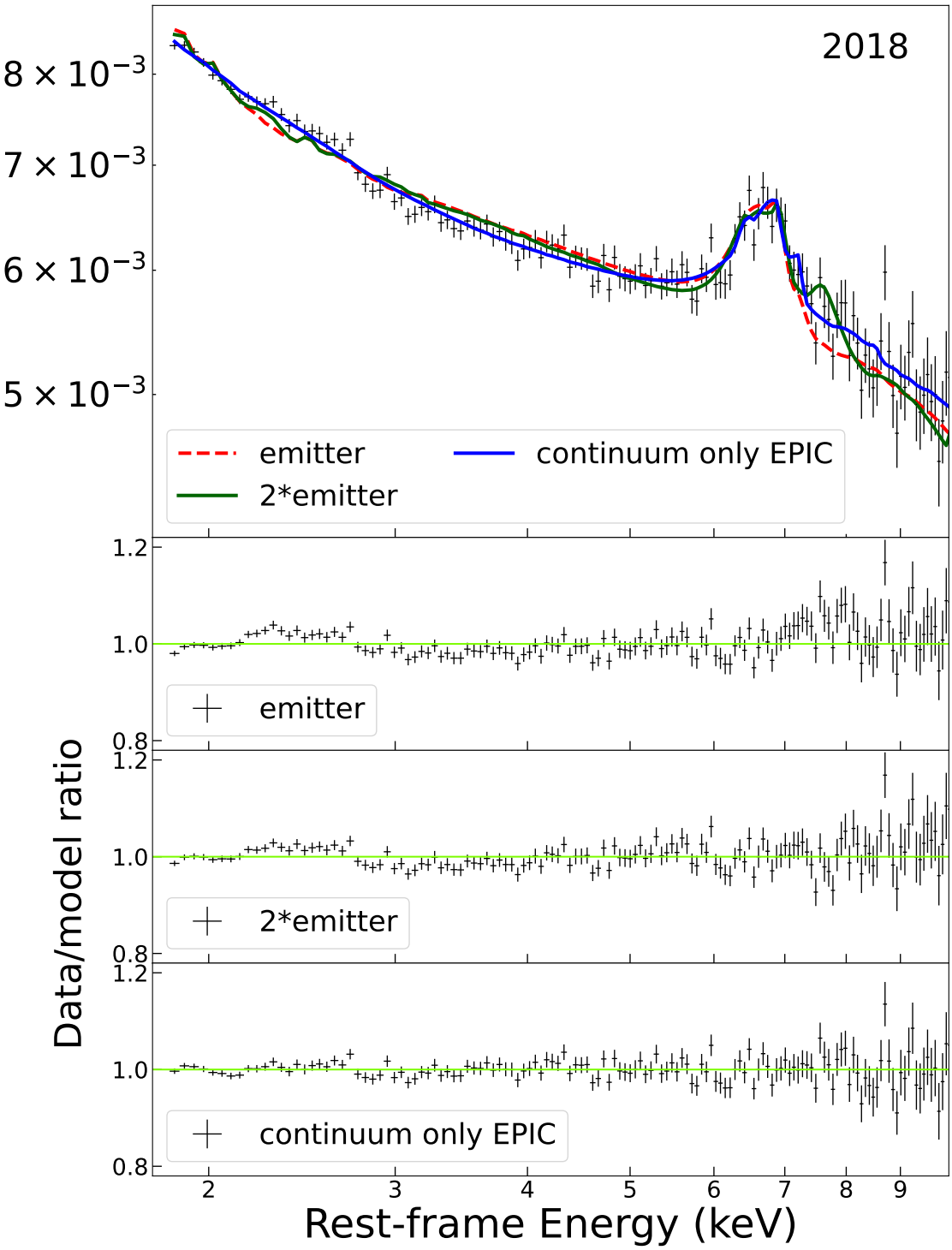

Fig. 4.7 The stacked 2018 EPIC spectra of Mrk 1044. The fits of the continuum plus one or two emitter(s) to the RGS+EPIC data are shown in *red* dashed and *green* solid lines, respectively. The fit of the continuum model to only EPIC data (1.77–10 keV for consistency with other fits) is shown in the *blue* line. The corresponding data/model ratios are shown in the following panels.

4.4.1 Evolution of the Wind Components

In Sec.4.3.3, we have measured the properties of the absorption and emission components at different flux levels. To further investigate the relations between wind properties and source luminosity, we plot the column density, ionization parameter, and velocity of absorbing and emitting gas versus the calculated fluxes in Fig.4.8 and 4.9, respectively. The blueshift of the features, measured by the `Gaussian` model, are included as well. The absorption line is assumed to come from Ne X ($E_{rest} = 1.022\,keV$), while the emission line is O VIII ($E_{rest} = 0.6535\,keV$). We fit these parameters with a linear function in a logarithmic space. The same fit with a slope fixed at unity is also performed on the ionization parameter to show the expected behavior in photoionization equilibrium, according to the definition of the ionization parameter (Eq.1.9). All of the fits provide positive correlations between wind properties and the source luminosity.

4.4.1.1 Absorbing gas

For the absorption component, the Pearson correlation coefficients of the best-fit values of (N_H, F), $(\log\xi, F)$, (v, F), (v_{gaus}, F) points considering their uncertainties are 0.76, 0.86, -0.86 and -0.96 respectively [48], suggesting a moderate correlation between (N_H, F) and strong correlation among the others. The Log/Log fits give:

$$\log\frac{N_H}{10^{21}\,cm^{-2}} = (-0.9\pm0.8) + (1.59\pm0.98)\log(\frac{F_{0.4-10}}{10^{-11}}), \tag{4.1}$$

$$\log\frac{\xi}{erg\,cm/s} = (2.96\pm0.33) + (1.08\pm0.41)\log(\frac{F_{0.4-10}}{10^{-11}}), \tag{4.2}$$

$$\log\frac{|v|}{c} = (-1.12\pm0.14) + (0.39\pm0.16)\log(\frac{F_{0.4-10}}{10^{-11}}), \tag{4.3}$$

$$\log\frac{|v_{gaus}|}{c} = (-1.40\pm0.16) + (0.73\pm0.19)\log(\frac{F_{0.4-10}}{10^{-11}}). \tag{4.4}$$

The best-fit value of the slope in Eq.4.2 is consistent with unity, despite the large uncertainty, indicating that the absorbing gas responds to the variability of the source radiation instantaneously, which implies a high volume density. The weakly increasing trend of the column density is opposite to the relation shown in IRAS 13224-3809 (see Fig.7 in [259]), where the column density slightly decreases along with the increasing ionization parameter ($\log\xi$ up to 6) and luminosity. It means the UFO in Mrk 1044 probably has not been over-ionized, as suggested by the modest ionization state ($\log\xi \sim 3.7-4.0$), and still requires a larger

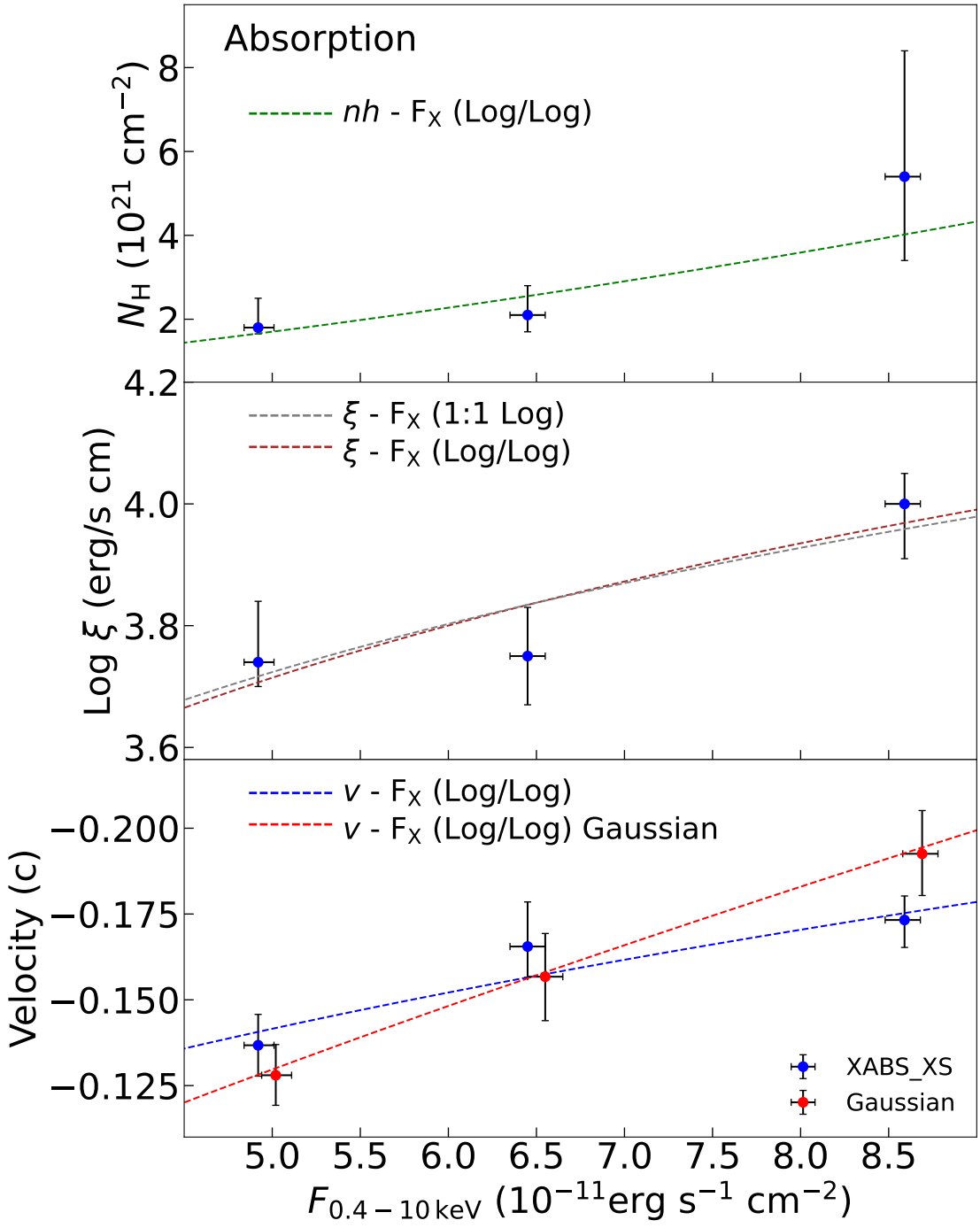

Fig. 4.8 The column density (*top*), ionization parameter (*middle*), and velocity (*bottom*) of the photoionized absorbing plasmas versus the unabsorbed X-ray flux for the flux-resolved spectra. The blueshift of the main absorption feature (i.e. Ne X) measured by `Gaussian` is also included, where the corresponding flux is manually shifted for clarity. The linear function fits, with (1:1 Log) and without (Log/Log) a slope fixed at unity, are performed in a logarithmic space. See details in Sec.4.4.1.

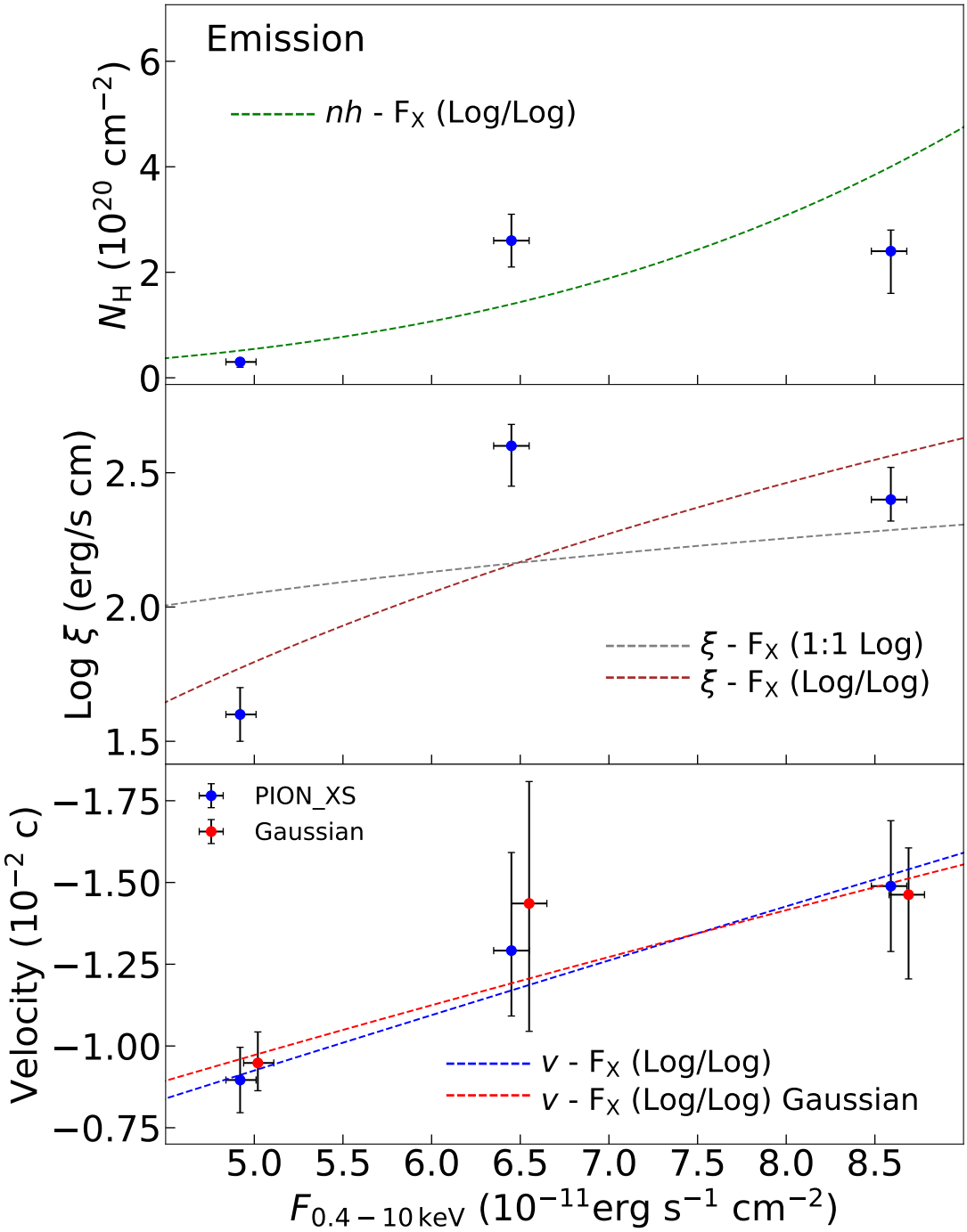

Fig. 4.9 The column density (*top*), ionization parameter (*middle*), and velocity (*bottom*) of the photoionized emitting plasmas versus the unabsorbed X-ray flux for the flux-resolved spectra. The blueshift of the main emission feature (i.e. O VIII) measured by `Gaussian` is also included, where the corresponding flux is manually shifted for clarity. The linear function fits, with (1:1 Log) and without (Log/Log) a slope fixed at unity, are performed in a logarithmic space. See details in Sec.4.4.1.

column density to visualize the absorption features at a higher ionization state (e.g. see Fig. 10 in [264]).

The positive correlation between the velocity and the X-ray flux suggests that the wind is radiatively driven, which is also observed in other high-accretion systems, IRAS 13224-3809 [259] and PDS 456 [220]. According to Eq.4 in Matzeu et al. [220], the net radiatively-driven (i.e. radiative minus gravitational force) outflow should have a relationship among the velocity, the ionizing luminosity $L_{\rm ion}$ and the launching radius $R_{\rm w}$,

$$v/c \propto k_{0.4-10}^{1/2} L_{0.4-10}^{1/2} R_{\rm w}^{-1/2}, \tag{4.5}$$

where $k_{0.4-10} = L_{\rm bol}/L_{0.4-10}$ is the bolometric correction factor. The relation observed in Mrk 1044 (from `XABS_XS` instead of the phenomenological model) is consistent with the power index (0.5) in Eq.4.5 within uncertainties, at variance with the results derived from IRAS 13224-3809 (0.05 ± 0.02) and PDS 456 (0.22 ± 0.04).

4.4.1.2 Emitting gas

For the emission component, the Pearson correlation coefficients of the best-fit values of $(N_{\rm H}, F)$, $(\log\xi, F)$, (v, F), $(v_{\rm gaus}, F)$ points considering their uncertainties are 0.73, 0.68, -0.83, and -0.69, respectively, suggesting moderate correlations, except for a strong correlation between (v, F). The fits provide:

$$\log \frac{N_{\rm H}}{10^{20}\,{\rm cm}^{-2}} = (-2.8 \pm 2.3) + (3.68 \pm 2.79) \log(\frac{F_{0.4-10}}{10^{-11}}), \tag{4.6}$$

$$\log \frac{\xi}{{\rm erg\,cm/s}} = (-0.49 \pm 2.16) + (3.27 \pm 2.64) \log(\frac{F_{0.4-10}}{10^{-11}}), \tag{4.7}$$

$$\log \frac{|v|}{0.01{\rm c}} = (-0.68 \pm 0.14) + (0.92 \pm 0.17) \log(\frac{F_{0.4-10}}{10^{-11}}), \tag{4.8}$$

$$\log \frac{|v_{\rm gaus}|}{0.01{\rm c}} = (-0.57 \pm 0.17) + (0.80 \pm 0.22) \log(\frac{F_{0.4-10}}{10^{-11}}). \tag{4.9}$$

However, the extremely large uncertainties of the fitted parameters, except for the velocity-related fits, preclude any authentic conclusions on the emitting gas. Moreover, a large range of locations of the emission, suggested by the moderate ionization state, a low column density, and a narrow line width, will result in a low coherence between the plasma and the source [143], impeding the discovery of correlations.

4.4.2 Outflow Properties

The kinetic power of UFO is estimated by Eq.1.14. We estimate the ionizing luminosity (1–1000 Rydberg) from the SED presented in Fig.4.5 at $L_{\rm ion} \sim 3.9 \times 10^{43}\,{\rm erg/s}$ and find, $L_{\rm kin} \sim 5.89 \times 10^{44} \Omega C_{\rm V}\,{\rm erg/s}$ by inputting the results of the UFO obtained in the 2018 spectrum. Here we adopt a conservative value of the opening angle $\Omega = 0.3$ from the GRMHD simulations of radiatively-driven outflows in high-accretion systems [330]. The filling factor $C_{\rm V} = 7 \times 10^{-3}$ is derived from Eq.23 in Kobayashi et al. [167] assuming that the outflow mass rate is comparable with the accretion mass rate and the accretion efficiency is $\eta = 0.1$. The conservative value of the UFO kinetic energy is thus $L_{\rm UFO} \sim 1.54 \times 10^{43}\,{\rm erg/s} \sim 4.4\% L_{\rm Edd}$, surpassing the theoretical criterion, suggesting that the UFO in Mrk 1044 is very likely to influence the evolution of the host galaxy.

According to Eq.1.11, we can estimate the lower limit of the outflow location, $R \geq 2GM_{\rm BH}/v_{\rm UFO}^2 \geq 98 R_{\rm g}$. It provides an upper limit of the outflow density, $n_{\rm H} = L_{\rm ion}/\xi R^2 < 4.5 \times 10^{12}\,{\rm cm^{-3}}$. On the other hand, by using the time-dependent photoionization model `TPHO` [303], we simulate the response of plasma with different densities to the source variability to estimate the lower limit of the plasma density and further the upper limit of the outflow location. The duration of the low, middle, and high states of the source are 3 ks, 1.5 ks, 3 ks respectively, provided by the timescale of segments of flux-resolved spectra, shown in the top panel of Fig.4.10. The time-dependent evolution of the ionic concentration of predominant absorption lines, i.e., Ne X and Fe XXII-XXIV, are shown in the lower four panels of Fig.4.10. Gases with a density above $10^9\,{\rm cm^{-3}}$ respond quickly to the luminosity. If we assume the UFO in Mrk 1044 responds to the source instantaneously, suggested by Eq.4.2, the lower limit of the density is $10^9\,{\rm cm^{-3}}$. The recombination timescale of the plasma at $\log \xi = 3.7$ can be evaluated through the `rec_time` code in SPEX. For example, the recombination time of the Fe XXIV line, the predominant line in UFO, is calculated $t_{\rm rec} < 19\,{\rm s}$, consistent with our assumption. The volume density of the UFO is thus estimated between $n_{\rm H} = 10^9$–$4.5 \times 10^{12}\,{\rm cm^{-3}}$ and the corresponding location is $R = \sqrt{L_{\rm ion}/n_{\rm H}\xi} = 98$–$6600\,R_{\rm g}$.

For the emitting gas, we have to adopt another method to derive the upper limit of its location, since its response to the source is unconstrained. Through Eq.1.12, the upper limit of the location can be estimated, $R \leq C_{\rm V} L_{\rm ion}/\xi N_{\rm H} \leq 7.8 \times 10^6\,R_{\rm g}$. The lower limit could be calculated by the same method for absorbing gas at $> 1.2 \times 10^4\,R_{\rm g}$. However, since the emission comes from a wide range of distances, the observed velocity is an averaged value and may not be representative of the escape velocity of the emitting gas close to the center. If we assume the emitting gas shares the same origin with the UFO detected in T4, the lower limit of the location can be estimated at $> 320\,R_{\rm g}$. Our constraints on the

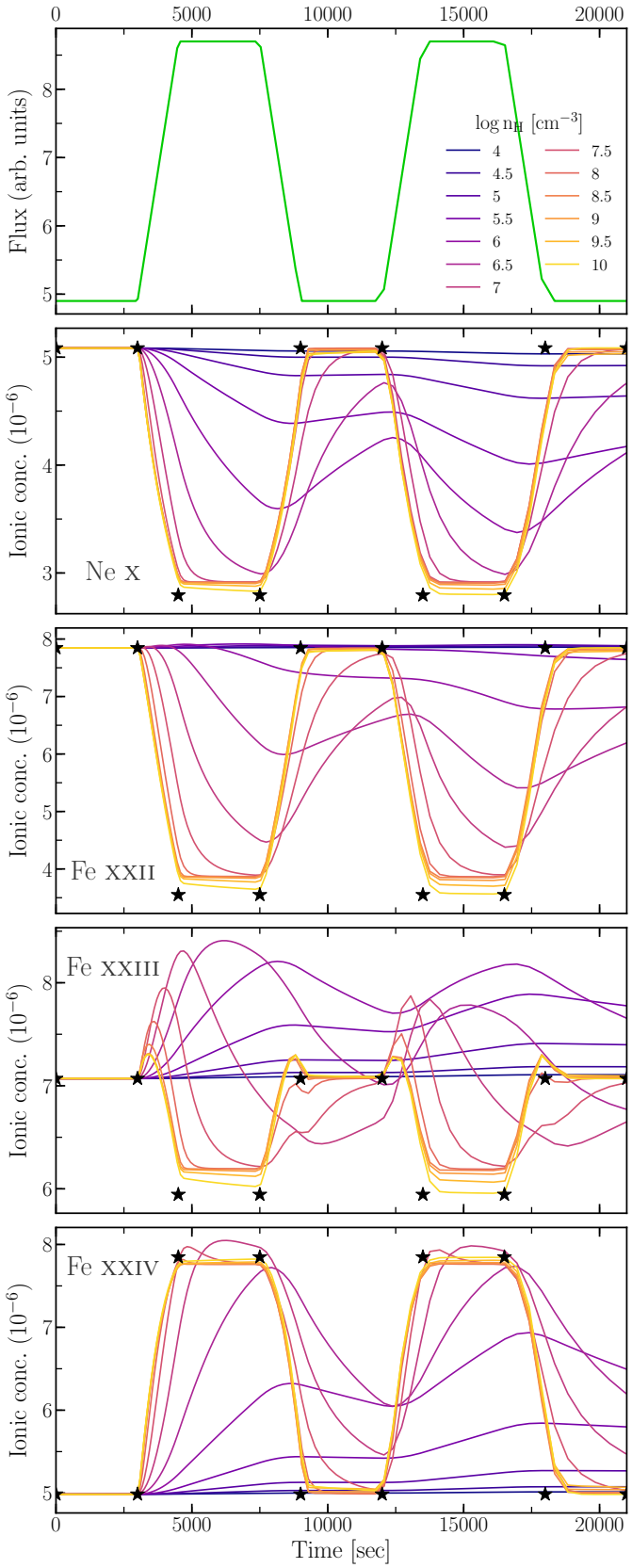

Fig. 4.10 *Top* panel: The input light curve that we expect in Mrk 1044 (an approximation) for the TPHO model. The duration of the low state, the middle, and the high state are 3 ks, 1.5 ks, and 3 ks respectively. *Middle* and *Botton* panels: The time-dependent evolution of Ne X and Fe XXII-XXIV relative concentration for different densities and are compared with the ionic concentrations for a plasma in photoionization equilibrium (*black* stars).

location of the emission components are rather loose and span the whole range of distances, 3×10^2–$7.8 \times 10^6\, R_{\rm g}$, from the accretion disk to the interface between the outer disk and the BLR. The range of the corresponding density is 1.2×10^4–$7 \times 10^{11}\,{\rm cm}^{-3}$.

4.4.3 Comparison with other AGN

By comparison with UFOs discovered in other AGN, the ionization state ($\log \xi \sim 3.7$) and the velocity ($v \sim 0.15c$) of the UFO in Mrk 1044 are typical ($\log \xi \sim 3$–6, $v \sim 0.08$–$0.3c$, [235, 173, 248, 219, 187]). The column density ($N_{\rm H} \sim 2.3 \times 10^{21}\,{\rm cm}^{-2}$) is not as thick as typical UFOs discovered from Fe K absorption feature ($\log(N_{\rm H}/{\rm cm}^{-2}) \sim 22$–$24$). However, the low column density is common in UFOs detected in the soft X-ray band [197, 269, 373]. Alternatively, another potential explanation is the relatively low inclination angle of Mrk 1044 ($i \sim 34^\circ$) that we are therefore seeing a narrower wind region.

The correlation between the velocity of the UFO and the source luminosity is consistent with the phenomenon observed in PDS 456 [220] and IRAS 13224-3809 [259], while different from 1H 0707-495 [372]. The reason might come from their different Eddington ratios, as the former three (PDS 456, $\lambda_{\rm Edd} \sim 0.77$, [235]; IRAS 13224-3809, $\lambda_{\rm Edd} = 1$–3, [7]; Mrk 1044, $\lambda_{\rm Edd} \sim 0.4$) are not so highly accreting as 1H 0707-495 ($\lambda_{\rm Edd} > 0.7$, [372], or $\lambda_{\rm Edd} = 140$–260, [63]) of which the structure of the accretion flow does not significantly deviate from the standard thin disk model [316].

Blue-shifted emission lines are rarely observed in AGN. To our knowledge, among Type 1 AGN, only four sources (1H 0707-495, [372]; ESO 323-G077, [139]; NGC 4151, [11]; NGC 7469, [109]) reveal blueshifted emission lines, as well as the partially absorbed emission lines in NGC 4051 [277]. Given the fact that blueshifted emission lines were also found in some Ultra-luminous X-ray (ULX) sources (e.g., NGC 55 ULX and NGC 247 X-1, [260, 263, 172]), we propose that blueshifted emission lines are related to high accretion rates and plot the blueshift of emission lines versus the Eddington ratios in Fig.4.11 [139, 66, 226, 372, 376]. The Eddington ratio of 1H 0707-495 is assumed at its lower limit, 0.7, as we cannot constrain the upper limit and only know it is a super-Eddington AGN. The Pearson coefficient is 0.87, suggesting they are highly correlated. The linear fit gives:

$$v_{\rm EM}({\rm km/s}) = (11560 \pm 1756)\lambda_{\rm Edd} + (170 \pm 240). \tag{4.10}$$

Although the fit seems to strongly support our hypothesis, due to the small size of the sample and the uncertainty on the $\lambda_{\rm Edd}$, we are unable to confirm that correlation. The reason why there are no blueshifted emission lines in other high-Eddington AGN is probably a too-strong continuum, washing out the lines, or the small viewing angle close to face-on. The validation

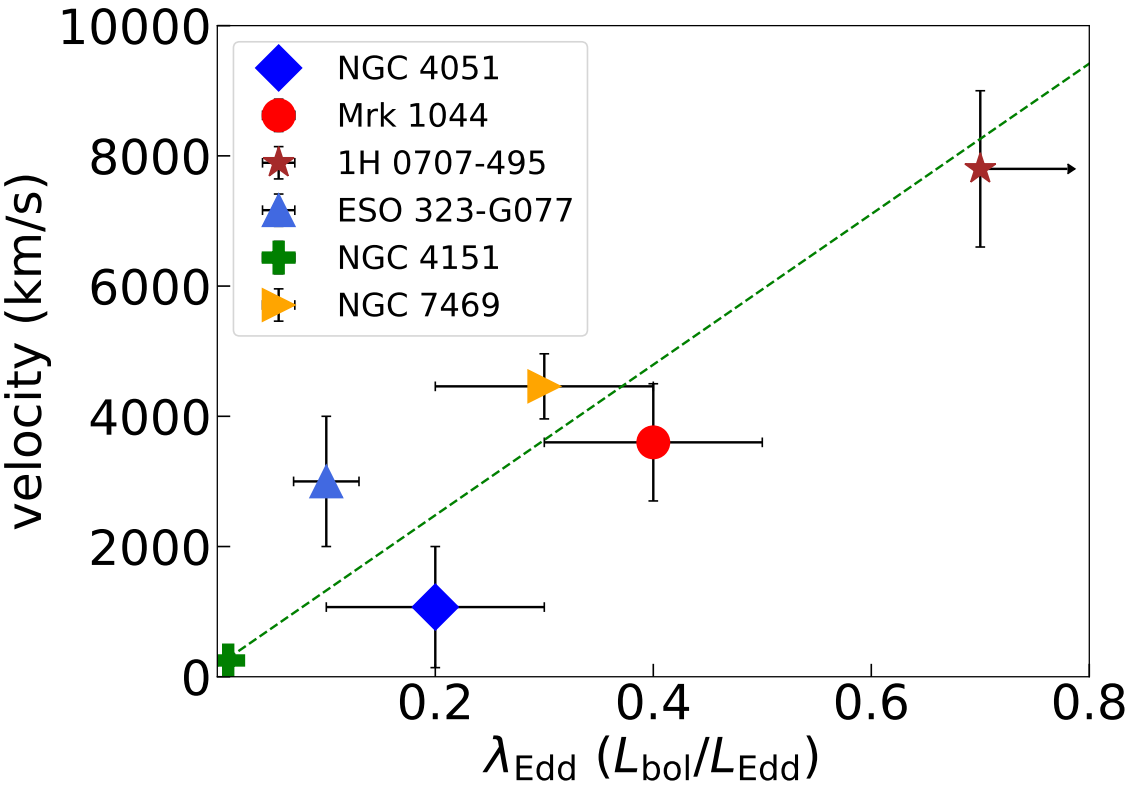

Fig. 4.11 The velocity of emission lines versus the estimated Eddington ratio of Type 1 AGN. See more details in Sec.4.4.3.

of this correlation requires a systematic analysis of a large sample of AGN at different accretion rates.

4.5 Conclusions

In this Chapter, through the time- and flux-resolved X-ray spectroscopy on four *XMM-Newton* observations of Mrk 1044, we investigate the dependence of the wind properties on the source luminosity. We find that the absorbing gas quickly responds to the source variability, suggesting a high-density plasma ($n_{\rm H} \sim 10^9$–$4.5 \times 10^{12}\,{\rm cm}^{-3}$). Furthermore, the UFO velocity is correlated with the X-ray luminosity, suggesting that the UFO in Mrk 1044 is accelerated by the radiation field. The emitting gas is located at a large range of distances from the SMBH and shows a blueshift of 2700–4500 km/s. By comparing with the discovered blueshifted emission lines in other AGN, we propose that the blueshift of emission lines is probably correlated with the source accretion rate, which can be verified with a large sample study.

Chapter 5

Ejection-accretion connection in a narrow-line Seyfert 1 AGN 1H 1934-063

Abstract

In this Chapter, we present a high-resolution spectral analysis of a simultaneous *XMM-Newton* and *NuSTAR* observation of a NLS1 AGN 1H 1934-063, to investigate outflows and their connection to the accretion. Through the time-resolved and flux-resolved X-ray spectroscopy, we discover a potentially variable WA and a relatively stable ultra-fast outflow (UFO, $v_{\rm UFO} \sim -0.075\,c$) with a mild ionization state ($\log(\xi/{\rm erg\,cm\,s^{-1}}) \sim 1.6$). The detected emission lines (especially a strong and broad feature around 1 keV) are of unknown origin and cannot be explained with emission from plasmas in photo- or collisional-ionization equilibrium. Such emission lines could be well described by a strongly blueshifted ($z \sim -0.3$) secondary reflection off the base of the equatorial outflows, which may reveal the link between the reprocessing of the inner accretion flow photons and the ejection. However, this scenario although very promising is only tentative and will be tested with future observations.

5.1 Introduction

By assuming that the escape velocity is equal to that observed in the outflowing gas, the fastest UFOs are thought to be launched in the inner region of the accretion disk, which is the same region that is probed by the inner-disk reflection spectroscopy. If the inner layer of the outflow is thick enough, probably at or above the Eddington limit, it may reflect part of the X-ray disk/corona emission producing a Doppler-shifted reflection signal. This scenario has been proposed to explain the strongly blueshifted Fe K emission line in a super-Eddington AGN Swift J1644+57 [157]. Therefore the reflection emission might reveal the physical properties of the wind launching region and improve our understanding of UFOs.

1H 1934-063 (hereafter 1H 1934; also known as IGR J19378-0617, SS 442, and IRAS 19348-0619) is a radio-quiet NLS1 [244] galaxy at a redshift of $z = 0.0102$ [301], which ranked seventh in 10–20 ks excess variance among 161 AGN in the *XMM-Newton* archive (CAIXA, [265]). It hosts a SMBH with a mass of $M_{\rm BH} = 3 \times 10^6\,M_{\odot}$, estimated from FWHM H$\beta$ [300, 207]. This source was twice observed by *XMM-Newton* in 2009 (18 ks, [244]) and 2015 (140 ks, [84]) joint with a 65 ks *NuSTAR* observation. 1H 1934 has two different

measurements of the black hole spin, $a_\star < 0.1$ [84] and $a_\star > 0.4$ [136], depending on whether a high density was adopted in the reflection model. Frederick et al. [84] also discovered a time lag ($\sim$20 s) of the disk reflection components behind the coronal power-law continuum, indicating a $9 \pm 4\,R_{\rm g}$ distance between the corona and the accretion disk.

The fact that this AGN is bright ($F_{\rm X} \sim 5 \times 10^{-11}\,{\rm erg/cm^2/s}$) and rapidly variable in the X-ray energy band may enable us to study any potential outflow and its variability. We present the high-resolution soft X-ray analysis based on the concurrent *XMM-Newton* and *NuSTAR* observation of 1H 1934 (PI: E. Kara). This Chapter is organized as follows. We present the data reduction procedure and products in Sec.5.2. Details on our analysis and results are shown in Sec.5.3. We discuss the results and provide our conclusions in Sec.5.4 and Sec.5.5, respectively.

5.2 Data Reduction and Products

5.2.1 Data Reduction

1H 1934 was simultaneously observed by *XMM-Newton* (Obs. ID: 0761870201) and *NuSTAR* (Obs. ID: 60101003002) on 2015 October 1-3 with a total exposure time of 140 and 65 ks, respectively. We utilize the data from *XMM-Newton*/EPIC and *NuSTAR*/FPMs to determine the X-ray broadband spectrum. The results of this paper are mostly based on the high-resolution RGS spectrum. The OM spectrum is also included to get the SED for photoionization modeling.

The *XMM-Newton* data are reduced with the Science Analysis System (SAS v19.1.0) and calibration files available by May 2021, following the standard SAS threads. In brief, the EPIC-pn and EPIC-MOS data are processed with EPPROC and EMPROC packages, respectively. The filtering criteria of the background flare contamination are set at the standard values of 0.5 and 0.35 counts/sec (in the 10–12 keV) for pn and MOS separately. We extracted EPIC source spectra from a circular region of radius 30 arcsec, and background spectra from a nearby source-free region of the same radius. We do not find any significant pile-up in both pn and MOS above 7 keV, which was marginally reported in Frederick et al. [84]. We stack MOS1 and MOS2 spectra to maximize the signal-to-noise. The EPIC spectra are grouped to over-sample the instrumental resolution by a factor of 3 and to a minimum of 30 counts per energy bin. The RGS data are processed with the RGSPROC tool, for which background flares are excluded by a threshold of 0.2 counts/sec. We extract the first-order RGS spectra in a cross-dispersion region of 1' width and the background spectra by selecting photons beyond the 98% of the source point-spread-function as default. We only use the

good time intervals common to both RGS 1 and 2 and stack their spectra for the high signal-to-noise. We regroup the RGS spectrum so that each bin is not narrower than 1/3 of the spectral resolution. Only the UVW2 (2120 Å) filter of OM operated during the observation, which is reduced using the OMICHAIN pipeline, including all necessary calibration processes.

NuSTAR observed 1H 1934 simultaneously with *XMM-Newton* for exposure times of roughly 65 ks per instrument. The reduction of the *NuSTAR* data is conducted following the standard procedures with the NuSTAR Data Analysis Software (NUSTARDAS v.2.0.0) and the updated calibration files from NuSTAR CALDB v20210427 using the NUPIPELINE task. The source spectrum is extracted from a circular region of radius 80 arcsec and the background spectrum is from a free-source region with a radius of 120 arcsec. The spectra are grouped to at least 30 counts per bin to have a sufficiently high S/N.

5.2.2 Light Curve

We show the EPIC-pn (0.3–10 keV) light curve with a time bin of 100 s and the corresponding count rate histogram in Fig.5.1. The light curve is color-coded according to the hardness ratio (HR=H/H+S, H: 2–10 keV; S: 0.3–2 keV). 1H 1934 presents a softer-when-brighter behavior during the observation with a strong flux dip by a factor of ~ 6, which was proposed to result from the strong light-bending effect while the change in accretion rate was excluded due to the stable UV flux [84]. To resolve any narrow and variable spectral features, we divide the entire light curve into two flux intervals, marked by the horizontal grey dash line, based on the intersection (21.5 c/s) between two Gaussians that were fitted to the count rate distribution (see red lines in the bottom panel of Fig.5.1). We caution that this cut is just a way to carve up the data, not indicating two processes [5]. Accordingly, the low- and high-flux spectra are extracted as well as the flux-resolved *NuSTAR* spectra at the exactly same time intervals. The ratio of total counts between the low- and high-flux is about 0.5.

5.3 Results

5.3.1 Spectral Variability

As we are mainly interested in the search for resolved spectral lines and evidence for outflows in 1H 1934, we start with a model-independent spectral-variability analysis, i.e. PCA and RMS analysis (described in Sec.2.4).

We apply the PCA method with the code of Parker et al. [247] to the RGS data to search for narrow spectral features. We adopt 10 ks time bins and 100 energy points in the logarithmic space between 0.3 and 10 keV. The light curve of *XMM-Newton* is accordingly

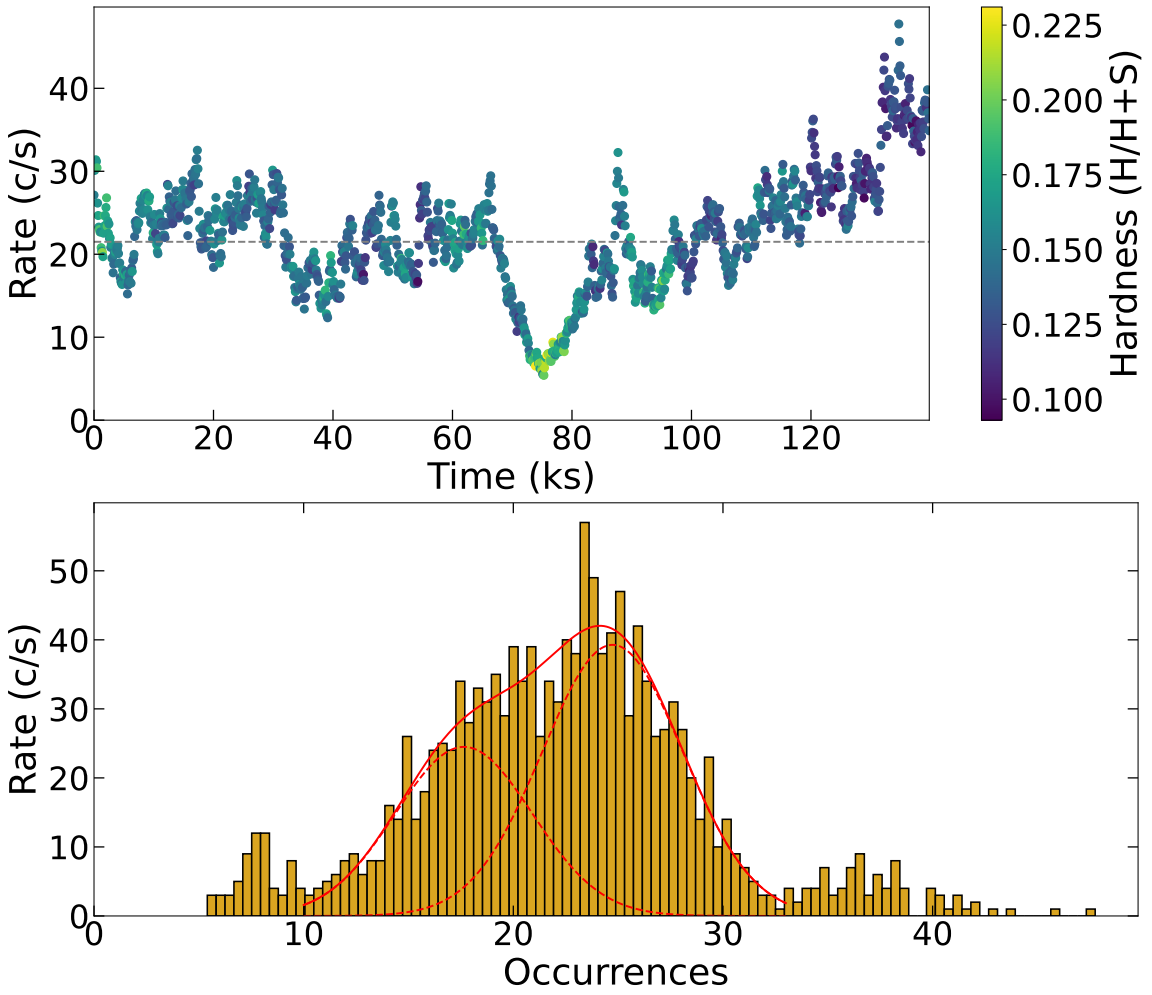

Fig. 5.1 The EPIC-pn (0.3–10 keV) light curve with a time bin of 100 s (*top*) and the corresponding count rate histogram (*bottom*). The light curve is coded according to the hardness ratio. S and H denote the counts in the soft and hard energy bands defined as 0.3–2 and 2–10 keV, respectively. The horizontal dashed grey line indicates the threshold of the flux intervals, which is determined by the intersection (21.5 c/s) between the two Gaussian lines fitted (red lines in the bottom panel) to the count rate histogram.

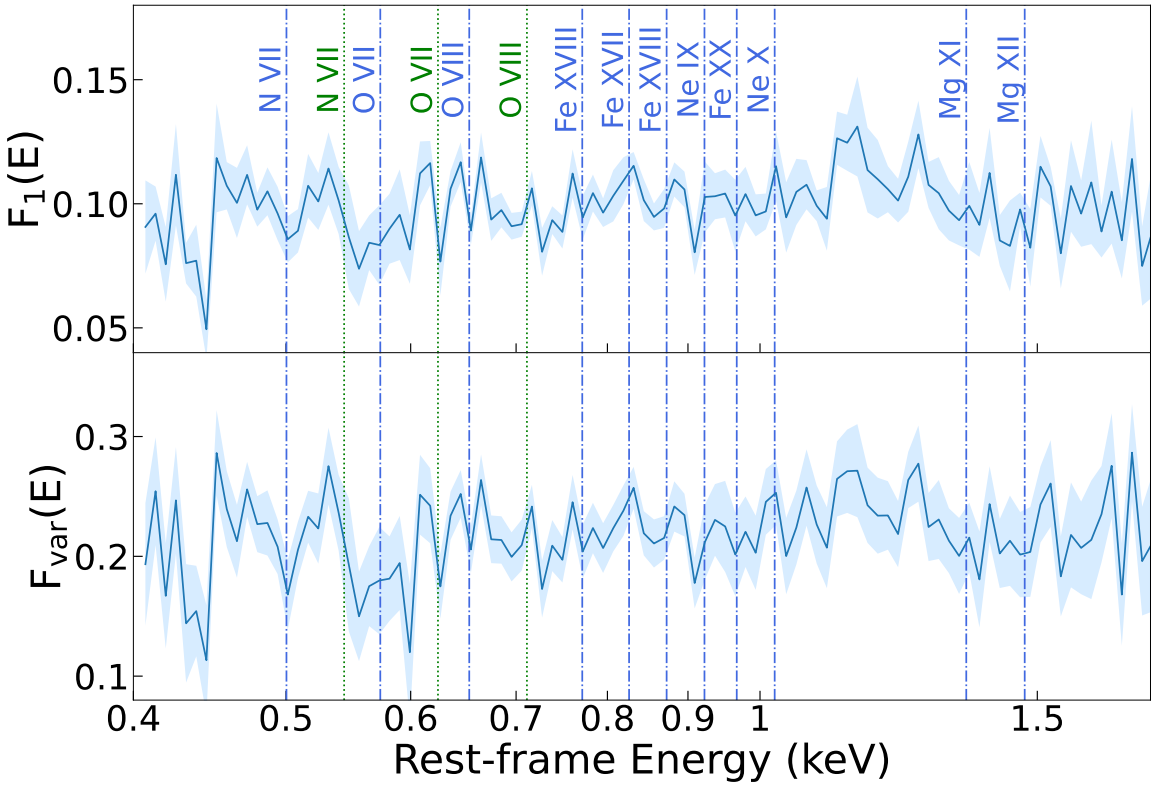

Fig. 5.2 The first component of PCA (*top*) and the fractional excess variability (*bottom*) of RGS spectrum are shown. The rest-frame positions of the ion transition lines among the RGS band are marked by the vertical *blue dashed-dotted* lines. Three highly blueshifted ($z \sim -0.078$) absorption features are also indicated with vertical *green dotted* lines.

split into 13 segments. The first principal component (PC1) of RGS is shown in the top panel of Fig.5.2. The RGS PC1 spectrum shows some dips in correspondence to the energies of the dominant X-ray transitions. Later on, we will attempt their identification through spectral modeling. However, some peaks do not always match such transitions, probably indicating the presence of Doppler-shifted variable lines.

We adopt the same spectra used for the PCA to compute the RMS spectrum. The result is displayed in the bottom panel of Fig.5.2. The shape of the RMS spectrum is remarkably similar to that of PCA, which only shows the amplitude of the *correlated* variability.

5.3.2 *XMM-Newton* and *NuSTAR* Continuum Modelling

We begin the broadband X-ray spectroscopy by fitting the time-averaged RGS, EPIC, and FPM spectra simultaneously using the XSPEC (v12.11.1) package [12]. The instrumental differences are taken into account by employing a variable cross-calibration factor (except for RGS fixed to unity, [204]). We adopt the χ^2 statistics and estimate all parameter uncertainties

at the 90% confidence level corresponding to $\Delta\chi^2 = 2.71$ in this Chapter. The luminosity calculations are based on the assumptions of $H_0 = 70\,\mathrm{km/s/Mpc}$, $\Omega_\Lambda = 0.73$ and $\Omega_M = 0.27$. After checking the consistency of residuals between EPIC and RGS spectra to the continuum model in soft energies, we use the RGS data between 0.4–1.77 keV and EPIC (pn+MOS) data between 1.77–10 keV for spectral fittings, because the relatively low resolution but higher count rate of EPIC may affect the detection and identification of atomic spectral features by increasing model degeneracies. Due to the background contamination, we limit the analysis of the *NuSTAR* (FPMA/B) spectra to the 3–30 keV energy band. The same selection applies to the flux-resolved spectra.

We adopt a similar model to the best-fit one found in Frederick et al. [84]: `tbabs*zashift *(diskbb+relxilllpCp)`, to explain the broadband continuum. Briefly, this model takes into account the galactic hydrogen absorption (`tbabs`) with the solar abundance calculated by Wilms et al. [367], the redshift of the source (`zashift`), the X-ray soft excess in the form of a multi-color disk blackbody (`diskbb`), and the coronal continuum as a power-law like component, plus the lamppost-geometry relativistic reflection (`relxilllpCp`, [94]), respectively. The galactic column density, $N_{\rm H}^{\rm Gal}$, is allowed to vary due to the discrepancy between $N_{\rm H}^{\rm Gal} = 1.5 \times 10^{21}\,\mathrm{cm^{-2}}$ [61] and $N_{\rm H}^{\rm Gal} = 1.06 \times 10^{21}\,\mathrm{cm^{-2}}$ [150]. The inner radius of the reflection component is assumed at the ISCO. Here we adopt a phenomenological model for the soft excess as its nature is still being debated [46, 99, 229, 371]. The result of the time-averaged spectrum reveals the primary continuum with a slope of $\Gamma = 2.15^{+0.01}_{-0.01}$, a soft excess characterized by a disk black-body with a temperature of $T_{\rm in} \sim 0.13\,\mathrm{keV}$, and a relativistic reflection component with a reflection fraction (a ratio of the intensity emitted towards the disk compared to that one escaping to infinity) of $f_{\rm Refl} = 0.62^{+0.08}_{-0.04}$. The inclination angle, ionization state and the iron abundance (in units of Solar abundance) of the disk are required to be $i \sim 39^\circ$, $\log(\xi/\mathrm{erg\,cm\,s^{-1}}) = 3.08^{+0.04}_{-0.04}$ and $A_{\rm Fe} = 6.6^{+2.0}_{-1.7}$ respectively. The corona is measured at a height of $4.7^{+2.2}_{-2.3}\,R_{\rm Horizon}$ above the SMBH with a spin of $a_\star = 0.21^{+0.35}_{-0.21}$ if we assume the corona as a compact point. All of these are similar to previous results [84, 356]. It is noticed that Jiang et al. [136] adopted a high-density reflection model without `diskbb` to fit the same data and obtained a high spin value of $a_\star > 0.45$ with a similar abundance of $A_{\rm Fe} = 5.9^{+0.6}_{-1.4}$ and a disk density of $\log(n_{\rm e}/\mathrm{cm^{-3}}) \sim 17.7$ (fixed at $\log(n_{\rm e}/\mathrm{cm^{-3}}) = 15$ in `relxilllpCp`). We tried the same high-density model for our spectra and found that the fits are much poorer ($\Delta\chi^2 \sim 475$) than the current model, perhaps because they only consider the EPIC spectrum above 0.5 keV, while we extend that to 0.4 keV and the high-density reflection cannot explain that band well.

The same best-fit model applies to the flux-resolved spectra, with several parameters linked to the time-average results, including the inclination angle, black hole spin, iron

Table 5.1 Best-fit parameters of the 1H 1934-063 time-average and flux-resolved spectra modeling.

Description	Parameter	avg	low-flux	high-flux
`tbabs`	$N_{\rm H}^{\rm Gal}$ (10^{21} cm^{-2})		$2.1^{+0.1}_{-0.1}$	
`diskbb`	$T_{\rm in}$ (keV)	$0.130^{+0.005}_{-0.005}$	$0.129^{+0.004}_{-0.004}$	$0.133^{+0.003}_{-0.003}$
	$N_{\rm BB}$ (10^4)	$1.2^{+0.4}_{-0.3}$	$0.9^{+0.2}_{-0.2}$	$1.3^{+0.2}_{-0.2}$
`relxilllpCp`	h ($R_{\rm Horizon}$)	$4.7^{+2.2}_{-2.3}$	< 2.9	$6.4^{+3.2}_{-2.4}$
	$a_\star$ (cJ/GM^2)		$0.21^{+0.35}_{-0.21}$	
	i (deg)		$39.0^{+1.5}_{-1.2}$	
	Γ	$2.15^{+0.01}_{-0.01}$	$2.09^{+0.01}_{-0.01}$	$2.18^{+0.01}_{-0.01}$
	$\log(\xi/{\rm erg\,cm\,s^{-1}})$	$3.08^{+0.04}_{-0.04}$	$3.03^{+0.05}_{-0.06}$	$3.12^{+0.06}_{-0.05}$
	$A_{\rm Fe}$		$6.6^{+2.0}_{-1.7}$	
	$kT_{\rm e}$ (keV)		400^{+0}_{-317}	
	$f_{\rm Refl}$	$0.62^{+0.08}_{-0.04}$	$0.84^{+0.08}_{-0.10}$	$0.53^{+0.07}_{-0.07}$
	$N_{\rm refl}$ (10^{-3})	$0.19^{+0.14}_{-0.04}$	$2.4^{+8.6}_{-2.1}$	$0.19^{+0.05}_{-0.02}$
broadband	χ^2/d.o.f.	2143/1564	1552/1341	1943/1455
`xstar_abs1`	$N_{\rm H}$ (10^{20} cm^{-2})	$2.0^{+0.5}_{-0.4}$	$5.9^{+2.5}_{-2.6}$	$2.1^{+0.6}_{-0.5}$
(WA)	$\log(\xi/{\rm erg\,cm\,s^{-1}})$	$1.68^{+0.12}_{-0.20}$	$2.42^{+0.09}_{-0.13}$	$1.71^{+0.06}_{-0.18}$
	$z_{\rm LOS}$ (10^{-4})	$-0.78^{+3.6}_{-3.6}$	$-2.9^{+6.5}_{-7.7}$	$-0.1^{+3.7}_{-4.5}$
broadband+abs1	χ^2/d.o.f.	2029/1561	1518/1338	1857/1452
`xstar_abs2`	$N_{\rm H}$ (10^{19} cm^{-2})	$6.6^{+4.1}_{-2.1}$	$7.9^{+6.4}_{-4.3}$	$5.1^{+3.2}_{-2.3}$
(UFO)	$\log(\xi/{\rm erg\,cm\,s^{-1}})$	$1.6^{+0.1}_{-0.1}$	$1.8^{+0.4}_{-0.4}$	$1.5^{+0.2}_{-0.3}$
	$z_{\rm LOS}$ (10^{-2})	$-7.75^{+0.09}_{-0.13}$	$-7.75^{+0.26}_{-0.19}$	$-7.83^{+0.17}_{-0.38}$
broadband+abs1+abs2	χ^2/d.o.f.	1985/1558	1502/1335	1834/1449

abundance, and the temperature of the corona, which are not expected to vary over a few hours. The details of fits are shown in Tab.5.1. As explained by Frederick et al. [84], the decreasing corona height and ionization parameter plus the increasing reflection fraction during the low-flux state could be attributed to the light-bending effect, where the corona may drop down closer to the accretion disk causing the dip in flux.

5.3.3 Gaussian Line Scan

To search for any strong and narrow features upon the continuum, we perform a Gaussian line scan, described in Sec.2.3.1, over the continuum in the *XMM-Newton* energy band. We ignore *NuSTAR* data due to its lower spectral resolution. We fit a Gaussian line spanning the 0.4–10 keV range with a logarithmic grid of energy steps. The grid of the line width σ_v in km/s ranges from 500 to 5000 km/s and the corresponding line width in keV is $\sigma_E = \frac{\sigma_v}{c} E$. For the sake of the balance between the computational cost and the resolving power, we employ different numbers of points N_v for each line width so that the product of σ_v and N_v equals to 10^6.

The results of the scan over the time-averaged and flux-resolved spectra are expressed as the square root of $\Delta\chi^2$ times the sign of the normalization, shown in Fig.5.3. This quantity provides a rough estimate of the single trial detection significance of each Gaussian line (ignoring the look-elsewhere effect). The zoom-in result for the time-averaged RGS spectrum is shown in the top panel of Fig.5.4. The *grey* region marks the 3σ significance level. We mark the rest-frame positions of the main ionic transition lines within the *XMM-Newton* band with the vertical *blue dashed-dotted* lines. Coincidentally, we identify several absorption lines at their rest-frame energies: N VII, O VII, O VIII, Fe XVIII, and Ne IX. Other unidentified lines are also marked as the reference. As for the other more or less significant absorption lines, three of them could be identified as N VII, O VII, and O VIII blueshifted by $\sim$23400 km/s (corresponding to $z \sim -0.078$), presented by the vertical *green dotted* lines. Compared with the absorption features, the emission lines seem to be blue- or red-shifted and are not easy to identify as the emission from the same outflowing gas. In particular, there is a strong broad emission around 1 keV, halfway between the rest-frame positions of Fe XX and Ne X. We also find that the residuals and normalization of the Gaussian lines appear to be slightly stronger in the high-flux spectrum, although the trend cannot be confirmed due to the limited statistics.

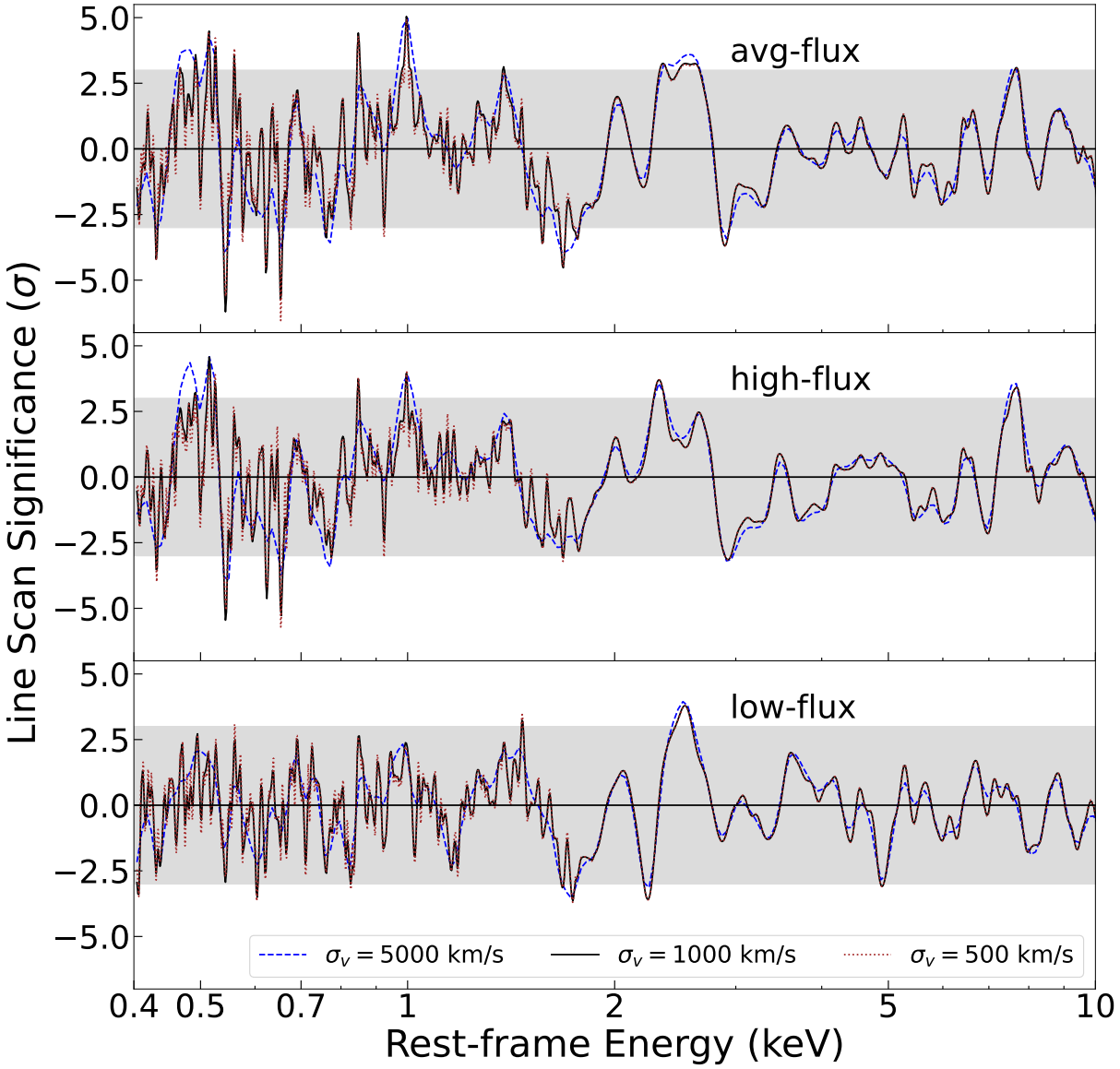

Fig. 5.3 The results of the line search over the *XMM-Newton* broadband time-average (*top*) and flux-resolved (*middle* and *bottom*) spectra in the AGN rest frame. The line width in velocity σ_v ranges from 500 to 5000 km/s. The significance is expressed with the square root of $\Delta\chi^2$ times the sign of the Gaussian normalization. The *grey* region corresponds to a 3σ value of the single trial significance.

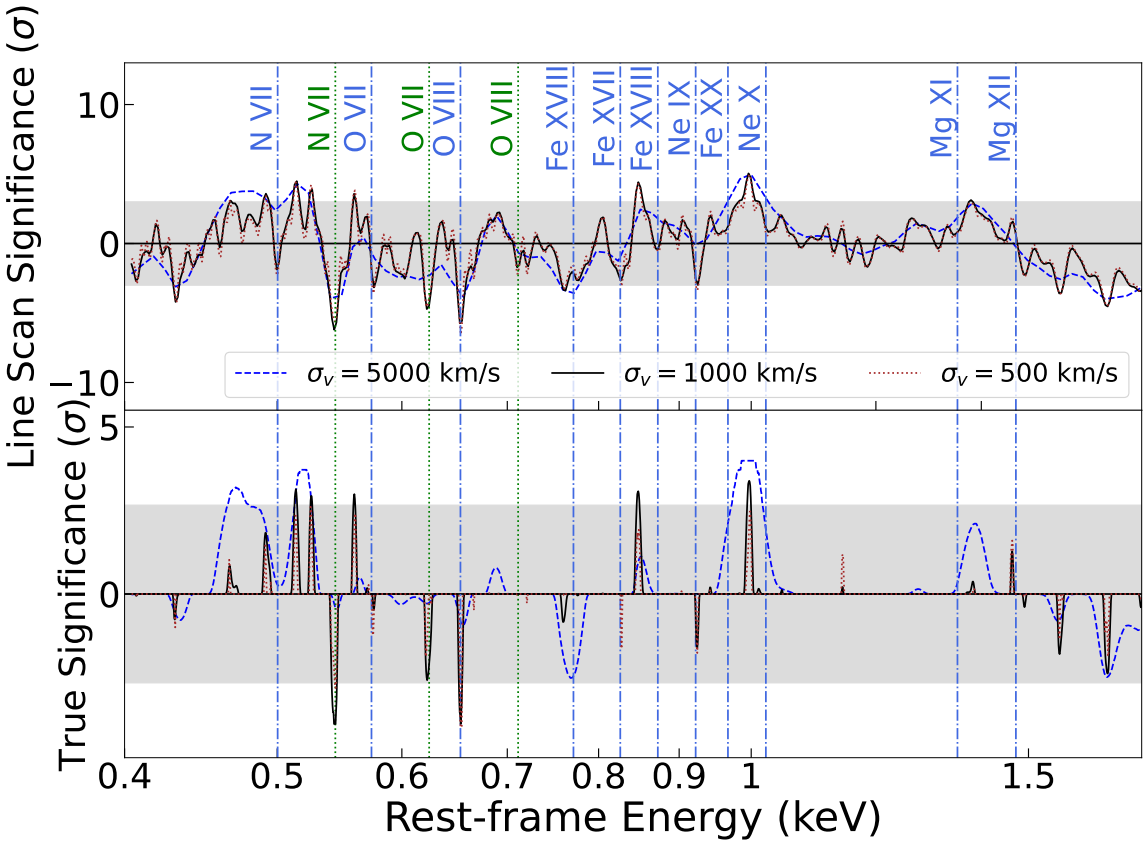

Fig. 5.4 The single trial significance obtained from the Gaussian line scan with different line widths over the RGS spectrum is displayed in the *top* panel. The *grey* region marks the significance 3σ. The true significance of the residuals (*bottom*) is obtained from the MC simulations with the same line widths. The *grey* region represents 99% significance level.

5.3.4 Cross-Correlation Based Monte Carlo Simulation

Although the Gaussian line scan is powerful in locating any possible spectral lines, many spurious features might appear significant due to the look-elsewhere effect [352]. To account for this effect, we perform the cross-correlation-based MC method, described in Sec.2.3.3. Since we are interested in the resolved soft X-ray features, the cross-correlation method is only applied to the time-average RGS spectrum.

We perform 10000 simulations with the `fakeit` tool in XSPEC based on the best-fit continuum model. A set of Gaussian line models to be cross-correlated is generated, with a centroid energy spanning over the RGS band with a logarithmic grid of 2000 points, a line width ranging from 0 to 5000 km/s, and a normalization fixed at unity. The true significance of lines is shown in the bottom panel of Fig.5.4. The true significance confirms the existence of absorption lines including O VIII, blueshifted N VII, and O VII. We also find five emission lines above the 99% significance level, particularly the $\sim$1 keV emission, which is also found in Sec.5.3.3 and will be investigated in Sec.5.3.6. We caution that lines with a weak true significance are not necessarily fake as the true significance provides a very conservative approach by assuming the worst case of a single and independent line with any shift in the observed spectrum. The photoionization model is therefore required to model these lines simultaneously.

5.3.5 Search For Outflows

In this section, we employ the photoionization code XSTAR [151], to describe the absorption features in 1H 1934 spectrum and to investigate the outflow variability during the observation. XSTAR computes the physical conditions and synthetic spectra of the gas photoionized by a given radiation field. It calculates the intensity for a large number of lines and enables fits to data through the constructed table of synthetic spectra.

The intrinsic SED of 1H 1934 input into XSTAR is computed from the UV/optical to hard X-ray energies by adding the OM data. The UV/optical fluxes are described by an additional `diskbb` component characterized by a temperature of $\sim 12\,\mathrm{eV}$. The interstellar extinction ($E_{\mathrm{B-V}} = 0.293$, [299]) has been taken into account. The time-averaged and flux-resolved SEDs are shown in Fig.5.5 as compared with other Seyfert galaxy SEDs, where 1H 1934 SEDs look similar to that of IRAS 13224-3809. Accordingly, we estimate the accretion rate by measuring the bolometric luminosity from the time-averaged SED (10^{-3}–10^{3} keV), which is $L_{\mathrm{bol}} \sim 1.725 \times 10^{44}\,\mathrm{erg}$. The accretion rate is thus high since we obtain $\dot{m} = L_{\mathrm{bol}}/L_{\mathrm{Edd}} \sim 0.40^{+0.91}_{-0.27}$ if we adopt a SMBH mass of $3 \times 10^{6}\,M_{\odot}$ with a typical $\sim$0.5 dex uncertainty [300, 207].

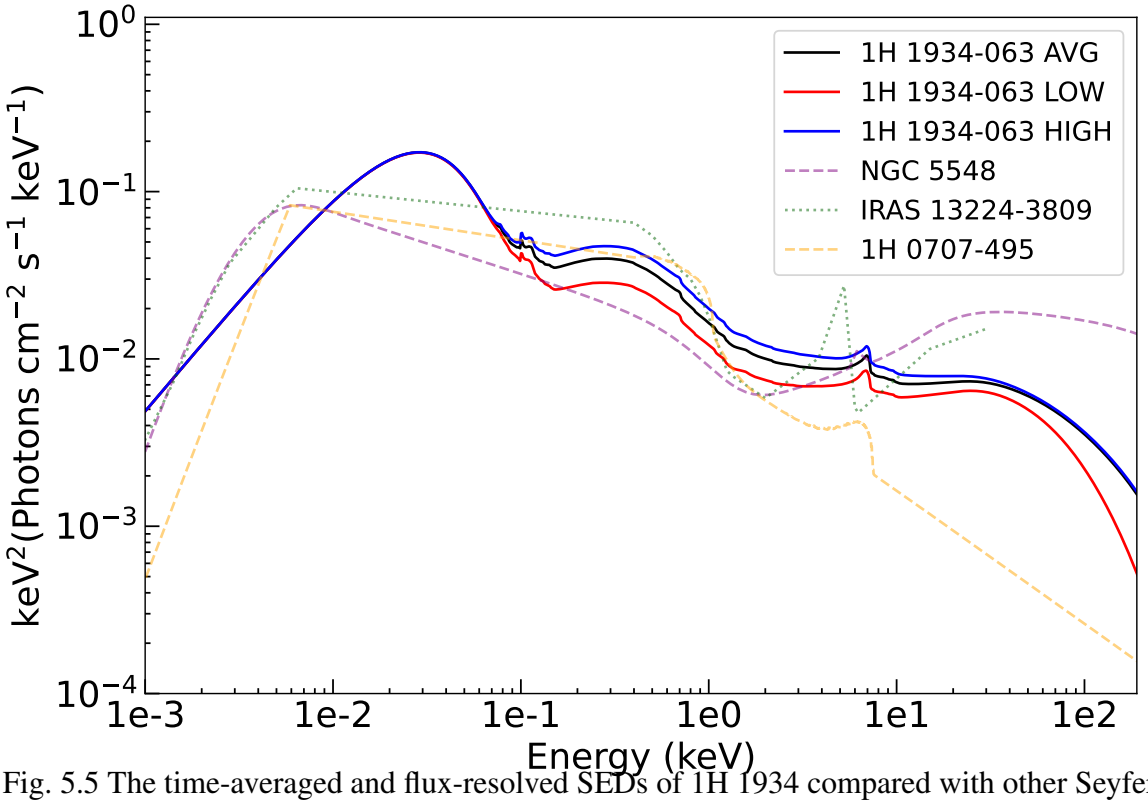

Fig. 5.5 The time-averaged and flux-resolved SEDs of 1H 1934 compared with other Seyfert galaxies (NGC 5548, [228]; IRAS 13224-3809, [138]; 1H 0707-495, [372]). The UV/optical fluxes are predicted by a color-corrected ($E_{\mathrm{B-V}} = 0.293$, [299]) additional `diskbb` characterized by a temperature of $\sim 12\,\mathrm{eV}$.

For the modeling of outflows in flux-resolved spectra, we still employ the XSTAR model generated by the time-averaged SED because the SED does not significantly vary during the observation. The input SED ranges from 1 eV to 30 keV to avoid the possible effects from > 30 keV band, which cannot be constrained with the available data. We adopt a grid that has a turbulence velocity of 100 km/s (due to narrow lines detected in Fig.5.3) and covers a wide range of ionization states ($\log(\xi/\mathrm{erg\,cm\,s^{-1}}) = 0$–$6$) and column densities ($N_{\rm H}\,(\mathrm{cm^{-2}}) = 10^{19}$–$10^{24}$) to compute the XSTAR table model. The code returns one emission and one absorption spectrum table, and here we use the absorption component (`XSTAR_ABS`) for modeling. In Sec.5.3.6, we will use the emission component (`XSTAR_EM`) to model emission features.

5.3.5.1 Best-fit Outflow Model

To locate the global best-fit solution, we build a systematic scan over a large grid of the parameter space of `XSTAR_ABS` before directly fitting to the spectra, described in Sec.2.3.2. We create a multi-dimension grid of the $\log\xi$ (0–6 with $\Delta\log\xi = 0.12$) and $z_{\rm LOS}$ (from -0.25 to 0.02 with $\Delta z_{\rm LOS} = 0.001$), and allow $N_{\rm H}$ to be free.

The scan result for the time-averaged spectrum is shown in the left panel of Fig.5.6. The line-of-sight redshift is relativistically corrected. The search achieves a very strong detection ($\Delta\chi^2 \sim 120$) of a mildly ionized ($\log(\xi/\mathrm{erg\,cm\,s^{-1}}) \sim 1.7$) absorber at the rest frame of AGN ($v \sim 0$). The spectral fit reveals the column density of $N_{\rm H} = 2.0^{+0.5}_{-0.4} \times 10^{20}\,\mathrm{cm^{-2}}$. These properties suggest that this solution corresponds to a common WA as those found in other AGN [58, 146]. It is noted that there are several secondary peaks ($v < -0.05\,c$) in the plot, indicating the presence of a fast ionized outflow component in the spectrum. However, the secondary peaks might not be independent of the primary WA as they might explain the same residuals with different models.

We, therefore, perform a further `XSTAR_ABS` scan over a new baseline model, which includes a best-fit WA and the broadband continuum. The searched parameter space remains the same. The result is shown in the right panel of Fig.5.6. There is a less strong but still significant detection ($\Delta\chi^2 = 48$) of a secondary component, which is an ultra-fast (relativistically corrected velocity, $v \sim -0.075\,c$) outflow with a similar ionization parameter ($\log(\xi/\mathrm{erg\,cm\,s^{-1}}) \sim 1.6$). With such high $\Delta\chi^2$ statistics, MC simulations are redundant. The fitting results of two `XSTAR_ABS` components over the time-averaged spectrum are presented in the third column of Tab.5.1. The column density of the UFO ($N_{\rm H} \sim 6.6 \times 10^{19}\,\mathrm{cm^{-2}}$) is significantly lower than that of the WA, resulting in weaker spectral features. The spectral features of the WA are mainly located at the rest frame of N VII, O VII and O VIII 1s-2p lines, while the main absorption lines of the UFO are the blueshifted N VII and O VII and

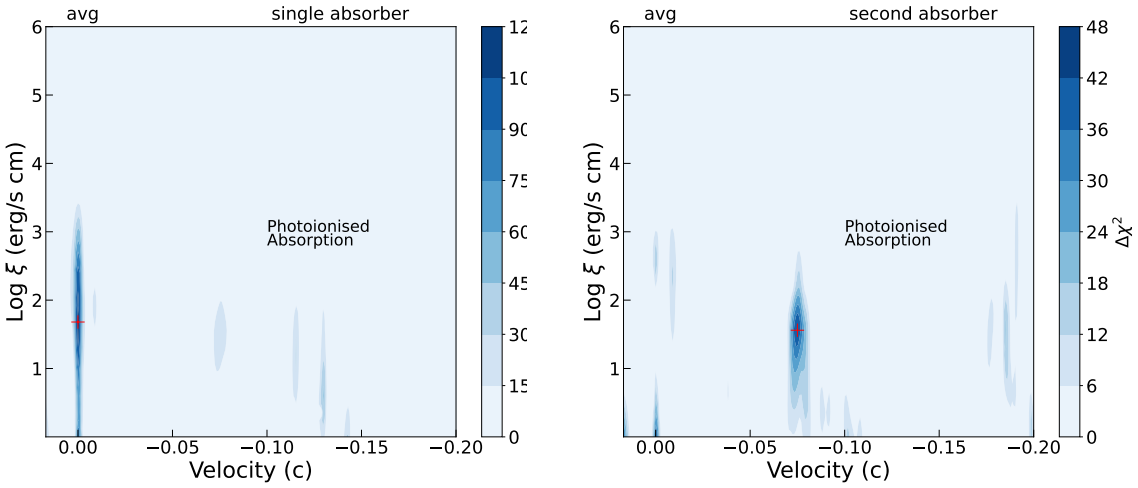

Fig. 5.6 Photoionization absorption model search for the time-averaged spectrum of 1H 1934 over the broadband continuum model (*left*) and with the addition of a WA (*right*) in the AGN rest frame. The velocity on the X-axis is relativistically corrected. The color illustrates the statistical improvement after adding an absorbing model. The best-fit solution is marked by a red cross.

a weaker O VIII, marked in Fig.5.4. Such differences illustrate that the best-fit value of the UFO ionization parameter might be lower than that of the WA, although it cannot be confirmed within the uncertainties.

5.3.5.2 Outflow variability

As for the flux-resolved spectra, we directly fit them with the best-fit model (continuum plus two absorbers), and the parameters are shown in Tab.5.1. The statistical improvement of the high-flux spectrum is larger than that of the low-flux one, which is compatible with what we found in the line scan result (see Sec.5.3.3). Although the UFO could be regarded as stable during the observation within the uncertainties, the WA slightly varies from the low- to high-flux state in the column density ($N_{\rm H}(10^{20}\,{\rm cm}^{-2})$ from $5.9^{+2.5}_{-2.6}$ to $2.1^{+0.6}_{-0.5}$) and the ionization parameter ($\log\xi$ from $2.42^{+0.09}_{-0.13}$ to $1.71^{+0.06}_{-0.18}$) at 90% confidence level. It would be interesting if this is real and this variability comes from the response to the change in source luminosity (or to the interaction of the UFO with the surrounding medium - should the WA represent the UFO shock front), as the WA is usually expected to be stable far from the central SMBH and the response timescale should be much larger than dozens of hours.

To investigate the validity of this discovery, we have checked the results of the same wind search on the flux-resolved spectra. The ionization parameter of the WA in both spectra ranges from 0 to 3, suggesting that the observed variation might be artificial if we slightly

loosen the confidence level of the parameters. However, the possibility of a variable WA cannot be excluded without more observations. The statistical improvements of the UFO detection in low- and high-flux spectra are comparable ($\Delta\chi^2 \sim 16$ and ~ 24 respectively), rather than the dramatic change in those of the WA ($\Delta\chi^2 \sim 34$ and ~ 85 separately). The main change in the outflow during the exposure therefore seems to originate from the WA. More observations are needed to confirm this.

5.3.6 Emission Line Modelling

In this section, we explore the nature of the unknown emission, especially for the line around 1 keV, in the time-averaged spectrum of 1H 1934 for enough counts. Compared to the absorption, the emission is more complex and highly depends on the geometry, as it collects all photons that are not directed along the LOS towards the source. None of the emission lines detected in Fig.5.4 are at the rest-frame of any known strong photoionization emission lines, implying that either they are Doppler-shifted photoionization lines or they are produced by other processes. The baseline model used in this section is the broadband continuum plus two absorbers adopted in Sec.5.3.5.

5.3.6.1 Photoionization Emission

It is natural to expect photoionized emission in the spectrum after finding two photoionization absorption components. We hence launch a physical emission model scan on the spectrum fitted with the new baseline model, where we adopt the XSTAR emission spectrum table (`XSTAR_EM`) generated in Sec.5.3.5. The range of the searched grid of the ionization parameter is the same as that of the absorption component, while the redshift spans between -0.1 and 0.1 as we are not sure whether the emission lines are blue- or red-shifted and do not expect a high velocity of emitting gas. The results are shown in Fig.5.7, presenting a series of peaks at different shifts with weak detection statistics.

The best-fit solution ($\Delta\chi^2 \sim 28$) of `XSTAR_EM` requires a column density of $N_{\rm H} < 3.3 \times 10^{23}\,{\rm cm}^{-2}$, an ionization parameter of $\log(\xi/{\rm erg\,cm\,s^{-1}}) = 4.1^{+0.2}_{-0.1}$, and a redshift of $z_{\rm LOS} = 1.5^{+5.2}_{-11.4} \times 10^{-4}$. The velocity is consistent with the rest frame, and the ionization parameter is over two orders of magnitude higher than that of the absorption component, indicating that the light elements are fully ionized and the emission may originate from a different plasma than the absorbing gas. The best-fit spectrum is shown in the top panel of Fig.5.8, where the contribution of `XSTAR_EM` is negligible in RGS band due to the high ionization state. We have checked that `XSTAR_EM` mainly explains the high-ionization features such as Fe XXV/XXVI. Even if we add another photoionization emission component, the secondary

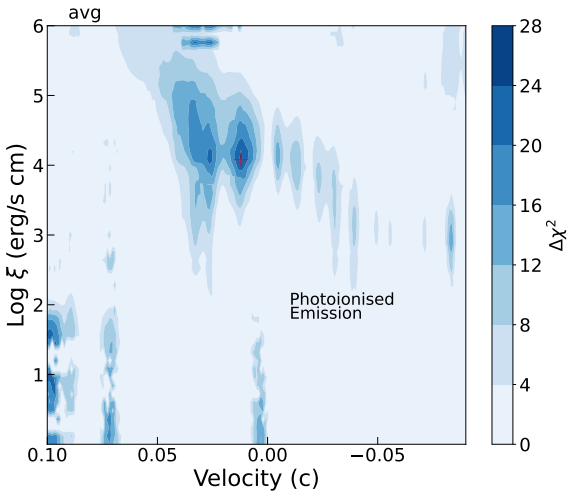

Fig. 5.7 Photoionization emission model search for the time-averaged spectrum for the broadband model plus two absorbers, similar to Fig.5.6.

emitter only explains some putative redshifted ($z_{\rm LOS} \sim 0.0024$) O VII lines at a low ionization state ($\log(\xi\,/{\rm erg\,cm\,s^{-1}}) < 1.6$) with an even weaker improvement ($\Delta\chi^2 \sim 13$). Regardless of the detection significance and plausibility of the highly photoionized emission, it seems that photoionization cannot well model the broad line around 1 keV, even if we tried using a convolution model (`gsmooth` in XSPEC) to broaden the line width of `XSTAR_EM`.

5.3.6.2 Collision Ionization Emission

Collision ionization provides an alternative origin since it could predict emission lines around 1 keV (Fe L-shell transitions) stronger than photoionization [166]. We adopt the well-known `bvapec` model in XSPEC with Solar abundance. This reproduces the emission spectrum of a plasma in collisional ionization equilibrium (CIE), which is characterized by its temperature and turbulent velocity. The best-fit model requires a temperature of $kT_{\rm e}^{\rm CIE} = 1.18^{+0.11}_{-0.09}\,{\rm keV}$, a velocity broadening of $\sigma_v^{\rm CIE} < 7500\,{\rm km/s}$, and a redshift of $z_{\rm LOS}^{\rm CIE} = 0.011^{+0.001}_{-0.001}$. The corresponding spectrum is presented in the middle panel of Fig.5.8, revealing a series of emission lines around 1 keV. The strongest and over-predicted line is Fe XXI with a rest-frame wavelength of 12.286 Å (i.e. 1.009 keV). A fit with a free Fe abundance does not provide better statistics. The remarkable fit improvement ($\Delta\chi^2 \sim 42$) suggests that the collision ionization seems to be a promising explanation for the 1 keV emission but it overpredicts the emission around 1 keV.

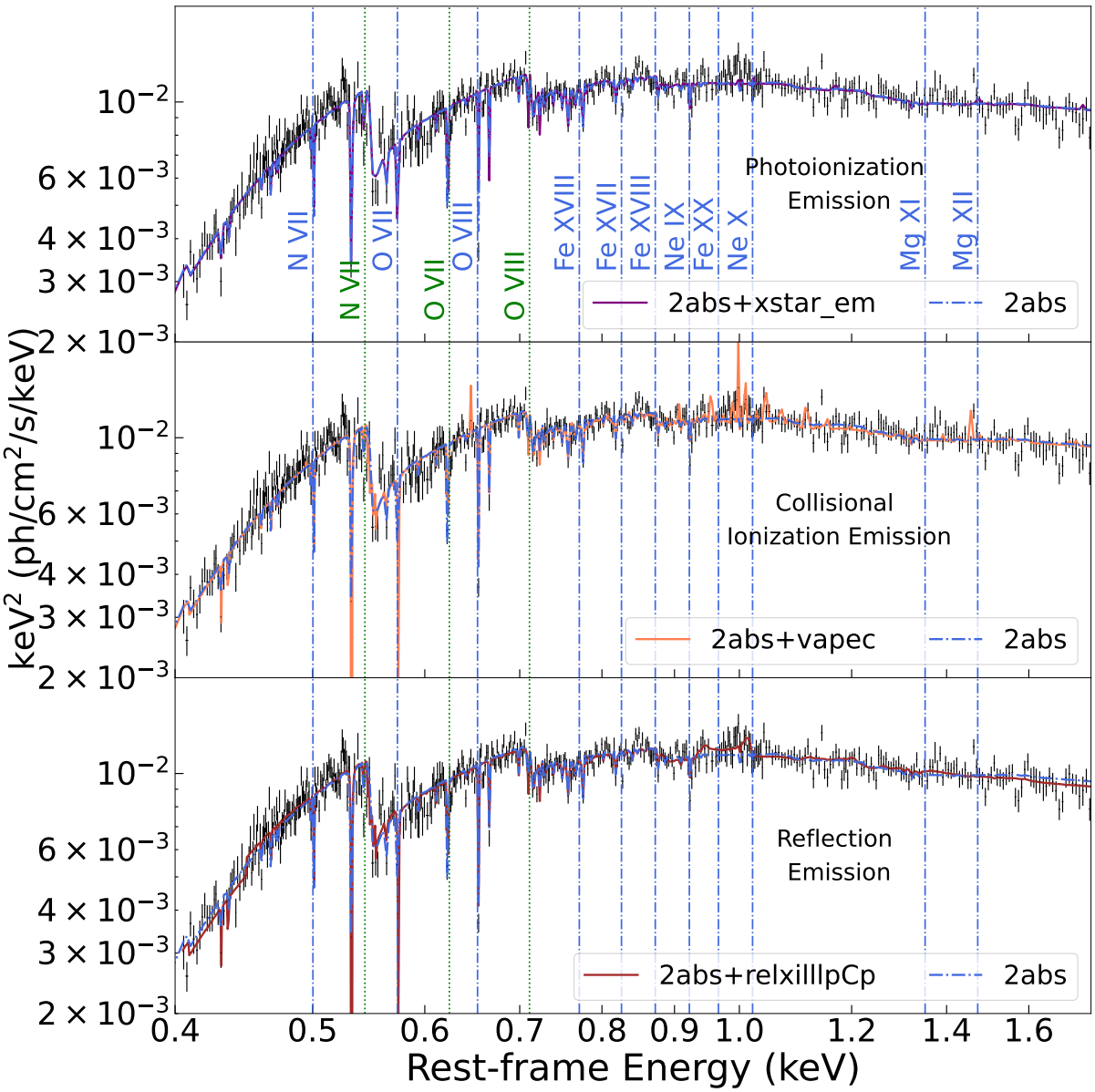

Fig. 5.8 Fits with different emission models, including photo- (*top*), collision-ionization (*middle*), and reflection (*bottom*) for the time-averaged RGS spectrum. The baseline model is the broadband continuum plus two absorption components (see Tab.5.1).

5.3.6.3 Emission of a secondary reflector

Fluorescence from the disk-reprocessing of the inner coronal photons is another potential origin, as the time-averaged spectrum is dominated by the reflection ($f_{\rm Refl} \sim 0.6$). The reflection lines in a rotational disk are anticipated to have asymmetric double peaks where the blue wing is stronger due to the relativistic beaming (see details in Sec.2.2.1.2).

Initially, we utilized a phenomenological model, `diskline`, to describe line emission from a relativistic accretion disk. We adopted two disk line components to model the line around 1 keV and the possible N VII emission at 0.5 keV, because of the indicative wings around these two energies (see Fig.5.4). The inclination angle is linked to the primary reflection component angle. The outer radius is fixed at $1000\,R_{\rm g}$, and the inner disk radii of these two components are tied together as we do not expect their positions to be significantly different. The fit returns a $\Delta\chi^2 \sim 80$ improvement with a inner radius of $56^{+10}_{-11}\,R_{\rm g}$. The emissivity index is around 3, consistent with the solution in Newtonian spacetime. The best-fit centroid of the higher energy line is at $0.996^{+0.027}_{-0.046}$ keV, which agrees with the Gaussian line fit.

Then we replace the phenomenological disk line models with a physical model, another `relxilllpCp` component. The parameters are linked to those of the first `relxilllpCp` component, except for the free inner disk radius, ionization parameter, and normalization. The redshift is also allowed to vary because the strongest reflection line in the soft band is O VIII and we thus tested whether such a strong 1 keV emission could be a blueshifted O VIII, which is plausible for reflection in the inner region of a rapidly rotational disk or the base of the wind. The best fit reveals a moderately ionized reflector with a strong blueshift of $z^{\rm Rel}_{\rm LOS} \sim -0.31$, resulting in a $\Delta\chi^2 \sim 32$ improvement. A reflection component that is blueshifted by $\sim$0.3 would predict a strong broad iron line at ~ 8 keV. Such a feature is not observed in the spectrum, and thus the normalization of this component is low, and thus under-predicts the 1 keV line, as well.

However, the fit highly improves if we free the spectral slope in the second reflection model. A much softer ($\Gamma > 3.2$) continuum irradiating the secondary reflector results in a remarkable statistical improvement of $\Delta\chi^2 \sim 75$, requiring a blueshifted ($z^{\rm Rel}_{\rm LOS} = -0.332^{+0.002}_{-0.002}$) ionized ($\log(\xi/{\rm erg\,cm\,s^{-1}}) = 2.50^{+0.25}_{-0.11}$) reflector with an inner radius of $R_{\rm in} = 186^{+66}_{-106}\,R_{\rm g}$. The best-fit RGS spectrum is illustrated in the bottom panel of Fig.5.8. The main contribution of the secondary reflector to the modeling is the flux around 1 keV with a double peak profile, which is produced by a distant inner radius. The requirement for such a soft continuum implies that the emission lines are from a gas irradiated by both the hot corona and the soft excess, no matter whether the soft excess originates from a warm corona or the relativistic reflection. We attempted to replace the `diskbb` with a Comptonization model `nthComp` and

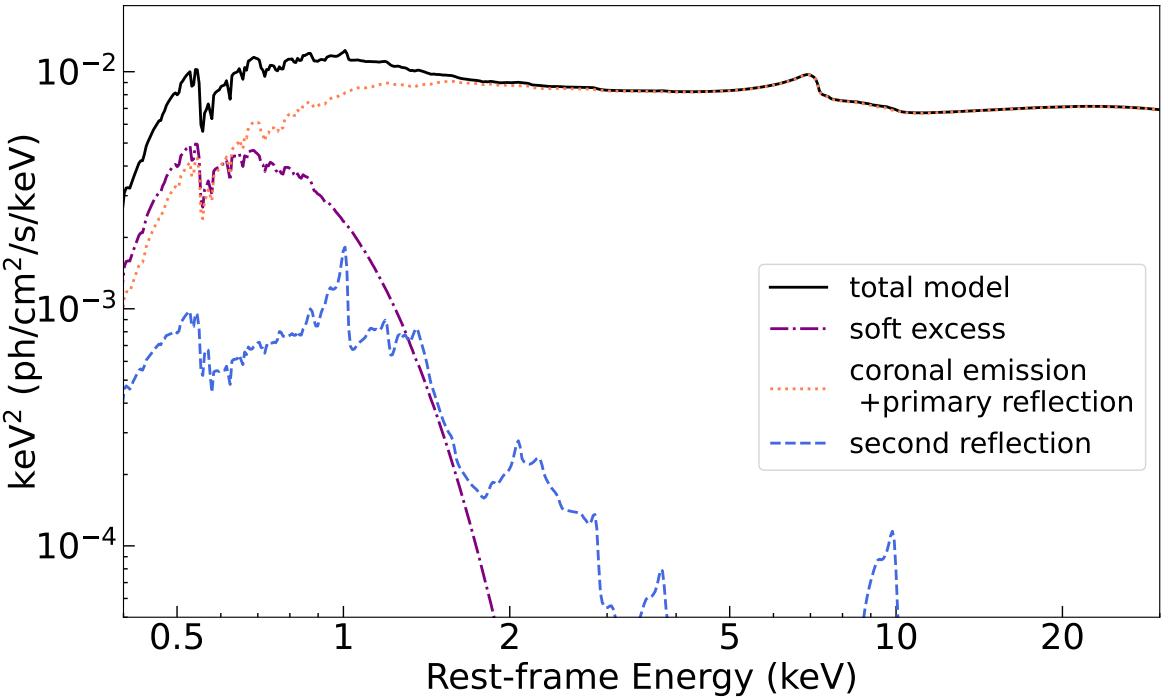

Fig. 5.9 Model components of the best-fit model derived in section **??**. The black solid line is the total contribution of the model components. The purple, orange, and blue dash lines are the soft excess, coronal emission plus the primary relativistic reflection, and the secondary reflection respectively.

adopted this as the radiation field of the second reflector, to investigate the origin of the X-ray radiation field. We did not find any significant improvement with respect to the disk model and thus preferred to keep the `diskbb` model as the detailed investigation of the radiation field for the secondary reflection is beyond the scope of this paper.

Interestingly, a further statistical improvement could be achieved by allowing the inclination angle of the second reflection to vary. We obtain a lower inclination angle ($i = 26^{+3}_{-3}$ deg), a smaller inner radius ($R_{\rm in} = 35^{+17}_{-27} R_{\rm g}$) with a $\Delta\chi^2/{\rm d.o.f.} = 7/1$ improvement, corresponding to the significance of $\sim 2.7\sigma$. The model components are illustrated in Fig.5.9. The smaller inner radius leads to a skewed broadened line profile due to the relativistic effects rather than a double-peak profile, but the modeling for the 1 keV emission is even better according to the statistics. As a result, it seems that a strongly blueshifted reflection component with a soft continuum is a physically promising explanation, and the differences caused by the free inclination angle suggest a more complex scenario for the reflection, which is discussed in Sec.5.4.2.

5.4 Discussion

5.4.1 Multi-phase Absorber

Through the line scan and the MC simulations, we detect and confirm several absorption lines at the rest-frame positions of ion transitions and three blueshifted features in the RGS spectrum of 1H 1934, which respectively correspond to a WA and a UFO. The ionization states of these two absorbers are similar ($\log \xi \sim 1.6$–1.7), while the velocities differ.

Tombesi et al. [337] suggested that the UFO and the WA originate from a single large-scale wind, where the UFO is denser, faster, and more ionized than the WA. However, the discovered UFO in 1H 1934 is not highly ionized and even less dense than the WA, inconsistent with this scenario. Alternatively, Pounds and King [271] considered another explanation that the WA is produced in the shock where a UFO collides with the surrounding medium. In this case, the weakly ionized UFO discovered in 1H 1934 could be explained by the entrained UFO, which is pushed at a velocity comparable to that of the UFO and retains its ionization state and column density of the surrounding medium. Such E-UFO has also been observed in IRAS 17020+4544 and PG 1114+445, where there is evidence for three kinds of outflows, including WAs, E-UFOs, and UFOs [309, 314]. E-UFOs could be the missing link between the high-ionization UFOs and the slow WAs.

Apart from the outflow explanation, an alternative scenario has been proposed that the highly blueshifted absorption lines seen in the spectrum might be the results of the reflection component passing through a thin, highly-ionized absorbing layer at the surface of the accretion disk (e.g. PG 1211+143 and IRAS 13224-3809, [93, 75]). It should be noted that only the part of the absorber in front of the inner reflected emission contributes to the absorption. The observed velocity originates from the projected Keplerian motion along our LOS, $v_{\rm LOS} = v_{\rm abs}\sin\theta \approx v_{\rm abs}R_{\rm em}/R_{\rm abs}$, where $v_{\rm abs}$ is the Keplerian velocity of the absorber, $v_{\rm abs} = \sqrt{GM/R_{\rm abs}}$, and $R_{\rm em}$ and $R_{\rm abs}$ are the radii of the reflector and absorber respectively. If we assume the reflection occurs at the ISCO of a Schwarzschild black hole ($a_\star = 0$), $R_{\rm em} = 6R_{\rm g}$, the absorber is thus around $18.6R_{\rm g}$, where the relativistic beaming effect probably leads to a single blueshifted absorption line. The actual test for this interpretation requires an accurate calculation of the absorption through the disk atmosphere and will be considered in a future paper with more data.

5.4.2 Explanations for the Line Emitter

The emission features detected in the 1H 1934 spectrum are unknown and, in particular, the 1 keV emission line has never been well explained in previous work, although a similar

broad feature at $\sim$1 keV was found in 1ES 1927+654 [296]. According to our results, we find that the second blueshifted reflection model fits such emission feature better than photo- and collisional-ionization models provided that the ionizing field is softer ($\Gamma > 3.2$) than its primary continuum ($\Gamma \sim 2.15$) and the gas is hotter ($\log(\xi/\mathrm{erg\,cm\,s^{-1}}) \sim 2.5$) than any absorption component ($\log\xi \sim 1.6$–1.7). Coupling the inclination of two reflection components ($i \sim 39^\circ$) constrains the inner radius of the second reflection to $R_{\rm in} \sim 70$–$252\,R_{\rm g}$, while leaving them free yields $R_{\rm in} \sim 8$–$52\,R_{\rm g}$ and a lower inclination angle ($i \sim 26^\circ$). The fact that fluorescence provides a better description than recombination of photoionized gas means that the line-emitting gas is likely optically thick, consisting of a layer very close or part of the inner accretion disk. Such plasma is blueshifted as indicated and is outside the line of sight towards the X-ray emitting region (otherwise the soft energy band of the spectra would be highly suppressed).

Disk atmospheric origin: The scenario proposed by Gallo and Fabian [93] and Fabian et al. [75] for the blueshifted absorption lines could also be applied to the emission when the disk inclination ($i \sim 40^\circ$) is not as large as that of IRAS 13224-3809 ($i \sim 70^\circ$), at which the wind absorption may be smaller and more of the inner accretion flow should be observed. In this scenario, the strong blueshift originates from the circulation of the accretion disk, resulting in a velocity shift comparable to the Keplerian velocity expected from a radius close to the $R_{\rm in}$. The static disk reflection explanation implies an inclination angle common between the two reflection components. The corresponding inner radius of the second reflection is among 70–$252\,R_{\rm g}$, which is almost an order of magnitude larger than the Keplerian radius, $R_{\rm K} = GM/v^2 \sim 11\,R_{\rm g}$, related to a relativistically corrected velocity ($v \sim -0.293\,c$) from the modeling. Hence, our fits disfavor a purely static disk reflection origin, which requires an inclination angle identical to the primary reflector.

Magnetic outflows: An alternative scenario is that the emission lines are produced by the reflection of the inner accretion flow photons off the base of the magnetically-driven outflow (see the top panel of Fig.5.10). Under this circumstance, the base of the high-speed outflow is launched at a small angle concerning the disk surface and does not obscure the corona but only generates emission lines by reflection (e.g. 1 keV line). The wind will then be lifted, maximizing the velocity exactly in our LOS, yielding a high blueshift. The absorption features will only be observed when the gas rotates following the magnetic field lines with a velocity vector becoming close to the polar direction. The projection of the velocity in LOS is expected to be smaller than the emission lines, which is consistent with our results. However, it is unclear whether the wind orientation could dramatically change within a small region at a speed of $\sim 0.3\,c$, which occurs in a timescale of a few seconds. The requirements of the small region are due to the short recombination time scale of ions

(e.g. $\sim$ 1 sec for O VIII, [264]) and the fact that outflows will be porous after leaving the base. Moreover, if the velocity of the UFO absorption phase ($\sim 0.075\,c$) is indeed due to a projection of the actual velocity, we can estimate the inclination of the LOS with respect to the UFO, θ, by calculating $\theta = \arccos\frac{0.075\,c}{0.293\,c} \sim 75^\circ$. The angle between our LOS and the disk axis thus should be $> 75^\circ$, implying a Seyfert 1.5–2 galaxy and more obscuration than what we observed.

Radiative outflows: The standard quasar-like equatorial outflow is another possible scenario, where the outflow is launched at an intermediate angle (e.g. close to 40°) with emission lines produced by the reflection of the inner region photons off the base of the wind (see the bottom panel of Fig.5.10). Here the base of winds is the inner thick disk puffed up by the strong radiation field. The primary reflection probably comes from the reprocessing in the inner thin disk. The reflection lines will be observed at a blueshift close to the maximal velocity, while the signatures of the photoionization are hardly detected in the form of either emission or absorption lines because of the over-ionization in the inner region. The UFO moving at $\sim -0.075\,c$ might be the optically thin outflow from a broad range of radii with a $\sim -0.075\,c$ part making the largest contribution in our LOS. In this case, the wind is inclined concerning the disk, implying that the inclination angle of the second reflection should be different from the angle between the disk axis and our LOS, compatible with our discovery of a lower inclination angle $i \sim 26^\circ$. By assuming the derived velocity as the escape velocity, the launching radius of the outflow would be $R_{\rm esc} = 2GM/v^2 \sim 22R_{\rm g}$, consistent with our fitted $R_{\rm in} \sim 8$–$52R_{\rm g}$. In addition, Thomsen et al. [333] predicted that the iron line profile produced from the super-Eddington thick disk is symmetric in shape. The line profile revealed by the line scan (see the 1 keV emission in the middle panel of Fig.**??**) looks symmetric, supporting the hypothesis of the reflection off a super-Eddington disk. Consequently, the standard quasar-like equatorial outflow could be an explanation for our results to be verified with future observations.

5.4.3 Outflow Properties

The kinetic energy of the UFO is estimated through Eq.1.14. By measuring the ionizing luminosity (1–1000 Rydberg) at $L_{\rm ion} \sim 1.68 \times 10^{43}\,{\rm erg/s}$, we find:

$$L_{\rm UFO} = 0.5 v_{\rm UFO}^3 m_{\rm p} \mu L_{\rm ion} \Omega C/\xi \sim 4.77 \times 10^{45} \Omega C_{\rm V}\,{\rm erg/s} \tag{5.1}$$

using the UFO results derived from the time-averaged spectrum. If we adopt the conservative value 0.3 for the solid angle from GR-MHD simulations of radiatively-driven winds in super-Eddington systems [330], and the filling factor $C_{\rm V} \sim 3 \times 10^{-4}$ through Eq. 23 in

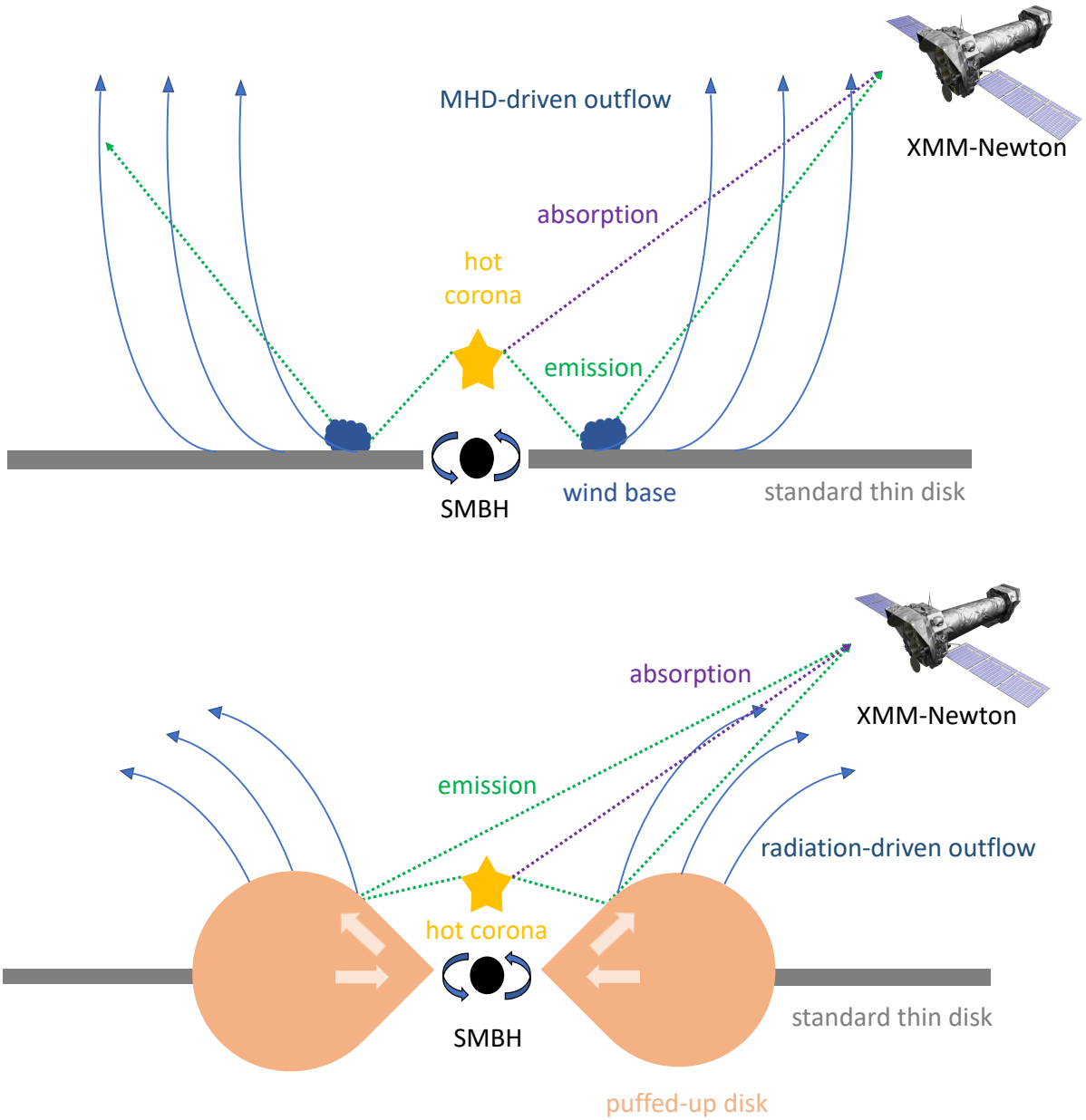

Fig. 5.10 Simplified scheme of the possible explanations for the outflow in 1H 1934-063. The SMBH is surrounded by a standard thin disk (*top*) or a thick inner disk (*bottom*), and the lamppost geometry is assumed for the hot corona. The absorption lines are observed through the outflow in front of the hot corona. *Top panel*: The outflow driven by the magneto-rotational force is launched at a small angle concerning the disk and then could be quickly lifted to the polar direction. The emission originates from the reflection on the wind base within the disk. *Bottom panel*: The radiation pressure in the Eddington-limit system thickens the inner disk and drives the outflow to the equatorial direction. The emission lines come from the reflection on the inner thick disk.

Kobayashi et al. [167] by assuming that the outflow rate is comparable to the accretion rate, the kinetic energy is $L_{\rm UFO} \sim 5.2 \times 10^{42}\,{\rm erg/s} \sim 3\%L_{\rm bol}$ or $1\%L_{\rm Edd}$, above the theoretical criterion $0.5\%L_{\rm Edd}$ to affect the surrounding medium and host galaxy [60, 127]. The detection of reflection off a faster and more ionized phase of the UFO would suggest stronger feedback.

Furthermore, we estimate the location of the detected $\sim -0.075\,c$ UFO. According to Eq.1.11, the UFO is at least at $R > 2GM_{\rm BH}/v_{\rm UFO}^2 \gtrsim 358\,R_{\rm g}$. On the other hand, the upper limit of the radius is obtained $R \leq C_{\rm V}L_{\rm ion}/\xi N_{\rm H} \sim 4.2 \times 10^6\,R_{\rm g}$ through Eq.1.12. Hence, the location of that UFO is estimated between 3.6×10^2–$4.2 \times 10^6\,R_{\rm g}$ and the density of the wind is thus constrained within $n_{\rm H} = L_{\rm ion}\xi/R^2 \sim 1.2 \times 10^5$–$1.7 \times 10^{13}\,{\rm cm^{-3}}$.

5.4.4 Comparison with other AGN

The properties of the warm absorber in 1H 1934 do not stand out if compared with other AGN. The velocity of the UFO (0.075 c) is at the low end among other AGN, such as Mrk 1044 (0.08 c, [181]), PG 1448+273 (0.09 c, [173]) and IRAS 13224-3809 (0.24 c, [252]). However, the other parameters of UFO ($\log(N_{\rm H}/{\rm cm^{-2}}) = 6.6^{+4.1}_{-2.1} \times 10^{19}$ and $\log(\xi/{\rm erg\,cm\,s^{-1}}) = 1.6^{+0.1}_{-0.1}$) are smaller than the typical UFO region, where the ionization parameter and the column density spans from $\log\xi \sim 3$–6 and $\log(N_{\rm H}/{\rm cm^{-2}}) \sim 22$–24 respectively [339]. The estimated kinetic energy of UFO is thus weaker but still effective enough to affect the host galaxy. For comparison, a similar weak UFO has also been found in other two sources, PG 1114+445 [314] and IRAS 17020+4544 [309], where the column density of UFO is similar or lower than that of the warm absorber. This can be explained with an entrained UFO, produced by the interaction between the UFO and surrounding materials, fitting in between the UFO and the warm absorber.

The variability of the warm absorber has been observed on a time scale of days or weeks in several Seyfert 1 galaxies, e.g. MCG-6-30-15 [72], Swift J2127.4+5654 [310] and Fairall 51 [327], while the variation only happens in the column density and could be explained by the X-ray eclipse. If the potential variation of the warm absorber in 1H 1934 is true, the change occurs in the ionization state within ~ 1.5 days due to the variable ionization.

An origin within relativistic reflection off the base of outflows with a strong blueshift is a rather new topic. Kara et al. [157] invoked a strongly blueshifted Fe K reflection line through the X-ray reverberation in a super-Eddington AGN, Swift J1644+57, where the high accretion rate is induced by a tidal disruption event (TDE), in which an AGN destroyed a star and the fallback surpassed Eddington. In 1H 1934, we do not observe a TDE and the same strong blueshift is associated with the soft X-ray emission rather than the Fe K line. We notice that there is a broad emission feature at 1 keV in 1ES 1927+654, which was presumed to be the Ne X (1.02 keV) or the ionized Fe L emission from Fe XX-XIV [296]. But another

interpretation similar to ours was proposed by Masterson et al. [216] that the broad 1 keV emission line could be reproduced by a high-density ($\log n_{\rm e} > 18\,{\rm cm}^{-3}$) and blueshifted ($z \sim -0.3$) reflection model, implying the base of the outflow after the TDE. In our case, we attempt to replace the secondary reflection model with a free-density version but only obtain an upper limit of $\log n_{\rm e} < 16.6\,{\rm cm}^{-3}$. It is reasonable since our lines are not as broad as in 1ES 1927+654 and imply the base of the wind instead of the standard disk photosphere, which should be very dense at the inner disk. Ideally, more strongly blueshifted fluorescent lines should be observed to justify this origin, which will be checked with observations.

5.5 Conclusions

In this Chapter, we perform a variability analysis, and a time- and flux-resolved X-ray spectroscopy on a joint *XMM-Newton* and *NuSTAR* observation of NLS1 1H 1934-063 in 2015 to investigate the nature of the soft X-ray features. We find some absorption features are close to their rest frame and come from a distant warm absorber, which seems to weakly vary within the exposure time. Some absorption features are consistent with a UFO ($v_{\rm UFO} \sim -0.075\,{\rm c}$), which might be an E-UFO as a result of the interaction between the UFO and surrounding medium. The detected emission lines do not match any known rest-frame ion transitions. A secondary blueshifted ($z \sim -0.3\,c$) reflection model fits such emission features better than photo- or collisional-ionization plasma models. We explain this with the reprocessing of inner accretion flow photons off the base of an equatorial wind, which could be the link between reflection and ejection in high-accretion AGN.

Chapter 6

A systematic study of the ultra-fast outflow responses to luminosity variations in active galactic nuclei

Abstract

In this Chapter, we performed high-resolution spectroscopy of archival *XMM-Newton* observations on six highly-accreting NLS1 galaxies, to study the launching mechanisms of UFOs. The methods of the line scan and photoionization model scan are used to discover three previously unreported UFOs. We investigate the response of UFO properties, such as the column density $N_{\rm H}$, ionization parameter $\log \xi$, and velocity v, to the luminosity variations. Combined with the published results of four AGN, we compare the best-fit slope of the correlations between the UFO properties and luminosity, i.e. Γ_{N_H}, $\Gamma_{\log \xi}$, and $\Gamma_{\rm velocity}$, with the intrinsic AGN properties. 5 out of 7 UFOs within the sample exhibit positive Γ_{N_H} and $\Gamma_{\log \xi}$, suggesting UFOs respond to the radiation field, while only 2 of them present a positive $\Gamma_{\rm velocity}$, indicating a radiatively accelerated outflow. We observe no significant dependence of Γ_{N_H} and $\Gamma_{\log \xi}$ on intrinsic AGN properties, but there is an anti-correlation between the UFO acceleration $\Gamma_{\rm velocity}$ and the Eddington ratio $\lambda_{\rm Edd}$. Our results imply that UFOs in highly accreting AGN are likely driven by radiation pressure, but the acceleration decreases as the radiative accretion rate approaches or exceeds the Eddington limit.

6.1 Introduction

Despite numerous UFOs detected in AGN, their wind-driven mechanisms remain poorly understood. In Chapter 3 and 4, we explored UFO launching mechanisms by analyzing their variability in one super-Eddington and sub-Eddington AGN. However, so far only four UFOs have been extensively studied in relation to luminosity variations, leading to limited knowledge about their launching mechanisms. To address this gap, we intend to conduct a systematic study of UFO responses to source variability, aiming to enhance our understanding of their nature and the underlying mechanisms.

In this Chapter, we will show the detailed high-resolution spectroscopic analysis of a sample of UFOs in 6 nearby NLS1 galaxies, observed by *XMM-Newton*, mainly focusing on RGS data. In Sec.6.2 and Sec.6.3, we will list the sample selection criteria and our data reduction processes respectively. The adopted analysis methods are described in Sec.6.4.

Our results are summarized in Sec.6.5, where we find previously unreported UFOs in three AGN, and further study the relationship between the UFO properties and the source. We discuss our results and compare them with the literature in Sec.6.6. Finally, in Sec.6.7 we draw our conclusions and point out prospects.

6.2 Sample Selection

The systems of interest in our study are AGN with UFOs. We thus explored the archival *XMM-Newton* dataset, in particular RGS spectra, which possess both high spectral resolution and sufficient photons due to its large effective area in the soft X-ray band. Our selection is based on the following considerations:

1. A UFO has to be detected in the system. Since we are also interested in discovering new UFOs in AGN, the search is not limited to the UFO-reported AGN but rather is extended to all Seyfert galaxies and quasars with an *XMM-Newton* exposure time of > 50 ks, resulting in a sample of 307 targets. The long exposure time is necessary for RGS to detect and resolve narrow lines (e.g. see Fig. 11 in [171]).

2. The UFO absorption features in the soft X-ray band might be heavily contaminated by the transient obscuration event or the persistent torus obscuration. Thus only AGN with a neutral column density $\log N_{\rm H}/{\rm cm}^{-2} < 22$ are selected, leading to the sample size down to 179.

3. To detect the potential UFO response to the source variability, we need enough counts to perform time- or flux-resolved spectroscopy. In the initial stage, we adopted the product of the averaged RGS flux at 15Å and the total exposure time as a probe for the number of soft X-ray counts, which is easily accessed through the *XMM-Newton* Science Archive (XSA). The exact number of counts is obtained by extracting the RGS spectra (listed in column 6 of Tab.6.1). The threshold is set at half the soft counts of PDS 456, which is the target with the least soft X-ray counts among four previously analyzed sources, i.e. 50000, to ensure statistics. The resulting sample size becomes 29.

4. The detection significance of UFO is a key quantity for the strict constraints on parameters, which are indispensable for the discovery of UFO response. Therefore, we selected out sources with a UFO detection of ΔC-stat > 30 for 4 d.o.f., i.e.$> 4.6\sigma$, in the stacked spectrum to ensure constraints on UFO parameters in the time- or flux-resolved spectra. This filter cannot be directly applied before performing the physical

modeling, so we modified the size of our sample during the analysis and ended up with the number of 6.

Our final sample consists of 6 AGN, all of which are nearby NLS1 galaxies. Their basic information is shown in Tab. 6.1, ordered by the accumulated RGS counts. The black hole mass ($M_{\rm BH}$) and the bolometric luminosity ($L_{\rm bol}$) are obtained from the literature, while the latter is also estimated in this work as well as the accordingly calculated Eddington ratio. All of them are high- or super-Eddington AGN, expected to launch outflows [240]. The disk inclination angles are obtained based on the reflection spectroscopy results from the literature and this work, except for RE J1034+396, which exhibits no discernible reflection features in the spectra. For this particular case, the value is loosely constrained by the simulations [129].

6.3 Data Reduction

The analyzed observations of the sources in our sample are shown in Tab.6.2. We discarded the observations with less than 20 ks exposure time. Specifically for RE J1034+396, we also excluded several observations before 2020 that had a similar flux level with the extensive campaigns in 2020 and 2021. This was to avoid potential influence from the long-term continuum variation on flux-resolved spectroscopy. The data sets were reduced following the standard SAS threads with the *XMM-Newton* Science Analysis System (SAS v20.0.0) and calibration files available by September 2022. In this Chapter, apart from the RGS data, we also use EPIC-pn and OM data to help constrain the SED of the AGN.

Briefly, we reduced the EPIC-pn data using EPPROC and filtered the time intervals affected by the background flares, which show the count rates larger than 0.5 counts/sec in the 10–12 keV range. The source and background spectra were extracted from a circular region with a radius of 30 arcsec centered on and offset but near the source respectively. The pile-up effect was examined by task EPATPLOT. Only one observation of RE J1034+396 (0506440101) and four observations of PG 1211+143 (0112610101, 05020501(2)01, 0745110301) are affected by pile-up. Therefore, an annulus region with an inner radius of 32 arcsec and an outer radius of 45 arcsec was applied to extract the source spectrum of RE J1034+396, while an annulus with an inner radius of 10 arcsec and an outer radius of 30 arcsec was adopted for the PG 1211+143 source spectra. The RGS data were processed by the RGSPROC package with a flare filter of 0.3 counts/sec. The first-order RGS spectra were extracted from a cross-dispersion region of 1 arcmin width and the background spectra were extracted from photons beyond 98% of the source point-spread function as default. We only used the GTI common to both RGS 1 and 2 and combined their spectra for

Table 6.1 Table of the 6 sources in this sample plus 4 previously studied sources, including the source name (1), AGN type (2), redshift (3), black hole mass (4), total on-axis *XMM-Newton* exposure time without solar flare correction (5), total counts in the RGS band with solar flare correction (6), bolometric luminosity (7), Eddington ratio (8) and disk inclination angle (9). See more details in Sec. 6.2.

Source	Type	Redshift	$\log(M_{\rm BH}/M_\odot)$	Exposure	RGS Counts	$L_{\rm bol}$	$\lambda_{\rm Edd}$	i
		z		(ks)	(10^5)	(10^{44} erg/s)	($\equiv L_{\rm bol}/L_{\rm Edd}$)	(deg)
(1)	(2)	(3)	(4)	(5)	(6)	(7)	(8)	(9)
This work								
1H 1934-063	NLS1	0.0102	$6.46^{a,b}$	492	4.2	$1.73^{m,n}$	0.47 ± 0.22	42^{n}
RE J1034+396	NLS1	0.042	6.40^{c}	1417	3.7	$2.7–5.4^{n,o}$	1.29 ± 0.77	30^{w}
PG 1244+026	NLS1	0.048	$7.11^{b,d,e}$	764	2.8	$14–17^{n,p}$	1.04 ± 0.59	31^{n}
PG 1211+143	NLS1/quasar	0.0809	8.16^{f}	876	2.3	$31–53^{n,q}$	0.23 ± 0.08	30^{n}
I ZW 1	NLS1	0.061	7.45^{g}	528	1.8	$22–39^{n,r}$	0.88 ± 0.21	39^{n}
IRAS 17020+4544	NLS1	0.0604	$6.72^{b,h}$	209	0.8	$7.8–9.9^{n,s}$	1.33 ± 0.31	55^{n}
Published work								
Mrk 1044	NLS1	0.016	6.45^{i}	733	9.8	$1.3–1.6^{t}$	0.40 ± 0.12	34^{x}
1H 0707-495	NLS1	0.0406	6.30^{j}	1385	4.1	$2–55^{u}$	9.05 ± 5.43	43^{y}
IRAS 13224-3809	NLS1	0.0658	6.54^{k}	2131	3.3	$4–13^{v}$	1.13 ± 0.58	59^{y}
PDS 456	quasar	0.184	9.3^{l}	1146	1.1	1800^{l}	0.72 ± 0.66	65^{l}

References: a: [207], b: [265], c: [22], d: [154], e: [211], f: [254], g: [354], h: [358], i: [64], j: [63], k: [41], l: [290], m: [373], n: This Chapter, o: [49], p: [140], q: [176], r: [268], s: [107], t: [130], u: [372], v: [32], w: [129], x: [374], y: [249].

Table 6.2 Table of the 6 sources analyzed in this work. The second column lists the stacking approach according to the observations. The number in the brackets means the number of the generated spectra after stacking. The individual *XMM-Newton* observations are shown in the third column. For clarity, the corresponding labels of the stacked and individual spectra are listed in the fourth column, where the time-resolved spectra are referred to as T1…T11 chronologically and the flux-resolved spectra are referred to as F1…F4, from the faintest to brightest state. For each source, except for 1H 1934-063, the time-averaged spectrum from all observations is also generated and referred to as the 'avg' spectrum, while for 1H 1934-063, the two new observations (Obs. ID: 08910101(2)01) are stacked and named as '2021'.

Sources	Stacking Approach	Obs. ID	Labels
1H 1934-063	individual (1)	0761870201	2015
	flux-resolved (2)	0891010101, 0891010201	F1, F2
RE J1034+396	time-averaged (1)	0506440101, 0561580201, 0675440301	High
	flux-resolved (2)	0865010101, 0865011001, 0865011101, 0865011201, 0865011301, 0865011401, 0865011501, 0865011601, 0865011701, 0865011801	F1, F2
PG 1244+026	flux-resolved (4)	0675320101, 0744440101, 0744440201 0744440301, 0744440401, 0744440501	F1, F2, F3, F4
PG 1211+143	time-resolved (11)	0112610101, 0208020101, 0502050101, 0502050201	T1, T2, T3, T4
		0745110101, 0745110201, 0745110301, 0745110401	T5, T6, T7, T8
		0745110501, 0745110601, 0745110701	T9, T10, T11
I ZW 1	individual (1)	0300470101	2005
	flux-resolved (2)	0743050301, 0743050801	F1, F2
	time-averaged (1)	0851990101, 0851990201	2020
IRAS 17020+4544	flux-resolved (3)	0206860101, 0206860201, 0721220101, 0721220301	F1, F2, F3

the high S/N. The OM data were reduced with OMICHAIN and stacked into a time-averaged spectrum for each source, since they are relatively stable and much less variable than the X-ray flux, at most 25% variations in our sample.

To investigate the dependence of UFOs on source variability, we adopted different stacking approaches for the EPIC-pn and RGS spectra of each object and generated the time-averaged, time-resolved, and flux-resolved spectra. The stacking approaches and corresponding labels are listed in Tab.6.2. The EPIC-pn (0.3–10 keV) light curves and corresponding hardness ratios (HR $= \mathrm{H}/\mathrm{H}+\mathrm{S}$, H: 2–10 keV; S: 0.3–2 keV) are extracted with the EPICLCCORR task and shown in Fig.6.1 and 6.2. For the flux-resolved approach, we equally divided the light curves into several flux levels (the number shown in Tab.6.2), which makes the number of counts of each level comparable ($> 10^4$ counts). The GTI files were created with the TABGITGEN package and the flux-resolved spectra were subsequently extracted and stacked. For each source, except for 1H 1934-063, a time-averaged spectrum from all observations is also extracted and labeled as 'avg', while the averaged spectrum of 1H 1934-063 results from stacking two new observations in 2021 and refers to as '2021'. The EPIC-pn and RGS spectra were separately stacked with EPICSPECCOMBINE and RGSCOMBINE and grouped to over-sample the instrumental resolution at least by a factor of 3.

6.4 Methods

In this section, we present the results of our analysis methods, including the spectral modeling (see Sec.6.4.1), Gaussian line scan (see Sec.6.4.2), and the photoionization model scan (see Sec.6.4.3) to visualize the UFO absorption lines in each spectrum, identify the best-fit solution for UFOs and obtain the UFO properties.

6.4.1 Continuum Modelling

The X-ray data analysis software XSPEC (v12.12.1, [12]) is used for broadband-band spectral analysis of the EPIC-pn and RGS data. We consider the RGS spectra between 0.4–1.77 keV, and the EPIC-pn spectra only between 1.77–10 keV (except for RE J1034+396 and PG 1244+026 between 1.77–8 keV due to the background domination above 8 keV) in our analysis, due to the influence of the lower resolution but higher count rate of EPIC-pn on the detection of atomic features. The instrumental differences are taken into account by adopting a variable cross-calibration factor `constant`. We use the C–stat [35] statistics and estimate the uncertainties of all parameters at the 1σ (i.e. ΔC–stat $= 1$) confidence level. In this Chapter, the luminosities are calculated by the `cflux` model with the assumption

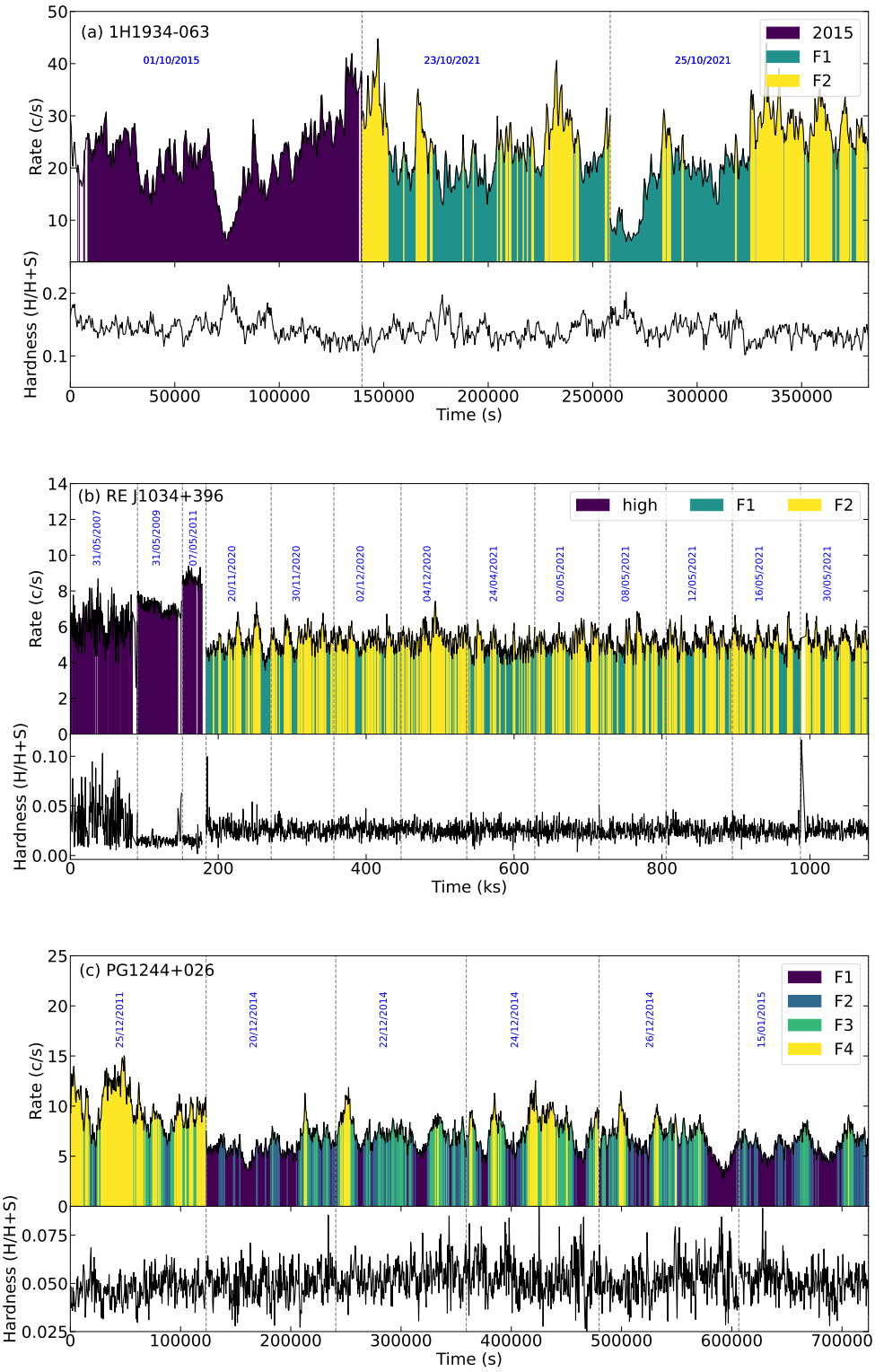

Fig. 6.1 The EPIC-pn (0.3–10 keV) light curve (*upper*) and the corresponding hardness ratio (*lower*) of the observations of 1H 1934-063 (*a*), RE J1034+396 (*b*), and PG 1244+026 (*c*). The individual and flux-/time-resolved spectra of each source stacked by different approaches (listed in Tab.6.2) are marked in different colors with labels.

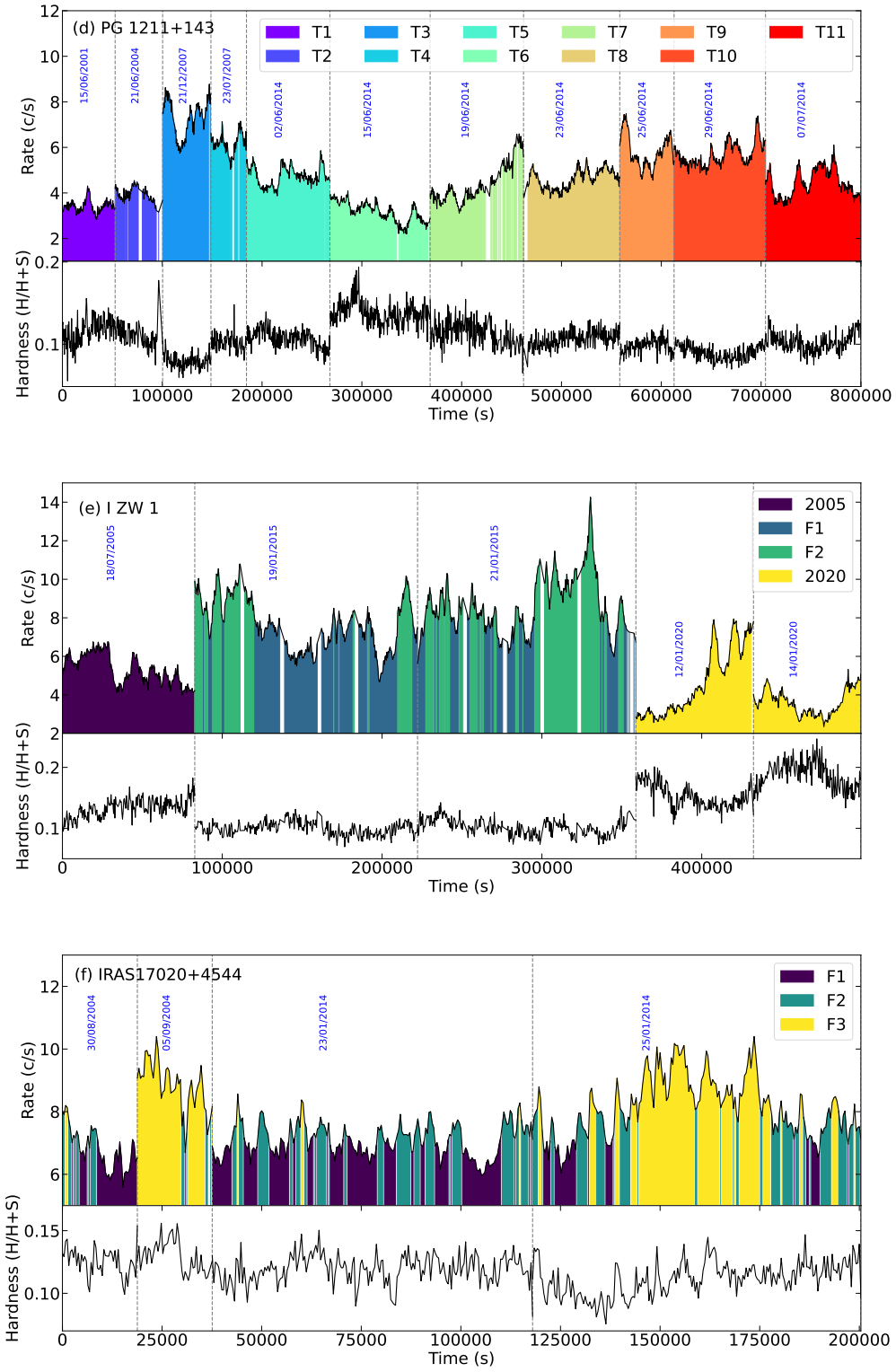

Fig. 6.2 Similar to Fig.6.1, but for PG 1211+143 (*d*), I ZW 1 (*e*) and IRAS 17020+4544 (*f*).

of $H_0 = 70\,\mathrm{km/s/Mpc}$, $\Omega_\Lambda = 0.73$ and $\Omega_\mathrm{M} = 0.27$. We use `tbabs` in XSPEC to model the Galactic absorption with Galactic column densities provided by HI4PI Collaboration et al. [120], except for 1H 1934-063. For this particular case, we accounted for the relatively heavy Galactic absorption ($\sim 10^{21}\,\mathrm{cm}^{-2}$) using the high-resolution photoabsorption model `ismabs` instead. We adopt the solar abundance calculated by Lodders et al. [196] to keep consistent with the subsequently used photoionization model in Sec.6.4.3. The redshift of AGN is taken into account by `zashift` in XSPEC. In this Chapter, since we are only interested in the atomic features instead of the origin of the broadband continuum, we adopt the model `diskbb`, characterized by the temperature at the inner accretion disk, to phenomenologically account for the soft excess for the sake of simplicity. The primary and reprocessing emissions are explained by a flavor of the relativistic reflection model (RELXILL v1.4.3, [94]), which includes a hot Comptonization continuum (`relxillCp`).

Therefore, the general continuum model for most targets in this work is:

```
constant*tbabs*zashift*cflux*(diskbb+relxillCp),
```

except for RE J1034+396 and IRAS 17020+4544. Due to the lack of discernible reflection features in the spectra of RE J1034+396, we adopted the best model combination from Jin et al. [142], which assumes the warm Comptonization explanation for the soft excess and consists of three Comptonization components for the hot, intermediate, and warm Comptonization emission. In IRAS 17020+4544, a single reflection component cannot explain the relativistically broadened Fe K emission. Therefore, following the best-fit continuum model from Gonzalez et al. [107], we included an additional `laor` component, which models the disk line affected by strong gravity, with disk parameters (the inclination angle, inner and outer disk radius) linked to those of `relxillCp`, while the line energy, emissivity index, and normalization are left free. For the remaining targets, our general continuum model also aligns with the best combination in prior studies on those sources [154, 194, 373, 364]. The long-term invariants, such as the black hole spin, disk inclination angle, and iron abundance, were linked together across the averaged, time- and flux-resolved spectra of the same source during the analysis. Moreover, we have tested a few different continuum models, such as changing the flavors of RELXILL and replacing the phenomenological model `diskbb` with a warm corona or a high-density relativistic reflection model. We found that the choice of the continuum model does not affect the following results on the line modeling and detection of UFOs. Details of continuum parameters are unrelated to our goal and thus are not shown in this work. Only inclination angles derived from the reflection model are listed in Tab.6.1 for further analysis in Section 6.5.2.

6.4.2 Gaussian Line Scan

To identify both the narrow and broad atomic features, we perform blind line search, described in Sec.2.3.1, by assuming the line widths at σ_v of 500, 1500, 4500 km/s, and the corresponding numbers of the energy steps at 2000, 700, 300, respectively. This analysis approach is performed for every spectrum extracted from the observations of the sources in our sample. The results are shown in Figs. A.1 to A.6, where the centroid of prominent UFO absorption features discovered in the following photoionization modeling are highlighted by the vertical dashed red lines. The details of the line scan results over each spectrum of individual sources are presented in Appendix A.

6.4.3 Photoionization Model Scan

As we have done in Chapter 4, we adopted the code used in Parker et al. [251] to construct the tabulated XSPEC version of `PION` for photoionization modeling. In this Chapter, we only make use of the absorption component of `PION`, i.e., `XABS`, and the re-built model is thus named as `XABS_XS`.

The intrinsic SEDs of individual sources are derived from the UV, constrained by OM spectra, to the hard X-ray band (from 1 eV to 10 keV). We adopted the AGN SED model, `AGNSLIM` [184, 185], sharing the same temperature between the disk and the seed photon of the warm Comptonization, only for SED calculations. This model allows us to directly measure the Eddington ratio, listed in Tab.6.1. The relativistic reflection component was included as well and fixed at the best fit derived from the continuum modeling in Section 6.4.1 without the primary continuum in the model. The Galactic extinction is also considered by the `redden` model according to Schlafly and Finkbeiner [311]. Nonetheless, for RE J1034+396, PG 1244+026, and I ZW 1, the UV/optical data cannot be well explained by `AGNSLIM`. In these cases, we employed the phenomenological model `diskbb` for the UV/optical spectra. Specifically, the characterized disk temperatures of these sources are 30^{+16}_{-15}, 28^{+17}_{-15}, and 12^{+10}_{-9} eV respectively. We roughly estimated their Eddington ratios by calculating the bolometric luminosity (10^{-3}–10^{3} keV) predicted by the model. The intrinsic time-averaged SEDs of each source are shown in Fig. 6.3. Due to the concerns about the potential impact of the loosely constrained UV/optical measurements on photoionization modeling, we investigated and confirmed that variations in the disk temperature within the uncertainties do not significantly affect the ionization balance of the plasma, and the conclusions of this work.

We then launch a systematic scan over a multi-dimension grid of the parameters ($\log \xi, z_{\rm LOS}, \sigma_v$) of `XABS_XS` upon the continuum model for each spectrum, as introduced in Sec.2.3.2.

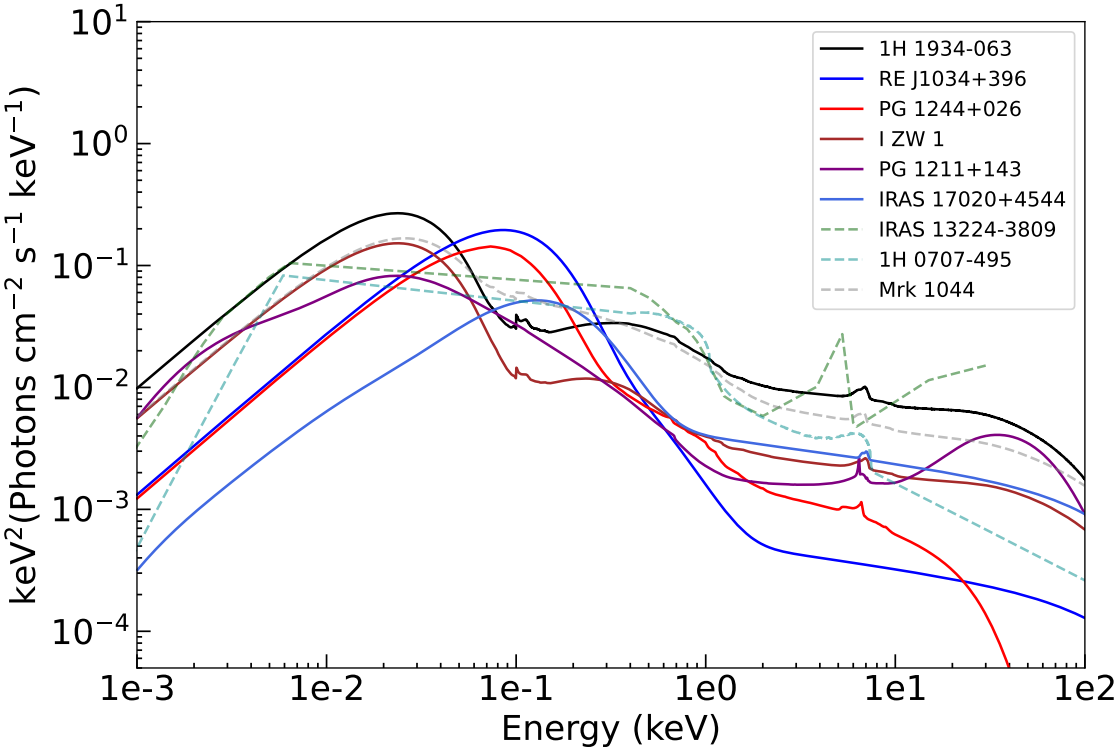

Fig. 6.3 The averaged SED of sources in our sample compared with 1H 0707-495 [372], IRAS 13224-3809 [138], and Mrk 1044 [374].

The grids consist of the ionization parameter $\log\xi$, ranging from 0 to 5 with a step of $\Delta\log\xi = 0.1$, the turbulent velocity σ_v ($\sigma_v = 500, 1500, 4500$ km/s) and the LOS velocity $v_{\rm LOS}$, from -105000 km/s to 0 with an increment depending on the choice of σ_v ($c\Delta z_{\rm LOS} = 500, 700, 1500$ km/s for $\sigma_v = 500, 1500, 4500$ km/s respectively).

The photoionization model scan is performed on every spectrum in our sample. If the secondary solutions have a significance above 3σ in a single trial, i.e. ΔC-stat= 16.25 for 4 degrees of freedom, we will iteratively include an additional absorption component into the model and re-perform the scan upon the new baseline model until the significance of adding a further absorption component to the model falls below 3σ. For clarity, we only present the scan results detecting UFOs across the time-averaged spectrum of each target in Fig.6.4, while the results detecting WAs, such as 1H 1934-063 [373], RE J1034+396 (firstly detected), I ZW 1 [43, 303], and IRAS 17020+4544 [309] are not shown. We exhibit results with a line width of 1500 km/s except PG 1211+143 (σ_v =500 km/s) due to the consistency among scan results with different line widths. The velocity on the X-axis is relativistically corrected. The grid with the strongest detection is marked by a red cross but it may not be the final result, because during the direct spectral modeling, the line width is free to vary and the best fit may fall in another solution. But the scan plots at least provide a reference map for the globally best-fit solution of UFOs.

6.5 Results

In this section, we present the results of the photoionization modeling (Sec.6.5.1), the tentative dependence of UFO detection on viewing angles (Sec.6.5.2), the evolution of UFO properties across various flux states (Sec.6.5.3), and the potential correlations between the evolution slopes and intrinsic source properties (Sec.6.5.4).

6.5.1 Photoionization Modeling

According to the scan results in Fig.6.4, we directly fit the photoionization absorption model with a free turbulent velocity to each spectrum in our sample with the initial values obtained from the scan results. Conservatively, we also test other peaks in the scan plots in case their significance is larger than those obtained from the scan with a fixed line width, e.g. the best-fit UFO in 1H 1934-063, RE J1034+396 and PG 1211+143. The final best-fit parameters of UFOs are listed in Tab.6.3, while those of WAs are listed in Tab.A.1. Only the absorbers with a significance above 3σ (i.e. ΔC–stat > 16) are taken into account, which explains why some previously reported UFOs are not included in our results, e.g. 4 UFOs in IRAS

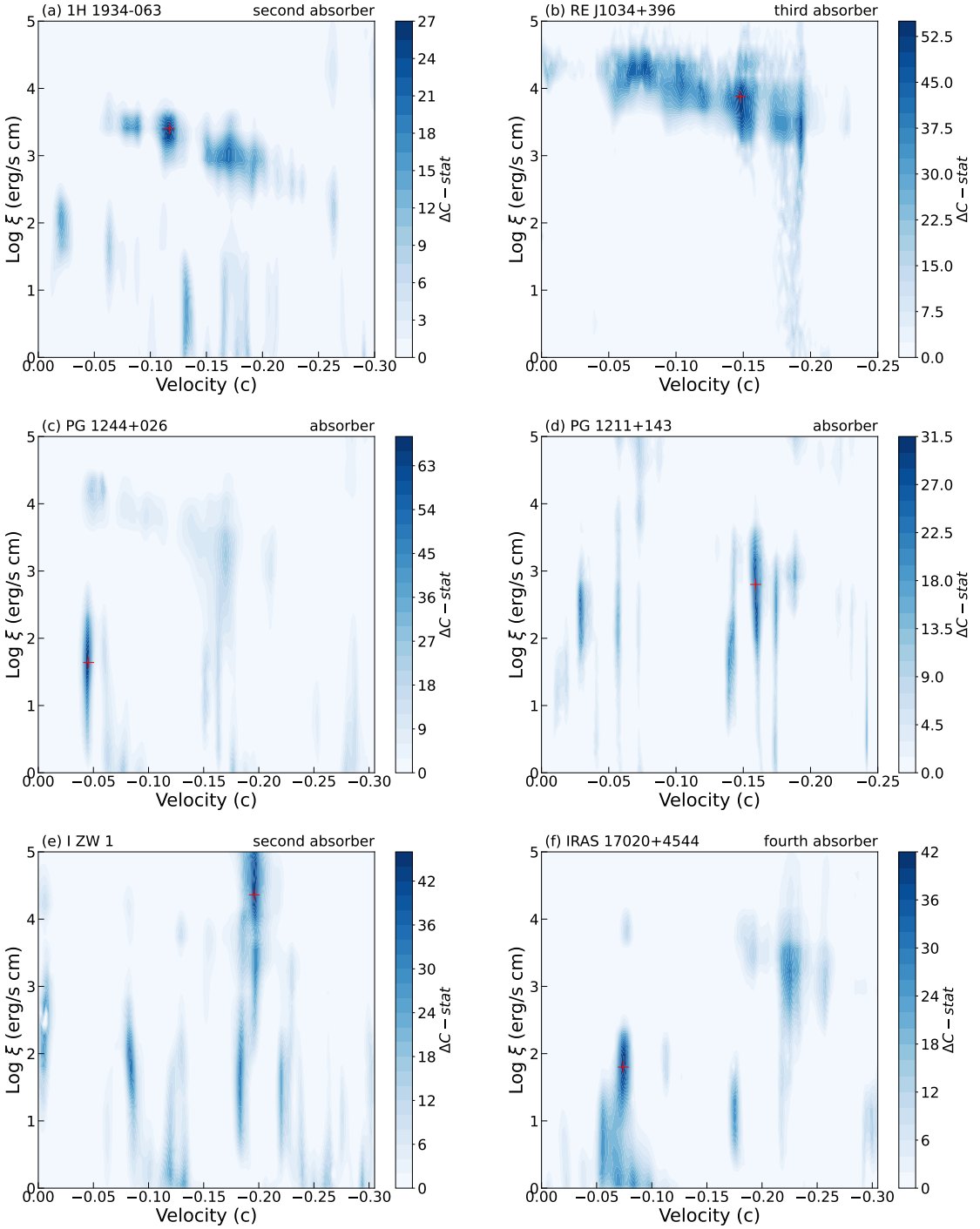

Fig. 6.4 Photoionization absorption model search for the time-averaged spectra of 1H 1934-063 (*a*), RE J1034+396 (*b*), PG 1244+026 (*c*), PG 1211+143 (*d*), I ZW 1 (*e*) and IRAS 17020+4544 (*f*) over the baseline model (continuum or plus WAs). The color illustrates the statistical improvement after adding an absorption component with a line width of 1500 km/s (except PG 1211+143 with $\sigma_v = 500$ km/s). The solution with the most significant detection is marked by a red cross.

17020+4544 but only 1 UFO with ΔC–stat > 16 [309]. Despite the presence of numerous solutions in the scan plots, multiple UFOs are not detected in our results, except for PG 1211+143 and I ZW 1. This is because the solutions partially degenerate and account for the same line features, making the secondary solutions insufficiently apparent once the primary UFO is considered. We have also estimated the potential influence of the strong emission lines in some spectra on the modeling of the absorption component. We compared the fits before and after including a photoionization emission component i.e. `PION_XS` and found it does not significantly affect the fits and our conclusions, due to the narrow line widths of the emission lines.

Notably, two sources, RE J1034+396 and PG 1244+026, had no previously reported UFOs. Furthermore, there was no UFO detection in the soft X-ray band of the I ZW 1 spectrum [318]. Importantly, this detection is not merely a result of including new and previously unanalyzed observations of these sources but is primarily attributed to the effectiveness of our methodology. The description of UFOs in individual sources is presented as follows, while that of WAs is shown in Appendix.A:

1H 1934-063: UFOs detected in the 2021 observations exhibit distinct properties from that in 2015 (see Chapter 5), with higher ionization states, larger column densities, and faster speeds. However, the observations of these two epochs share similar X-ray luminosity (see panel *a* of Fig.6.1), indicating that the difference is unrelated to the radiation field. The origin of the UFO change remains mysterious, perhaps resulting from different phases of UFOs or unknown prior variable accretion rates. In the flux-resolved spectra from consecutive 2021 observations, most UFO properties remain stable within their uncertainties, except that the velocity tends to be higher when the source is brighter (see Tab.6.3).

RE J1034+396: UFOs in RE J1034+396 are degenerated to explain similar Fe complex absorption lines between 1–1.2 keV (Fig.A.2), indicating the same origin. The degenerated region can be observed in panel *b* of Fig.6.4, where the best-fit UFO solutions for F1 and F2 spectra manifest at the high-speed end of the degenerate solutions while the 'high' spectrum solution is notably confined to the low-speed domain. The statistical difference between these two distinct solutions within the 'high' spectrum is ΔC–stat $= 16$ and it becomes even larger for UFOs in flux-resolved spectra, disfavoring the explanation of stochastic variability. The origin of this UFO change is still unknown, although the ionization parameter and column density appear to be correlated to the luminosity while the velocity does not exhibit the same behavior. Within the two flux-resolved spectra of 2020–2021, when the variation in the source luminosity is negligible, UFO properties remain constant within their uncertainties.

PG 1244+026: The UFO in PG 1244+026 has a stable velocity while simultaneously exhibiting tentative flux-dependent trends in the ionization state and column density. These

Table 6.3 Table of the best-fit UFO parameters derived from extracted spectra of targets in Chapter 6. The uncertainties of parameters are estimated at 1σ error bars.

Sources	UFO					Luminosity
	$\log \xi$ erg cm s^{-1}	$N_{\rm H}$ (10^{21} cm^{-2})	$\sigma_{\rm v}$ (km/s)	$v_{\rm LOS}$ (km/s)	ΔC-stat	$L_{0.4-10\,\rm keV}$ (10^{43} erg/s)
1H 1934-063						
2015	$1.26^{+0.14}_{-0.10}$	$0.05^{+0.01}_{-0.01}$	867^{+365}_{-316}	-24000^{+300}_{-300}	30	$1.74^{+0.02}_{-0.01}$
2021	$2.94^{+0.15}_{-0.06}$	$1.1^{+0.5}_{-0.4}$	6151^{+3529}_{-3307}	-55200^{+1800}_{-2700}	32	$1.73^{+0.02}_{-0.02}$
F1	$2.90^{+0.14}_{-0.07}$	$0.9^{+0.5}_{-0.3}$	2368^{+2297}_{-1363}	-53100^{+900}_{-1200}	20	$1.44^{+0.01}_{-0.02}$
F2	$3.05^{+0.14}_{-0.38}$	$1.3^{+0.5}_{-0.6}$	2433^{+3038}_{-1909}	-60300^{+1200}_{-1500}	17	$2.22^{+0.02}_{-0.02}$
RE J1034+396						
avg	$3.38^{+0.06}_{-0.07}$	$2.7^{+1.2}_{-0.5}$	49^{+24}_{-21}	-63480^{+180}_{-90}	75	$3.8^{+0.1}_{-0.1}$
F1	$3.26^{+0.14}_{-0.11}$	$1.8^{+1.3}_{-1.1}$	186^{+364}_{-101}	-63270^{+240}_{-180}	28	$3.3^{+0.1}_{-0.2}$
F2	$3.43^{+0.11}_{-0.14}$	$2.9^{+1.3}_{-1.6}$	42^{+53}_{-30}	-63720^{+300}_{-150}	34	$4.0^{+0.2}_{-0.2}$
high	$4.40^{+0.06}_{-0.18}$	14^{+4}_{-3}	3163^{+1146}_{-1937}	-20100^{+1500}_{-1200}	32	$4.2^{+0.1}_{-0.1}$
PG 1244+026						
avg	$1.42^{+0.09}_{-0.09}$	$0.15^{+0.05}_{-0.03}$	108^{+38}_{-24}	-13530^{+60}_{-60}	114	$7.0^{+0.1}_{-0.1}$
F1	$1.59^{+0.09}_{-0.16}$	$0.23^{+0.02}_{-0.07}$	63^{+25}_{-23}	-13170^{+150}_{-180}	32	$5.4^{+0.1}_{-0.1}$
F2	$1.46^{+0.13}_{-0.14}$	$0.25^{+0.04}_{-0.05}$	99^{+45}_{-14}	-13710^{+120}_{-120}	53	$7.1^{+0.1}_{-0.1}$
F3	$1.3^{+0.2}_{-0.2}$	$0.12^{+0.09}_{-0.05}$	73^{+94}_{-34}	-13650^{+180}_{-210}	22	$8.3^{+0.1}_{-0.1}$
F4	$1.3^{+0.2}_{-0.2}$	$0.04^{+0.01}_{-0.01}$	319^{+322}_{-125}	-13470^{+180}_{-180}	18	$10.7^{+0.2}_{-0.2}$
PG 1211+143						
avg	$1.79^{+0.06}_{-0.06}$	$0.42^{+0.04}_{-0.04}$	39^{+11}_{-11}	-17580^{+90}_{-90}	126	$19.9^{+0.2}_{-0.2}$
	$2.25^{+0.10}_{-0.14}$	$0.15^{+0.10}_{-0.04}$	3170^{+2600}_{-280}	-10780^{+600}_{-600}	48	
T1*	$2.33^{+0.06}_{-0.06}$	$2.7^{+0.6}_{-0.5}$	99^{+43}_{-28}	-20700^{+150}_{-150}	57	33^{+12}_{-9}
	$5.0^{+0}_{-0.1}$	600^{+700}_{-400}	448^{+363}_{-252}	-27300^{+300}_{-300}	24	
T3	$3.03^{+0.11}_{-0.15}$	$2.6^{+1.0}_{-0.6}$	218^{+322}_{-91}	-12780^{+210}_{-210}	69	$28.3^{+0.6}_{-0.6}$
T4	$1.63^{+0.16}_{-0.06}$	$0.6^{+0.2}_{-0.2}$	< 51	-17820^{+330}_{-360}	22	$27.0^{+0.6}_{-0.6}$
T5	$4.5^{+0.2}_{-0.1}$	1271^{+629}_{-369}	< 58	-51930^{+330}_{-360}	23	57^{+11}_{-11}
T6	$1.53^{+0.14}_{-0.10}$	$2.3^{+0.2}_{-0.1}$	58^{+21}_{-21}	-17760^{+180}_{-180}	100	$15.7^{+0.4}_{-0.3}$
T7	$2.22^{+0.09}_{-0.11}$	$0.7^{+0.3}_{-0.2}$	231^{+92}_{-59}	-17550^{+150}_{-150}	73	$18.5^{+0.3}_{-0.3}$
T8	$3.33^{+0.19}_{-0.09}$	20^{+14}_{-7}	< 14	-41220^{+270}_{-930}	17	$18.6^{+0.8}_{-0.7}$
T10	$2.17^{+0.14}_{-0.15}$	$0.4^{+0.2}_{-0.1}$	89^{+87}_{-36}	-10110^{+180}_{-180}	23	$21.6^{+0.4}_{-0.4}$
T11	$4.19^{+0.22}_{-0.05}$	110^{+156}_{-54}	127^{+169}_{-58}	-72930^{+180}_{-450}	23	19^{+3}_{-1}
I ZW 1						
avg*	$4.80^{+0.06}_{-0.08}$	1500^{+100}_{-300}	< 21	-64230^{+210}_{-120}	56	72^{+16}_{-12}
	$2.26^{+0.12}_{-0.17}$	$0.14^{+0.07}_{-0.05}$	2024^{+482}_{-625}	-25800^{+300}_{-300}	48	
F1*	$4.54^{+0.14}_{-0.06}$	1500^{+500}_{-500}	49^{+23}_{-17}	-63990^{+150}_{-150}	51	71^{+19}_{-21}
	$2.06^{+0.20}_{-0.04}$	$0.15^{+0.10}_{-0.05}$	2489^{+643}_{-800}	-26100^{+600}_{-600}	23	
F2*	$4.50^{+0.04}_{-0.08}$	1500^{+300}_{-300}	< 22	-65400^{+120}_{-240}	19	87^{+23}_{-22}
	$2.69^{+0.15}_{-0.24}$	$0.36^{+0.23}_{-0.15}$	1473^{+609}_{-581}	-25800^{+300}_{-300}	29	
2020	$3.76^{+0.11}_{-0.04}$	7^{+2}_{-2}	650^{+541}_{-338}	-41310^{+390}_{-300}	18	$12.6^{+0.3}_{-0.3}$
IRAS 17020+4544						
avg	$1.9^{+0.1}_{-0.2}$	$0.30^{+0.03}_{-0.03}$	2471^{+391}_{-383}	-23155^{+300}_{-300}	49	$22.6^{+0.5}_{-0.5}$
F1	$1.5^{+0.4}_{-0.1}$	$0.19^{+0.05}_{-0.07}$	2992^{+1986}_{-641}	-23110^{+1200}_{-1500}	17	$20.5^{+0.2}_{-0.8}$
F2	$1.8^{+0.2}_{-0.2}$	$0.26^{+0.07}_{-0.05}$	1707^{+550}_{-740}	-23110^{+420}_{-420}	19	$22.6^{+0.6}_{-0.6}$
F3	$1.9^{+0.1}_{-0.2}$	$0.33^{+0.06}_{-0.05}$	1958^{+645}_{-846}	-23200^{+480}_{-480}	22	$28.7^{+1.0}_{-0.8}$

* A secondary UFO is detected in this spectrum.

trends are illustrated by the increasing ratio between blueshifted O VII and O VIII with enhanced luminosity (see Fig.A.3), indicative of a decreasing ionization parameter and column density. However, deciphering the underlying reason for this decreasing trend is challenging. We notice that one observation (2011) occurred three years before the others (2014). Through the trial of the time-resolved spectroscopy, we found that the UFO properties in that observation resemble those found in the others, ruling out the explanation of different UFO phases. Even after removing the 2011 observation, time-resolved results still lead to a decreasing trend of the ionization parameter within 1σ, excluding the possibility of long time-gap accretion variations. Given its low and stable velocity $v_{\rm LOS} \sim -13500$ km/s, the UFO may originate from a distant place from the SMBH, leading to a less responsive UFO to the source variation, which awaits future investigation.

PG 1211+143: Consistent with the literature [269, 288], we found that UFOs in PG 1211+143 are highly variable and multi-phase. The LOS velocity ranges from -10000 to -72000 km/s and the ionization parameter $\log \xi$ spans between 1.6 and 5. The predominant UFO features are blueshifted Fe UTA lines in the soft X-ray regime, along with S XVI, Ar XVIII, and Fe XXV/XXVI features in the hard X-ray band. We do not find any UFOs with a significance ΔC–stat > 16 in the T2 and T9 spectrum, whereas a secondary UFO attains noteworthy significance in the T1 spectrum. The most robust UFO detection falls in the faintest T6 spectrum (ΔC–stat $= 100$), attributed to the passage of an absorbing cloud [288]. Among UFOs in our results, the solution featuring $v_{\rm LOS} \sim -18000$ km/s emerges as the most recurrent, while others manifest a notably stochastic behavior. Given the consecutive observations of 2014, such complexity cannot be attributed to the long time-gap accretion variations and was explained by some intrinsic disk instability or different phases of a stratified wind [269].

I ZW 1: We found a highly-ionized ($\log \xi > 4.5$) and fast-moving UFO in 2015 observations through blueshifted Fe XXV-XXVI absorption lines, consistent with previous works [285]. The UFO detected within the 2020 spectrum exhibits a comparable ionization parameter ($\log \xi \sim 3.8$) to the one found in Rogantini et al. [302], accounting for residuals around ~ 1.2 keV and in Fe K region [364]. The contribution to the Fe XXV residuals suggests a common origin between the UFO detected in 2020 and those in 2015, despite a five-year gap between observations, and different velocities and ionization parameters. Moreover, in 2015 observations, our scan uncovers a previously unreported secondary UFO in the soft X-rays, particularly evident for the absorption feature around 0.7 keV (Fig.A.5). The column density and velocity of this UFO are stable in 2015 observations. There is a marginal correlation between the ionization parameter and X-ray luminosity, although this correlation disappears when uncertainties are considered at a 2σ level.

IRAS 17020+4544: We discovered a moderately ionized ($\log\xi \sim 1.9$) UFO with a LOS velocity of $v_{\rm LOS} \sim -23100$ km/s in the soft X-ray band. It accounts for the residual around 0.71 keV (Fig.A.6). This UFO is consistent with the findings of Sanfrutos et al. [309], while the remaining three UFOs in their work disappear in our analyses due to their tiny significance (ΔC-stat<10). The properties of such UFO are remarkably stable across flux-resolved spectra.

6.5.2 Inclination-dependent UFO detection?

By employing the relativistic reflection model for modeling the Fe K emission, we can constrain the inclination angle of the accretion disk. It is observed that most UFOs in our sample are detected in AGN with $i > 30^\circ$. Combined with the sample of Parker et al. [249], most of which are Type 1 AGN, we expand the population size to 26 AGN, including UFO detection and inclination angles derived from relativistic reflection spectroscopy, shown in Fig.6.5. UFO detections are strongly concentrated at 30–60°, suggesting UFOs are detectable only within specific viewing angles. However, this phenomenon most likely results from selection effects. At low inclinations, our LOS intersects directly the innermost region of the accretion disk, where the plasma may be fully ionized and undetectable, even if a UFO exists [259]. In the edge-on scenario, the nucleus is heavily obscured by the dusty torus (typically Type 2 AGN), preventing the detection of soft X-ray UFOs. In cases that are not Compton-thick with a column density of $N_{\rm H} < 10^{24}\,{\rm cm}^{-2}$, UFOs are detectable in hard X-rays, while UFOs in Type 2 AGN, which have a similar detection fraction as that in Type 1 AGN [339], are not equally included in the sample, leading to the lack of UFO detection at high inclinations. Another caveat is the degeneracy between the inclination angle and other parameters of the reflection model (e.g. Fe abundance $A_{\rm Fe}$ and ionization parameter $\log\xi$), which may affect the values of the inclination angle [293]. Consequently, due to the biases mentioned above, the hypothesis of inclination-dependent UFO detection is tentative, awaiting an enhanced sample size of AGN with detections of both UFOs and relativistic reflection, as well as model-independent measurements of inclination angles.

6.5.3 The evolution of UFO properties across different X-ray luminosities

To further investigate the dependence of the wind properties on the source luminosity, we plot the best-fitting column density, ionization parameter, and velocity of UFOs in our sample versus the unabsorbed luminosity between 0.4–10 keV in Fig.6.6 and fit them with a power-law function, as depicted by the dashed lines. The 'I ZW 1-2' refers to the second

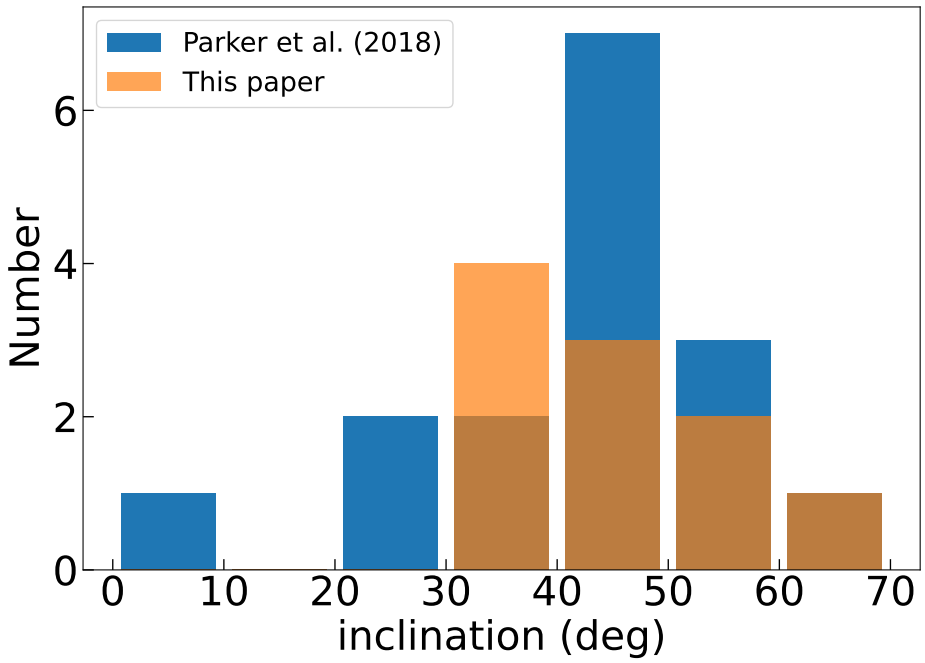

Fig. 6.5 The distribution of disk inclination angle of sources in our sample plus four studied sources compared with the sample of Parker et al. [249]. Most UFOs in the sample are detected with a disk inclination angle between 30–60°.

UFO in I ZW 1. Given the variable and multi-phase nature of UFOs, discerning whether UFOs exhibiting distinct properties are manifestations of the same plasma is challenging. Consequently, to ensure that we are tracing the same absorber at different fluxes rather than comparing different UFOs in different epochs, in our fitting, we exclude UFOs that significantly differ from others and have long intervals from the rest within the same system, i.e. excluding the UFO in the '2015' spectrum of 1H 1934-063 during the fitting. The second UFO observed in the T1 spectrum of PG 1211+143 is marked by the same label as others within PG 1211+143 and all UFOs in PG 1211+143 are fitted together because UFOs in this AGN have too many phases to identify which UFOs share the same origin. The fitted power indexes, referred to as Γ_{N_H}, $\Gamma_{\log\xi}$ and $\Gamma_{\rm velocity}$, are listed in Tab.6.4, which also include results from previous archival studies, where only $\Gamma_{\rm velocity}$ was calculated for PDS 456. The uncertainty of slopes fitted from only two points (i.e. 1H 1934-063 and I ZW 1-2) is large and calculated from the error propagation formula instead of the Levenberg-Marquardt algorithm.

In our sample, the majority of UFOs (5 out of 7) exhibit positive Γ_{N_H} and $\Gamma_{\log\xi}$ within $1\,\sigma$ uncertainties. It means that UFOs likely become increasingly ionized in response to an enhanced radiation field and to remain observable at higher ionization states, their corresponding column density usually also increases. The column density and ionization

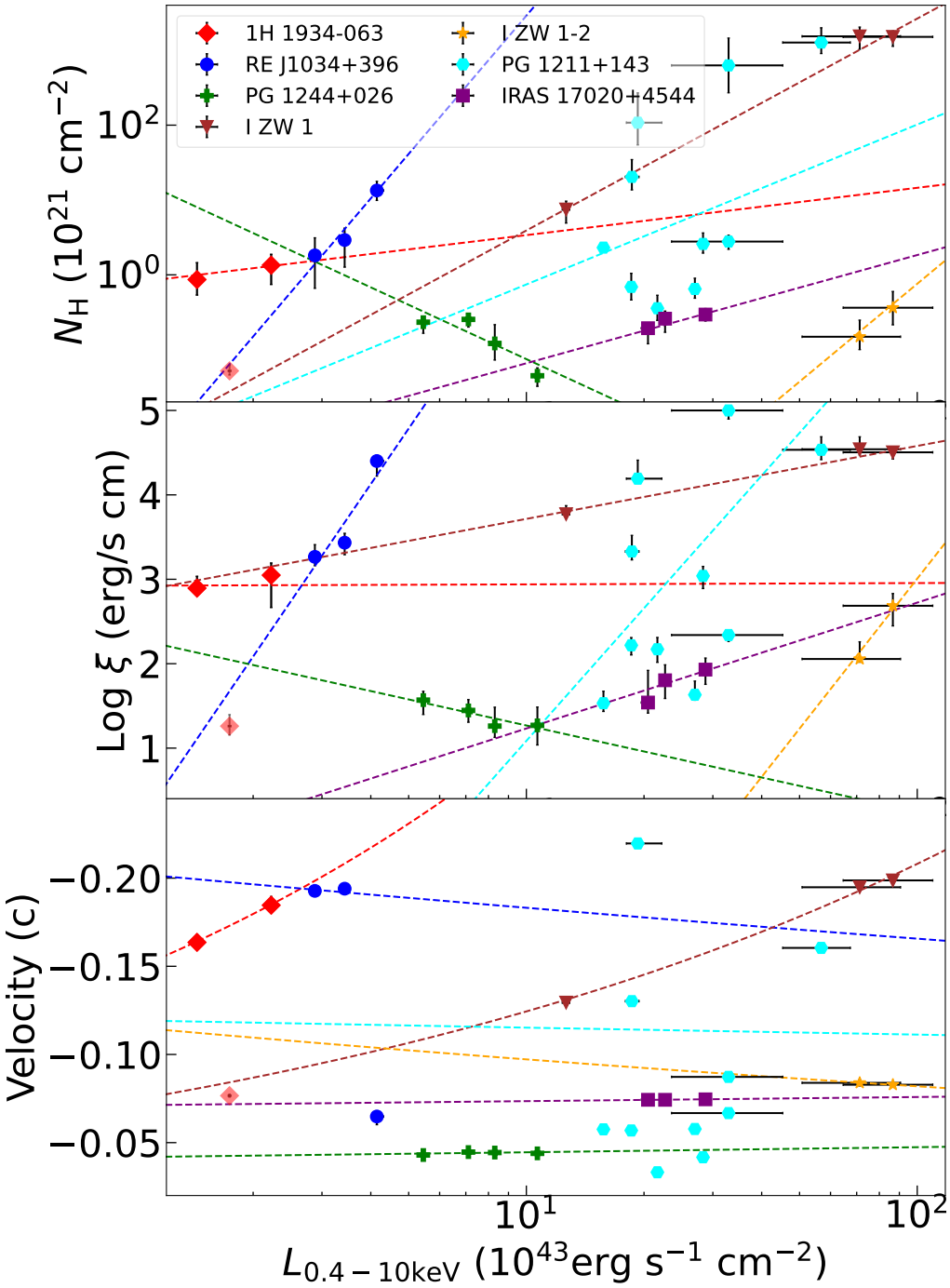

Fig. 6.6 The column density (*top*), ionization parameter (*middle*) and velocity (*bottom*) of the photoionized absorbing plasma in our sample versus the unabsorbed luminosity between 0.4–10 keV. The 'I ZW 1-2' refers to the second UFO in I ZW 1. The fits with a power function are performed and depicted by *dashed* lines. See details in Section 6.5.3.

Table 6.4 Table of the fitted power indexes of the column density, ionization parameter, and velocity of the photoionized plasma in our sample (plus the published results) with their $1\,\sigma$ uncertainties versus the unabsorbed luminosity between 0.4–10 keV.

Names	Γ_{N_H}	$\Gamma_{\log\xi}$	$\Gamma_{\rm velocity}$
This work			
1H 1934-063	0.63 ± 1.49	0.02 ± 1.58	0.27 ± 0.09
RE J1034+396	6.13 ± 1.62	6.79 ± 2.65	-0.04 ± 0.54
PG 1244+026	-2.41 ± 1.10	-1.02 ± 0.18	0.03 ± 0.04
PG 1211+143	2.14 ± 1.35	5.22 ± 3.08	-0.02 ± 0.52
I ZW 1	2.83 ± 0.30	0.86 ± 0.15	0.22 ± 0.03
I ZW 1-2	4.34 ± 3.76	5.90 ± 2.66	-0.07 ± 0.14
IRAS 17020+4544	1.45 ± 0.55	1.49 ± 0.31	0.014 ± 0.004
Published work			
Mrk 1044[a]	1.59 ± 0.98	1.08 ± 0.41	0.39 ± 0.16
1H 0707-495[b]	1.25 ± 0.51	1.83 ± 0.77	-0.15 ± 0.05
IRAS 13224-3809[c]	-0.08 ± 0.04	0.28 ± 0.11	0.05 ± 0.02
PDS 456[d]			0.24 ± 0.03

References: a: [374], b: [372], c: [259], d: [220]

parameter of the UFO in 1H 1934-063 remain constant with large uncertainties, due to the limited observations. As we described in Sec.6.5.1, the UFO in PG 1244+026 shows well-constrained anticorrelations, likely due to the less responsive UFO at distant places, awaiting future investigations. According to the definition of the ionization parameter (Eq.1.9 introduced in Sec.1.2.2.1.1), the slope $\Gamma_{\log\xi}$ that is consistent with unity suggests a UFO responding to the ionizing luminosity instantaneously. However, in our sample, strictly speaking, only the UFO in I ZW 1 presents the instantaneous response, although that in IRAS 17020+4544 is also likely to be another case if we slightly relax the uncertainty range above $1\,\sigma$. As for the other three UFOs with positive slopes (i.e. RE J1034+396, PG 1211+143, and I ZW 1-2), the values are way higher than the unity but with large uncertainties, due to either degenerated solutions, or a multi-phase nature, or only two points. As a result, we prefer to claim that most UFOs in our sample (5/7) respond to the radiation field (hotter-when-brighter) but 4 UFOs (three plus 1H 1934-063) do not have well-constrained trends of the column density and ionization parameter, due to the complex nature of UFOs and limited data.

Different from $N_{\rm H}$ and $\log\xi$, UFO velocities are precisely measured thanks to the powerful resolution of RGS and narrow line width of absorption lines, leading to relatively better constrained $\Gamma_{\rm velocity}$. However, only 2 out of 7 UFOs (1H 1934-063 and I ZW 1) exhibit positive $\Gamma_{\rm velocity}$ ($\geq 3\sigma$), while the others are consistent with being zero within their uncertainties.

Again, 3 out of 5 constant cases (RE J1034+396, PG 1211+143, and I ZW 1-2) have large uncertainties due to the complex nature of UFOs and limited data points. Although $\Gamma_{\rm velocity}$ of IRAS 17020+4544 is also positive within 1σ, the proximity of its value to zero, a probability of 37% to be constant given by Akaike information criterion (AIC, [119]) calculations, leads to its classification as constant. The positive $\Gamma_{\rm velocity}$ points towards a radiatively-driven UFO, while a constant value may result from the stacked flux-resolved spectra smearing out the lines and trends. Theoretical predictions, as presented by Matzeu et al. [220], i.e. Eq.4.5, suggest that the net radiatively-driven (i.e. radiative minus gravitational force) outflow should exhibit a relationship involving the outflow velocity, luminosity, and launching radius $R_{\rm w}$. However, none of the positive $\Gamma_{\rm velocity}$ in our sample reach up to 0.5 as predicted. This deviation may be attributed to the variations in the launching radius or a variable correction factor, due to the relatively stable UV/optical flux and the fluctuating X-ray flux. Another consideration is the possible influence of the magnetic launching mechanism.

6.5.4 Correlations between evolution slopes and intrinsic AGN properties

Furthermore, we explored the potential correlations between the slopes of UFO properties as a function of luminosity and the intrinsic properties of AGN, listed in Tab.6.1. The properties consists of the black hole mass $M_{\rm BH}$, bolometric luminosity $L_{\rm bol}$, Eddington ratio $\lambda_{\rm Edd}$, and inclination angle i. The plots for each combination are depicted in Fig.A.7. The Pearson correlation coefficients r and the corresponding p-values were calculated for each pair of quantities.

We do not find any statistically significant correlations among all pairs of quantities, as suggested in previous works by [337, 106], except for the combination between the Eddington ratios $\lambda_{\rm Edd}$ and velocity slopes $\Gamma_{\rm velocity}$ (see the bottom plot of panel c of Fig.A.7), showing a moderate anti-correlation with a Pearson correlation coefficient of $r = -0.57$ and a p-value of 0.065. However, we caveat that the results of PG 1211+143 derived from multi-phase UFOs are included as well during the correlation calculations. After removing PG 1211+143, we find an anti-correlation with a Pearson correlation coefficient of $r = -0.79$ and a p-value of 0.007. That pair is depicted in Fig.6.7. The linear regression is conducted on the data in the linear-log scale, yielding

$$\Gamma_{\rm velocity} = (-0.51 \pm 0.14) \log \lambda_{\rm Edd} + (0.07 \pm 0.04). \tag{6.1}$$

The fit is illustrated in Fig.6.7 with the blue line and 1σ uncertainty is represented by the shaded area. The explanation for this anti-correlation is discussed in Section 6.6.1.

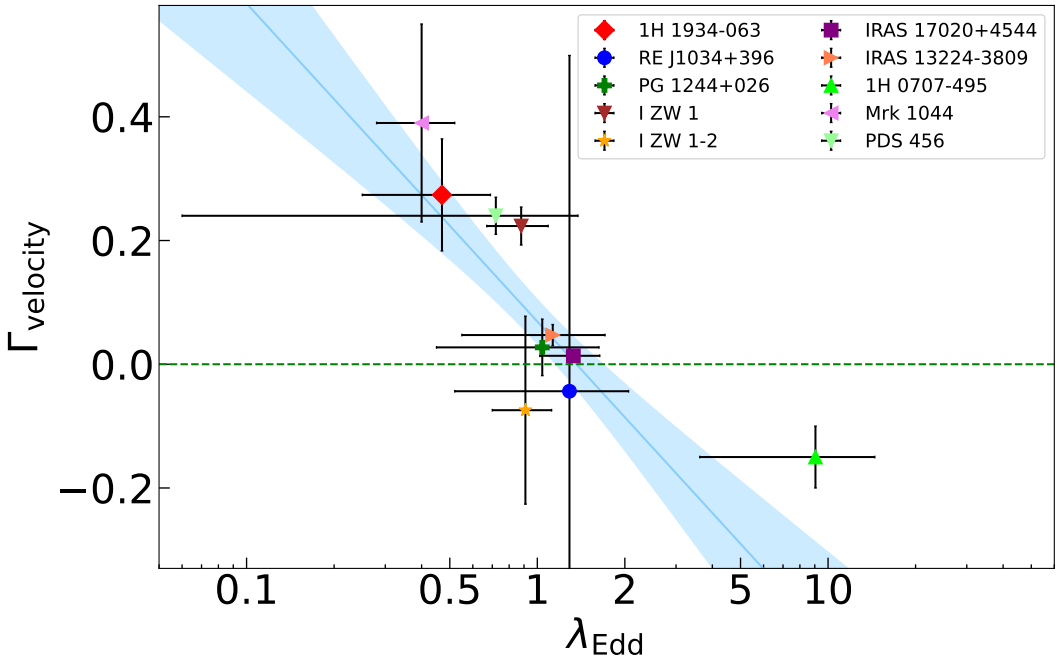

Fig. 6.7 The evolution slopes of the UFO velocity $\Gamma_{\rm velocity}$ versus Eddington ratio $\lambda_{\rm Edd}$. The data come from the results listed in Tab.6.1 and 6.4. The horizontal dashed line denotes $\Gamma_{\rm velocity} = 0$. The blue line shows the linear regression fitted to the data in the linear-log scale with 1σ uncertainty shaded. PG 1211+143 is excluded from this plot due to multi-phase UFOs.

6.6 Discussion

6.6.1 Anti-correlation between $\Gamma_{\rm velocity}$ and $\lambda_{\rm Edd}$

In Sec.6.5.4, we have shown evidence for an anti-correlation between the evolution slope of velocity as a function of luminosity and the Eddington ratio with a high statistical significance. This indicates that the outflow is less responsive, in velocity space, to the same change of the ionizing luminosity. The dependence of the velocity on the source luminosity, $\Gamma_{\rm velocity}$, represents a form of 'radiation acceleration'. According to the standard thin disk accretion model [316], an anticipated outcome of the force multiplier is the increasing acceleration of UFOs as the Eddington ratio rises. However, during the transition to the high-/super-Eddington regime, remarkable changes occur in the geometric configuration, as depicted in Figure 6.8. It has been ubiquitously accepted that the inner part of the accretion disk would become slim around highly-accreting black holes [2, 240, 136, 47].

In this scenario, the approximation, to first order, is to assume that winds are launched at the point where the local Eddington limit is approached, or the so-called spherization radius $R_{\rm sp}$ [316, 278]. In the high/super-Eddington regime, this radius is proportional to the dimensionless mass accretion rate normalized by Eddington mass accretion rate, $\dot{m} \equiv \dot{M}_{\rm acc}/\dot{M}_{\rm Edd}$, where $\dot{M}_{\rm Edd}$ is the mass accretion rate at the Eddington limit,

$$R_{\rm sp} \propto R_{\rm in}\dot{m}. \tag{6.2}$$

The wind launching radius will thus increase as the Eddington ratio rises, coupled with reduced Keplerian velocity, thus leading to a slower launching velocity.

Within the slim disk, especially below $R_{\rm sp}$, the frequent interaction between matter and photons delays the liberation of the radiation energy arising in the deep disk. The radiation energy is thus trapped in the accretion flow and can fall onto the black hole with the accreting gas without being radiated away [241]. Therefore, the observed luminosity in the slim disk is expected to increase slower than that of the thin accretion disk as the accretion rate increases, resulting in reduced radiation acceleration.

Additionally, the intense radiation field can result in an over-ionization of plasma in the inner part of the accretion disk, leading to a decrease in the cross-section σ [307, 152],

$$\sigma \propto \frac{\log E}{E} \tag{6.3}$$

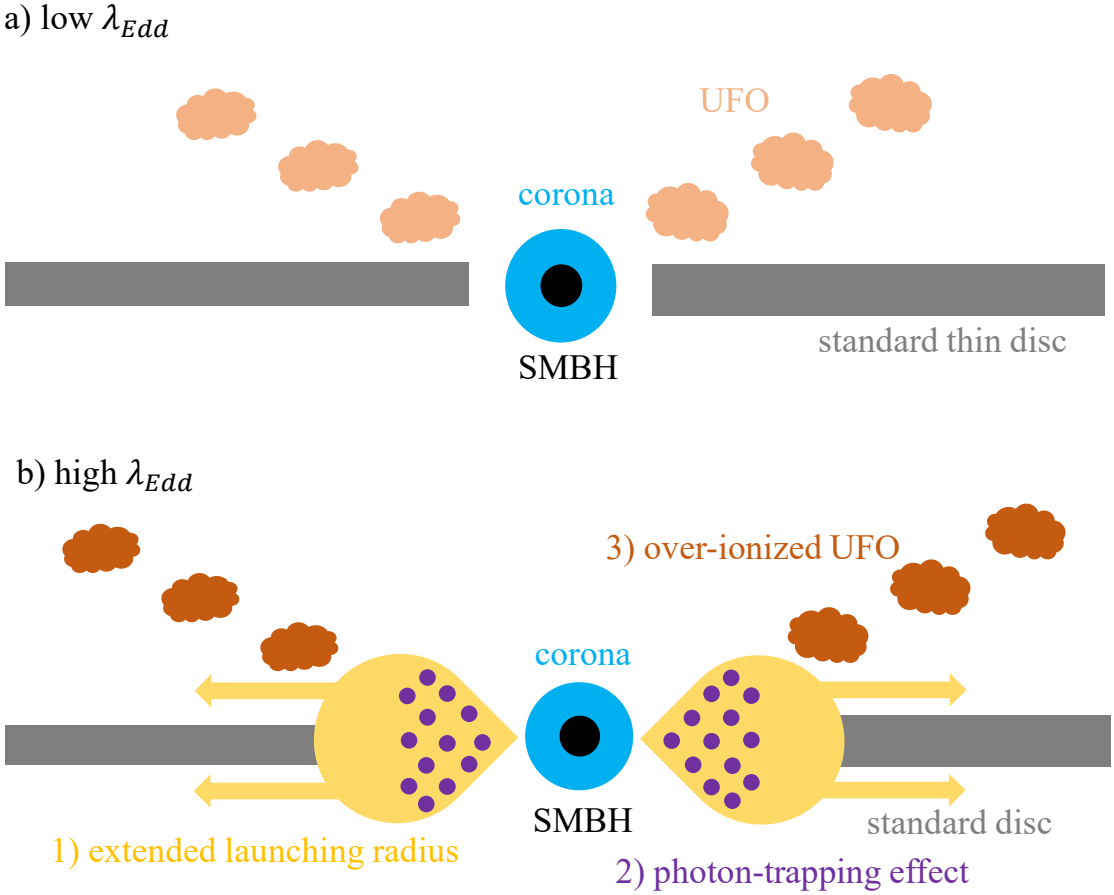

Fig. 6.8 The simplified schemes of AGN with low (*top*) and high (*bottom*) accretion rates. The SMBH is surrounded by a standard thin disk and a hot corona. *Top panel*: The ultra-fast outflow is launched by the radiation field from the accretion disk. *Bottom panel*: The inner part of the accretion disk becomes slim in the high-accretion regime. The UFO launching radius could be extended outwards with a lower Keplerian velocity, leading to a slower UFO launching velocity. Within the slim disk, the photon-trapping effect becomes non-negligible, reducing the observed luminosity. Moreover, the plasma from the inner accretion region can be over-ionized by the bright X-ray luminosity and experience less radiative force.

where E is the energy available for the ionization of plasma. The launched winds thus become transparent to X-ray photons and experience low radiatively-driven force, dampening the radiation acceleration.

The combination of these three mechanisms is likely to result in the reduction of acceleration, reproducing the observed anti-correlation between $\Gamma_{\rm velocity}$ and $\lambda_{\rm Edd}$. Nevertheless, we have to caution that the observed trend is based on a sample of only 10 points. The systematic flux-resolved analysis of AGN across various accretion rates ($\lambda_{Edd} < 0.1$ or $\lambda_{Edd} > 1$) is required to constrain the discovered trend. Furthermore, theoretical simulations about how the properties of UFOs launched by different mechanisms evolve with the accretion rates should be done in the future for comparison with the observational results.

6.6.2 Implications for AGN feedback

According to Eq.1.14, we estimate the kinetic power of UFOs in our sample (plus the published results), listed in Tab.6.5. UFO properties are taken from results of stacked spectra, so the secondary UFO of PG 1211+143 in the time-averaged spectrum is also included and denoted as 'PG 1211+143-2'. The conservative value of the solid angle is $\Omega = 0.3$ determined by the observational UFO detection rate [339] and is consistent with the GR-MHD simulations of radiatively-driven winds in super-Eddington systems [330]. By assuming that the outflow mass rate is comparable to the accretion rate $\dot{M}_{\rm out} \sim \dot{M}_{\rm acc}$, which is reasonable in high-accretion systems, the filling factor could be derived through Eq. 23 in [167].

In general, the lower limit and upper limit on location can be constrained by Eq.1.11 and 1.12. Correspondingly, the density is derived through the ionization definition. Alternatively, we can use the rapid UFO ionization responses to the continuum, exemplified by I ZW 1 and IRAS 17020+4544, both of which have $\Gamma_{\log\xi}$ values close to unity, to derive constraints on their respective locations [145]. The average duration of time segments sharing the same flux level (i.e. regions with the same color in Fig.6.2) is 3260 s for I ZW 1 and 1300 s for IRAS 17020+4544. The on-time response requires that the ionic recombination must be completed within this duration. Therefore, the upper limit on the location can be estimated through the ionization definition by considering the recombination time, which is inversely proportional to the plasma density. Using the `rec_time` code in SPEX, we estimated that UFOs are launched from distances $< 203\,R_{\rm g}$ for I ZW 1 and $< 7000\,R_{\rm g}$ for IRAS 17020+4544.

The kinetic energy of most UFOs in our samples has surpassed the theoretical criterion, suggesting that UFOs have enough influence on the surrounding medium and host galaxy. An exception is observed for UFOs in PG 1211+143, consistent with what was found in Danehkar et al. [51]. However, the total kinetic power of two UFOs reaches the threshold.

Table 6.5 Table of the ionizing luminosity $L_{\rm ion}$ (1–1000 Ryd), kinetic power $L_{\rm kin}$, filling factor $C_{\rm V}$, ratio between the kinetic energy and Eddington luminosity $L_{\rm kin}/L_{\rm Edd}$, location R, and density $n_{\rm H}$ of UFOs in our sample (plus the published results).

Names	$L_{\rm ion}$ (1–1000 Ryd) (10^{43} erg/s)	$C_{\rm V}^{a}$ (10^{-3})	$L_{\rm kin}^{b}$ (10^{43} erg/s)	$L_{\rm kin}/L_{\rm Edd}$ %	R ($R_{\rm g}$)	$n_{\rm H}$ (cm^{-3})
This work						
1H 1934-063	1.7	2.7	2.7	7.1	69–1.2×10^{5}	8.3×10^{6}–2.3×10^{13}
RE J1034+396	3.8	7.1	8.2	26.0	54–1.8×10^{5}	3.5×10^{6}–4.0×10^{13}
PG 1244+026	7.0	0.7	1.6	1.0	10^{3}–6.4×10^{6}	1.7×10^{4}–6.7×10^{11}
PG 1211+143	20	1.2	7.4	0.4	6.2×10^{2}–4.3×10^{5}	3.7×10^{4}–1.8×10^{10}
PG 1211+143-2	20	5.6	2.8	0.1	1.6×10^{3}–2.0×10^{6}	6.4×10^{2}–9.6×10^{8}
I ZW 1	72.2	71.2	62.9	17.8	52–133	3.8×10^{10}–2.5×10^{11}
I ZW 1-2	72.2	0.5	11.2	3.2	2.9×10^{2}–3.4×10^{6}	2.0×10^{4}–2.7×10^{12}
IRAS 17020+4544	22.6	0.2	2.7	3.6	3.6×10^{2}–7.0×10^{3}	9.2×10^{10}–3.5×10^{13}
Published work						
Mrk 1044[c]	3.9	7.0	1.5	4.4	98–6.6×10^{3}	10^{9}–4.5×10^{12}
1H 0707-495[d]	14.2	8.0	2.7	13.7	95–1.9×10^{3}	5×10^{10}–10^{13}
IRAS 13224-3809[e,f]			2.8	3.7	50–170	10^{10}–10^{12}
PDS 456[g]	5000		2000	15.0	32–500	3.2×10^{6}–7.4×10^{8}

Notes: a: The filling factor is calculated by assuming an outflow rate comparable to the accretion rate $\dot{M}_{\rm out}\sim\dot{M}_{\rm acc}$ [167]. b: $L_{\rm kin}$ in this work is calculated by assuming a covering factor of $\Omega=0.3$ [339, 330]. **References:** c: [374], d: [372], e: [252], f: [259], g: [235]

Moreover, due to their transient occurrence, the other high-velocity and highly ionized UFOs in PG 1211+143 are not included but may have a larger influence on the host galaxy. Within our sample, the UFO in RE J1034+396 is the most significant contributor ($\sim 26\% L_{\rm Edd}$) to its host galaxy, even larger than those in the powerful quasar PDS 456 and the super-Eddington NLS1 1H 0707-495. The primary UFO in I ZW 1 is the second-largest contributor to its host galaxy in our sample ($\sim 18\%$), which is consistent with the estimation from Reeves and Braito [285] (15–25%). Additionally, the location of this UFO is tightly constrained, $R \sim 52$–$133\,R_{\rm g}$, indicating its origin within the inner accretion disk with a high density $> 10^{10}\,{\rm cm}^{-3}$.

6.7 Conclusions

In this Chapter, we present a systematic analysis of the available archival *XMM-Newton* observations of six highly accreting NLS1 galaxies through high-resolution time- and flux-resolved spectroscopy. In summary, the results of our analysis are the following:

- The powerful method of the photoionization model scan over the high-resolution RGS spectra reveals three previously unreported UFOs in the archival datasets of RE J1034+396, PG 1244+026, and I ZW 1.
- The UFO detection in our sample combined with the literature [249] exhibits an inclination-dependent behavior, where most UFOs are detected in AGN with an inclination angle between 30–60°, most likely due to selection effects.
- 5 out of 7 UFOs in our sample present a positive dependence of the column density and ionization state on the X-ray luminosity, suggesting that they respond to the radiation field.
- The ionization parameter and column density of the UFO in PG 1244+026 are anti-correlated with the X-ray luminosity, which is challenging to explain and awaits further investigations.
- Only 2 out of 7 UFOs within the sample show a positive correlation between the velocity and X-ray luminosity, indicating a radiatively-driven UFO. while the rest remains constant, probably due to the smeared lines of flux-resolved spectra.
- We do not find any correlation between the dependence of the UFO column density and ionization parameter on X-ray luminosity and AGN intrinsic properties, such as the black hole mass, bolometric luminosity, Eddington ratio, and inclination.

- We discover an anti-correlation between the evolution slope of UFO velocity with luminosity (i.e. radiation acceleration) and the Eddington ratio. It may be explained by the combination of an extended wind launching radius, photon-trapping effect, and the over-ionization of plasma in highly-accreting systems.
- We estimate the location and energetics of UFOs and conclude that they could exert a significant feedback impact on the surrounding environment.

Chapter 7

Conclusions and Future Research

7.1 Conclusions

In this thesis, I have employed high-resolution X-ray spectroscopy, complemented by variability analysis, to study the nature, launching mechanisms, and structure of UFOs and their impact on the accretion flow and the surrounding environments in a total of eight highly accreting AGN.

The main conclusions are:

- UFOs exhibit significant variability and commonly display characteristics of multi-phase structures, indicating a stratified wind structure in AGN.
- The presence of blueshifted emission lines, which are rarely observed in AGN spectra, may be associated with the high Eddington accretion rates.
- UFOs originating from inner areas of the accretion disk may interact with the accretion inflows, leaving imprints in X-ray spectra.
- UFOs in high- and super-Eddington AGN are likely driven by the radiation pressure but the radiation acceleration can decrease as the accretion rate approaches or exceeds the Eddington limit.
- UFOs may have sufficient kinetic energy for driving AGN feedback to affect the evolution of host galaxies.

7.2 Open questions on AGN outflows

This thesis has revealed the complexity of UFO launching mechanisms and the variable nature of UFOs based on a limited sample of AGN and one of the most advanced high-resolution instruments (i.e. *XMM-Newton*/RGS) for the last 24 years. However, there are still several open questions on AGN outflows:

1. What are the net accretion (growth) rates of SMBHs?
   The estimation of the net accretion rate of SMBHs heavily depends on the detection and characterization of outflows in the system. It may be underestimated by orders of magnitude if outflows are overlooked or loosely constrained. High-quality high-resolution data and efficient search methods are both indispensable to discovering outflows and strictly constraining plasma parameters.

2. What drives the UFOs?
   Radiation pressure and magnetic fields are both likely to drive UFOs. The UFO launching mechanisms could be determined by constraining UFO velocity responses to variations in the source luminosity. However, the quality of current data limits our exploration in this direction and only ten AGN in Chapter 6 are well investigated. Additionally, resolved absorption line profiles can also determine the wind launching mechanisms, as mentioned in Sec.1.2.2.2.3, requiring high-resolution observatories.

3. Is there any connection between different types of AGN winds?
   The structure of AGN winds and the connection between various types of winds, e.g. UFOs, E-UFOs, WAs, and galaxy-wide winds (detected in multi-wavelengths) are still unclear, although WAs were proposed to be generated by the Compton cooling of UFOs shocking against the ISM with E-UFOs as an intermediate state and propagating into galaxy scales [337, 271, 340, 314]. High-resolution X-ray observatories capable of distinguishing different X-ray winds and the utilization of multi-wavelength observations are necessary to facilitate the exploration of connections among them.

4. Are outflow rates energetic enough to affect the evolution of the host galaxy?
   The lack of constraints on the location of X-ray absorbers limits our ability to estimate their kinetic energy and to make meaningful comparisons with winds observed at multiple wavelengths. Determining the location of these winds necessitates an initial constraint on their gas density through the ionization parameter's definition (see Eq. 1.9). There are two effective methods to gauge gas density, including density-sensitive spectral lines and the recombination timescale of ions, as described in Sec.1.2.2.1.2.

However, the density-sensitive absorption lines in the X-ray band are rather weak in most AGN, requiring observatories with large collecting areas. The method using recombination timescale of ions depends on the development of time-dependent photoionization models, such as `TPHO` and `TEPID` [201], as well as the high-quality data capable of tracing the plasma response to source variations.

7.3 Future Research and Missions

This section will introduce my near-future plan for X-ray studies of AGN outflows, and introduce recent and near-future X-ray missions, including *XRISM*, *NewAthena*, and *LEM*, which could help solve open questions mentioned in Sec.7.2.

7.3.1 Efficient Ionized Outflow Search

As previously introduced in Sec.2.3, automated routines have been developed and employed for the detection of ionized winds in X-ray spectra across this thesis. The detection statistical significance is determined by MC simulations. An efficient MC method based on cross-correlation, described in Sec.2.3.3, can reduce the computational cost by four orders of magnitude, while so far it has only been developed for line searches and applied in Chapter 5 and on ULX spectra [173].

Recently, I have made significant enhancements and extensions to this method, shifting its application from line searches to photoionization model scans. For instance, I simulated 10000 spectra and obtained their residual spectra based on the RGS spectrum of 1H 1934-063 in Chapter 5, and then created a set of model spectra generated by a multi-dimensional grid of `XABS` parameters to cross-correlate residual spectra. The resulting significance map, including look-elsewhere effects, is shown in Fig.7.1 (similar to the right panel of Fig.5.6), where the significance of the best solution is around 3.2σ. This advancement facilitates rapid wind detection and parameter recovery of any ionized plasma within X-ray spectra, decreasing the required computation time from 10^8 seconds down to 10^4 seconds. Its remarkable efficiency paves the way for extensive population studies of UFOs, especially in the era of high-resolution X-ray observatories. These missions will produce a wealth of high-quality, high-resolution data, which would demand substantial computational time for traditional spectral fitting approaches.

I will carry out a large population study of AGN ionized winds, in particular searching the *XMM-Newton* and *Chandra* archives of AGN, as well as upcoming *XRISM* observations. By systematically analyzing UFOs in a large sample, including those detected in AGN with

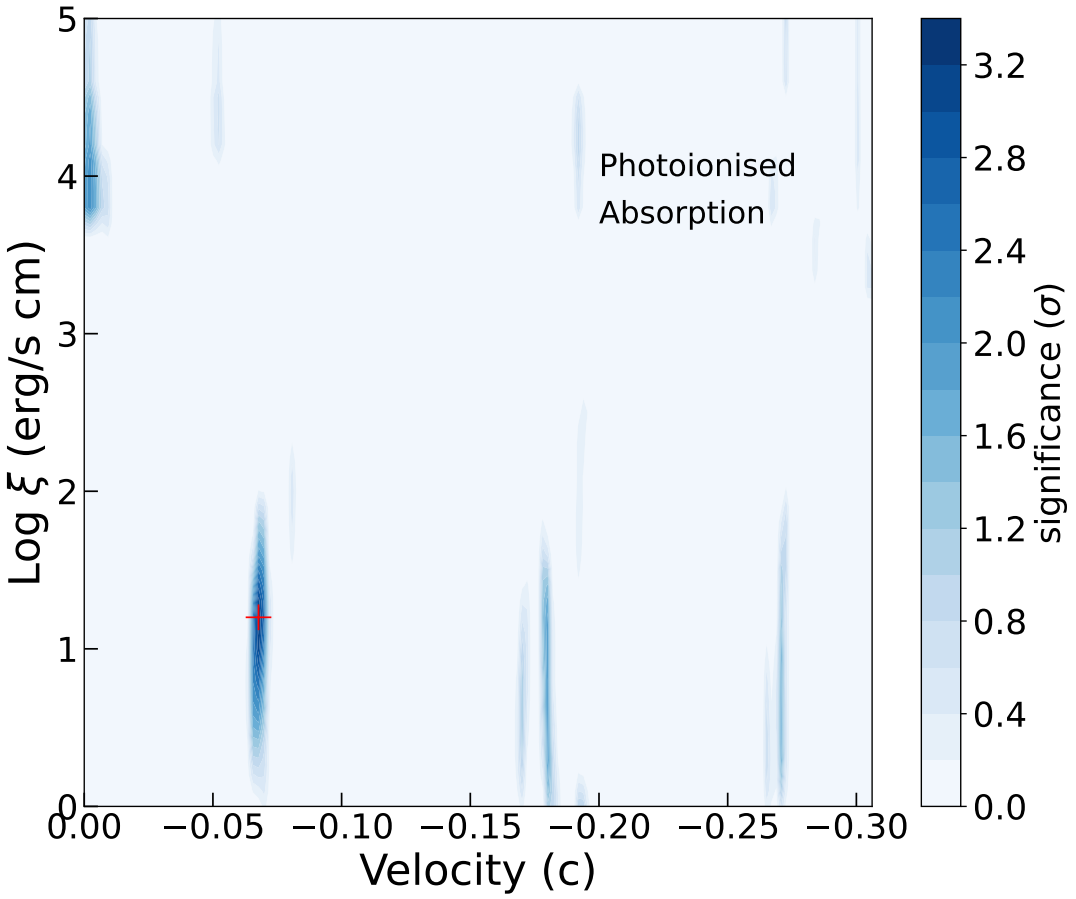

Fig. 7.1 The true detection significance of UFO solutions in 2015 X-ray spectrum of 1H 1934-063 [373]. The real and simulated spectra were searched in a multi-dimensional grid of the ionization state and velocity with a line width of 900 km/s, based on the cross-correlation rather than time-consuming spectral fits, decreasing the required computation time from 10^8 seconds down to 10^4 seconds.

Eddington ratios beyond the scope of this thesis, $\lambda_{\rm Edd} > 1$ or $\lambda_{\rm Edd} < 0.1$, I aim to gain a comprehensive understanding of UFO launching mechanisms. Comparing the energetics, structure, and location of different winds will potentially provide insights into the impact of these winds on the surrounding AGN environments.

7.3.2 Future X-ray missions

7.3.2.1 X-ray Imaging and Spectroscopy Mission (*XRISM*)

In September 2023, the X-ray Imaging and Spectroscopy Mission (*XRISM*, [332]) with unprecedented spectral resolution in the hard X-ray band, has been launched, which will open a new era of high-resolution X-ray spectroscopy. The main instrument onboard *XRISM* is an X-ray micro-calorimeter named Resolve, with a high spectral resolution of 5 eV approximately constant across the energy band of 0.3–12 keV. This results in a moderate resolution of $R = E/\Delta E \sim 200$ at 1 keV (comparable or worse than *XMM-Newton*/RGS at this energy) but a high resolution of $R \gtrsim 1000$ in the iron K band (around 7 keV, see top panel of Fig.7.2). *XRISM* therefore is an ideal instrument for studies of highly ionized plasma in the iron K band.

The effective area of the mirrors onboard *XRISM* is 150–300 $\rm cm^2$ across the energy band (slightly better than RGS, see bottom panel of Fig.7.2). It offers a relatively poor 1–2 arcmin spatial resolution and a field of view of 3×3 arcmin separated into 36 pixels, each acting as an individual micro-calorimeter. The high spectral resolution but limited collecting area and spatial resolution means that *XRISM* is most useful for observations of sources such as X-ray binaries, and bright nearby AGN (see Fig.7.3 for an example simulation) and ULXs. *XRISM* can separate the broad iron K reflection features from the narrow wind absorption lines, resulting in much more confident detection of (perhaps multiphase) winds in AGN and X-ray binaries. Furthermore, *XRISM* will bring a revolution beyond the field of winds, particularly to studies of extended X-ray sources such as galaxy clusters and supernova remnants [370].

7.3.2.2 New Advanced Telescope for High Energy Astrophysics (*NewAthena*)

The New Advanced Telescope for High Energy Astrophysics (*NewAthena*) mission, a re-designed version of *Athena* [234], is one of the European Space Agency flagship observatories to be launched in late 2030s. It will carry two main instruments: the Wide Field Imager (WFI, [284]) and the X-ray Integral Field Unit (X-IFU, [18, 17]). WFI is a wide field (40 arcmin) CCD camera with moderate spectral resolution (50–100 eV), benefiting from the ~ 5 arcsec spatial resolution of the telescope. X-IFU is a micro-calorimeter similar to Resolve

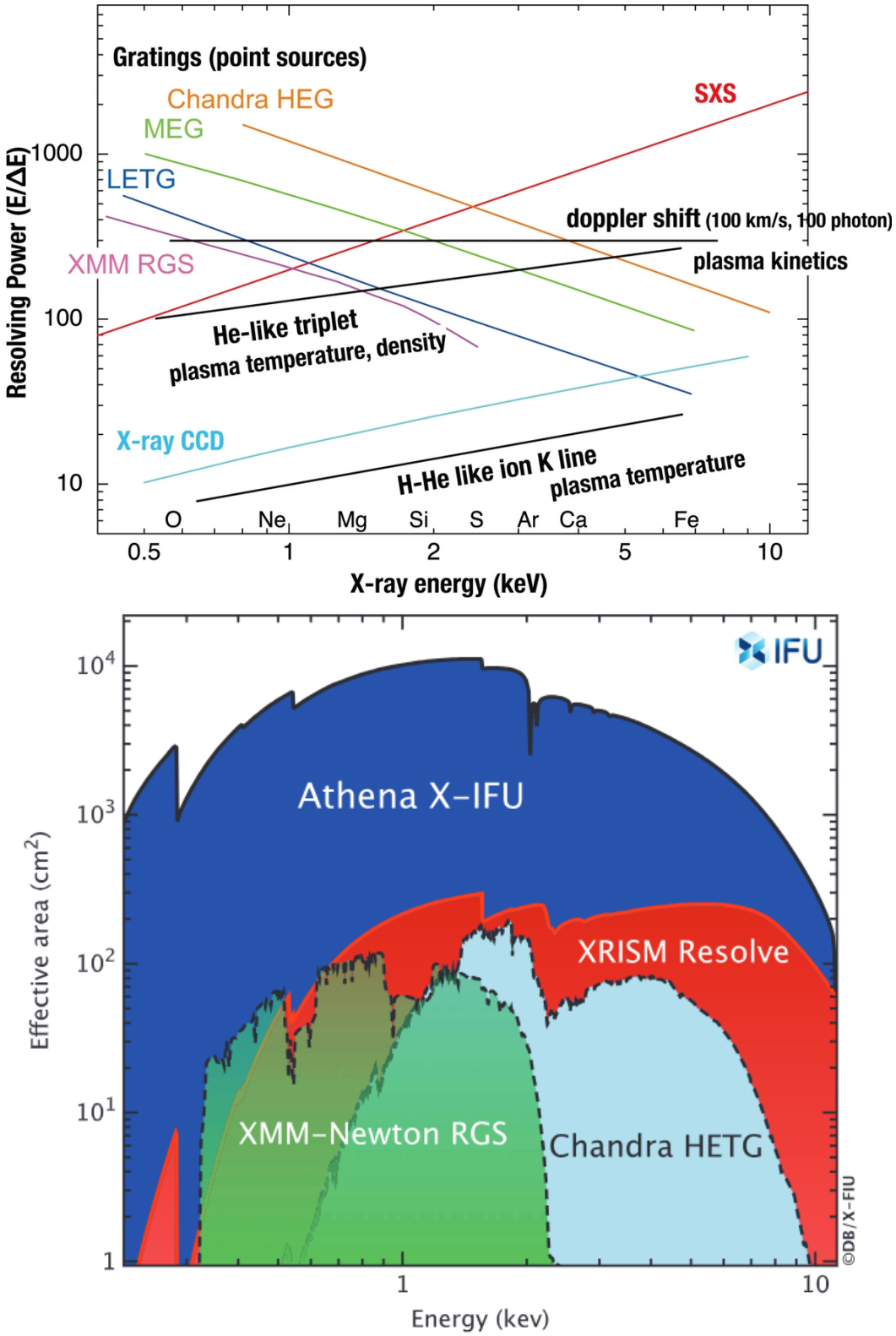

Fig. 7.2 *Top*: Resolving power of *Hitomi*/SXS [328] compared with *XMM-Newton*/RGS, *Chandra*/HETG and CCD detectors (credit to [233, 69]), where *XRISM*/Resolve is the replacement for the Soft X-ray Spectrometer (SXS) onboard *Hitomi* (lost in 2016). Black lines indicate the resolving power required to distinguish K lines from H- and He-like ions, triplet lines from He-like ions, and a Doppler shift with 100 km/s accuracy. *Bottom*: Effective areas of *Athena*/X-IFU, *XRISM*, *XMM-Newton*/RGS, and *Chandra*/HETG (credit to [18]).

onboard *XRISM*, but with a better spectral resolution of 2–3 eV across 0.2–12 keV and with significantly more (4000) active pixels (vs 36 on *XRISM*).

Both instruments will benefit from a large mirror with a total collecting area of $1.4\,m^2$. The large collecting area will be the main driver for the science of accretion disc winds with *NewAthena*, allowing objects $50\times$ fainter to be studied with a similar level of detail as the objects observed with XRISM. For point X-ray sources, X-IFU will be able to carry out similar science as the micro-calorimeter onboard XRISM, but with much shorter exposures (see Fig.7.3), or for much more distant objects. It will therefore be able to perform a large population study of accretion disk winds to great detail, as well as detect disk winds in high-redshift AGN. For the bright X-ray sources, X-IFU will be able to perform time-resolved spectral studies on the dynamical timescales of winds to determine the launching mechanism and location of winds. Beyond the disk wind science, *NewAthena* will bring another revolution in the studies of extended sources due to very good spatial resolution and a large number of X-IFU active pixels.

7.3.2.3 Line Emission Mapper (*LEM*)

Line Emission Mapper (*LEM*, [175]) is a proposed X-ray mission concept which, if approved, could be launched in the late 2030s. The main instrument onboard *LEM* will be a revolutionary microcalorimeter array consisting of 13,806 pixels, with a spectral resolution of 1–2 eV across 0.2–2 keV. It will have a large field of view 30×30 arcmin, and a high collecting area ($1600\,cm^2$). The instrument will offer high-quality data around the wavelength of O VII and O VIII transitions, allowing for detailed studies of less ionized outflows (which are often observed in AGN) in an energy band where *XRISM* and *NewAthena* will offer relatively poor spectral resolutions ($R < 400$). Furthermore, the combination of a large collecting area and field of view make *LEM* an exquisite observatory to study faint diffuse structures.

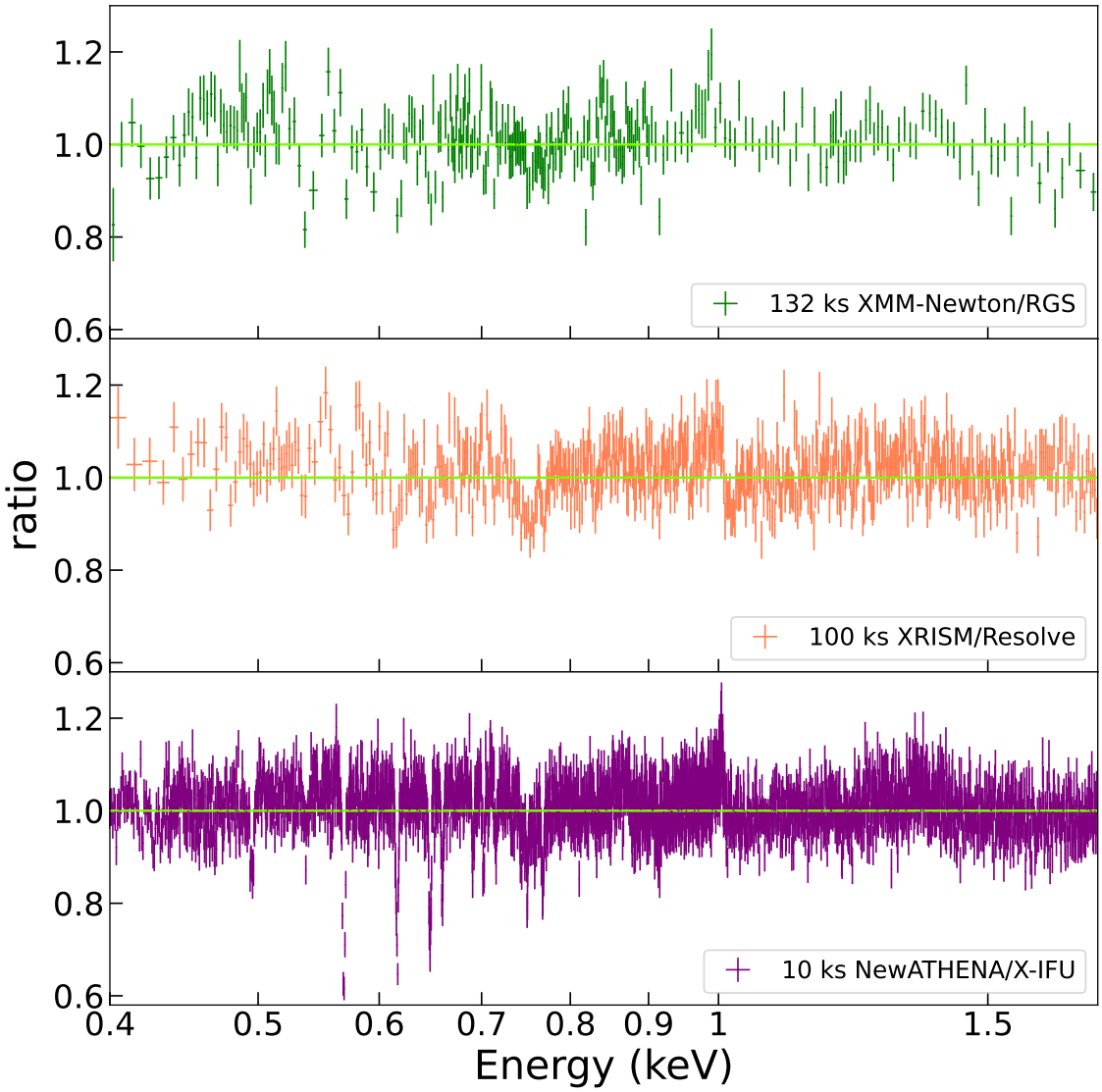

Fig. 7.3 The data/model ratio for the *XRISM*/Resolve (*middle*, 100 ks) and *NewAthena*/X-IFU (*bottom*, 10 ks) spectrum, simulated by the best-fit model obtained in Chapter 5, with the respect to the baseline continuum model. The ratio for the *XMM-Newton*/RGS spectrum is shown in the *top* panel for comparison.

References

[1] Abramowicz, M. A., Calvani, M., and Nobili, L. (1980). Thick accretion disks with super-Eddington luminosities. *ApJ*, 242:772–788.

[2] Abramowicz, M. A., Czerny, B., Lasota, J. P., and Szuszkiewicz, E. (1988). Slim Accretion Disks. *ApJ*, 332:646.

[3] Ai, Y. L., Yuan, W., Zhou, H., Wang, T. G., Dong, X. B., Wang, J. G., and Lu, H. L. (2013). A Comparative Study of Optical/Ultraviolet Variability of Narrow-line Seyfert 1 and Broad-line Seyfert 1 Active Galactic Nuclei. *AJ*, 145(4):90.

[4] Aird, J., Nandra, K., Laird, E. S., Georgakakis, A., Ashby, M. L. N., Barmby, P., Coil, A. L., Huang, J. S., Koekemoer, A. M., Steidel, C. C., and Willmer, C. N. A. (2010). The evolution of the hard X-ray luminosity function of AGN. *MNRAS*, 401(4):2531–2551.

[5] Alston, W. N. (2019). Non-stationary variability in accreting compact objects. *MNRAS*, 485(1):260–265.

[6] Alston, W. N., Done, C., and Vaughan, S. (2014a). X-ray time delays in the narrow line Seyfert 1 galaxy PG 1244+026. *MNRAS*, 439(2):1548–1555.

[7] Alston, W. N., Fabian, A. C., Buisson, D. J. K., Kara, E., Parker, M. L., Lohfink, A. M., Uttley, P., Wilkins, D. R., Pinto, C., De Marco, B., Cackett, E. M., Middleton, M. J., Walton, D. J., Reynolds, C. S., Jiang, J., Gallo, L. C., Zogbhi, A., Miniutti, G., Dovciak, M., and Young, A. J. (2019). The remarkable X-ray variability of IRAS 13224-3809 - I. The variability process. *MNRAS*, 482(2):2088–2106.

[8] Alston, W. N., Markeviciute, J., Kara, E., Fabian, A. C., and Middleton, M. (2014b). Detection of a QPO in five XMM-Newton observations of RE J1034+396. *MNRAS*, 445:L16–L20.

[9] Antonucci, R. (1993). Unified models for active galactic nuclei and quasars. *ARA&A*, 31:473–521.

[10] Arav, N., Chamberlain, C., Kriss, G. A., Kaastra, J. S., Cappi, M., Mehdipour, M., Petrucci, P. O., Steenbrugge, K. C., Behar, E., Bianchi, S., Boissay, R., Branduardi-Raymont, G., Costantini, E., Ely, J. C., Ebrero, J., di Gesu, L., Harrison, F. A., Kaspi, S., Malzac, J., De Marco, B., Matt, G., Nandra, K. P., Paltani, S., Peterson, B. M., Pinto, C., Ponti, G., Pozo Nuñez, F., De Rosa, A., Seta, H., Ursini, F., de Vries, C. P., Walton, D. J., and Whewell, M. (2015). Anatomy of the AGN in NGC 5548. II. The spatial, temporal, and physical nature of the outflow from HST/COS Observations. *A&A*, 577:A37.

[11] Armentrout, B. K., Kraemer, S. B., and Turner, T. J. (2007). A Photoionization Model for the Soft X-Ray Spectrum of NGC 4151. *ApJ*, 665(1):237–246.

[12] Arnaud, K. A. (1996). XSPEC: The First Ten Years. In Jacoby, G. H. and Barnes, J., editors, *Astronomical Data Analysis Software and Systems V*, volume 101 of *Astronomical Society of the Pacific Conference Series*, page 17.

[13] Balbus, S. A. and Hawley, J. F. (1991). A Powerful Local Shear Instability in Weakly Magnetized Disks. I. Linear Analysis. *ApJ*, 376:214.

[14] Balbus, S. A. and Hawley, J. F. (1998). Instability, turbulence, and enhanced transport in accretion disks. *Reviews of Modern Physics*, 70(1):1–53.

[15] Bambi, C. (2017). *Black Holes: A Laboratory for Testing Strong Gravity*.

[16] Bardeen, J. M., Press, W. H., and Teukolsky, S. A. (1972). Rotating Black Holes: Locally Nonrotating Frames, Energy Extraction, and Scalar Synchrotron Radiation. *ApJ*, 178:347–370.

[17] Barret, D., Albouys, V., Herder, J.-W. d., Piro, L., Cappi, M., Huovelin, J., Kelley, R., Mas-Hesse, J. M., Paltani, S., Rauw, G., Rozanska, A., Svoboda, J., Wilms, J., Yamasaki, N., Audard, M., Bandler, S., Barbera, M., Barcons, X., Bozzo, E., Ceballos, M. T., Charles, I., Costantini, E., Dauser, T., Decourchelle, A., Duband, L., Duval, J.-M., Fiore, F., Gatti, F., Goldwurm, A., Hartog, R. d., Jackson, B., Jonker, P., Kilbourne, C., Korpela, S., Macculi, C., Mendez, M., Mitsuda, K., Molendi, S., Pajot, F., Pointecouteau, E., Porter, F., Pratt, G. W., Prêle, D., Ravera, L., Sato, K., Schaye, J., Shinozaki, K., Skup, K., Soucek, J., Thibert, T., Vink, J., Webb, N., Chaoul, L., Raulin, D., Simionescu, A., Torrejon, J. M., Acero, F., Branduardi-Raymont, G., Ettori, S., Finoguenov, A., Grosso, N., Kaastra, J., Mazzotta, P., Miller, J., Miniutti, G., Nicastro, F., Sciortino, S., Yamaguchi, H., Beaumont, S., Cucchetti, E., D'Andrea, M., Eckart, M., Ferrando, P., Kammoun, E., Lotti, S., Mesnager, J.-M., Natalucci, L., Peille, P., de Plaa, J., Ardellier, F., Argan, A., Bellouard, E., Carron, J., Cavazzuti, E., Fiorini, M., Khosropanah, P., Martin, S., Perry, J., Pinsard, F., Pradines, A., Rigano, M., Roelfsema, P., Schwander, D., Torrioli, G., Ullom, J., Vera, I., Villegas, E. M., Zuchniak, M., Brachet, F., Cicero, U. L., Doriese, W., Durkin, M., Fioretti, V., Geoffray, H., Jacques, L., Kirsch, C., Smith, S., Adams, J., Gloaguen, E., Hoogeveen, R., van der Hulst, P., Kiviranta, M., van der Kuur, J., Ledot, A., van Leeuwen, B.-J., van Loon, D., Lyautey, B., Parot, Y., Sakai, K., van Weers, H., Abdoelkariem, S., Adam, T., Adami, C., Aicardi, C., Akamatsu, H., Alonso, P. E. M., Amato, R., André, J., Angelinelli, M., Anon-Cancela, M., Anvar, S., Atienza, R., Attard, A., Auricchio, N., Balado, A., Bancel, F., Barusso, L. F., Bascuñan, A., Bernard, V., Berrocal, A., Blin, S., Bonino, D., Bonnet, F., Bonny, P., Boorman, P., Boreux, C., Bounab, A., Boutelier, M., Boyce, K., Brienza, D., Bruijn, M., Bulgarelli, A., Calarco, S., Callanan, P., Campello, A. P., Camus, T., Canourgues, F., Capobianco, V., Cardiel, N., Castellani, F., Cheatom, O., Chervenak, J., Chiarello, F., Clerc, L., Clerc, N., Cobo, B., Coeur-Joly, O., Coleiro, A., Colonges, S., Corcione, L., Coriat, M., Coynel, A., Cuttaia, F., D'Ai, A., D'anca, F., Dadina, M., Daniel, C., Dauner, L., DeNigris, N., Dercksen, J., DiPirro, M., Doumayrou, E., Dubbeldam, L., Dupieux, M., Dupourqué, S., Durand, J. L., Eckert, D., Eiriz, V., Ercolani, E., Etcheverry, C., Finkbeiner, F., Fiocchi, M., Fossecave, H., Franssen, P., Frericks, M., Gabici, S., Gant, F., Gao, J.-R., Gastaldello, F., Genolet, L., Ghizzardi, S., Gil, M. A. A., Giovannini, E., Godet, O., Gomez-Elvira, J., Gonzalez, R., Gonzalez, M., Gottardi, L., Granat, D., Gros,

M., Guignard, N., Hieltjes, P., Hurtado, A. J., Irwin, K., Jacquey, C., Janiuk, A., Jaubert, J., Jiménez, M., Jolly, A., Jourdan, T., Julien, S., Kedziora, B., Korb, A., Kreykenbohm, I., König, O., Langer, M., Laudet, P., Laurent, P., Laurenza, M., Lesrel, J., Ligori, S., Lorenz, M., Luminari, A., Maffei, B., Maisonnave, O., Marelli, L., Massonet, D., Maussang, I., Melchor, A. G., Le Mer, I., Millan, F. J. S., Millerioux, J.-P., Mineo, T., Minervini, G., Molin, A., Monestes, D., Montinaro, N., Mot, B., Murat, D., Nagayoshi, K., Nazé, Y., Noguès, L., Pailot, D., Panessa, F., Parodi, L., Petit, P., Piconcelli, E., Pinto, C., Plaza, J. M. E., Plaza, B., Poyatos, D., Prouvé, T., Ptak, A., Puccetti, S., Puccio, E., Ramon, P., Reina, M., Rioland, G., Rodriguez, L., Roig, A., Rollet, B., Roncarelli, M., Roudil, G., Rudnicki, T., Sanisidro, J., Sciortino, L., Silva, V., Sordet, M., Soto-Aguilar, J., Spizzi, P., Surace, C., Fernández Sánchez, M., Taralli, E., Terrasa, G., Terrier, R., Todaro, M., Ubertini, P., Uslenghi, M., de Vaate, J. G. B., Vaccaro, D., Varisco, S., Varnière, P., Vibert, L., Vidriales, M., Villa, F., Vodopivec, B. M., Volpe, A., de Vries, C., Wakeham, N., Walmsley, G., Wise, M., de Wit, M., and Woźniak, G. (2023). The Athena X-ray Integral Field Unit: a consolidated design for the system requirement review of the preliminary definition phase. *Experimental Astronomy*, 55(2):373–426.

[18] Barret, D., Decourchelle, A., Fabian, A., Guainazzi, M., Nandra, K., Smith, R., and den Herder, J.-W. (2020). The Athena space X-ray observatory and the astrophysics of hot plasma†. *Astronomische Nachrichten*, 341(2):224–235.

[19] Begelman, M. C. and McKee, C. F. (1983). Compton heated winds and coronae above accretion disks. II. Radiativetransfer and observable consequences. *ApJ*, 271:89–112.

[20] Begelman, M. C., McKee, C. F., and Shields, G. A. (1983). Compton heated winds and coronae above accretion disks. I. Dynamics. *ApJ*, 271:70–88.

[21] Begelman, M. C., Volonteri, M., and Rees, M. J. (2006). Formation of supermassive black holes by direct collapse in pre-galactic haloes. *MNRAS*, 370(1):289–298.

[22] Bian, W.-H. and Huang, K. (2010). The host galaxy of a narrow-line Seyfert 1 galaxy, RE J1034+396, with X-ray quasi-periodic oscillations. *MNRAS*, 401(1):507–512.

[23] Blandford, R., Meier, D., and Readhead, A. (2019). Relativistic Jets from Active Galactic Nuclei. *ARA&A*, 57:467–509.

[24] Blandford, R. D. and Payne, D. G. (1982). Hydromagnetic flows from accretion disks and the production of radio jets. *MNRAS*, 199:883–903.

[25] Blustin, A. J., Page, M. J., Fuerst, S. V., Branduardi-Raymont, G., and Ashton, C. E. (2005). The nature and origin of Seyfert warm absorbers. *A&A*, 431:111–125.

[26] Boissay-Malaquin, R., Danehkar, A., Marshall, H. L., and Nowak, M. A. (2019). Relativistic Components of the Ultra-fast Outflow in the Quasar PDS 456 from Chandra/HETGS, NuSTAR, and XMM-Newton Observations. *ApJ*, 873(1):29.

[27] Boller, T., Liu, T., Weber, P., Arcodia, R., Dauser, T., Wilms, J., Nandra, K., Buchner, J., Merloni, A., Freyberg, M. J., Krumpe, M., and Waddell, S. G. H. (2021). Extreme ultra-soft X-ray variability in an eROSITA observation of the narrow-line Seyfert 1 galaxy 1H 0707-495. *A&A*, 647:A6.

[28] Boroson, T. A. (2002). Black Hole Mass and Eddington Ratio as Drivers for the Observable Properties of Radio-loud and Radio-quiet QSOs. *ApJ*, 565(1):78–85.

[29] Boroson, T. A. and Green, R. F. (1992). The Emission-Line Properties of Low-Redshift Quasi-stellar Objects. *ApJS*, 80:109.

[30] Bouwens, R. J., Illingworth, G. D., Oesch, P. A., Franx, M., Labbé, I., Trenti, M., van Dokkum, P., Carollo, C. M., González, V., Smit, R., and Magee, D. (2012). UV-continuum Slopes at z ~4-7 from the HUDF09+ERS+CANDELS Observations: Discovery of a Well-defined UV Color-Magnitude Relationship for z >= 4 Star-forming Galaxies. *ApJ*, 754(2):83.

[31] Brinkman, B. C., Gunsing, T., Kaastra, J. S., van der Meer, R., Mewe, R., Paerels, F. B., Raassen, T., van Rooijen, J., Braeuninger, H. W., Burwitz, V., Hartner, G. D., Kettenring, G., Predehl, P., Drake, J. J., Johnson, C. O., Kenter, A. T., Kraft, R. P., Murray, S. S., Ratzlaff, P. W., and Wargelin, B. J. (2000). Description and performance of the low-energy transmission grating spectrometer on board Chandra. In Truemper, J. E. and Aschenbach, B., editors, *X-Ray Optics, Instruments, and Missions III*, volume 4012 of *Society of Photo-Optical Instrumentation Engineers (SPIE) Conference Series*, pages 81–90.

[32] Buisson, D. J. K., Lohfink, A. M., Alston, W. N., Cackett, E. M., Chiang, C. Y., Dauser, T., De Marco, B., Fabian, A. C., Gallo, L. C., García, J. A., Jiang, J., Kara, E., Middleton, M. J., Miniutti, G., Parker, M. L., Pinto, C., Uttley, P., Walton, D. J., and Wilkins, D. R. (2018). Is there a UV/X-ray connection in IRAS 13224-3809? *MNRAS*, 475(2):2306–2313.

[33] Canizares, C. R., Davis, J. E., Dewey, D., Flanagan, K. A., Galton, E. B., Huenemoerder, D. P., Ishibashi, K., Markert, T. H., Marshall, H. L., McGuirk, M., Schattenburg, M. L., Schulz, N. S., Smith, H. I., and Wise, M. (2005). The Chandra High-Energy Transmission Grating: Design, Fabrication, Ground Calibration, and 5 Years in Flight. *PASP*, 117(836):1144–1171.

[34] Carter, B. (1971). Axisymmetric Black Hole Has Only Two Degrees of Freedom. *PhRvL*, 26(6):331–333.

[35] Cash, W. (1979). Parameter estimation in astronomy through application of the likelihood ratio. *ApJ*, 228:939–947.

[36] Castor, J. I., Abbott, D. C., and Klein, R. I. (1975). Radiation-driven winds in Of stars. *ApJ*, 195:157–174.

[37] Chartas, G., Brandt, W. N., and Gallagher, S. C. (2003). XMM-Newton Reveals the Quasar Outflow in PG 1115+080. *ApJ*, 595(1):85–93.

[38] Chartas, G., Brandt, W. N., Gallagher, S. C., and Garmire, G. P. (2002). CHANDRA Detects Relativistic Broad Absorption Lines from APM 08279+5255. *ApJ*, 579(1):169–175.

[39] Chartas, G. and Canas, M. H. (2018). The Variable Relativistic Outflow of IRAS 13224-3809. *ApJ*, 867(2):103.

[40] Chaudhury, K., Chitnis, V. R., Rao, A. R., Singh, K. P., Bhattacharyya, S., Dewangan, G. C., Chakraborty, S., Chandra, S., Stewart, G. C., Mukerjee, K., and Dey, R. K. (2018). Long-term X-ray variability characteristics of the narrow-line Seyfert 1 galaxy RE J1034+396. *MNRAS*, 478(4):4830–4836.

[41] Chiang, C.-Y., Walton, D. J., Fabian, A. C., Wilkins, D. R., and Gallo, L. C. (2015). Modelling the extreme X-ray spectrum of IRAS 13224-3809. *MNRAS*, 446(1):759–769.

[42] Collin, S. and Kawaguchi, T. (2004). Super-Eddington accretion rates in Narrow Line Seyfert 1 galaxies. *A&A*, 426:797–808.

[43] Costantini, E., Gallo, L. C., Brandt, W. N., Fabian, A. C., and Boller, T. (2007). A longer XMM-Newton look at IZwicky1: physical conditions and variability of the ionized absorbers. *MNRAS*, 378(3):873–880.

[44] Crenshaw, D. M. and Kraemer, S. B. (2012). Feedback from Mass Outflows in Nearby Active Galactic Nuclei. I. Ultraviolet and X-Ray Absorbers. *ApJ*, 753(1):75.

[45] Crenshaw, D. M., Kraemer, S. B., and George, I. M. (2003). Mass Loss from the Nuclei of Active Galaxies. *ARA&A*, 41:117–167.

[46] Crummy, J., Fabian, A. C., Gallo, L., and Ross, R. R. (2006). An explanation for the soft X-ray excess in active galactic nuclei. *MNRAS*, 365(4):1067–1081.

[47] Curd, B. and Narayan, R. (2023). GRRMHD simulations of MAD accretion discs declining from super-Eddington to sub-Eddington accretion rates. *MNRAS*, 518(3):3441–3461.

[48] Curran, P. A. (2014). Monte Carlo error analyses of Spearman's rank test. *arXiv e-prints*, page arXiv:1411.3816.

[49] Czerny, B., You, B., Kurcz, A., Średzińska, J., Hryniewicz, K., Nikołajuk, M., Krupa, M., Wang, J. M., Hu, C., and Życki, P. T. (2016). The mass of the black hole in RE J1034+396. *A&A*, 594:A102.

[50] Dadina, M., Cappi, M., Malaguti, G., Ponti, G., and de Rosa, A. (2005). X-ray absorption lines suggest matter infalling onto the central black-hole of Mrk 509. *A&A*, 442(2):461–468.

[51] Danehkar, A., Nowak, M. A., Lee, J. C., Kriss, G. A., Young, A. J., Hardcastle, M. J., Chakravorty, S., Fang, T., Neilsen, J., Rahoui, F., and Smith, R. K. (2018). The Ultra-fast Outflow of the Quasar PG 1211+143 as Viewed by Time-averaged Chandra Grating Spectroscopy. *ApJ*, 853(2):165.

[52] Dauser, T., Garcia, J., Parker, M. L., Fabian, A. C., and Wilms, J. (2014). The role of the reflection fraction in constraining black hole spin. *MNRAS*, 444:L100–L104.

[53] Dauser, T., Garcia, J., Wilms, J., Böck, M., Brenneman, L. W., Falanga, M., Fukumura, K., and Reynolds, C. S. (2013). Irradiation of an accretion disc by a jet: general properties and implications for spin measurements of black holes. *MNRAS*, 430(3):1694–1708.

[54] Dauser, T., Svoboda, J., Schartel, N., Wilms, J., Dovčiak, M., Ehle, M., Karas, V., Santos-Lleó, M., and Marshall, H. L. (2012). Spectral analysis of 1H 0707-495 with XMM-Newton. *MNRAS*, 422(3):1914–1921.

[55] Dauser, T., Wilms, J., Reynolds, C. S., and Brenneman, L. W. (2010). Broad emission lines for a negatively spinning black hole. *MNRAS*, 409(4):1534–1540.

[56] de Marco, B., Ponti, G., Uttley, P., Cappi, M., Dadina, M., Fabian, A. C., and Miniutti, G. (2011). PG 1211+143: probing high-frequency lags in a high-mass active galactic nucleus. *MNRAS*, 417(1):L98–L102.

[57] den Herder, J. W., Brinkman, A. C., Kahn, S. M., Branduardi-Raymont, G., Thomsen, K., Aarts, H., Audard, M., Bixler, J. V., den Boggende, A. J., Cottam, J., Decker, T., Dubbeldam, L., Erd, C., Goulooze, H., Güdel, M., Guttridge, P., Hailey, C. J., Janabi, K. A., Kaastra, J. S., de Korte, P. A. J., van Leeuwen, B. J., Mauche, C., McCalden, A. J., Mewe, R., Naber, A., Paerels, F. B., Peterson, J. R., Rasmussen, A. P., Rees, K., Sakelliou, I., Sako, M., Spodek, J., Stern, M., Tamura, T., Tandy, J., de Vries, C. P., Welch, S., and Zehnder, A. (2001). The Reflection Grating Spectrometer on board XMM-Newton. *A&A*, 365:L7–L17.

[58] Detmers, R. G., Kaastra, J. S., Steenbrugge, K. C., Ebrero, J., Kriss, G. A., Arav, N., Behar, E., Costantini, E., Branduardi-Raymont, G., Mehdipour, M., Bianchi, S., Cappi, M., Petrucci, P., Ponti, G., Pinto, C., Ratti, E. M., and Holczer, T. (2011). Multiwavelength campaign on Mrk 509. III. The 600 ks RGS spectrum: unravelling the inner region of an AGN. *A&A*, 534:A38.

[59] Dewangan, G. C., Griffiths, R. E., Dasgupta, S., and Rao, A. R. (2007). An Investigation of the Origin of Soft X-Ray Excess Emission from Ark 564 and Mrk 1044. *ApJ*, 671(2):1284–1296.

[60] Di Matteo, T., Springel, V., and Hernquist, L. (2005). Energy input from quasars regulates the growth and activity of black holes and their host galaxies. *Nature*, 433(7026):604–607.

[61] Dickey, J. M. and Lockman, F. J. (1990). H I in the galaxy. *ARA&A*, 28:215–261.

[62] Done, C., Davis, S. W., Jin, C., Blaes, O., and Ward, M. (2012). Intrinsic disc emission and the soft X-ray excess in active galactic nuclei. *MNRAS*, 420(3):1848–1860.

[63] Done, C. and Jin, C. (2016). The mass and spin of the extreme Narrow Line Seyfert 1 Galaxy 1H 0707-495 and its implications for the trigger for relativistic jets. *MNRAS*, 460(2):1716–1724.

[64] Du, P., Hu, C., Lu, K.-X., Huang, Y.-K., Cheng, C., Qiu, J., Li, Y.-R., Zhang, Y.-W., Fan, X.-L., Bai, J.-M., Bian, W.-H., Yuan, Y.-F., Kaspi, S., Ho, L. C., Netzer, H., Wang, J.-M., and SEAMBH Collaboration (2015). Supermassive Black Holes with High Accretion Rates in Active Galactic Nuclei. IV. Hβ Time Lags and Implications for Super-Eddington Accretion. *ApJ*, 806(1):22.

[65] Eddington, A. S. (1926). *The Internal Constitution of the Stars*.

[66] Edelson, R., Gelbord, J., Cackett, E., Connolly, S., Done, C., Fausnaugh, M., Gardner, E., Gehrels, N., Goad, M., Horne, K., McHardy, I., Peterson, B. M., Vaughan, S., Vestergaard, M., Breeveld, A., Barth, A. J., Bentz, M., Bottorff, M., Brandt, W. N., Crawford, S. M., Dalla Bontà, E., Emmanoulopoulos, D., Evans, P., Figuera Jaimes, R., Filippenko, A. V., Ferland, G., Grupe, D., Joner, M., Kennea, J., Korista, K. T., Krimm, H. A., Kriss, G., Leonard, D. C., Mathur, S., Netzer, H., Nousek, J., Page, K., Romero-Colmenero, E., Siegel, M., Starkey, D. A., Treu, T., Vogler, H. A., Winkler, H., and Zheng, W. (2017). Swift Monitoring of NGC 4151: Evidence for a Second X-Ray/UV Reprocessing. *ApJ*, 840(1):41.

[67] Edelson, R., Turner, T. J., Pounds, K., Vaughan, S., Markowitz, A., Marshall, H., Dobbie, P., and Warwick, R. (2002). X-Ray Spectral Variability and Rapid Variability of the Soft X-Ray Spectrum Seyfert 1 Galaxies Arakelian 564 and Ton S180. *ApJ*, 568(2):610–626.

[68] Einstein, A. (1916). Die Grundlage der allgemeinen Relativitätstheorie. *Annalen der Physik*, 354(7):769–822.

[69] Ezoe, Y., Ohashi, T., and Mitsuda, K. (2021). High-resolution X-ray spectroscopy of astrophysical plasmas with X-ray microcalorimeters. *Reviews of Modern Plasma Physics*, 5(1):4.

[70] Fabian, A. C. (2006). A short introduction to broad and variable iron lines around black holes. *Astronomische Nachrichten*, 327(10):943.

[71] Fabian, A. C. (2012). Observational Evidence of Active Galactic Nuclei Feedback. *ARA&A*, 50:455–489.

[72] Fabian, A. C., Kunieda, H., Inoue, S., Matsuoka, M., Mihara, T., Miyamoto, S., Otani, C., Ricker, G., Tanaka, Y., Yamauchi, M., and Yaqoob, T. (1994). ASCA Observations of the Warm Absorber in MCG-6–30–15: the Discovery of a Change in Column Density. *PASJ*, 46:L59–L63.

[73] Fabian, A. C., Lohfink, A., Kara, E., Parker, M. L., Vasudevan, R., and Reynolds, C. S. (2015). Properties of AGN coronae in the NuSTAR era. *MNRAS*, 451(4):4375–4383.

[74] Fabian, A. C., Rees, M. J., Stella, L., and White, N. E. (1989). X-ray fluorescence from the inner disc in Cygnus X-1. *MNRAS*, 238:729–736.

[75] Fabian, A. C., Reynolds, C. S., Jiang, J., Pinto, C., Gallo, L. C., Parker, M. L., Lasenby, A. N., Alston, W. N., Buisson, D. J. K., Cackett, E. M., De Marco, B., Garcia, J., Kara, E., Kosec, P., Middleton, M. J., Miller, J. M., Miniutti, G., Walton, D. J., Wilkins, D. R., and Young, A. J. (2020). Blueshifted absorption lines from X-ray reflection in IRAS 13224-3809. *MNRAS*, 493(2):2518–2522.

[76] Fabian, A. C., Sanders, J. S., Allen, S. W., Crawford, C. S., Iwasawa, K., Johnstone, R. M., Schmidt, R. W., and Taylor, G. B. (2003). A deep Chandra observation of the Perseus cluster: shocks and ripples. *MNRAS*, 344(3):L43–L47.

[77] Fabian, A. C., Vasudevan, R. V., and Gandhi, P. (2008). The effect of radiation pressure on dusty absorbing gas around active galactic nuclei. *MNRAS*, 385(1):L43–L47.

[78] Fabian, A. C., Zoghbi, A., Ross, R. R., Uttley, P., Gallo, L. C., Brandt, W. N., Blustin, A. J., Boller, T., Caballero-Garcia, M. D., Larsson, J., Miller, J. M., Miniutti, G., Ponti, G., Reis, R. C., Reynolds, C. S., Tanaka, Y., and Young, A. J. (2009). Broad line emission from iron K- and L-shell transitions in the active galaxy 1H0707-495. *Nature*, 459(7246):540–542.

[79] Fabian, A. C., Zoghbi, A., Wilkins, D., Dwelly, T., Uttley, P., Schartel, N., Miniutti, G., Gallo, L., Grupe, D., Komossa, S., and Santos-Lleó, M. (2012). 1H 0707-495 in 2011: an X-ray source within a gravitational radius of the event horizon. *MNRAS*, 419(1):116–123.

[80] Ferland, G. J., Korista, K. T., Verner, D. A., Ferguson, J. W., Kingdon, J. B., and Verner, E. M. (1998). CLOUDY 90: Numerical Simulation of Plasmas and Their Spectra. *PASP*, 110(749):761–778.

[81] Ferrarese, L. and Ford, H. (2005). Supermassive Black Holes in Galactic Nuclei: Past, Present and Future Research. *SSRv*, 116(3-4):523–624.

[82] Ferrarese, L. and Merritt, D. (2000). A Fundamental Relation between Supermassive Black Holes and Their Host Galaxies. *ApJL*, 539(1):L9–L12.

[83] Fields, D. L., Mathur, S., Pogge, R. W., Nicastro, F., and Komossa, S. (2005). Supersolar N/C in the Narrow-Line Seyfert 1 Galaxy Markarian 1044. *ApJ*, 620(1):183–190.

[84] Frederick, S., Kara, E., Reynolds, C., Pinto, C., and Fabian, A. (2018). X-Ray Reverberation Mapping and Dramatic Variability of Seyfert 1 Galaxy 1H 1934-063. *ApJ*, 867(1):67.

[85] Fukumura, K., Dadina, M., Matzeu, G., Tombesi, F., Shrader, C., and Kazanas, D. (2022). Tell-tale Spectral Signatures of MHD-driven Ultrafast Outflows in AGNs. *ApJ*, 940(1):6.

[86] Fukumura, K., Kazanas, D., Contopoulos, I., and Behar, E. (2010a). Magnetohydrodynamic Accretion Disk Winds as X-ray Absorbers in Active Galactic Nuclei. *ApJ*, 715(1):636–650.

[87] Fukumura, K., Kazanas, D., Contopoulos, I., and Behar, E. (2010b). Magnetohydrodynamic Accretion Disk Winds as X-ray Absorbers in Active Galactic Nuclei. *ApJ*, 715(1):636–650.

[88] Fukumura, K., Kazanas, D., Contopoulos, I., and Behar, E. (2010c). Modeling High-velocity QSO Absorbers with Photoionized Magnetohydrodynamic Disk Winds. *ApJL*, 723(2):L228–L232.

[89] Fukumura, K., Kazanas, D., Shrader, C., Behar, E., Tombesi, F., and Contopoulos, I. (2018). Variable Nature of Magnetically Driven Ultra-fast Outflows. *ApJL*, 864(2):L27.

[90] Fukumura, K., Tombesi, F., Kazanas, D., Shrader, C., Behar, E., and Contopoulos, I. (2015). Magnetically Driven Accretion Disk Winds and Ultra-fast Outflows in PG 1211+143. *ApJ*, 805(1):17.

[91] Gallo, L. C., Boller, T., Brandt, W. N., Fabian, A. C., and Vaughan, S. (2004). I Zw 1 observed with XMM-Newton . Low-energy spectral complexity, iron lines, and hard X-ray flares. *A&A*, 417:29–38.

[92] Gallo, L. C., Brandt, W. N., Costantini, E., Fabian, A. C., Iwasawa, K., and Papadakis, I. E. (2007). A longer XMM-Newton look at I Zwicky 1: variability of the X-ray continuum, absorption and iron Kα line. *MNRAS*, 377(1):391–401.

[93] Gallo, L. C. and Fabian, A. C. (2013). The origin of blueshifted absorption features in the X-ray spectrum of PG 1211+143: outflow or disc. *MNRAS*, 434:L66–L69.

[94] García, J., Dauser, T., Lohfink, A., Kallman, T. R., Steiner, J. F., McClintock, J. E., Brenneman, L., Wilms, J., Eikmann, W., Reynolds, C. S., and Tombesi, F. (2014). Improved Reflection Models of Black Hole Accretion Disks: Treating the Angular Distribution of X-Rays. *ApJ*, 782(2):76.

[95] García, J., Dauser, T., Reynolds, C. S., Kallman, T. R., McClintock, J. E., Wilms, J., and Eikmann, W. (2013). X-Ray Reflected Spectra from Accretion Disk Models. III. A Complete Grid of Ionized Reflection Calculations. *ApJ*, 768(2):146.

[96] García, J. and Kallman, T. R. (2010). X-ray Reflected Spectra from Accretion Disk Models. I. Constant Density Atmospheres. *ApJ*, 718(2):695–706.

[97] García, J., Kallman, T. R., and Mushotzky, R. F. (2011). X-ray Reflected Spectra from Accretion Disk Models. II. Diagnostic Tools for X-ray Observations. *ApJ*, 731(2):131.

[98] García, J. A., Fabian, A. C., Kallman, T. R., Dauser, T., Parker, M. L., McClintock, J. E., Steiner, J. F., and Wilms, J. (2016). The effects of high density on the X-ray spectrum reflected from accretion discs around black holes. *MNRAS*, 462(1):751–760.

[99] García, J. A., Kara, E., Walton, D., Beuchert, T., Dauser, T., Gatuzz, E., Balokovic, M., Steiner, J. F., Tombesi, F., Connors, R. M. T., Kallman, T. R., Harrison, F. A., Fabian, A., Wilms, J., Stern, D., Lanz, L., Ricci, C., and Ballantyne, D. R. (2019). Implications of the Warm Corona and Relativistic Reflection Models for the Soft Excess in Mrk 509. *ApJ*, 871(1):88.

[100] George, I. M. and Fabian, A. C. (1991). X-ray reflection from cold matter in Active Galactic Nuclei and X-ray binaries. *MNRAS*, 249:352.

[101] George, I. M., Mushotzky, R., Turner, T. J., Yaqoob, T., Ptak, A., Nandra, K., and Netzer, H. (1998a). The X-Ray Spectral Variability of the Seyfert Galaxy NGC 3227. *ApJ*, 509(1):146–162.

[102] George, I. M., Turner, T. J., Netzer, H., Nandra, K., Mushotzky, R. F., and Yaqoob, T. (1998b). ASCA Observations of Seyfert 1 Galaxies. III. The Evidence for Absorption and Emission Due to Photoionized Gas. *ApJS*, 114(1):73–120.

[103] Gezari, S., Hung, T., Cenko, S. B., Blagorodnova, N., Yan, L., Kulkarni, S. R., Mooley, K., Kong, A. K. H., Cantwell, T. M., Yu, P. C., Cao, Y., Fremling, C., Neill, J. D., Ngeow, C. C., Nugent, P. E., and Wozniak, P. (2017). iPTF Discovery of the Rapid "Turn-on" of a Luminous Quasar. *ApJ*, 835(2):144.

[104] Gierliński, M., Middleton, M., Ward, M., and Done, C. (2008). A periodicity of ∼1hour in X-ray emission from the active galaxy RE J1034+396. *Nature*, 455(7211):369–371.

[105] Giroletti, M., Panessa, F., Longinotti, A. L., Krongold, Y., Guainazzi, M., Costantini, E., and Santos-Lleo, M. (2017). Coexistence of a non-thermal jet and a complex ultra-fast X-ray outflow in a moderately luminous AGN. *A&A*, 600:A87.

[106] Gofford, J., Reeves, J. N., Tombesi, F., Braito, V., Turner, T. J., Miller, L., and Cappi, M. (2013). The Suzaku view of highly ionized outflows in AGN - I. Statistical detection and global absorber properties. *MNRAS*, 430(1):60–80.

[107] Gonzalez, A. G., Gallo, L. C., Kosec, P., Fabian, A. C., Alston, W. N., Berton, M., and Wilkins, D. R. (2020). Characterizing continuum variability in the radio-loud narrow-line Seyfert 1 galaxy IRAS 17020+4544. *MNRAS*, 496(3):3708–3724.

[108] Goodrich, R. W. (1989). Spectropolarimetry and Variability of Seyfert 1.8 and 1.9 Galaxies. *ApJ*, 340:190.

[109] Grafton-Waters, S., Branduardi-Raymont, G., Mehdipour, M., Page, M. J., Behar, E., Kaastra, J., Arav, N., Bianchi, S., Costantini, E., Ebrero, J., Di Gesu, L., Kaspi, S., Kriss, G. A., De Marco, B., Mao, J., Middei, R., Peretz, U., Petrucci, P. O., and Ponti, G. (2020). Multi-wavelength campaign on NGC 7469. VI. Photoionisation modelling of the emission line regions and the warm absorber. *A&A*, 633:A62.

[110] Grupe, D., Komossa, S., Leighly, K. M., and Page, K. L. (2010). The Simultaneous Optical-to-X-Ray Spectral Energy Distribution of Soft X-Ray Selected Active Galactic Nuclei Observed by Swift. *ApJS*, 187(1):64–106.

[111] Grupe, D. and Mathur, S. (2004). M_{BH}-σ Relation for a Complete Sample of Soft X-Ray-selected Active Galactic Nuclei. *ApJL*, 606(1):L41–L44.

[112] Gültekin, K., Richstone, D. O., Gebhardt, K., Lauer, T. R., Tremaine, S., Aller, M. C., Bender, R., Dressler, A., Faber, S. M., Filippenko, A. V., Green, R., Ho, L. C., Kormendy, J., Magorrian, J., Pinkney, J., and Siopis, C. (2009). The M-σ and M-L Relations in Galactic Bulges, and Determinations of Their Intrinsic Scatter. *ApJ*, 698(1):198–221.

[113] Haardt, F. and Maraschi, L. (1991). A Two-Phase Model for the X-Ray Emission from Seyfert Galaxies. *ApJL*, 380:L51.

[114] Haardt, F. and Maraschi, L. (1993). X-Ray Spectra from Two-Phase Accretion Disks. *ApJ*, 413:507.

[115] Hagino, K., Odaka, H., Done, C., Tomaru, R., Watanabe, S., and Takahashi, T. (2016). A disc wind interpretation of the strong Fe Kα features in 1H 0707-495. *MNRAS*, 461(4):3954–3963.

[116] Halpern, J. P. (1984). Variable X-ray absorption in the QSO MR 2251-178. *ApJ*, 281:90–94.

[117] Harrison, C. M. (2016). *Observational Constraints on the Influence of Active Galactic Nuclei on the Evolution of Galaxies*.

[118] Harrison, F. A., Craig, W. W., Christensen, F. E., Hailey, C. J., Zhang, W. W., Boggs, S. E., Stern, D., Cook, W. R., Forster, K., Giommi, P., Grefenstette, B. W., Kim, Y., Kitaguchi, T., Koglin, J. E., Madsen, K. K., Mao, P. H., Miyasaka, H., Mori, K., Perri, M., Pivovaroff, M. J., Puccetti, S., Rana, V. R., Westergaard, N. J., Willis, J., Zoglauer, A., An, H., Bachetti, M., Barrière, N. M., Bellm, E. C., Bhalerao, V., Brejnholt, N. F., Fuerst, F., Liebe, C. C., Markwardt, C. B., Nynka, M., Vogel, J. K., Walton, D. J., Wik, D. R., Alexander, D. M., Cominsky, L. R., Hornschemeier, A. E., Hornstrup, A., Kaspi, V. M., Madejski, G. M., Matt, G., Molendi, S., Smith, D. M., Tomsick, J. A., Ajello, M., Ballantyne, D. R., Baloković, M., Barret, D., Bauer, F. E., Blandford, R. D., Brandt, W. N., Brenneman, L. W., Chiang, J., Chakrabarty, D., Chenevez, J., Comastri, A., Dufour, F., Elvis, M., Fabian, A. C., Farrah, D., Fryer, C. L., Gotthelf, E. V., Grindlay, J. E., Helfand, D. J., Krivonos, R., Meier, D. L., Miller, J. M., Natalucci, L., Ogle, P., Ofek, E. O., Ptak, A., Reynolds, S. P., Rigby, J. R., Tagliaferri, G., Thorsett, S. E., Treister, E., and Urry, C. M. (2013). The Nuclear Spectroscopic Telescope Array (NuSTAR) High-energy X-Ray Mission. *ApJ*, 770(2):103.

[119] Hebbar, P. R., Heinke, C. O., Sivakoff, G. R., and Shaw, A. W. (2019). X-ray spectroscopy of the candidate AGNs in Henize 2-10 and NGC 4178: likely supernova remnants. *MNRAS*, 485(4):5604–5615.

[120] HI4PI Collaboration, Ben Bekhti, N., Flöer, L., Keller, R., Kerp, J., Lenz, D., Winkel, B., Bailin, J., Calabretta, M. R., Dedes, L., Ford, H. A., Gibson, B. K., Haud, U., Janowiecki, S., Kalberla, P. M. W., Lockman, F. J., McClure-Griffiths, N. M., Murphy, T., Nakanishi, H., Pisano, D. J., and Staveley-Smith, L. (2016). HI4PI: A full-sky H I survey based on EBHIS and GASS. *A&A*, 594:A116.

[121] Hickox, R. C. and Alexander, D. M. (2018). Obscured Active Galactic Nuclei. *ARA&A*, 56:625–671.

[122] Ho, L. C. (2008). Nuclear activity in nearby galaxies. *ARA&A*, 46:475–539.

[123] Holczer, T., Behar, E., and Arav, N. (2010). X-ray Absorption Analysis of MCG -6-30-15: Discerning Three Kinematic Systems. *ApJ*, 708(2):981–994.

[124] Hönig, S. F. (2019). Redefining the Torus: A Unifying View of AGNs in the Infrared and Submillimeter. *ApJ*, 884(2):171.

[125] Hönig, S. F., Kishimoto, M., Tristram, K. R. W., Prieto, M. A., Gandhi, P., Asmus, D., Antonucci, R., Burtscher, L., Duschl, W. J., and Weigelt, G. (2013). Dust in the Polar Region as a Major Contributor to the Infrared Emission of Active Galactic Nuclei. *ApJ*, 771(2):87.

[126] Hopkins, A. M. (2004). On the Evolution of Star-forming Galaxies. *ApJ*, 615(1):209–221.

[127] Hopkins, P. F. and Elvis, M. (2010). Quasar feedback: more bang for your buck. *MNRAS*, 401(1):7–14.

[128] Hopkins, P. F., Richards, G. T., and Hernquist, L. (2007). An Observational Determination of the Bolometric Quasar Luminosity Function. *ApJ*, 654(2):731–753.

[129] Hu, C.-P., Chou, Y., Yang, T.-C., and Su, Y.-H. (2014). Tracking the Evolution of Quasi-periodic Oscillation in RE J1034+396 Using the Hilbert-Huang Transform. *ApJ*, 788(1):31.

[130] Husemann, B., Singha, M., Scharwächter, J., McElroy, R., Neumann, J., Smirnova-Pinchukova, I., Urrutia, T., Baum, S. A., Bennert, V. N., Combes, F., Croom, S. M., Davis, T. A., Fournier, Y., Galkin, A., Gaspari, M., Enke, H., Krumpe, M., O'Dea, C. P., Pérez-Torres, M., Rose, T., Tremblay, G. R., and Walcher, C. J. (2022). The Close AGN Reference Survey (CARS). IFU survey data and the BH mass dependence of long-term AGN variability. *A&A*, 659:A124.

[131] Igo, Z., Parker, M. L., Matzeu, G. A., Alston, W., Alvarez Crespo, N., Fürst, F., Buisson, D. J. K., Lobban, A., Joyce, A. M., Mallick, L., Schartel, N., and Santos-Lleó, M. (2020). Searching for ultra-fast outflows in AGN using variability spectra. *MNRAS*, 493(1):1088–1108.

[132] Ishibashi, W. and Fabian, A. C. (2015). AGN feedback: galactic-scale outflows driven by radiation pressure on dust. *MNRAS*, 451(1):93–102.

[133] Ishibashi, W., Fabian, A. C., and Arakawa, N. (2021). AGN-driven galactic outflows: comparing models to observations. *MNRAS*, 502(3):3638–3645.

[134] Ishibashi, W., Fabian, A. C., and Maiolino, R. (2018). The energetics of AGN radiation pressure-driven outflows. *MNRAS*, 476(1):512–519.

[135] Jansen, F., Lumb, D., Altieri, B., Clavel, J., Ehle, M., Erd, C., Gabriel, C., Guainazzi, M., Gondoin, P., Much, R., Munoz, R., Santos, M., Schartel, N., Texier, D., and Vacanti, G. (2001). XMM-Newton observatory. I. The spacecraft and operations. *A&A*, 365:L1–L6.

[136] Jiang, J., Fabian, A. C., Dauser, T., Gallo, L., García, J. A., Kara, E., Parker, M. L., Tomsick, J. A., Walton, D. J., and Reynolds, C. S. (2019). High Density Reflection Spectroscopy - II. The density of the inner black hole accretion disc in AGN. *MNRAS*, 489(3):3436–3455.

[137] Jiang, J., Parker, M. L., Fabian, A. C., Alston, W. N., Buisson, D. J. K., Cackett, E. M., Chiang, C. Y., Dauser, T., Gallo, L. C., García, J. A., Harrison, F. A., Lohfink, A. M., De Marco, B., Kara, E., Miller, J. M., Miniutti, G., Pinto, C., Walton, D. J., and Wilkins, D. R. (2018a). The 1.5 Ms observing campaign on IRAS 13224-3809 - I. X-ray spectral analysis. *MNRAS*, 477(3):3711–3726.

[138] Jiang, J., Walton, D. J., Parker, M. L., and Fabian, A. C. (2018b). The ultrafast outflow of WKK 4438: Suzaku and NuSTAR X-ray spectral analysis. *MNRAS*, 481(1):639–644.

[139] Jiménez-Bailón, E., Krongold, Y., Bianchi, S., Matt, G., Santos-Lleó, M., Piconcelli, E., and Schartel, N. (2008). Detection of blueshifted emission and absorption and a relativistic iron line in the X-ray spectrum of ESO323-G077. *MNRAS*, 391(3):1359–1368.

[140] Jin, C., Done, C., Middleton, M., and Ward, M. (2013). A long XMM-Newton observation of an extreme narrow-line Seyfert 1: PG 1244+026. *MNRAS*, 436(4):3173–3185.

[141] Jin, C., Done, C., and Ward, M. (2020). Reobserving the NLS1 galaxy RE J1034+396 - I. The long-term, recurrent X-ray QPO with a high significance. *MNRAS*, 495(4):3538–3550.

[142] Jin, C., Done, C., and Ward, M. (2021). Re-observing the NLS1 galaxy RE J1034+396 - II. New insights on the soft X-ray excess, QPO, and the analogy with GRS 1915+105. *MNRAS*, 500(2):2475–2495.

[143] Juráňová, A., Costantini, E., and Uttley, P. (2022). Spectral-timing of AGN ionized outflows with Athena. *MNRAS*, 510(3):4225–4235.

[144] Kaastra, J. S. and Bleeker, J. A. M. (2016). Optimal binning of X-ray spectra and response matrix design. *A&A*, 587:A151.

[145] Kaastra, J. S., Detmers, R. G., Mehdipour, M., Arav, N., Behar, E., Bianchi, S., Branduardi-Raymont, G., Cappi, M., Costantini, E., Ebrero, J., Kriss, G. A., Paltani, S., Petrucci, P. O., Pinto, C., Ponti, G., Steenbrugge, K. C., and de Vries, C. P. (2012). Multiwavelength campaign on Mrk 509. VIII. Location of the X-ray absorber. *A&A*, 539:A117.

[146] Kaastra, J. S., Kriss, G. A., Cappi, M., Mehdipour, M., Petrucci, P. O., Steenbrugge, K. C., Arav, N., Behar, E., Bianchi, S., Boissay, R., Branduardi-Raymont, G., Chamberlain, C., Costantini, E., Ely, J. C., Ebrero, J., Di Gesu, L., Harrison, F. A., Kaspi, S., Malzac, J., De Marco, B., Matt, G., Nandra, K., Paltani, S., Person, R., Peterson, B. M., Pinto, C., Ponti, G., Nuñez, F. P., De Rosa, A., Seta, H., Ursini, F., de Vries, C. P., Walton, D. J., and Whewell, M. (2014). A fast and long-lived outflow from the supermassive black hole in NGC 5548. *Science*, 345(6192):64–68.

[147] Kaastra, J. S., Mewe, R., Liedahl, D. A., Komossa, S., and Brinkman, A. C. (2000). X-ray absorption lines in the Seyfert 1 galaxy NGC 5548 discovered with Chandra-LETGS. *A&A*, 354:L83–L86.

[148] Kaastra, J. S., Mewe, R., and Nieuwenhuijzen, H. (1996). SPEX: a new code for spectral analysis of X & UV spectra. In *UV and X-ray Spectroscopy of Astrophysical and Laboratory Plasmas*, pages 411–414.

[149] Kaastra, J. S., Raassen, A. J. J., Mewe, R., Arav, N., Behar, E., Costantini, E., Gabel, J. R., Kriss, G. A., Proga, D., Sako, M., and Steenbrugge, K. C. (2004). X-ray/UV campaign on the Mrk 279 outflow: Density diagnostics in Active Galactic Nuclei using O V K-shell absorption lines. *A&A*, 428:57–66.

[150] Kalberla, P. M. W., Burton, W. B., Hartmann, D., Arnal, E. M., Bajaja, E., Morras, R., and Pöppel, W. G. L. (2005). The Leiden/Argentine/Bonn (LAB) Survey of Galactic HI. Final data release of the combined LDS and IAR surveys with improved stray-radiation corrections. *A&A*, 440(2):775–782.

[151] Kallman, T. and Bautista, M. (2001). Photoionization and High-Density Gas. *ApJS*, 133(1):221–253.

[152] Kallman, T. R. and Palmeri, P. (2007). Atomic data for x-ray astrophysics. *Reviews of Modern Physics*, 79(1):79–133.

[153] Kamraj, N., Brightman, M., Harrison, F. A., Stern, D., García, J. A., Baloković, M., Ricci, C., Koss, M. J., Mejía-Restrepo, J. E., Oh, K., Powell, M. C., and Urry, C. M. (2022). X-Ray Coronal Properties of Swift/BAT-selected Seyfert 1 Active Galactic Nuclei. *ApJ*, 927(1):42.

[154] Kara, E., Cackett, E. M., Fabian, A. C., Reynolds, C., and Uttley, P. (2014). The curious time lags of PG 1244+026: discovery of the iron K reverberation lag. *MNRAS*, 439:L26–L30.

[155] Kara, E., Fabian, A. C., Cackett, E. M., Miniutti, G., and Uttley, P. (2013). Revealing the X-ray source in IRAS 13224-3809 through flux-dependent reverberation lags. *MNRAS*, 430(2):1408–1413.

[156] Kara, E., García, J. A., Lohfink, A., Fabian, A. C., Reynolds, C. S., Tombesi, F., and Wilkins, D. R. (2017). The high-Eddington NLS1 Ark 564 has the coolest corona. *MNRAS*, 468(3):3489–3498.

[157] Kara, E., Miller, J. M., Reynolds, C., and Dai, L. (2016). Relativistic reverberation in the accretion flow of a tidal disruption event. *Nature*, 535(7612):388–390.

[158] Kaspi, S., Brandt, W. N., George, I. M., Netzer, H., Crenshaw, D. M., Gabel, J. R., Hamann, F. W., Kaiser, M. E., Koratkar, A., Kraemer, S. B., Kriss, G. A., Mathur, S., Mushotzky, R. F., Nandra, K., Peterson, B. M., Shields, J. C., Turner, T. J., and Zheng, W. (2002). The Ionized Gas and Nuclear Environment in NGC 3783. I. Time-averaged 900 Kilosecond Chandra Grating Spectroscopy. *ApJ*, 574(2):643–662.

[159] Kaspi, S., Brandt, W. N., Netzer, H., George, I. M., Chartas, G., Behar, E., Sambruna, R. M., Garmire, G. P., and Nousek, J. A. (2001). High-Resolution X-Ray Spectroscopy and Modeling of the Absorbing and Emitting Outflow in NGC 3783. *ApJ*, 554(1):216–232.

[160] Kato, Y., Mineshige, S., and Shibata, K. (2004). Magnetohydrodynamic Accretion Flows: Formation of Magnetic Tower Jet and Subsequent Quasi-Steady State. *ApJ*, 605(1):307–320.

[161] Kellermann, K. I., Sramek, R., Schmidt, M., Shaffer, D. B., and Green, R. (1989). VLA Observations of Objects in the Palomar Bright Quasar Survey. *AJ*, 98:1195.

[162] Kerr, R. P. (1963). Gravitational Field of a Spinning Mass as an Example of Algebraically Special Metrics. *PhRvL*, 11(5):237–238.

[163] King, A. and Pounds, K. (2015). Powerful Outflows and Feedback from Active Galactic Nuclei. *ARA&A*, 53:115–154.

[164] King, A. R. (2010). Black hole outflows. *MNRAS*, 402(3):1516–1522.

[165] King, A. R. and Pounds, K. A. (2003). Black hole winds. *MNRAS*, 345(2):657–659.

[166] Kinkhabwala, A., Sako, M., Behar, E., Kahn, S. M., Paerels, F., Brinkman, A. C., Kaastra, J. S., Gu, M. F., and Liedahl, D. A. (2002). XMM-Newton Reflection Grating Spectrometer Observations of Discrete Soft X-Ray Emission Features from NGC 1068. *ApJ*, 575(2):732–746.

[167] Kobayashi, H., Ohsuga, K., Takahashi, H. R., Kawashima, T., Asahina, Y., Takeuchi, S., and Mineshige, S. (2018). Three-dimensional structure of clumpy outflow from supercritical accretion flow onto black holes. *PASJ*, 70(2):22.

[168] Kormendy, J. and Ho, L. C. (2013). Coevolution (Or Not) of Supermassive Black Holes and Host Galaxies. *ARA&A*, 51(1):511–653.

[169] Kormendy, J. and Richstone, D. (1995). Inward Bound—The Search For Supermassive Black Holes In Galactic Nuclei. *ARA&A*, 33:581.

[170] Kosec, P., Buisson, D. J. K., Parker, M. L., Pinto, C., Fabian, A. C., and Walton, D. J. (2018a). A stratified ultrafast outflow in 1H0707-495? *MNRAS*, 481(1):947–953.

[171] Kosec, P., Pinto, C., Fabian, A. C., and Walton, D. J. (2018b). Searching for outflows in ultraluminous X-ray sources through high-resolution X-ray spectroscopy. *MNRAS*, 473(4):5680–5697.

[172] Kosec, P., Pinto, C., Reynolds, C. S., Guainazzi, M., Kara, E., Walton, D. J., Fabian, A. C., Parker, M. L., and Valtchanov, I. (2021). Ionized emission and absorption in a large sample of ultraluminous X-ray sources. *MNRAS*, 508(3):3569–3588.

[173] Kosec, P., Zoghbi, A., Walton, D. J., Pinto, C., Fabian, A. C., Parker, M. L., and Reynolds, C. S. (2020). Detection of a variable ultrafast outflow in the narrow-line Seyfert 1 galaxy PG 1448+273. *MNRAS*, 495(4):4769–4781.

[174] Kraemer, S. B., Crenshaw, D. M., Gabel, J. R., Kriss, G. A., Netzer, H., Peterson, B. M., George, I. M., Gull, T. R., Hutchings, J. B., Mushotzky, R. F., and Turner, T. J. (2006). Simultaneous Ultraviolet and X-Ray Observations of the Seyfert Galaxy NGC 4151. II. Physical Conditions in the UV Absorbers. *ApJS*, 167(2):161–176.

[175] Kraft, R., Markevitch, M., Kilbourne, C., Adams, J. S., Akamatsu, H., Ayromlou, M., Bandler, S. R., Barbera, M., Bennett, D. A., Bhardwaj, A., Biffi, V., Bodewits, D., Bogdan, A., Bonamente, M., Borgani, S., Branduardi-Raymont, G., Bregman, J. N., Burchett, J. N., Cann, J., Carter, J., Chakraborty, P., Churazov, E., Crain, R. A., Cumbee, R., Dave, R., DiPirro, M., Dolag, K., Bertrand Doriese, W., Drake, J., Dunn, W., Eckart, M., Eckert, D., Ettori, S., Forman, W., Galeazzi, M., Gall, A., Gatuzz, E., Hell, N., Hodges-Kluck, E., Jackman, C., Jahromi, A., Jennings, F., Jones, C., Kaaret, P., Kavanagh, P. J., Kelley, R. L., Khabibullin, I., Kim, C.-G., Koutroumpa, D., Kovacs, O., Kuntz, K. D., Lau, E., Lee, S.-H., Leutenegger, M., Lin, S.-C., Lisse, C., Lo Cicero, U., Lovisari, L., McCammon, D., McEntee, S., Mernier, F., Miller, E. D., Nagai, D., Negro, M., Nelson, D., Ness, J.-U., Nulsen, P., Ogorzalek, A., Oppenheimer, B. D., Oskinova, L., Patnaude, D., Pfeifle, R. W., Pillepich, A., Plucinsky, P., Pooley, D., Porter, F. S., Randall, S., Rasia, E., Raymond, J., Ruszkowski, M., Sakai, K., Sarkar, A., Sasaki, M., Sato, K., Schellenberger, G., Schaye, J., Simionescu, A., Smith, S. J., Steiner, J. F., Stern, J., Su, Y., Sun, M., Tremblay, G., Truong, N., Tutt, J., Ursino, E., Veilleux, S., Vikhlinin, A., Vladutescu-Zopp, S., Vogelsberger, M., Walker, S. A., Weaver, K., Weigt, D. M., Werk, J., Werner, N., Wolk, S. J., Zhang, C., Zhang, W. W., Zhuravleva, I., and ZuHone, J. (2022). Line Emission Mapper (LEM): Probing the physics of cosmic ecosystems. *arXiv e-prints*, page arXiv:2211.09827.

[176] Kriss, G. A., Lee, J. C., Danehkar, A., Nowak, M. A., Fang, T., Hardcastle, M. J., Neilsen, J., and Young, A. (2018). Discovery of an Ultraviolet Counterpart to an Ultrafast X-Ray Outflow in the Quasar PG 1211+143. *ApJ*, 853(2):166.

[177] Krolik, J. H. and Begelman, M. C. (1988). Molecular Tori in Seyfert Galaxies: Feeding the Monster and Hiding It. *ApJ*, 329:702.

[178] Krolik, J. H. and Kriss, G. A. (1995). Observable Properties of X-Ray–heated Winds in Active Galactic Nuclei: Warm Reflectors and Warm Absorbers. *ApJ*, 447:512.

[179] Krolik, J. H. and Kriss, G. A. (2001). Warm Absorbers in Active Galactic Nuclei: A Multitemperature Wind. *ApJ*, 561(2):684–690.

[180] Krolik, J. H., McKee, C. F., and Tarter, C. B. (1981). Two-phase models of quasar emission line regions. *ApJ*, 249:422–442.

[181] Krongold, Y., Longinotti, A. L., Santos-Lleó, M., Mathur, S., Peterson, B. M., Nicastro, F., Gupta, A., Rodríguez-Pascual, P., and Elías-Chávez, M. (2021). Detection of a Multiphase Ultrafast Wind in the Narrow-line Seyfert 1 Galaxy Mrk 1044. *ApJ*, 917(1):39.

[182] Krongold, Y., Nicastro, F., Brickhouse, N. S., Elvis, M., and Mathur, S. (2005). Opacity Variations in the Ionized Absorption in NGC 3783: A Compact Absorber. *ApJ*, 622(2):842–846.

[183] Krongold, Y., Nicastro, F., Elvis, M., Brickhouse, N., Binette, L., Mathur, S., and Jiménez-Bailón, E. (2007). The Compact, Conical, Accretion-Disk Warm Absorber of the Seyfert 1 Galaxy NGC 4051 and Its Implications for IGM-Galaxy Feedback Processes. *ApJ*, 659(2):1022–1039.

[184] Kubota, A. and Done, C. (2018). A physical model of the broad-band continuum of AGN and its implications for the UV/X relation and optical variability. *MNRAS*, 480(1):1247–1262.

[185] Kubota, A. and Done, C. (2019). Modelling the spectral energy distribution of super-Eddington quasars. *MNRAS*, 489(1):524–533.

[186] Laha, S., Guainazzi, M., Dewangan, G. C., Chakravorty, S., and Kembhavi, A. K. (2014). Warm absorbers in X-rays (WAX), a comprehensive high-resolution grating spectral study of a sample of Seyfert galaxies - I. A global view and frequency of occurrence of warm absorbers. *MNRAS*, 441(3):2613–2643.

[187] Laha, S., Reynolds, C. S., Reeves, J., Kriss, G., Guainazzi, M., Smith, R., Veilleux, S., and Proga, D. (2021). Ionized outflows from active galactic nuclei as the essential elements of feedback. *Nature Astronomy*, 5:13–24.

[188] Laor, A. (1991). Line Profiles from a Disk around a Rotating Black Hole. *ApJ*, 376:90.

[189] Leighly, K. M. (1999). A Comprehensive Spectral and Variability Study of Narrow-Line Seyfert 1 Galaxies Observed by ASCA. II. Spectral Analysis and Correlations. *ApJS*, 125(2):317–348.

[190] Leighly, K. M. (2004). Hubble Space Telescope STIS Ultraviolet Spectral Evidence of Outflow in Extreme Narrow-Line Seyfert 1 Galaxies. II. Modeling and Interpretation. *ApJ*, 611(1):125–152.

[191] Leighly, K. M., Kay, L. E., Wills, B. J., Wills, D., and Grupe, D. (1997). The Optical Polarization and Warm Absorber in IRAS 17020+4544. *ApJL*, 489:L137.

[192] Leighly, K. M. and Moore, J. R. (2004). Hubble Space Telescope STIS Ultraviolet Spectral Evidence of Outflow in Extreme Narrow-Line Seyfert 1 Galaxies. I. Data and Analysis. *ApJ*, 611(1):107–124.

[193] Lin, D. N. C. and Shields, G. A. (1986). Accretion Disks and Periodic Outbursts of Active Galaxies Nuclei. *ApJ*, 305:28.

[194] Lobban, A. P., Pounds, K., Vaughan, S., and Reeves, J. N. (2016). Testing Relativistic Reflection and Resolving Outflows in PG 1211+143 with XMM-Newton and NuSTAR. *ApJ*, 831(2):201.

[195] Lobban, A. P., Vaughan, S., Pounds, K., and Reeves, J. N. (2018). X-ray time lags in PG 1211+143. *MNRAS*, 476(1):225–234.

[196] Lodders, K., Palme, H., and Gail, H. P. (2009). Abundances of the Elements in the Solar System. *Landolt Börnstein*, 4B:712.

[197] Longinotti, A. L., Krongold, Y., Guainazzi, M., Giroletti, M., Panessa, F., Costantini, E., Santos-Lleo, M., and Rodriguez-Pascual, P. (2015). X-Ray High-resolution Spectroscopy Reveals Feedback in a Seyfert Galaxy from an Ultra-fast Wind with Complex Ionization and Velocity Structure. *ApJL*, 813(2):L39.

[198] Longinotti, A. L., Vega, O., Krongold, Y., Aretxaga, I., Yun, M., Chavushyan, V., Feruglio, C., Gómez-Ruiz, A., Montaña, A., León-Tavares, J., Olguín-Iglesias, A., Giroletti, M., Guainazzi, M., Kotilainen, J., Panessa, F., Zapata, L. A., Cruz-Gonzalez, I., Patiño-Álvarez, V. M., Rosa-Gonzalez, D., Carramiñana, A., Carrasco, L., Costantini, E., Dultzin, D., Guichard, J., Puerari, I., and Santos-Lleo, M. (2018). Early Science with the Large Millimeter Telescope: An Energy-driven Wind Revealed by Massive Molecular and Fast X-Ray Outflows in the Seyfert Galaxy IRAS 17020+4544. *ApJL*, 867(1):L11.

[199] Lumb, D. H., Warwick, R. S., Page, M., and De Luca, A. (2002). X-ray background measurements with XMM-Newton EPIC. *A&A*, 389:93–105.

[200] Luminari, A., Nicastro, F., Elvis, M., Piconcelli, E., Tombesi, F., Zappacosta, L., and Fiore, F. (2021). Speed limits for radiation-driven SMBH winds. *A&A*, 646:A111.

[201] Luminari, A., Nicastro, F., Krongold, Y., Piro, L., and Thakur, A. L. (2023). Time Evolving Photo Ionisation Device (TEPID): A novel code for out-of-equilibrium gas ionisation. *A&A*, 679:A141.

[202] Luminari, A., Tombesi, F., Piconcelli, E., Nicastro, F., Fukumura, K., Kazanas, D., Fiore, F., and Zappacosta, L. (2020). The importance of special relativistic effects in modelling ultra-fast outflows. *A&A*, 633:A55.

[203] Madau, P. and Dickinson, M. (2014). Cosmic Star-Formation History. *ARA&A*, 52:415–486.

[204] Madsen, K. K., Harrison, F. A., Markwardt, C. B., An, H., Grefenstette, B. W., Bachetti, M., Miyasaka, H., Kitaguchi, T., Bhalerao, V., Boggs, S., Christensen, F. E., Craig, W. W., Forster, K., Fuerst, F., Hailey, C. J., Perri, M., Puccetti, S., Rana, V., Stern, D., Walton, D. J., Jørgen Westergaard, N., and Zhang, W. W. (2015). Calibration of the NuSTAR High-energy Focusing X-ray Telescope. *ApJS*, 220(1):8.

[205] Magorrian, J., Tremaine, S., Richstone, D., Bender, R., Bower, G., Dressler, A., Faber, S. M., Gebhardt, K., Green, R., Grillmair, C., Kormendy, J., and Lauer, T. (1998). The Demography of Massive Dark Objects in Galaxy Centers. *AJ*, 115(6):2285–2305.

[206] Maiolino, R., Russell, H. R., Fabian, A. C., Carniani, S., Gallagher, R., Cazzoli, S., Arribas, S., Belfiore, F., Bellocchi, E., Colina, L., Cresci, G., Ishibashi, W., Marconi, A., Mannucci, F., Oliva, E., and Sturm, E. (2017). Star formation inside a galactic outflow. *Nature*, 544(7649):202–206.

[207] Malizia, A., Bassani, L., Bird, A. J., Landi, R., Masetti, N., de Rosa, A., Panessa, F., Molina, M., Dean, A. J., Perri, M., and Tueller, J. (2008). First high-energy observations of narrow-line Seyfert 1s with INTEGRAL/IBIS. *MNRAS*, 389(3):1360–1366.

[208] Mallick, L., Alston, W. N., Parker, M. L., Fabian, A. C., Pinto, C., Dewangan, G. C., Markowitz, A., Gandhi, P., Kembhavi, A. K., and Misra, R. (2018). A high-density relativistic reflection origin for the soft and hard X-ray excess emission from Mrk 1044. *MNRAS*, 479(1):615–634.

[209] Malzac, J., Petrucci, P. O., Jourdain, E., Cadolle Bel, M., Sizun, P., Pooley, G., Cabanac, C., Chaty, S., Belloni, T., Rodriguez, J., Roques, J. P., Durouchoux, P., Goldwurm, A., and Laurent, P. (2006). Bimodal spectral variability of <ASTROBJ>Cygnus X-1</ASTROBJ> in an intermediate state. *A&A*, 448(3):1125–1137.

[210] Mao, J., Kaastra, J. S., Mehdipour, M., Raassen, A. J. J., Gu, L., and Miller, J. M. (2017). Density diagnostics of ionized outflows in active galactic nuclei. X-ray and UV absorption lines from metastable levels in Be-like to C-like ions. *A&A*, 607:A100.

[211] Marconi, A., Axon, D. J., Maiolino, R., Nagao, T., Pastorini, G., Pietrini, P., Robinson, A., and Torricelli, G. (2008). The Effect of Radiation Pressure on Virial Black Hole Mass Estimates and the Case of Narrow-Line Seyfert 1 Galaxies. *ApJ*, 678(2):693–700.

[212] Marconi, A. and Hunt, L. K. (2003). The Relation between Black Hole Mass, Bulge Mass, and Near-Infrared Luminosity. *ApJL*, 589(1):L21–L24.

[213] Marconi, A., Risaliti, G., Gilli, R., Hunt, L. K., Maiolino, R., and Salvati, M. (2004). Local supermassive black holes, relics of active galactic nuclei and the X-ray background. *MNRAS*, 351(1):169–185.

[214] Marinello, M., Rodríguez-Ardila, A., Garcia-Rissmann, A., Sigut, T. A. A., and Pradhan, A. K. (2016). The Fe II Emission in Active Galactic Nuclei: Excitation Mechanisms and Location of the Emitting Region. *ApJ*, 820(2):116.

[215] Mason, K. O., Breeveld, A., Much, R., Carter, M., Cordova, F. A., Cropper, M. S., Fordham, J., Huckle, H., Ho, C., Kawakami, H., Kennea, J., Kennedy, T., Mittaz, J., Pandel, D., Priedhorsky, W. C., Sasseen, T., Shirey, R., Smith, P., and Vreux, J. M. (2001). The XMM-Newton optical/UV monitor telescope. *A&A*, 365:L36–L44.

[216] Masterson, M., Kara, E., Ricci, C., García, J. A., Fabian, A. C., Pinto, C., Kosec, P., Remillard, R. A., Loewenstein, M., Trakhtenbrot, B., and Arcavi, I. (2022). Evolution of a Relativistic Outflow and X-Ray Corona in the Extreme Changing-look AGN 1ES 1927+654. *ApJ*, 934(1):35.

[217] Mathur, S. and Grupe, D. (2005). The Locus of Highly Accreting Active Galactic Nuclei on the M_{BH}-σ Plane: Selections, Limitations, and Implications. *ApJ*, 633(2):688–692.

[218] Matt, G., Perola, G. C., and Piro, L. (1991). The iron line and high energy bump as X-ray signatures of cold matter in Seyfert 1 galaxies. *A&A*, 247:25.

[219] Matzeu, G. A., Brusa, M., Lanzuisi, G., Dadina, M., Bianchi, S., Kriss, G., Mehdipour, M., Nardini, E., Chartas, G., Middei, R., Piconcelli, E., Gianolli, V., Comastri, A., Longinotti, A. L., Krongold, Y., Ricci, F., Petrucci, P. O., Tombesi, F., Luminari, A., Zappacosta, L., Miniutti, G., Gaspari, M., Behar, E., Bischetti, M., Mathur, S., Perna, M., Giustini, M., Grandi, P., Torresi, E., Vignali, C., Bruni, G., Cappi, M., Costantini, E., Cresci, G., De Marco, B., De Rosa, A., Gilli, R., Guainazzi, M., Kaastra, J., Kraemer, S., La Franca, F., Marconi, A., Panessa, F., Ponti, G., Proga, D., Ursini, F., Fiore, F., King, A. R., Maiolino, R., Matt, G., and Merloni, A. (2022). Supermassive Black Hole Winds in X-rays – SUBWAYS. I. Ultra-fast outflows in QSOs beyond the local Universe. *arXiv e-prints*, page arXiv:2212.02960.

[220] Matzeu, G. A., Reeves, J. N., Braito, V., Nardini, E., McLaughlin, D. E., Lobban, A. P., Tombesi, F., and Costa, M. T. (2017). Evidence for a radiatively driven disc-wind in PDS 456? *MNRAS*, 472(1):L15–L19.

[221] McHardy, I. M., Koerding, E., Knigge, C., Uttley, P., and Fender, R. P. (2006). Active galactic nuclei as scaled-up Galactic black holes. *Nature*, 444(7120):730–732.

[222] McKernan, B., Yaqoob, T., and Reynolds, C. S. (2007). A soft X-ray study of type I active galactic nuclei observed with Chandra high-energy transmission grating spectrometer. *MNRAS*, 379(4):1359–1372.

[223] McNamara, B. R., Nulsen, P. E. J., Wise, M. W., Rafferty, D. A., Carilli, C., Sarazin, C. L., and Blanton, E. L. (2005). The heating of gas in a galaxy cluster by X-ray cavities and large-scale shock fronts. *Nature*, 433(7021):45–47.

[224] McNamara, B. R., Wise, M., Nulsen, P. E. J., David, L. P., Sarazin, C. L., Bautz, M., Markevitch, M., Vikhlinin, A., Forman, W. R., Jones, C., and Harris, D. E. (2000). Chandra X-Ray Observations of the Hydra A Cluster: An Interaction between the Radio Source and the X-Ray-emitting Gas. *ApJL*, 534(2):L135–L138.

[225] Mehdipour, M. and Costantini, E. (2019). Relation between winds and jets in radio-loud AGN. *A&A*, 625:A25.

[226] Mehdipour, M., Kaastra, J. S., Costantini, E., Behar, E., Kriss, G. A., Bianchi, S., Branduardi-Raymont, G., Cappi, M., Ebrero, J., Di Gesu, L., Kaspi, S., Mao, J., De Marco, B., Middei, R., Peretz, U., Petrucci, P. O., Ponti, G., and Ursini, F. (2018). Multi-wavelength campaign on NGC 7469. III. Spectral energy distribution and the AGN wind photoionisation modelling, plus detection of diffuse X-rays from the starburst with Chandra HETGS. *A&A*, 615:A72.

[227] Mehdipour, M., Kaastra, J. S., and Kallman, T. (2016). Systematic comparison of photoionised plasma codes with application to spectroscopic studies of AGN in X-rays. *A&A*, 596:A65.

[228] Mehdipour, M., Kaastra, J. S., Kriss, G. A., Cappi, M., Petrucci, P. O., Steenbrugge, K. C., Arav, N., Behar, E., Bianchi, S., Boissay, R., Branduardi-Raymont, G., Costantini, E., Ebrero, J., Di Gesu, L., Harrison, F. A., Kaspi, S., De Marco, B., Matt, G., Paltani, S., Peterson, B. M., Ponti, G., Pozo Nuñez, F., De Rosa, A., Ursini, F., de Vries, C. P., Walton, D. J., and Whewell, M. (2015). Anatomy of the AGN in NGC 5548. I. A global model for the broadband spectral energy distribution. *A&A*, 575:A22.

[229] Middei, R., Petrucci, P. O., Bianchi, S., Ursini, F., Cappi, M., Clavel, M., De Rosa, A., Marinucci, A., Matt, G., and Tortosa, A. (2020). The soft excess of the NLS1 galaxy Mrk 359 studied with an XMM-Newton-NuSTAR monitoring campaign. *A&A*, 640:A99.

[230] Middleton, M., Done, C., Ward, M., Gierliński, M., and Schurch, N. (2009). RE J1034+396: the origin of the soft X-ray excess and quasi-periodic oscillation. *MNRAS*, 394(1):250–260.

[231] Miller, L., Turner, T. J., and Reeves, J. N. (2008). An absorption origin for the X-ray spectral variability of MCG-6-30-15. *A&A*, 483(2):437–452.

[232] Milosavljević, M. and Merritt, D. (2001). Formation of Galactic Nuclei. *ApJ*, 563(1):34–62.

[233] Mitsuda, K., Kelley, R. L., Boyce, K. R., Brown, G. V., Costantini, E., Dipirro, M. J., Ezoe, Y., Fujimoto, R., Gendreau, K. C., den Herder, J.-W., Hoshino, A., Ishisaki, Y., Kilbourne, C. A., Kitamoto, S., McCammon, D., Murakami, M., Murakami, H., Ogawa, M., Ohashi, T., Okamoto, A., Paltani, S., Pohl, M., Porter, F. S., Sato, Y., Shinozaki, K., Shirron, P. J., Sneiderman, G. A., Sugita, H., Szymkowiak, A., Takei, Y., Tamagawa, T., Tashiro, M., Terada, Y., Tsujimoto, M., de Vries, C., Yamaguchi, H., and Yamasaki, N. Y. (2010). The high-resolution x-ray microcalorimeter spectrometer system for the SXS on ASTRO-H. In Arnaud, M., Murray, S. S., and Takahashi, T., editors, *Space Telescopes and Instrumentation 2010: Ultraviolet to Gamma Ray*, volume 7732 of *Society of Photo-Optical Instrumentation Engineers (SPIE) Conference Series*, page 773211.

[234] Nandra, K., Barret, D., Barcons, X., Fabian, A., den Herder, J.-W., Piro, L., Watson, M., Adami, C., Aird, J., Afonso, J. M., Alexander, D., Argiroffi, C., Amati, L., Arnaud, M., Atteia, J.-L., Audard, M., Badenes, C., Ballet, J., Ballo, L., Bamba, A., Bhardwaj, A., Stefano Battistelli, E., Becker, W., De Becker, M., Behar, E., Bianchi, S., Biffi, V., Bîrzan, L., Bocchino, F., Bogdanov, S., Boirin, L., Boller, T., Borgani, S., Borm, K., Bouché, N., Bourdin, H., Bower, R., Braito, V., Branchini, E., Branduardi-Raymont, G., Bregman, J., Brenneman, L., Brightman, M., Brüggen, M., Buchner, J., Bulbul, E., Brusa, M., Bursa,

M., Caccianiga, A., Cackett, E., Campana, S., Cappelluti, N., Cappi, M., Carrera, F., Ceballos, M., Christensen, F., Chu, Y.-H., Churazov, E., Clerc, N., Corbel, S., Corral, A., Comastri, A., Costantini, E., Croston, J., Dadina, M., D'Ai, A., Decourchelle, A., Della Ceca, R., Dennerl, K., Dolag, K., Done, C., Dovciak, M., Drake, J., Eckert, D., Edge, A., Ettori, S., Ezoe, Y., Feigelson, E., Fender, R., Feruglio, C., Finoguenov, A., Fiore, F., Galeazzi, M., Gallagher, S., Gandhi, P., Gaspari, M., Gastaldello, F., Georgakakis, A., Georgantopoulos, I., Gilfanov, M., Gitti, M., Gladstone, R., Goosmann, R., Gosset, E., Grosso, N., Guedel, M., Guerrero, M., Haberl, F., Hardcastle, M., Heinz, S., Alonso Herrero, A., Hervé, A., Holmstrom, M., Iwasawa, K., Jonker, P., Kaastra, J., Kara, E., Karas, V., Kastner, J., King, A., Kosenko, D., Koutroumpa, D., Kraft, R., Kreykenbohm, I., Lallement, R., Lanzuisi, G., Lee, J., Lemoine-Goumard, M., Lobban, A., Lodato, G., Lovisari, L., Lotti, S., McCharthy, I., McNamara, B., Maggio, A., Maiolino, R., De Marco, B., de Martino, D., Mateos, S., Matt, G., Maughan, B., Mazzotta, P., Mendez, M., Merloni, A., Micela, G., Miceli, M., Mignani, R., Miller, J., Miniutti, G., Molendi, S., Montez, R., Moretti, A., Motch, C., Nazé, Y., Nevalainen, J., Nicastro, F., Nulsen, P., Ohashi, T., O'Brien, P., Osborne, J., Oskinova, L., Pacaud, F., Paerels, F., Page, M., Papadakis, I., Pareschi, G., Petre, R., Petrucci, P.-O., Piconcelli, E., Pillitteri, I., Pinto, C., de Plaa, J., Pointecouteau, E., Ponman, T., Ponti, G., Porquet, D., Pounds, K., Pratt, G., Predehl, P., Proga, D., Psaltis, D., Rafferty, D., Ramos-Ceja, M., Ranalli, P., Rasia, E., Rau, A., Rauw, G., Rea, N., Read, A., Reeves, J., Reiprich, T., Renaud, M., Reynolds, C., Risaliti, G., Rodriguez, J., Rodriguez Hidalgo, P., Roncarelli, M., Rosario, D., Rossetti, M., Rozanska, A., Rovilos, E., Salvaterra, R., Salvato, M., Di Salvo, T., Sanders, J., Sanz-Forcada, J., Schawinski, K., Schaye, J., Schwope, A., Sciortino, S., Severgnini, P., Shankar, F., Sijacki, D., Sim, S., Schmid, C., Smith, R., Steiner, A., Stelzer, B., Stewart, G., Strohmayer, T., Strüder, L., Sun, M., Takei, Y., Tatischeff, V., Tiengo, A., Tombesi, F., Trinchieri, G., Tsuru, T. G., Ud-Doula, A., Ursino, E., Valencic, L., Vanzella, E., Vaughan, S., Vignali, C., Vink, J., Vito, F., Volonteri, M., Wang, D., Webb, N., Willingale, R., Wilms, J., Wise, M., Worrall, D., Young, A., Zampieri, L., In't Zand, J., Zane, S., Zezas, A., Zhang, Y., and Zhuravleva, I. (2013). The Hot and Energetic Universe: A White Paper presenting the science theme motivating the Athena+ mission. *arXiv e-prints*, page arXiv:1306.2307.

[235] Nardini, E., Reeves, J. N., Gofford, J., Harrison, F. A., Risaliti, G., Braito, V., Costa, M. T., Matzeu, G. A., Walton, D. J., Behar, E., Boggs, S. E., Christensen, F. E., Craig, W. W., Hailey, C. J., Matt, G., Miller, J. M., O'Brien, P. T., Stern, D., Turner, T. J., and Ward, M. J. (2015). Black hole feedback in the luminous quasar PDS 456. *Science*, 347(6224):860–863.

[236] Netzer, H. (2013). *The Physics and Evolution of Active Galactic Nuclei*.

[237] Netzer, H. (2015). Revisiting the Unified Model of Active Galactic Nuclei. *ARA&A*, 53:365–408.

[238] Noda, H. and Done, C. (2018). Explaining changing-look AGN with state transition triggered by rapid mass accretion rate drop. *MNRAS*, 480(3):3898–3906.

[239] Novikov, I. D. and Thorne, K. S. (1973). Astrophysics of black holes. In *Black Holes (Les Astres Occlus)*, pages 343–450.

[240] Ohsuga, K. (2007). Feedback from Supercritical Disk Accretion Flows: Two-dimensional Radiation-Hydrodynamic Simulations of Stable and Unstable Disks with Radiatively Driven Outflows. *ApJ*, 659(1):205–210.

[241] Ohsuga, K., Mineshige, S., Mori, M., and Umemura, M. (2002). Does the Slim-Disk Model Correctly Consider Photon-trapping Effects? *ApJ*, 574(1):315–324.

[242] Osterbrock, D. E. and Pogge, R. W. (1985). The spectra of narrow-line Seyfert 1 galaxies. *ApJ*, 297:166–176.

[243] Panessa, F. and Bassani, L. (2002). Unabsorbed Seyfert 2 galaxies. *A&A*, 394:435–442.

[244] Panessa, F., de Rosa, A., Bassani, L., Bazzano, A., Bird, A., Landi, R., Malizia, A., Miniutti, G., Molina, M., and Ubertini, P. (2011). Narrow-line Seyfert 1 galaxies at hard X-rays. *MNRAS*, 417(4):2426–2439.

[245] Papadakis, I. E. (2004). The scaling of the X-ray variability with black hole mass in active galactic nuclei. *MNRAS*, 348(1):207–213.

[246] Pappa, A., Georgantopoulos, I., Stewart, G. C., and Zezas, A. L. (2001). The X-ray spectra of optically selected Seyfert 2 galaxies: are there any Seyfert 2 galaxies with no absorption? *MNRAS*, 326(3):995–1006.

[247] Parker, M. L., Alston, W. N., Buisson, D. J. K., Fabian, A. C., Jiang, J., Kara, E., Lohfink, A., Pinto, C., and Reynolds, C. S. (2017a). Revealing the ultrafast outflow in IRAS 13224-3809 through spectral variability. *MNRAS*, 469(2):1553–1558.

[248] Parker, M. L., Alston, W. N., Härer, L., Igo, Z., Joyce, A., Buisson, D. J. K., Chainakun, P., Fabian, A. C., Jiang, J., Kosec, P., Matzeu, G. A., Pinto, C., Xu, Y., and Zaidouni, F. (2021). The nature of the extreme X-ray variability in the NLS1 1H 0707-495. *MNRAS*, 508(2):1798–1816.

[249] Parker, M. L., Buisson, D. J. K., Jiang, J., Gallo, L. C., Kara, E., Matzeu, G. A., and Walton, D. J. (2018). Constraining the geometry of AGN outflows with reflection spectroscopy. *MNRAS*, 479(1):L45–L49.

[250] Parker, M. L., Fabian, A. C., Matt, G., Koljonen, K. I. I., Kara, E., Alston, W., Walton, D. J., Marinucci, A., Brenneman, L., and Risaliti, G. (2015). Revealing the X-ray variability of AGN with principal component analysis. *MNRAS*, 447(1):72–96.

[251] Parker, M. L., Longinotti, A. L., Schartel, N., Grupe, D., Komossa, S., Kriss, G., Fabian, A. C., Gallo, L., Harrison, F. A., Jiang, J., Kara, E., Krongold, Y., Matzeu, G. A., Pinto, C., and Santos-Lleó, M. (2019). The nuclear environment of the NLS1 Mrk 335: Obscuration of the X-ray line emission by a variable outflow. *MNRAS*, 490(1):683–697.

[252] Parker, M. L., Pinto, C., Fabian, A. C., Lohfink, A., Buisson, D. J. K., Alston, W. N., Kara, E., Cackett, E. M., Chiang, C.-Y., Dauser, T., De Marco, B., Gallo, L. C., Garcia, J., Harrison, F. A., King, A. L., Middleton, M. J., Miller, J. M., Miniutti, G., Reynolds, C. S., Uttley, P., Vasudevan, R., Walton, D. J., Wilkins, D. R., and Zoghbi, A. (2017b). The response of relativistic outflowing gas to the inner accretion disk of a black hole. *Nature*, 543(7643):83–86.

[253] Pawar, P. K., Dewangan, G. C., Papadakis, I. E., Patil, M. K., Pal, M., and Kembhavi, A. K. (2017). Complex UV/X-ray variability of 1H 0707-495. *MNRAS*, 472(3):2823–2832.

[254] Peterson, B. M., Ferrarese, L., Gilbert, K. M., Kaspi, S., Malkan, M. A., Maoz, D., Merritt, D., Netzer, H., Onken, C. A., Pogge, R. W., Vestergaard, M., and Wandel, A. (2004). Central Masses and Broad-Line Region Sizes of Active Galactic Nuclei. II. A Homogeneous Analysis of a Large Reverberation-Mapping Database. *ApJ*, 613(2):682–699.

[255] Peterson, J. R., Paerels, F. B. S., Kaastra, J. S., Arnaud, M., Reiprich, T. H., Fabian, A. C., Mushotzky, R. F., Jernigan, J. G., and Sakelliou, I. (2001). X-ray imaging-spectroscopy of Abell 1835. *A&A*, 365:L104–L109.

[256] Petrucci, P. O., Gronkiewicz, D., Rozanska, A., Belmont, R., Bianchi, S., Czerny, B., Matt, G., Malzac, J., Middei, R., De Rosa, A., Ursini, F., and Cappi, M. (2020). Radiation spectra of warm and optically thick coronae in AGNs. *A&A*, 634:A85.

[257] Petrucci, P. O., Ursini, F., De Rosa, A., Bianchi, S., Cappi, M., Matt, G., Dadina, M., and Malzac, J. (2018). Testing warm Comptonization models for the origin of the soft X-ray excess in AGNs. *A&A*, 611:A59.

[258] Pier, E. A. and Krolik, J. H. (1992). Infrared Spectra of Obscuring Dust Tori around Active Galactic Nuclei. I. Calculational Method and Basic Trends. *ApJ*, 401:99.

[259] Pinto, C., Alston, W., Parker, M. L., Fabian, A. C., Gallo, L. C., Buisson, D. J. K., Walton, D. J., Kara, E., Jiang, J., Lohfink, A., and Reynolds, C. S. (2018). Ultrafast outflows disappear in high-radiation fields. *MNRAS*, 476(1):1021–1035.

[260] Pinto, C., Alston, W., Soria, R., Middleton, M. J., Walton, D. J., Sutton, A. D., Fabian, A. C., Earnshaw, H., Urquhart, R., Kara, E., and Roberts, T. P. (2017). From ultraluminous X-ray sources to ultraluminous supersoft sources: NGC 55 ULX, the missing link. *MNRAS*, 468(3):2865–2883.

[261] Pinto, C., Mehdipour, M., Walton, D. J., Middleton, M. J., Roberts, T. P., Fabian, A. C., Guainazzi, M., Soria, R., Kosec, P., and Ness, J. U. (2020a). Thermal stability of winds driven by radiation pressure in super-Eddington accretion discs. *MNRAS*, 491(4):5702–5716.

[262] Pinto, C., Middleton, M. J., and Fabian, A. C. (2016). Resolved atomic lines reveal outflows in two ultraluminous X-ray sources. *Nature*, 533(7601):64–67.

[263] Pinto, C., Soria, R., Walton, D. J., D'Aì, A., Pintore, F., Kosec, P., Alston, W. N., Fuerst, F., Middleton, M. J., Roberts, T. P., Del Santo, M., Barret, D., Ambrosi, E., Robba, A., Earnshaw, H., and Fabian, A. C. (2021). XMM-Newton campaign on the ultraluminous X-ray source NGC 247 ULX-1: outflows. *MNRAS*, 505(4):5058–5074.

[264] Pinto, C., Walton, D. J., Kara, E., Parker, M. L., Soria, R., Kosec, P., Middleton, M. J., Alston, W. N., Fabian, A. C., Guainazzi, M., Roberts, T. P., Fuerst, F., Earnshaw, H. P., Sathyaprakash, R., and Barret, D. (2020b). XMM-Newton campaign on ultraluminous X-ray source NGC 1313 X-1: wind versus state variability. *MNRAS*, 492(4):4646–4665.

[265] Ponti, G., Papadakis, I., Bianchi, S., Guainazzi, M., Matt, G., Uttley, P., and Bonilla, N. F. (2012). CAIXA: a catalogue of AGN in the XMM-Newton archive. III. Excess variance analysis. *A&A*, 542:A83.

[266] Porquet, D. and Dubau, J. (2000). X-ray photoionized plasma diagnostics with helium-like ions. Application to warm absorber-emitter in active galactic nuclei. *A&AS*, 143:495–514.

[267] Porquet, D., Dubau, J., and Grosso, N. (2010). He-like Ions as Practical Astrophysical Plasma Diagnostics: From Stellar Coronae to Active Galactic Nuclei. *SSRv*, 157(1-4):103–134.

[268] Porquet, D., Reeves, J. N., O'Brien, P., and Brinkmann, W. (2004). XMM-Newton EPIC observations of 21 low-redshift PG quasars. *A&A*, 422:85–95.

[269] Pounds, K., Lobban, A., Reeves, J., and Vaughan, S. (2016a). Detection of a second high-velocity component in the highly ionized wind from PG 1211+143. *MNRAS*, 457(3):2951–2957.

[270] Pounds, K. A. (2014). The soft X-ray spectrum of the luminous narrow line Seyfert galaxy PG 1211+143 - evidence for a second high-velocity outflow component. *MNRAS*, 437(4):3221–3227.

[271] Pounds, K. A. and King, A. R. (2013). The shocked outflow in NGC 4051 - momentum-driven feedback, ultrafast outflows and warm absorbers. *MNRAS*, 433(2):1369–1377.

[272] Pounds, K. A., Lobban, A., Reeves, J. N., Vaughan, S., and Costa, M. (2016b). Imprints of a high-velocity wind on the soft X-ray spectrum of PG1211+143. *MNRAS*, 459(4):4389–4396.

[273] Pounds, K. A., Nandra, K., Stewart, G. C., George, I. M., and Fabian, A. C. (1990). X-ray reflection from cold matter in the nuclei of active galaxies. *Nature*, 344(6262):132–133.

[274] Pounds, K. A. and Reeves, J. N. (2007). Is the X-ray spectrum of the narrow emission line QSO PG1211+143 defined by its energetic outflow? *MNRAS*, 374(3):823–831.

[275] Pounds, K. A. and Reeves, J. N. (2009). Quantifying the fast outflow in the luminous Seyfert galaxy PG1211+143. *MNRAS*, 397(1):249–257.

[276] Pounds, K. A., Reeves, J. N., King, A. R., Page, K. L., O'Brien, P. T., and Turner, M. J. L. (2003). A high-velocity ionized outflow and XUV photosphere in the narrow emission line quasar PG1211+143. *MNRAS*, 345(3):705–713.

[277] Pounds, K. A. and Vaughan, S. (2011). An extended XMM-Newton observation of the Seyfert galaxy NGC 4051 - II. Soft X-ray emission from a limb-brightened shell of post-shock gas. *MNRAS*, 415(3):2379–2387.

[278] Poutanen, J., Lipunova, G., Fabrika, S., Butkevich, A. G., and Abolmasov, P. (2007). Supercritically accreting stellar mass black holes as ultraluminous X-ray sources. *MNRAS*, 377(3):1187–1194.

[279] Pringle, J. E. (1981). Accretion discs in astrophysics. *ARA&A*, 19:137–162.

[280] Proga, D. (2007). Dynamics of Accretion Flows Irradiated by a Quasar. *ApJ*, 661(2):693–702.

[281] Proga, D. and Kallman, T. R. (2002). On the Role of the Ultraviolet and X-Ray Radiation in Driving a Disk Wind in X-Ray Binaries. *ApJ*, 565(1):455–470.

[282] Proga, D., Stone, J. M., and Kallman, T. R. (2000). Dynamics of Line-driven Disk Winds in Active Galactic Nuclei. *ApJ*, 543(2):686–696.

[283] Puchnarewicz, E. M., Mason, K. O., Siemiginowska, A., and Pounds, K. A. (1995). The high-temperature big blue bump in the Seyfert galaxy RE J1034+396. *MNRAS*, 276(1):20–32.

[284] Rau, A., Meidinger, N., Nandra, K., Porro, M., Barret, D., Santangelo, A., Schmid, C., Struder, L., Tenzer, C., Wilms, J., Amoros, C., Andritschke, R., Aschauer, F., Bahr, A., Gunther, B., Furmetz, M., Ott, B., Perinati, E., Rambaud, D., Reiffers, J., Treis, J., von Kienlin, A., and Weidenspointner, G. (2013). The Hot and Energetic Universe: The Wide Field Imager (WFI) for Athena+. *arXiv e-prints*, page arXiv:1308.6785.

[285] Reeves, J. N. and Braito, V. (2019). A Momentum-conserving Accretion Disk Wind in the Narrow-line Seyfert 1 I Zwicky 1. *ApJ*, 884(1):80.

[286] Reeves, J. N., Braito, V., Chartas, G., Hamann, F., Laha, S., and Nardini, E. (2020). Resolving the Soft X-Ray Ultrafast Outflow in PDS 456. *ApJ*, 895(1):37.

[287] Reeves, J. N., Braito, V., Nardini, E., Behar, E., O'Brien, P. T., Tombesi, F., Turner, T. J., and Costa, M. T. (2016). Discovery of Broad Soft X-ray Absorption Lines from the Quasar Wind in PDS 456. *ApJ*, 824(1):20.

[288] Reeves, J. N., Braito, V., Nardini, E., Lobban, A. P., Matzeu, G. A., and Costa, M. T. (2018). A New Relativistic Component of the Accretion Disk Wind in PDS 456. *ApJL*, 854(1):L8.

[289] Reeves, J. N., Braito, V., Porquet, D., Laurenti, M., Lobban, A., and Matzeu, G. (2023). Rapid Variability of the Accretion Disk Wind in the Narrow-line Seyfert 1, PG 1448+273. *ApJ*, 952(1):52.

[290] Reeves, J. N., O'Brien, P. T., Braito, V., Behar, E., Miller, L., Turner, T. J., Fabian, A. C., Kaspi, S., Mushotzky, R., and Ward, M. (2009). A Compton-thick Wind in the High-luminosity Quasar, PDS 456. *ApJ*, 701(1):493–507.

[291] Reeves, J. N., O'Brien, P. T., and Ward, M. J. (2003). A Massive X-Ray Outflow from the Quasar PDS 456. *ApJL*, 593(2):L65–L68.

[292] Reines, A. E. and Volonteri, M. (2015). Relations between Central Black Hole Mass and Total Galaxy Stellar Mass in the Local Universe. *ApJ*, 813(2):82.

[293] Reynolds, C. S. (2014). Measuring Black Hole Spin Using X-Ray Reflection Spectroscopy. *SSRv*, 183(1-4):277–294.

[294] Reynolds, C. S. and Fabian, A. C. (1995). Warm absorbers in active galactic nuclei. *MNRAS*, 273(4):1167–1176.

[295] Ricci, C., Ho, L. C., Fabian, A. C., Trakhtenbrot, B., Koss, M. J., Ueda, Y., Lohfink, A., Shimizu, T., Bauer, F. E., Mushotzky, R., Schawinski, K., Paltani, S., Lamperti, I., Treister, E., and Oh, K. (2018). BAT AGN Spectroscopic Survey - XII. The relation between coronal properties of active galactic nuclei and the Eddington ratio. *MNRAS*, 480(2):1819–1830.

[296] Ricci, C., Loewenstein, M., Kara, E., Remillard, R., Trakhtenbrot, B., Arcavi, I., Gendreau, K. C., Arzoumanian, Z., Fabian, A. C., Li, R., Ho, L. C., MacLeod, C. L., Cackett, E., Altamirano, D., Gandhi, P., Kosec, P., Pasham, D., Steiner, J., and Chan, C. H. (2021). The 450 Day X-Ray Monitoring of the Changing-look AGN 1ES 1927+654. *ApJS*, 255(1):7.

[297] Ricci, C. and Trakhtenbrot, B. (2023). Changing-look active galactic nuclei. *Nature Astronomy*, 7:1282–1294.

[298] Ricci, C., Trakhtenbrot, B., Koss, M. J., Ueda, Y., Del Vecchio, I., Treister, E., Schawinski, K., Paltani, S., Oh, K., Lamperti, I., Berney, S., Gandhi, P., Ichikawa, K., Bauer, F. E., Ho, L. C., Asmus, D., Beckmann, V., Soldi, S., Baloković, M., Gehrels, N., and Markwardt, C. B. (2017). BAT AGN Spectroscopic Survey. V. X-Ray Properties of the Swift/BAT 70-month AGN Catalog. *ApJS*, 233(2):17.

[299] Riffel, R., Rodríguez-Ardila, A., and Pastoriza, M. G. (2006). A 0.8-2.4 μm spectral atlas of active galactic nuclei. *A&A*, 457(1):61–70.

[300] Rodríguez-Ardila, A., Pastoriza, M. G., and Donzelli, C. J. (2000). Visible and Near-Infrared Spectroscopy of Seyfert 1 and Narrow-Line Seyfert 1 Galaxies. *ApJS*, 126(1):63–78.

[301] Rodríguez-Ardila, J., Tomsick, J. A., and Chaty, S. (2008). Swift follow-up observations of INTEGRAL sources of unknown nature. *A&A*, 482(2):731–737.

[302] Rogantini, D., Costantini, E., Gallo, L. C., Wilkins, D. R., Brandt, W. N., and Mehdipour, M. (2022a). The multi-epoch X-ray tale of I Zwicky 1 outflows. *MNRAS*, 516(4):5171–5186.

[303] Rogantini, D., Mehdipour, M., Kaastra, J., Costantini, E., Juráňová, A., and Kara, E. (2022b). TPHO: A Time-dependent Photoionization Model for AGN Outflows. *ApJ*, 940(2):122.

[304] Ross, R. R. and Fabian, A. C. (1993). The effects of photoionization on X-ray reflection spectra in active galactic nuclei. *MNRAS*, 261:74–82.

[305] Ross, R. R. and Fabian, A. C. (2005). A comprehensive range of X-ray ionized-reflection models. *MNRAS*, 358(1):211–216.

[306] Rowan-Robinson, M. (1995). A new model for the infrared emission of quasars. *MNRAS*, 272(4):737–748.

[307] Rybicki, G. B. and Lightman, A. P. (1979). *Radiative processes in astrophysics*.

[308] Sako, M., Kahn, S. M., Behar, E., Kaastra, J. S., Brinkman, A. C., Boller, T., Puchnarewicz, E. M., Starling, R., Liedahl, D. A., Clavel, J., and Santos-Lleo, M. (2001). Complex resonance absorption structure in the X-ray spectrum of <ASTROBJ>IRAS 13349+2438</ASTROBJ>. *A&A*, 365:L168–L173.

[309] Sanfrutos, M., Longinotti, A. L., Krongold, Y., Guainazzi, M., and Panessa, F. (2018). The Evolution of the Warm Absorber Reveals a Shocked Outflow in the Narrow Line Seyfert 1 Galaxy IRAS 17020+4544. *ApJ*, 868(2):111.

[310] Sanfrutos, M., Miniutti, G., Agís-González, B., Fabian, A. C., Miller, J. M., Panessa, F., and Zoghbi, A. (2013). The size of the X-ray emitting region in SWIFT J2127.4+5654 via a broad line region cloud X-ray eclipse. *MNRAS*, 436(2):1588–1594.

[311] Schlafly, E. F. and Finkbeiner, D. P. (2011). Measuring Reddening with Sloan Digital Sky Survey Stellar Spectra and Recalibrating SFD. *ApJ*, 737(2):103.

[312] Schmidt, M. (1963). 3C 273 : A Star-Like Object with Large Red-Shift. *Nature*, 197(4872):1040.

[313] Schwarzschild, K. (1916). Über das Gravitationsfeld eines Massenpunktes nach der Einsteinschen Theorie. *Sitzungsberichte der Königlich Preussischen Akademie der Wissenschaften*, pages 189–196.

[314] Serafinelli, R., Tombesi, F., Vagnetti, F., Piconcelli, E., Gaspari, M., and Saturni, F. G. (2019). Multiphase quasar-driven outflows in PG 1114+445. I. Entrained ultra-fast outflows. *A&A*, 627:A121.

[315] Seyfert, C. K. (1943). Nuclear Emission in Spiral Nebulae. *ApJ*, 97:28.

[316] Shakura, N. I. and Sunyaev, R. A. (1973). Black holes in binary systems. Observational appearance. *A&A*, 24:337–355.

[317] Silk, J. and Rees, M. J. (1998). Quasars and galaxy formation. *A&A*, 331:L1–L4.

[318] Silva, C. V., Costantini, E., Giustini, M., Kriss, G. A., Brandt, W. N., Gallo, L. C., and Wilkins, D. R. (2018). The variability of the warm absorber in I Zwicky 1 as seen by XMM-Newton. *MNRAS*, 480(2):2334–2342.

[319] Sim, S. A., Proga, D., Miller, L., Long, K. S., and Turner, T. J. (2010). Multidimensional modelling of X-ray spectra for AGN accretion disc outflows - III. Application to a hydrodynamical simulation. *MNRAS*, 408(3):1396–1408.

[320] Singh, K. P., Garmire, G. P., and Nousek, J. (1985). Observations of Soft X-Ray Spectra from a Seyfert 1 and a Narrow Emission-Line Galaxy. *ApJ*, 297:633.

[321] Snellen, I. A. G., Mack, K. H., Schilizzi, R. T., and Tschager, W. (2004). The CORALZ sample - I. Young radio-loud active galactic nuclei at low redshift. *MNRAS*, 348(1):227–234.

[322] Steenbrugge, K. C., Fenovčík, M., Kaastra, J. S., Costantini, E., and Verbunt, F. (2009). High-resolution X-ray spectroscopy of the low and high states of the Seyfert 1 galaxy NGC 4051 with Chandra LETGS. *A&A*, 496(1):107–119.

[323] Steenbrugge, K. C., Kaastra, J. S., Crenshaw, D. M., Kraemer, S. B., Arav, N., George, I. M., Liedahl, D. A., van der Meer, R. L. J., Paerels, F. B. S., Turner, T. J., and Yaqoob, T. (2005). Simultaneous X-ray and UV spectroscopy of the Seyfert galaxy NGC 5548. II. Physical conditions in the X-ray absorber. *A&A*, 434(2):569–584.

[324] Steenbrugge, K. C., Kaastra, J. S., de Vries, C. P., and Edelson, R. (2003). XMM-NEWTON High resolution spectroscopy of NGC 5548. *A&A*, 402:477–486.

[325] Strüder, L., Briel, U., Dennerl, K., Hartmann, R., Kendziorra, E., Meidinger, N., Pfeffermann, E., Reppin, C., Aschenbach, B., Bornemann, W., Bräuninger, H., Burkert, W., Elender, M., Freyberg, M., Haberl, F., Hartner, G., Heuschmann, F., Hippmann, H., Kastelic, E., Kemmer, S., Kettenring, G., Kink, W., Krause, N., Müller, S., Oppitz, A., Pietsch, W., Popp, M., Predehl, P., Read, A., Stephan, K. H., Stötter, D., Trümper, J., Holl, P., Kemmer, J., Soltau, H., Stötter, R., Weber, U., Weichert, U., von Zanthier, C., Carathanassis, D., Lutz, G., Richter, R. H., Solc, P., Böttcher, H., Kuster, M., Staubert, R., Abbey, A., Holland, A., Turner, M., Balasini, M., Bignami, G. F., La Palombara, N., Villa, G., Buttler, W., Gianini, F., Lainé, R., Lumb, D., and Dhez, P. (2001). The European Photon Imaging Camera on XMM-Newton: The pn-CCD camera. *A&A*, 365:L18–L26.

[326] Sunyaev, R. A. and Titarchuk, L. G. (1980). Comptonization of X-Rays in Plasma Clouds - Typical Radiation Spectra. *A&A*, 86:121.

[327] Svoboda, J., Beuchert, T., Guainazzi, M., Longinotti, A. L., Piconcelli, E., and Wilms, J. (2015). An X-ray variable absorber within the broad line region in Fairall 51. *A&A*, 578:A96.

[328] Takahashi, T., Kokubun, M., Mitsuda, K., Kelley, R. L., Ohashi, T., Aharonian, F., Akamatsu, H., Akimoto, F., Allen, S. W., Anabuki, N., Angelini, L., Arnaud, K., Asai, M., Audard, M., Awaki, H., Axelsson, M., Azzarello, P., Baluta, C., Bamba, A., Bando, N., Bautz, M. W., Bialas, T., Blandford, R., Boyce, K., Brenneman, L. W., Brown, G. V., Bulbul, E., Cackett, E. M., Canavan, E., Chernyakova, M., Chiao, M. P., Coppi, P. S., Costantini, E., O'Dell, S., DiPirro, M., Done, C., Dotani, T., Doty, J., Ebisawa, K., Eckart, M. E., Enoto, T., Ezoe, Y., Fabian, A. C., Ferrigno, C., Foster, A. R., Fujimoto, R., Fukazawa, Y., Funk, S., Furuzawa, A., Galeazzi, M., Gallo, L. C., Gandhi, P., Gilmore, K., Giustini, M., Goldwurm, A., Gu, L., Guainazzi, M., Haas, D., Haba, Y., Hagino, K., Hamaguchi, K., Harrus, I. M., Hatsukade, I., Hayashi, T., Hayashi, K., Hayashida, K., den Herder, J.-W., Hiraga, J. S., Hirose, K., Hornschemeier, A., Hoshino, A., Hughes, J. P., Ichinohe, Y., Iizuka, R., Inoue, H., Inoue, Y., Ishibashi, K., Ishida, M., Ishikawa, K., Ishimura, K., Ishisaki, Y., Itoh, M., Iwai, M., Iwata, N., Iyomoto, N., Jewell, C., Kaastra, J., Kallman, T., Kamae, T., Kara, E., Kataoka, J., Katsuda, S., Katsuta, J., Kawaharada, M., Kawai, N., Kawano, T., Kawasaki, S., Khangulyan, D., Kilbourne, C. A., Kimball, M., King, A., Kitaguchi, T., Kitamoto, S., Kitayama, T., Kohmura, T., Konami, S., Kosaka, T., Koujelev, A., Koyama, K., Koyama, S., Kretschmar, P., Krimm, H. A., Kubota, A., Kunieda, H., Laurent, P., Lee, S.-H., Leutenegger, M. A., Limousin, O., Loewenstein, M., Long, K. S., Lumb, D., Madejski, G., Maeda, Y., Maier, D., Makishima, K., Markevitch, M., Masters, C., Matsumoto, H., Matsushita, K., McCammon, D., Mcguinness, D., McNamara, B. R., Mehdipour, M., Miko, J., Miller, E. D., Miller, J. M., Mineshige, S., Minesugi, K., Mitsuishi, I., Miyazawa, T., Mizuno, T., Mori, H., Mori, K., Moroso, F., Moseley, H., Muench, T., Mukai, K., Murakami, H., Murakami, T., Mushotzky, R. F., Nagano, H., Nagino, R., Nakagawa, T., Nakajima, H., Nakamori, T., Nakano, T.,

Nakashima, S., Nakazawa, K., Namba, Y., Natsukari, C., Nishioka, Y., Nobukawa, K. K., Nobukawa, M., Noda, H., Nomachi, M., Odaka, H., Ogawa, H., Ogawa, M., Ogi, K., Ohno, M., Ohta, M., Okajima, T., Okamoto, A., Okazaki, T., Ota, N., Ozaki, M., Paerels, F., Paltani, S., Parmar, A., Petre, R., Pinto, C., de Plaa, J., Pohl, M., Pontius, J., Porter, F. S., Pottschmidt, K., Ramsey, B., Reynolds, C., Russell, H., Safi-Harb, S., Saito, S., Sakai, K., Sakai, S.-i., Sameshima, H., Sasaki, T., Sato, G., Sato, K., Sato, R., Sato, Y., Sawada, M., Schartel, N., Serlemitsos, P. J., Seta, H., Shibano, Y., Shida, M., Shidatsu, M., Shimada, T., Shinozaki, K., Shirron, P., Simionescu, A., Simmons, C., Smith, R. K., Sneiderman, G., Soong, Y., Stawarz, Ł., Sugawara, Y., Sugita, S., Sugita, H., Szymkowiak, A., Tajima, H., Takahashi, H., Takeda, S., Takei, Y., Tamagawa, T., Tamura, T., Tamura, K., Tanaka, T., Tanaka, Y., Tanaka, Y. T., Tashiro, M. S., Tawara, Y., Terada, Y., Terashima, Y., Tombesi, F., Tomida, H., Tsuboi, Y., Tsujimoto, M., Tsunemi, H., Tsuru, T. G., Uchida, H., Uchiyama, H., Uchiyama, Y., Ueda, S., Ueda, Y., Ueno, S., Uno, S., Urry, C. M., Ursino, E., de Vries, C. P., Wada, A., Watanabe, S., Watanabe, T., Werner, N., Wik, D. R., Wilkins, D. R., Williams, B. J., Yamada, S., Yamada, T., Yamaguchi, H., Yamaoka, K., Yamasaki, N. Y., Yamauchi, M., Yamauchi, S., Yaqoob, T., Yatsu, Y., Yonetoku, D., Yoshida, A., Yuasa, T., Zhuravleva, I., and Zoghbi, A. (2018). Hitomi (ASTRO-H) X-ray Astronomy Satellite. *Journal of Astronomical Telescopes, Instruments, and Systems*, 4:021402.

[329] Takeuchi, S., Mineshige, S., and Ohsuga, K. (2009). Modified Slim-Disk Model Based on Radiation-Hydrodynamic Simulation Data: The Conflict between Outflow and Photon Trapping. *PASJ*, 61:783.

[330] Takeuchi, S., Ohsuga, K., and Mineshige, S. (2013). Clumpy Outflows from Supercritical Accretion Flow. *PASJ*, 65:88.

[331] Tarter, C. B., Tucker, W. H., and Salpeter, E. E. (1969). The Interaction of X-Ray Sources with Optically Thin Environments. *ApJ*, 156:943.

[332] Tashiro, M., Maejima, H., Toda, K., Kelley, R., Reichenthal, L., Lobell, J., Petre, R., Guainazzi, M., Costantini, E., Edison, M., Fujimoto, R., Grim, M., Hayashida, K., den Herder, J.-W., Ishisaki, Y., Paltani, S., Matsushita, K., Mori, K., Sneiderman, G., Takei, Y., Terada, Y., Tomida, H., Akamatsu, H., Angelini, L., Arai, Y., Awaki, H., Babyk, I., Bamba, A., Barfknecht, P., Barnstable, K., Bialas, T., Blagojevic, B., Bonafede, J., Brambora, C., Brenneman, L., Brown, G., Brown, K., Burns, L., Canavan, E., Carnahan, T., Chiao, M., Comber, B., Corrales, L., de Vries, C., Dercksen, J., Diaz-Trigo, M., Dillard, T., DiPirro, M., Done, C., Dotani, T., Ebisawa, K., Eckart, M., Enoto, T., Ezoe, Y., Ferrigno, C., Fukazawa, Y., Fujita, Y., Furuzawa, A., Gallo, L., Graham, S., Gu, L., Hagino, K., Hamaguchi, K., Hatsukade, I., Hawes, D., Hayashi, T., Hegarty, C., Hell, N., Hiraga, J., Hodges-Kluck, E., Holland, M., Hornschemeier, A., Hoshino, A., Ichinohe, Y., Iizuka, R., Ishibashi, K., Ishida, M., Ishikawa, K., Ishimura, K., James, B., Kallman, T., Kara, E., Katsuda, S., Kenyon, S., Kilbourne, C., Kimball, M., Kitaguti, T., Kitamoto, S., Kobayashi, S., Kohmura, T., Koyama, S., Kubota, A., Leutenegger, M., Lockard, T., Loewenstein, M., Maeda, Y., Marbley, L., Markevitch, M., Matsumoto, H., Matsuzaki, K., McCammon, D., McNamara, B., Miko, J., Miller, E., Miller, J., Minesugi, K., Mitsuishi, I., Mizuno, T., Mori, H., Mukai, K., Murakami, H., Mushotzky, R., Nakajima, H., Nakamura, H., Nakashima, S., Nakazawa, K., Natsukari, C., Nigo, K., Nishioka, Y., Nobukawa, K., Nobukawa, M., Noda, H., Odaka, H., Ogawa, M., Ohashi, T., Ohno, M., Ohta, M., Okajima, T., Okamoto, A., Onizuka, M., Ota, N., Ozaki, M., Plucinsky, P., Porter, F. S.,

Pottschmidt, K., Sato, K., Sato, R., Sawada, M., Seta, H., Shelton, K., Shibano, Y., Shida, M., Shidatsu, M., Shirron, P., Simionescu, A., Smith, R., Someya, K., Soong, Y., Suagawara, Y., Szymkowiak, A., Takahashi, H., Tamagawa, T., Tamura, T., Tanaka, T., Terashima, Y., Tsuboi, Y., Tsujimoto, M., Tsunemi, H., Tsuru, T., Uchida, H., Uchiyama, H., Ueda, Y., Uno, S., Walsh, T., Watanabe, S., Williams, B., Wolfs, R., Wright, M., Yamada, S., Yamaguchi, H., Yamaoka, K., Yamasaki, N., Yamauchi, S., Yamauchi, M., Yanagase, K., Yaqoob, T., Yasuda, S., Yoshioka, N., Zabala, J., and Irina, Z. (2018). Concept of the X-ray Astronomy Recovery Mission. In den Herder, J.-W. A., Nikzad, S., and Nakazawa, K., editors, *Space Telescopes and Instrumentation 2018: Ultraviolet to Gamma Ray*, volume 10699 of *Society of Photo-Optical Instrumentation Engineers (SPIE) Conference Series*, page 1069922.

[333] Thomsen, L. L., Lixin Dai, J., Ramirez-Ruiz, E., Kara, E., and Reynolds, C. (2019). X-Ray Fluorescence from Super-Eddington Accreting Black Holes. *ApJL*, 884(1):L21.

[334] Thorne, K. S. (1974). Disk-Accretion onto a Black Hole. II. Evolution of the Hole. *ApJ*, 191:507–520.

[335] Titarchuk, L. (1994). Generalized Comptonization Models and Application to the Recent High-Energy Observations. *ApJ*, 434:570.

[336] Titarchuk, L. and Lyubarskij, Y. (1995). Power-Law Spectra as a Result of Comptonization of the Soft Radiation in a Plasma Cloud. *ApJ*, 450:876.

[337] Tombesi, F., Cappi, M., Reeves, J. N., Nemmen, R. S., Braito, V., Gaspari, M., and Reynolds, C. S. (2013). Unification of X-ray winds in Seyfert galaxies: from ultra-fast outflows to warm absorbers. *MNRAS*, 430(2):1102–1117.

[338] Tombesi, F., Cappi, M., Reeves, J. N., Palumbo, G. G. C., Braito, V., and Dadina, M. (2011). Evidence for Ultra-fast Outflows in Radio-quiet Active Galactic Nuclei. II. Detailed Photoionization Modeling of Fe K-shell Absorption Lines. *ApJ*, 742(1):44.

[339] Tombesi, F., Cappi, M., Reeves, J. N., Palumbo, G. G. C., Yaqoob, T., Braito, V., and Dadina, M. (2010a). Evidence for ultra-fast outflows in radio-quiet AGNs. I. Detection and statistical incidence of Fe K-shell absorption lines. *A&A*, 521:A57.

[340] Tombesi, F., Meléndez, M., Veilleux, S., Reeves, J. N., González-Alfonso, E., and Reynolds, C. S. (2015). Wind from the black-hole accretion disk driving a molecular outflow in an active galaxy. *Nature*, 519(7544):436–438.

[341] Tombesi, F., Sambruna, R. M., Reeves, J. N., Braito, V., Ballo, L., Gofford, J., Cappi, M., and Mushotzky, R. F. (2010b). Discovery of Ultra-fast Outflows in a Sample of Broad-line Radio Galaxies Observed with Suzaku. *ApJ*, 719(1):700–715.

[342] Trakhtenbrot, B., Arcavi, I., MacLeod, C. L., Ricci, C., Kara, E., Graham, M. L., Stern, D., Harrison, F. A., Burke, J., Hiramatsu, D., Hosseinzadeh, G., Howell, D. A., Smartt, S. J., Rest, A., Prieto, J. L., Shappee, B. J., Holoien, T. W. S., Bersier, D., Filippenko, A. V., Brink, T. G., Zheng, W., Li, R., Remillard, R. A., and Loewenstein, M. (2019). 1ES 1927+654: An AGN Caught Changing Look on a Timescale of Months. *ApJ*, 883(1):94.

[343] Turner, M. J. L., Abbey, A., Arnaud, M., Balasini, M., Barbera, M., Belsole, E., Bennie, P. J., Bernard, J. P., Bignami, G. F., Boer, M., Briel, U., Butler, I., Cara, C., Chabaud, C., Cole, R., Collura, A., Conte, M., Cros, A., Denby, M., Dhez, P., Di Coco, G., Dowson, J., Ferrando, P., Ghizzardi, S., Gianotti, F., Goodall, C. V., Gretton, L., Griffiths, R. G., Hainaut, O., Hochedez, J. F., Holland, A. D., Jourdain, E., Kendziorra, E., Lagostina, A., Laine, R., La Palombara, N., Lortholary, M., Lumb, D., Marty, P., Molendi, S., Pigot, C., Poindron, E., Pounds, K. A., Reeves, J. N., Reppin, C., Rothenflug, R., Salvetat, P., Sauvageot, J. L., Schmitt, D., Sembay, S., Short, A. D. T., Spragg, J., Stephen, J., Strüder, L., Tiengo, A., Trifoglio, M., Trümper, J., Vercellone, S., Vigroux, L., Villa, G., Ward, M. J., Whitehead, S., and Zonca, E. (2001). The European Photon Imaging Camera on XMM-Newton: The MOS cameras. *A&A*, 365:L27–L35.

[344] Turner, T. J. and Pounds, K. A. (1989). The EXOSAT spectral survey of AGN. *MNRAS*, 240:833–880.

[345] Turner, T. J., Reeves, J. N., Kraemer, S. B., and Miller, L. (2008). Tracing a disk wind in NGC 3516. *A&A*, 483(1):161–169.

[346] Ueda, Y., Akiyama, M., Ohta, K., and Miyaji, T. (2003). Cosmological Evolution of the Hard X-Ray Active Galactic Nucleus Luminosity Function and the Origin of the Hard X-Ray Background. *ApJ*, 598(2):886–908.

[347] Ueda, Y., Yamaoka, K., and Remillard, R. (2009). GRS 1915+105 in "Soft State": Nature of Accretion Disk Wind and Origin of X-ray Emission. *ApJ*, 695(2):888–899.

[348] Urry, C. M. and Padovani, P. (1995). Unified Schemes for Radio-Loud Active Galactic Nuclei. *PASP*, 107:803.

[349] van Velzen, S., Holoien, T. W. S., Onori, F., Hung, T., and Arcavi, I. (2020). Optical-Ultraviolet Tidal Disruption Events. *SSRv*, 216(8):124.

[350] Vaughan, S., Edelson, R., Warwick, R. S., and Uttley, P. (2003). On characterizing the variability properties of X-ray light curves from active galaxies. *MNRAS*, 345(4):1271–1284.

[351] Vaughan, S., Reeves, J., Warwick, R., and Edelson, R. (1999). X-ray spectral complexity in narrow-line Seyfert 1 galaxies. *MNRAS*, 309(1):113–124.

[352] Vaughan, S. and Uttley, P. (2008). On the evidence for narrow, relativistically shifted X-ray lines. *MNRAS*, 390(1):421–428.

[353] Véron-Cetty, M. P., Véron, P., and Gonçalves, A. C. (2001). A spectrophotometric atlas of Narrow-Line Seyfert 1 galaxies. *A&A*, 372:730–754.

[354] Vestergaard, M. and Peterson, B. M. (2006). Determining Central Black Hole Masses in Distant Active Galaxies and Quasars. II. Improved Optical and UV Scaling Relationships. *ApJ*, 641(2):689–709.

[355] Wada, K. and Norman, C. A. (2002). Obscuring Material around Seyfert Nuclei with Starbursts. *ApJL*, 566(1):L21–L24.

[356] Waddell, S. G. H. and Gallo, L. C. (2020). A Suzaku sample of unabsorbed narrow-line and broad-line Seyfert 1 galaxies - I. X-ray spectral properties. *MNRAS*, 498(4):5207–5226.

[357] Walton, D. J., Nardini, E., Gallo, L. C., Reynolds, M. T., Ricci, C., Dauser, T., Fabian, A. C., García, J. A., Harrison, F. A., Risaliti, G., and Stern, D. (2019). A low-flux state in IRAS 00521-7054 seen with NuSTAR and XMM-Newton: relativistic reflection and an ultrafast outflow. *MNRAS*, 484(2):2544–2555.

[358] Wang, T. and Lu, Y. (2001). Black hole mass and velocity dispersion of narrow line region in active galactic nuclei and narrow line Seyfert 1 galaxies. *A&A*, 377:52–59.

[359] Wang, Y. (2018). *Disc reflection in low-mass X-ray binaries*. PhD thesis, University of Groningen.

[360] Warner, C., Hamann, F., and Dietrich, M. (2004). Active Galactic Nucleus Emission-Line Properties Versus the Eddington Ratio. *ApJ*, 608(1):136–148.

[361] Weisskopf, M. C., Tananbaum, H. D., Van Speybroeck, L. P., and O'Dell, S. L. (2000). Chandra X-ray Observatory (CXO): overview. In Truemper, J. E. and Aschenbach, B., editors, *X-Ray Optics, Instruments, and Missions III*, volume 4012 of *Society of Photo-Optical Instrumentation Engineers (SPIE) Conference Series*, pages 2–16.

[362] Whewell, M., Branduardi-Raymont, G., Kaastra, J. S., Mehdipour, M., Steenbrugge, K. C., Bianchi, S., Behar, E., Ebrero, J., Cappi, M., Costantini, E., De Marco, B., Di Gesu, L., Kriss, G. A., Paltani, S., Peterson, B. M., Petrucci, P. O., Pinto, C., and Ponti, G. (2015). Anatomy of the AGN in NGC 5548. V. A clear view of the X-ray narrow emission lines. *A&A*, 581:A79.

[363] Wilkins, D. R., Gallo, L. C., Costantini, E., Brandt, W. N., and Blandford, R. D. (2021). Light bending and X-ray echoes from behind a supermassive black hole. *Nature*, 595(7869):657–660.

[364] Wilkins, D. R., Gallo, L. C., Costantini, E., Brandt, W. N., and Blandford, R. D. (2022). Acceleration and cooling of the corona during X-ray flares from the Seyfert galaxy I Zw 1. *MNRAS*, 512(1):761–775.

[365] Wilkins, D. R., Gallo, L. C., Silva, C. V., Costantini, E., Brandt, W. N., and Kriss, G. A. (2017). Revealing structure and evolution within the corona of the Seyfert galaxy I Zw 1. *MNRAS*, 471(4):4436–4451.

[366] Willingale, R., Starling, R. L. C., Beardmore, A. P., Tanvir, N. R., and O'Brien, P. T. (2013). Calibration of X-ray absorption in our Galaxy. *MNRAS*, 431(1):394–404.

[367] Wilms, J., Allen, A., and McCray, R. (2000). On the Absorption of X-Rays in the Interstellar Medium. *ApJ*, 542(2):914–924.

[368] Winkel, N., Husemann, B., Singha, M., Bennert, V. N., Combes, F., Davis, T. A., Gaspari, M., Jahnke, K., McElroy, R., O'Dea, C. P., and Pérez-Torres, M. A. (2022). The Close AGN Reference Survey (CARS). A parsec scale multi-phase outflow in the super-Eddington NLS1 Mrk 1044. *arXiv e-prints*, page arXiv:2211.00657.

[369] Wood, P. R., Bessell, M. S., and Fox, M. W. (1983). Long-period variables in the Magellanic Clouds : Supergiants, AGB stars, Supernova precursors, Planetary nebula precursors, and enrichment of the interstellar medium. *ApJ*, 272:99–115.

[370] XRISM Science Team (2020). Science with the X-ray Imaging and Spectroscopy Mission (XRISM). *arXiv e-prints*, page arXiv:2003.04962.

[371] Xu, Y., García, J. A., Walton, D. J., Connors, R. M. T., Madsen, K., and Harrison, F. A. (2021a). The Nature of Soft Excess in ESO 362-G18 Revealed by XMM-Newton and NuSTAR Spectroscopy. *ApJ*, 913(1):13.

[372] Xu, Y., Pinto, C., Bianchi, S., Kosec, P., Parker, M. L., Walton, D. J., Fabian, A. C., Guainazzi, M., Barret, D., and Cusumano, G. (2021b). Wind-luminosity evolution in NLS1 AGN 1H 0707-495. *MNRAS*, 508(4):6049–6067.

[373] Xu, Y., Pinto, C., Kara, E., Masterson, M., García, J. A., Fabian, A. C., Parker, M. L., Barret, D., Alston, W. N., and Cusumano, G. (2022). Ejection-accretion connection in NLS1 AGN 1H 1934-063. *MNRAS*, 513(2):1910–1924.

[374] Xu, Y., Pinto, C., Rogantini, D., Bianchi, S., Guainazzi, M., Kara, E., Jin, C., and Cusumano, G. (2023). Constraints on the ultrafast outflows in the narrow-line Seyfert 1 galaxy Mrk 1044 from high-resolution time- and flux-resolved spectroscopy. *MNRAS*, 523(2):2158–2171.

[375] Yuan, F. and Narayan, R. (2014). Hot Accretion Flows Around Black Holes. *ARA&A*, 52:529–588.

[376] Yuan, W., Macri, L. M., Peterson, B. M., Riess, A. G., Fausnaugh, M. M., Hoffmann, S. L., Anand, G. S., Bentz, M. C., Dalla Bontà, E., Davies, R. I., De Rosa, G., Ferrarese, L., Grier, C. J., Hicks, E. K. S., Onken, C. A., Pogge, R. W., Storchi-Bergmann, T., and Vestergaard, M. (2021). The Cepheid Distance to the Narrow-line Seyfert 1 Galaxy NGC 4051. *ApJ*, 913(1):3.

[377] Zdziarski, A. A. (1985). Power-law X-ray and gamma-ray emission from relativistic thermal plasmas. *ApJ*, 289:514–525.

[378] Zdziarski, A. A., Johnson, W. N., and Magdziarz, P. (1996). Broad-band γ-ray and X-ray spectra of NGC 4151 and their implications for physical processes and geometry. *MNRAS*, 283(1):193–206.

[379] Zhou, X.-L. and Wang, J.-M. (2005). Narrow Iron Kα Lines in Active Galactic Nuclei: Evolving Populations? *ApJL*, 618(2):L83–L86.

[380] Zoghbi, A., Fabian, A. C., Uttley, P., Miniutti, G., Gallo, L. C., Reynolds, C. S., Miller, J. M., and Ponti, G. (2010). Broad iron L line and X-ray reverberation in 1H0707-495. *MNRAS*, 401(4):2419–2432.

[381] Zoghbi, A., Miller, J. M., Walton, D. J., Harrison, F. A., Fabian, A. C., Reynolds, C. S., Boggs, S. E., Christensen, F. E., Craig, W., Hailey, C. J., Stern, D., and Zhang, W. W. (2015). NuSTAR Reveals Relativistic Reflection But No Ultra-Fast Outflow in the Quasar Pg$\sim$1211+143. *ApJL*, 799(2):L24.

[382] Życki, P. T., Done, C., and Smith, D. A. (1999). The 1989 May outburst of the soft X-ray transient GS 2023+338 (V404 Cyg). *MNRAS*, 309(3):561–575.

Appendix A

Details of individual targets and spectral analysis

In this appendix, we present an overview of basic information for six AGN shown in Chapter 6, alongside details of the Gaussian line scan results and the photoionization modeling of warm absorbers (listed in Tab.A.1).

A.1 1H 1934-063

1H 1934-063 is a nearby ($z = 0.0102$) radio-quiet NLS1 galaxy, presenting variable X-ray fluxes [265]. The spin of the central SMBH was estimated at $a_\star < 0.56$ [373] or $a_\star > 0.4$ [136] depending on whether a high-density relativistic reflection model was adopted. In the 2015 observation of 1H 1934-063, a $\sim$ 20s time lag was detected between the disk reprocessing component and the primary continuum, indicating a compact corona with a height of $9 \pm 4 R_{\rm g}$ ($R_{\rm g} \equiv GM_{\rm BH}/c^2$) in the lamppost geometry. In the RGS spectrum, distinct signatures of a WA and a moderately ionized UFO have been identified as well [373]. Moreover, the tentative evidence for the reprocessing of the coronal photons onto the base of winds has also been observed. Furthermore, two *XMM-Newton* observations were conducted on 1H 1934-063 in 2021.

The results of the Gaussian line scan in the RGS band are shown in Fig.A.1, highlighting the consistent presence of the WA features, such as N VII, O VIII, Fe XVIII, Fe XVII, and Ne IX across all spectra. The prominent UFO absorption features transition from O VII and O VIII to Fe complex lines, Fe XXI-XXIII between 2015 and 2021. In contrast, the properties of the WA remain constant for six years (see Tab.A.1).

Table A.1 Table of the best-fit WA parameters in extracted spectra of targets in Chapter 6. The uncertainties of parameters are estimated at 1σ error bars.

Sources	WA				
	$\log \xi$ erg cm s^{-1}	$N_{\rm H}$ (10^{20} cm^{-2})	$\sigma_{\rm v}$ (km/s)	$v_{\rm LOS}$ (km/s)	ΔC-stat
1H 1934-063					
2015	$1.88^{+0.03}_{-0.03}$	8^{+1}_{-1}	104^{+24}_{-10}	-360^{+60}_{-60}	159
2021	$1.89^{+0.02}_{-0.01}$	8^{+1}_{-1}	92^{+8}_{-12}	-270^{+30}_{-90}	215
F1	$1.88^{+0.03}_{-0.04}$	10^{+2}_{-1}	74^{+18}_{-18}	-240^{+90}_{-90}	99
F2	$1.88^{+0.03}_{-0.03}$	8^{+1}_{-1}	100^{+17}_{-10}	-330^{+60}_{-60}	142
RE J1034+396					
avg*	$3.61^{+0.02}_{-0.01}$	27^{+3}_{-3}	262^{+57}_{-60}	-1110^{+60}_{-60}	514
	$0.0^{+0.1}_{-0.1}$	$1.1^{+0.2}_{-0.1}$	7173^{+1256}_{-735}	-19800^{+1500}_{-600}	109
	$1.89^{+0.08}_{-0.10}$	$0.65^{+0.09}_{-0.07}$	316^{+33}_{-75}	-330^{+90}_{-60}	100
F1*	$3.64^{+0.05}_{-0.04}$	32^{+6}_{-6}	108^{+173}_{-40}	-1350^{+90}_{-90}	149
	$-0.9^{+0.7}_{-0.2}$	$2.4^{+0.2}_{-1.1}$	$10000^\bullet$	-30900^{+5100}_{-900}	36
	$1.97^{+0.12}_{-0.13}$	$1.6^{+0.8}_{-0.5}$	162^{+94}_{-63}	-330^{+90}_{-120}	53
F2*	$3.59^{+0.03}_{-0.03}$	27^{+4}_{-3}	314^{+41}_{-74}	-990^{+90}_{-90}	180
	$-0.2^{+0.1}_{-0.1}$	$1.1^{+0.2}_{-0.2}$	2040^{+573}_{-574}	-21300^{+300}_{-300}	67
	$1.78^{+0.17}_{-0.27}$	$0.6^{+0.2}_{-0.1}$	316^{+217}_{-62}	-570^{+120}_{-180}	23
high*	$3.46^{+0.05}_{-0.05}$	27^{+4}_{-4}	542^{+170}_{-161}	-720^{+150}_{-120}	100
	$0.0^{+0.3}_{-0.4}$	$1.2^{+0.5}_{-0.3}$	$10000^\bullet$	-21000^{+2400}_{-3900}	20
PG 1211+143					
T7	$2.40^{+0.08}_{-0.09}$	18^{+5}_{-5}	< 36	-3000^{+300}_{-300}	22
I ZW 1					
avg*	$-0.40^{+0.04}_{-0.04}$	$5.0^{+0.4}_{-0.4}$	207^{+23}_{-23}	-1830^{+60}_{-60}	384
	$2.70^{+0.06}_{-0.06}$	6^{+2}_{-2}	50^{+28}_{-21}	-2400^{+300}_{-300}	41
2005	$-0.34^{+0.11}_{-0.11}$	7^{+1}_{-1}	157^{+56}_{-56}	-1920^{+120}_{-120}	76
F1*	$-0.27^{+0.06}_{-0.06}$	$3.5^{+0.4}_{-0.3}$	500^{+121}_{-123}	-1830^{+90}_{-90}	111
	$2.44^{+0.20}_{-0.08}$	5^{+2}_{-1}	81^{+44}_{-31}	-1800^{+300}_{-300}	28
F2*	$-0.14^{+0.09}_{-0.09}$	$4.8^{+0.8}_{-0.7}$	120^{+42}_{-30}	-2010^{+90}_{-90}	91
	$2.78^{+0.05}_{-0.08}$	30^{+20}_{-10}	< 27	-2400^{+600}_{-300}	19
2020	$-1.00^{+0.09}_{-0.09}$	14^{+2}_{-1}	211^{+47}_{-45}	-1740^{+90}_{-90}	172
IRAS 17020+4544					
avg*	$-0.3^{+0.1}_{-0.1}$	$4.7^{+0.5}_{-0.5}$	733^{+54}_{-84}	30^{+60}_{-90}	638
	$1.9^{+0.1}_{-0.1}$	23^{+2}_{-2}	57^{+13}_{-11}	300^{+90}_{-90}	160
	$-2.8^{+0.1}_{-0.1}$	6^{+1}_{-1}	705^{+117}_{-115}	-3900^{+300}_{-300}	164
F1*	$-1.0^{+0.1}_{-0.1}$	$3.9^{+0.7}_{-0.5}$	1005^{+367}_{-54}	-6000^{+300}_{-300}	248
	$2.0^{+0.1}_{-0.1}$	16^{+2}_{-4}	73^{+24}_{-29}	240^{+120}_{-180}	72
	$-2.5^{+0.1}_{-0.1}$	9^{+1}_{-1}	744^{+102}_{-100}	-3900^{+300}_{-300}	68
F2*	$-0.2^{+0.3}_{-0.1}$	$5.0^{+1.1}_{-1.4}$	614^{+121}_{-64}	90^{+120}_{-90}	222
	$1.8^{+0.1}_{-0.1}$	21^{+3}_{-4}	71^{+22}_{-35}	180^{+120}_{-120}	104
	$-2.7^{+0.3}_{-0.1}$	5^{+1}_{-1}	1000^{+725}_{-169}	-4200^{+300}_{-300}	44
F3*	$0.0^{+0.1}_{-0.2}$	$4.7^{+0.6}_{-0.7}$	517^{+72}_{-127}	0^{+300}_{-300}	205
	$1.9^{+0.1}_{-0.1}$	29^{+4}_{-4}	30^{+17}_{-15}	360^{+150}_{-120}	92
	$-2.7^{+0.1}_{-0.1}$	8^{+1}_{-1}	672^{+81}_{-141}	-3900^{+300}_{-300}	81

* Multiple WAs are detected in this spectrum.

$^\bullet$ The parameter is fixed.

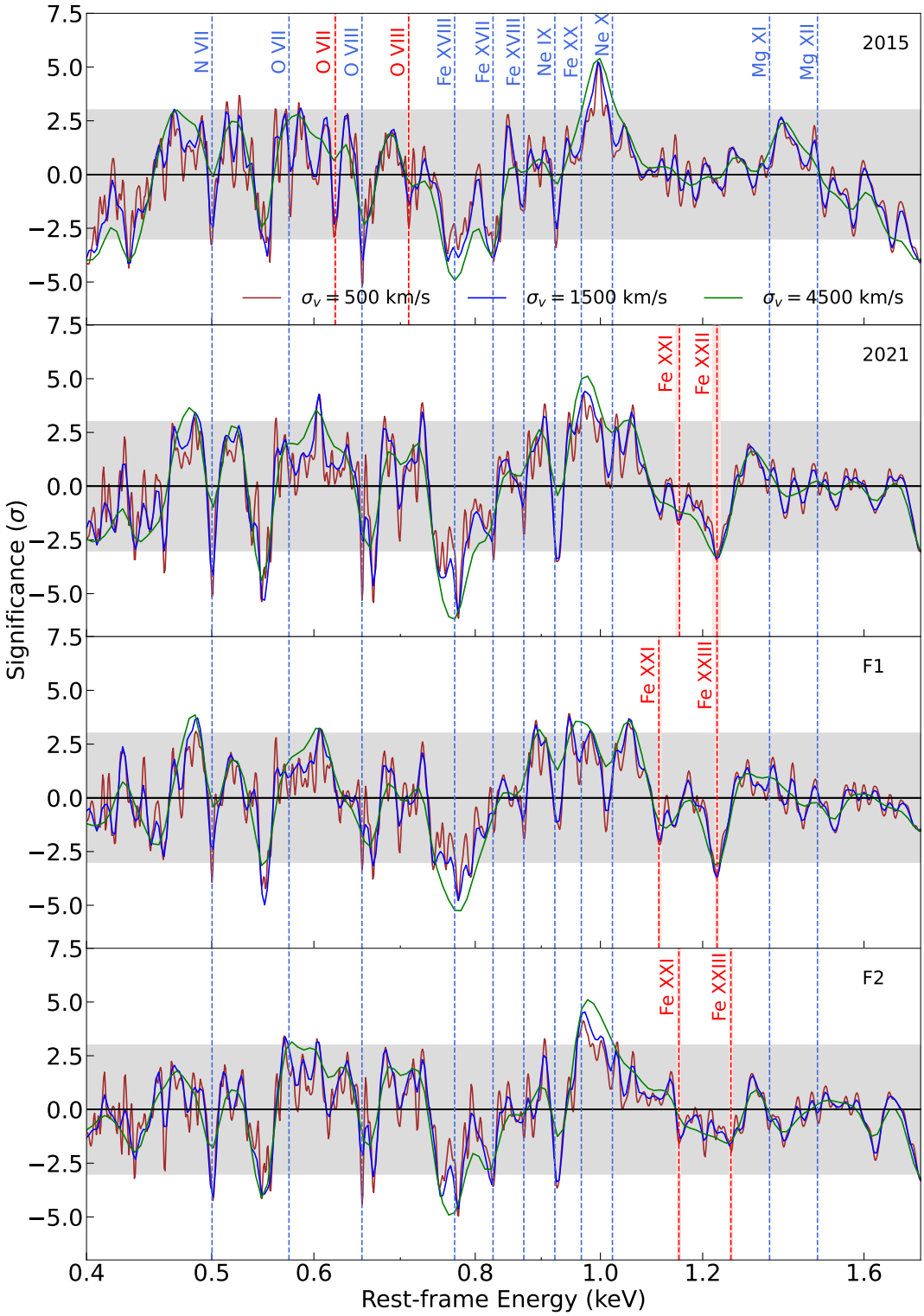

Fig. A.1 The single trial significance obtained from the Gaussian line scan with different line widths (500, 1500, 4500 km/s) over the rest-frame spectra of 1H 1934-063 in the RGS band. The vertical dashed *blue* lines represent the rest-frame energies of the known ion transitions as a reference, while the *red* lines and the shaded region respectively correspond to the centroid and 1σ uncertainties of the prominent UFO absorption lines detected in the following photoionization modeling. The gray region marks the 3σ significance.

A.2 RE J1034+396

RE J1034+396 is a nearby ($z = 0.042$) NLS1 galaxy, firstly exhibiting significant X-ray quasi-periodic oscillation (QPO) within an AGN with the period of 2.7×10^{-4} Hz [104, 8, 141]. It has an extraordinarily steep soft X-ray in the spectrum [283]. The mass of the central SMBH was estimated within 10^6–$10^7\,M_\odot$ (summarized by [49]), with the most probable mass range of $(1\text{–}4) \times 10^6\,M_\odot$ [104, 230, 40]. Over more than a decade, *XMM-Newton* has observed this source multiple times. A large observation campaign of this source was executed in 2020 and 2021 with a total amount of 855 ks exposure time. In Chapter 6, we focus on the data from the 2020-2021 campaign, as well as three archival observations capturing RE J1034+396 at bright states.

We present the outcomes of the Gaussian line scan over the continuum model in Fig.A.2. The results unveil a series of strong absorption lines at their rest-frame energies, including Ne IX, Fe XX, O VII, and O VIII. The spectra require two distinct WAs, each existing at different ionization states ($\log \xi \sim 3.6$ and $\log \xi \sim 1.9$). However, the cooler WA is superfluous for the 'high' spectrum (see Tab.A.1). A broad trough is evident on the blue side of the O VII line. We initially speculated its association with blueshifted O VII. However, our photoionization model scan suggests a neutral absorber ($\log \xi \sim 0$) with an ultra-fast velocity. In the F1 and 'high' spectra, the line width of this component is too broad to be constrained and thus fixed at 10000 km/s. This particular neutral ionization state precludes its classification as a UFO. Consequently, we name it a 'warm absorber', while its origin remains subject to future investigation.

A.3 PG 1244+026

PG 1244+026, identified as a highly variable NLS1 galaxy [140], exhibits notable features in the spectrum, including a strong soft excess and a highly ionized Fe K emission line [46]. Within this source, a soft lag at high frequencies and a hard lag at low frequencies were independently discovered by Alston et al. [6] and Kara et al. [154], suggesting the relativistic reflection in the inner accretion disk and the propagation of the accretion fluctuations respectively. Between 2011 and 2014, *XMM-Newton* conducted six observations of PG 1244+026, with five of these observations occurring consecutively in 2014. Despite these observations, the literature lacks any reports of UFOs in PG 1244+026.

The findings from the Gaussian line scan are presented in Fig.A.3. Within the time-averaged spectrum, a series of absorption lines appear as well as the N VII, O VII and ~ 0.9,keV emission lines. The identified UFO features encompass blueshifted O VII and O

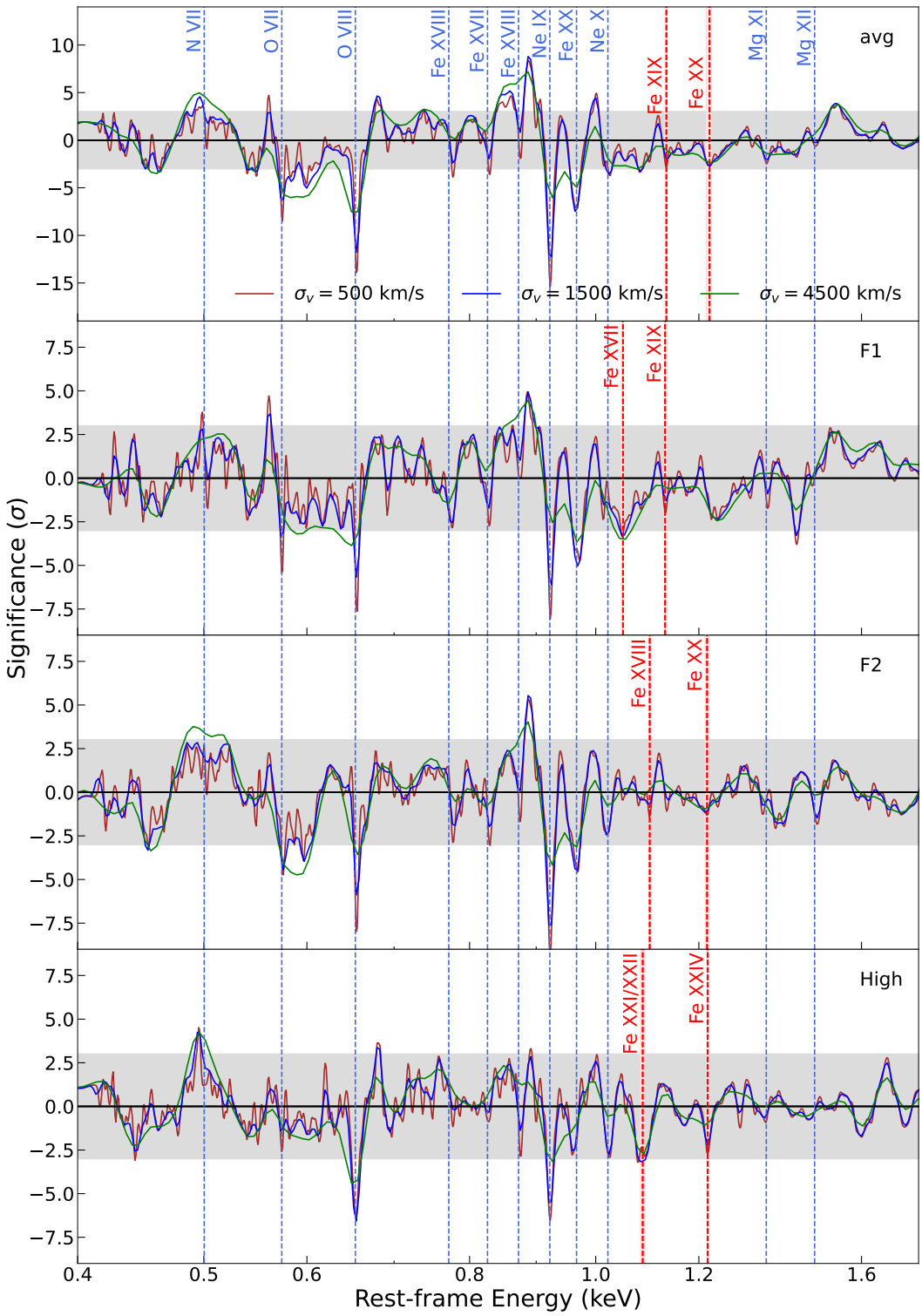

Fig. A.2 Similiar to Fig. A.1, but the scan is performed on spectra of RE J1034+396.

VIII, featuring a stable velocity of $v_{\rm LOS} \sim -13500$ km/s across all flux- and time-resolved spectra (time-resolved results are not shown). There is no warm absorber detection in this system.

A.4 PG 1211+143

PG 1211+143 is a well-studied and luminous NLS1/quasar at a redshift of $z = 0.0809$, showing a typical X-ray luminosity of $\sim 10^{44}$ erg/s and a bright optical flux with a strong 'Big Blue Bump'. This source is well-known for its spectral complexity and the presence of highly variable and multi-phase UFOs [276, 274, 275, 270, 272, 269, 288]. The velocity range of these UFOs spans from -18000 km/s to -81000 km/s [272, 51], revealing absorption lines across both soft and hard X-ray bands. Moreover, a corresponding UV counterpart to the UFO, outflowing at a comparable velocity, was documented by Kriss et al. [176]. In addition, a soft time lag of $\sim$ 500s at $\sim 10^{-4}$ Hz [56] and a hard lag up to $\sim$ 3ks at $\sim 10^{-5}$ Hz [195] were reported in this source. The total *XMM-Newton* exposure on this source culminates at $\sim$ 900 ks, with a majority of observations conducted consecutively at varying flux levels. As a result, a time-resolved spectroscopic analysis is undertaken to investigate both temporal and flux variability.

The Gaussian line scan results are shown in Fig.A.4, where the UFO features are marked by vertical red lines. The predominant UFO features are blueshifted O VIII and Fe UTA lines in the soft X-ray regime, along with S XVI, Ar XVIII, and Fe XXV/XXVI features in the hard X-ray band. The UFOs identified within our analysis are multi-phase and highly variable, compatible with prior investigations [288, 269]. According to our criterion for the outflow detection significance, we only find one fast warm absorber in the 'T7' spectrum (see Tab.A.1).

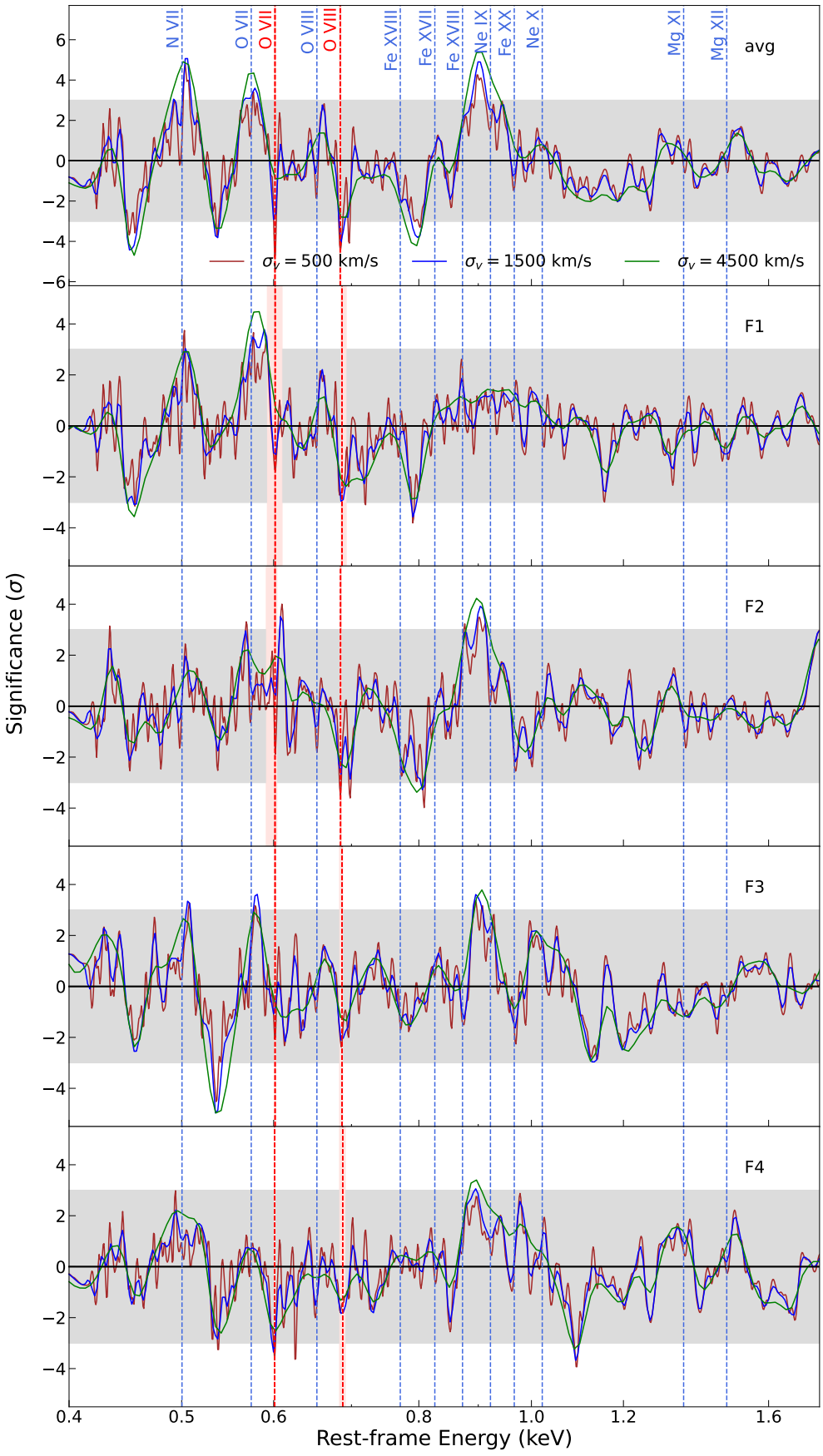

Fig. A.3 Similiar to Fig. A.1, but the scan is performed on the spectra of PG 1244+026.

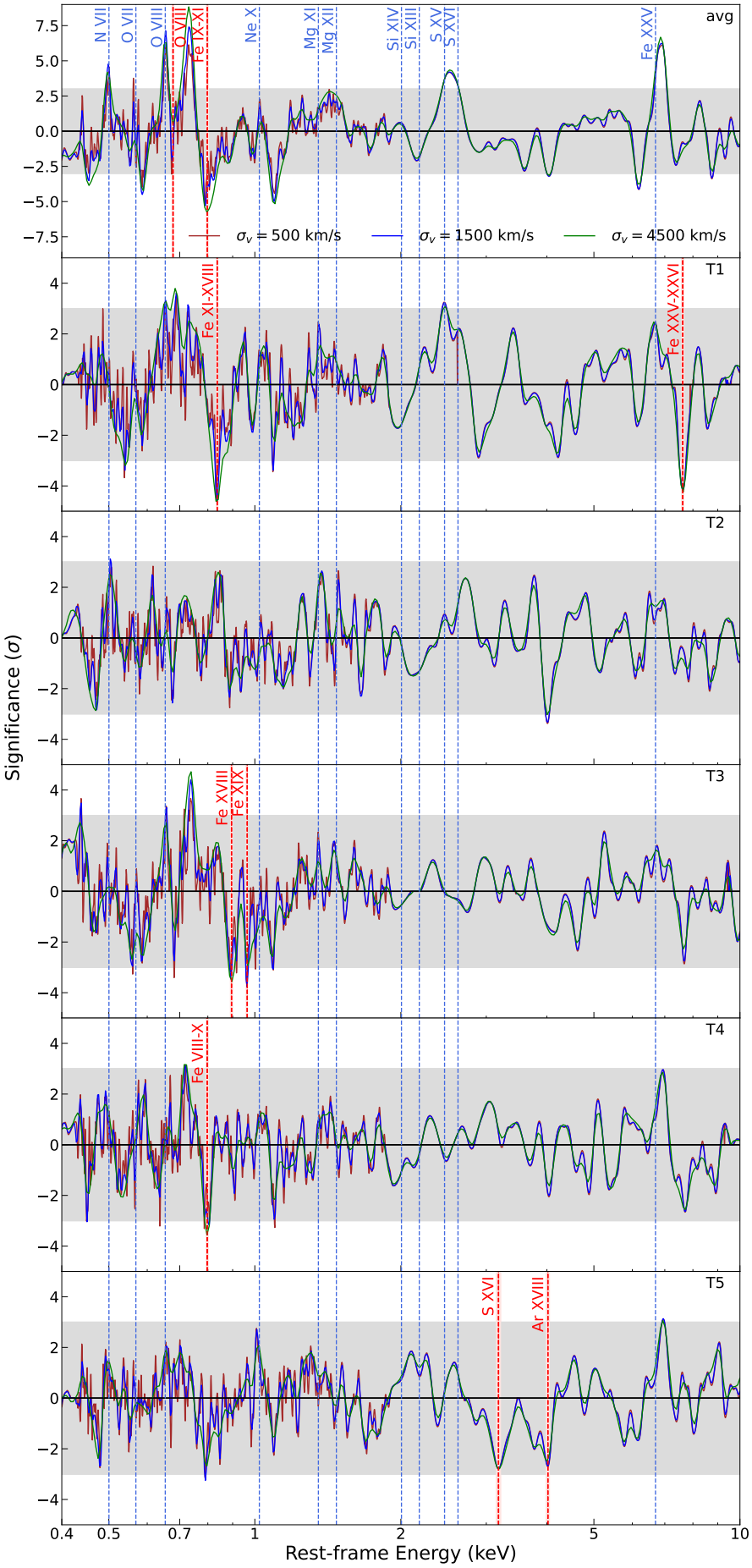

Fig. A.4 Similiar to Fig. A.1, but the scan is performed on the spectra of PG 1211+143.

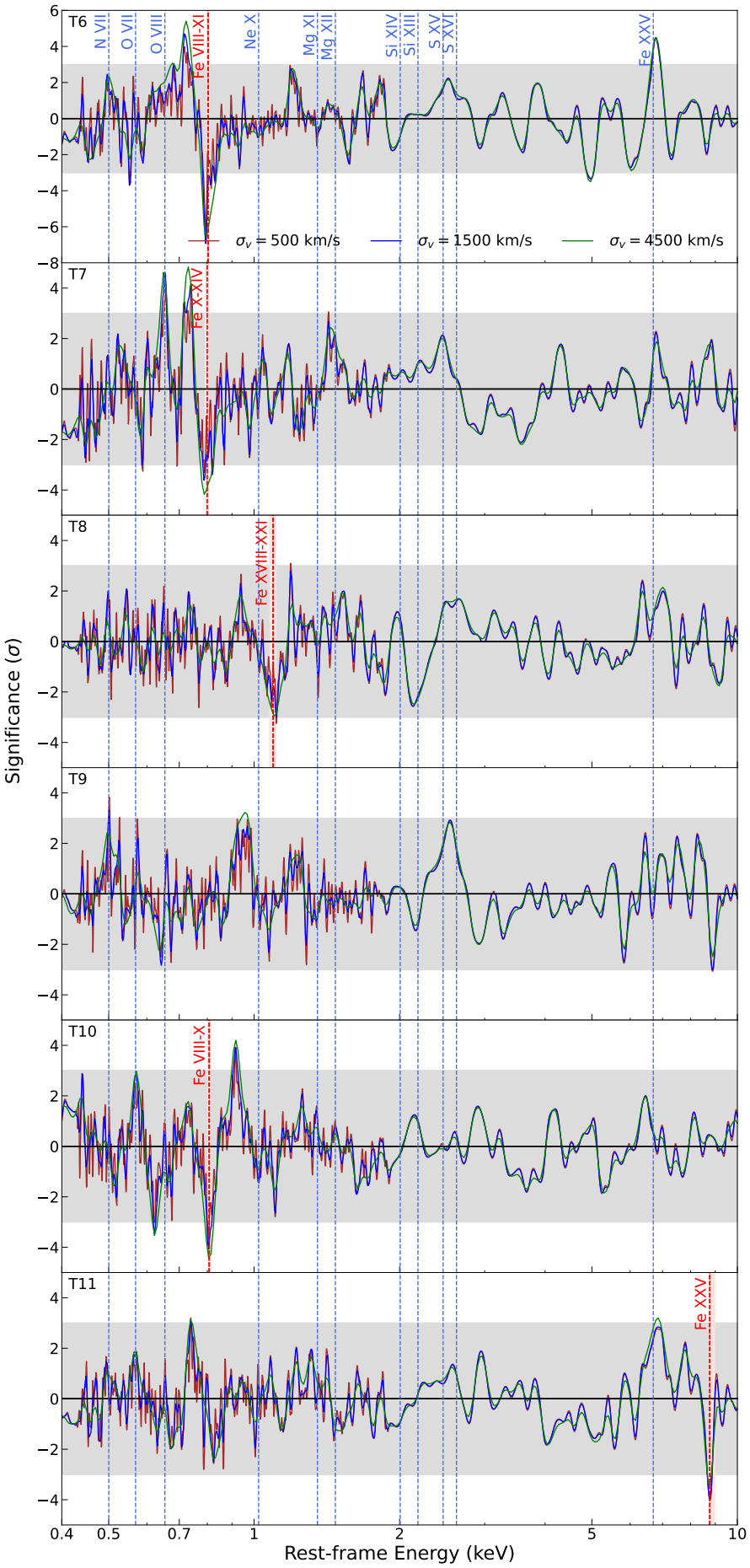

Fig.A.4 continued.

A.5 I ZW 1

I ZW 1 is a nearby ($z \sim 0.06$) NLS1 galaxy with a bright ($\sim 10^{44}$ erg/s, [91]) and variable X-ray luminosity [365]. Its X-ray spectrum reveals the presence of a strong Fe K emission and a weak soft excess [92]. Wilkins et al. [365] unveiled a time lag of ~ 160 s between the reflection-dominated energy and continuum-dominated band within $3\text{–}12 \times 10^{-4}$ Hz. Notably, the signatures of the light bending and X-ray echoes around the event horizon were observed through the delayed and redshifted flare emission observed in a luminous event in 2020 [363]. Furthermore, the soft X-ray spectrum of I ZW 1 reveals the presence of two WAs, exhibiting a long-term variable nature [43, 318]. It was attributed to the presence of either a two-phase WA originating from a shared clump or absorbing gas existing in a non-equilibrium state. The exploration of the hard X-ray spectrum unveils the existence of a highly ionized ($\log \xi \sim 4.9$) and high-speed ($v \sim -0.25c$) UFO during the 2005 and 2015 observations [285]. A subsequent observation in 2020, analyzed by Rogantini et al. [302], discovered a UFO, characterized by a similar velocity yet manifesting a lower ionization state ($\log \xi \sim 3.8$).

We present the results of the Gaussian line scan in Fig.A.5, where discernible absorption lines such as O VIII and Fe XVIII are identified at their rest-frame positions. A prominent trough appears around 0.53 keV across all spectra, which is associated with low-ionized oxygen. The UFO features are marked by the red vertical dashed lines in both soft (O VIII and Fe XXI-XXIII) and hard (Fe XXV-XXVI) X-rays. Consistent with findings by Silva et al. [318], our analyses have detected two distinct slow absorbers, characterized by neutral ($\log \xi \sim -0.4$) and high ($\log \xi \sim 2.7$) ionization states (see Tab.A.1). However, the high-ionization WA is not statistically necessary for the 2005 spectrum, according to our detection threshold. The limited photon counts of the 2005 spectrum cannot provide robust secondary absorber detection. While similar residuals around 0.7 keV are observed in the 2020 spectrum, they have already been explained by the warm absorber featuring a lower ionization parameter ($\log \xi \sim -1$), identified as Fe V-VI lines. The requirement for this lower ionization state is attributed to a distinct absorption feature solely within the 2020 spectrum, located around 0.63 keV. The absence of this feature within the 2015 spectra prevents the neutral warm absorber from entering the cooler regime, thus compelling the consideration of an alternative UFO to account for the unexplained 0.7 keV feature.

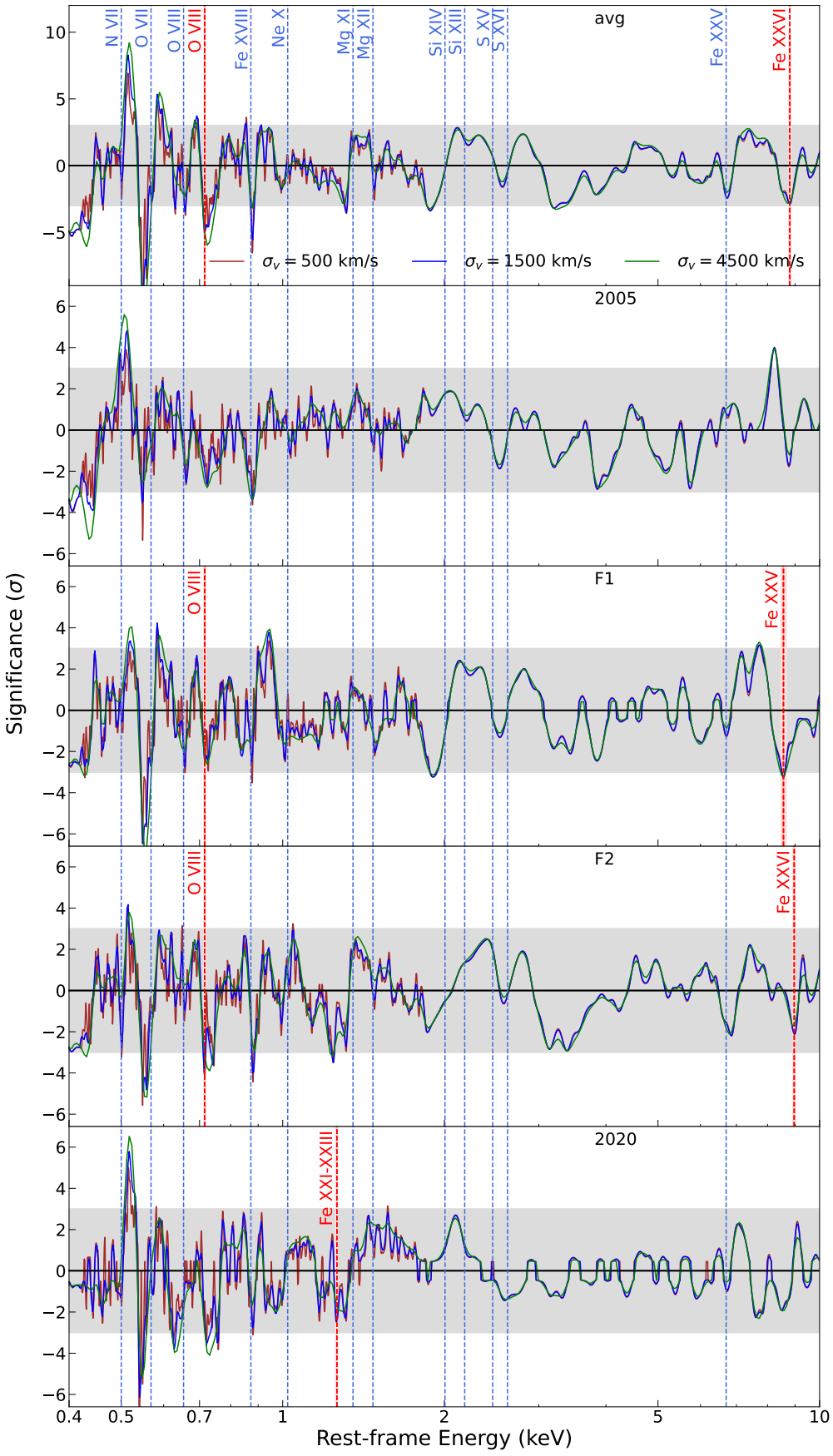

Fig. A.5 Similiar to Fig. A.1, but the scan is performed on the spectra of I ZW 1.

A.6 IRAS 17020+4544

IRAS 17020+4544 emerges as a nearby ($z = 0.0604$) radio-loud NLS1 galaxy, known to be characterized by a WA [191] and a compact radio emission [321]. The archival multi-wavelength campaign for IRAS 17020+4544 has revealed the presence of multi-phase UFOs ($v \sim 24000$–27000 km/s) in the X-ray spectra [197, 309], a galaxy-scale molecular outflow [198] in addition to a sub-relativistic jet on parsec scales in the radio band [105]. Moreover, a UV counterpart of the X-ray UFO outflow has been detected through Lyα absorption, showing a velocity similar to its X-ray counterpart. Collectively, these discoveries suggest that AGN-driven hot gas gives rise to large-scale shocks into the interstellar medium.

The outcomes of the line scan are depicted in Fig.A.6, exhibiting strong absorption and emission lines within the spectra. The prominent absorption features are located around 0.53, 0.75, and 0.88,keV. As reported in Sanfrutos et al. [309], our investigation identifies the presence of three distinct warm absorbers (WAs) in the spectra, each marked by substantial statistical significance (see Tab.A.1). WA1 and WA3 emerge as absorbers characterized by low ionization states, mainly explaining the absorption feature at 0.53 keV. On the other hand, WA2 is moderately ionized and models the feature around 0.75 and 0.88 keV.

A.7 The slope of the UFO properties versus $M_{\rm BH}$ and $L_{\rm ion}$

The slopes of the UFO properties including the column density Γ_{N_H}, ionization state $\Gamma_{\log\xi}$ and velocity Γ_v are collected to compare with the intrinsic AGN properties, consisting of the black hole mass $M_{\rm BH}$, bolometric luminosity $L_{\rm bol}$, Eddington ratio $\lambda_{\rm Edd}$, and inclination angle. The results are depicted in Fig.A.7. Our examination, facilitated by calculating the Pearson correlation coefficient, failed to reveal any significant correlations between the pairs of $\Gamma_{N_H}/\Gamma_{\log\xi}$ and AGN properties by calculating the Pearson correlation coefficients. Only an anticorrelation is observed between Γ_v and $\lambda_{\rm Edd}$, discussed in Section 6.5.4.

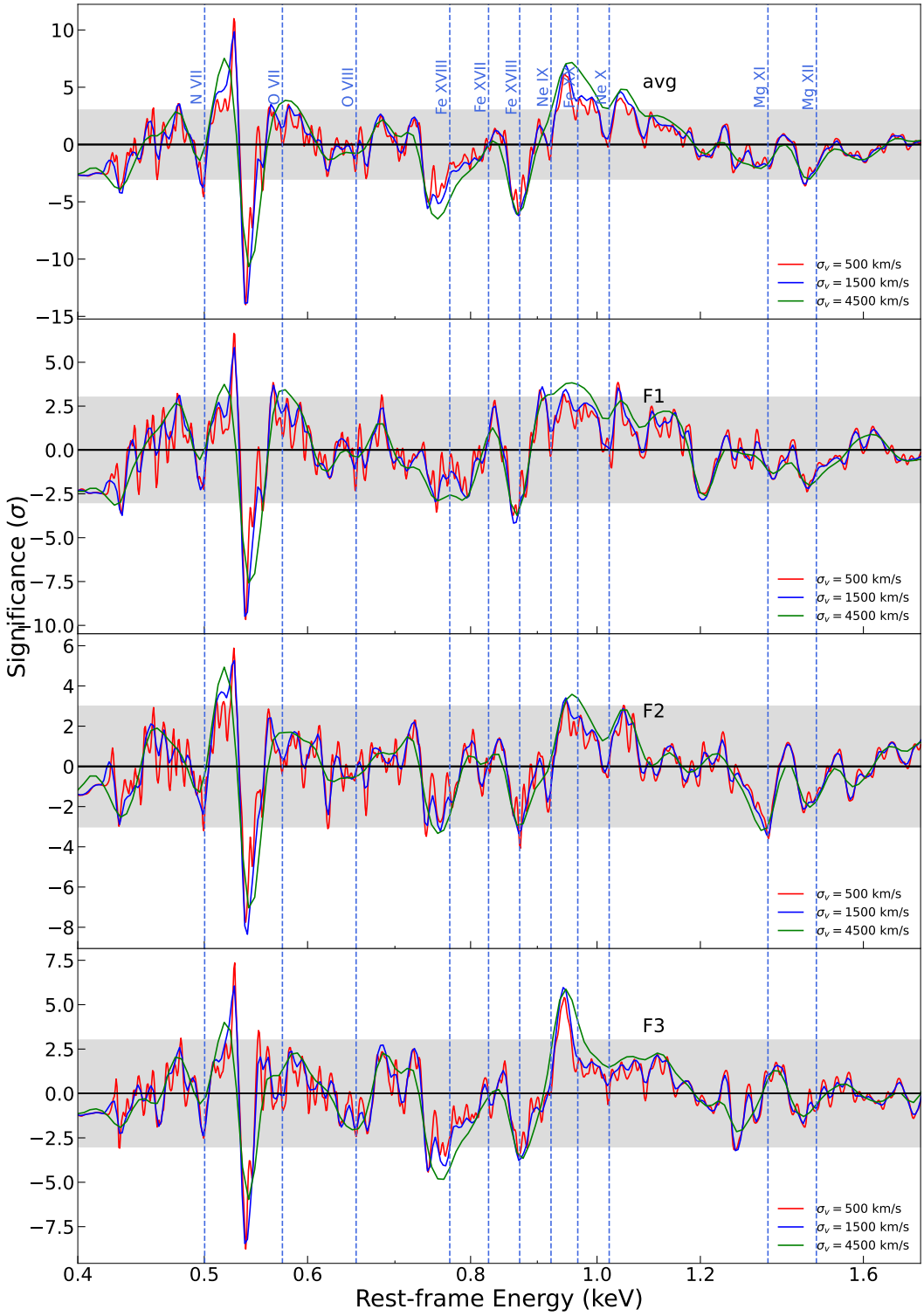

Fig. A.6 Similiar to Fig. A.1, but the scan is performed on the spectra of IRAS 17020+4544.

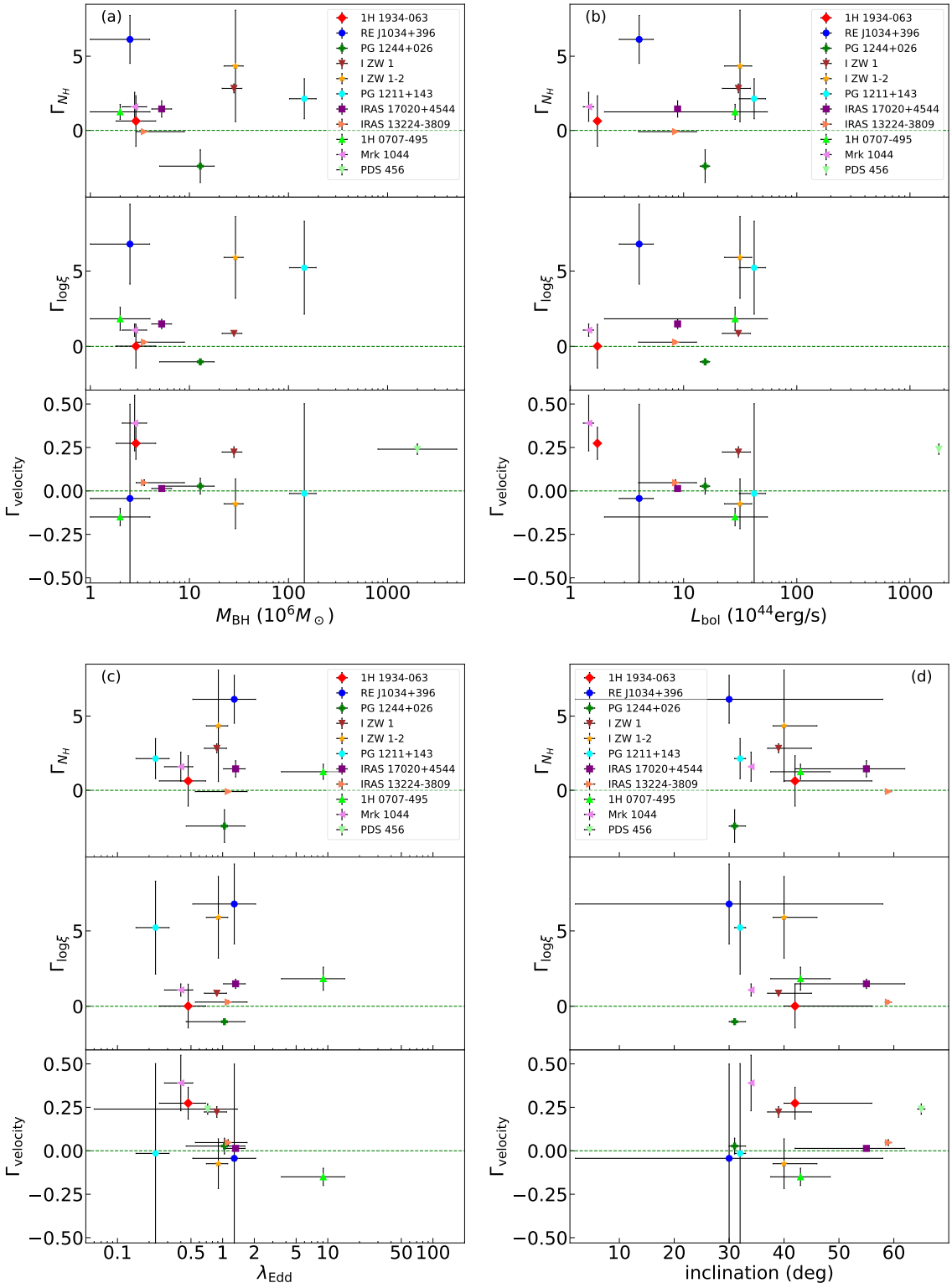

Fig. A.7 The evolution slopes of the UFO column density Γ_{N_H} (*top*), ionization state $\Gamma_{\log\xi}$ (*middle*) and velocity Γ_v (*bottom*) versus the black hole mass $M_{\rm BH}$ (*a*), bolometric luminosity $L_{\rm bol}$ (*b*), Eddington ratio $\lambda_{\rm Edd}$ (*c*), and inclination angle (*d*). The data come from the results listed in Tab.6.2 and 6.4. The horizontal dashed lines denote the zero value of the slope.